



Deliverable 2.9: Final technical report on the steel/cement material interactions

Work Package 2

This project has received funding from the European Union's Horizon 2020 research and innovation programme 2014-2018 under grant agreement N°847593.



<http://www.ejp-urad.eu/>

Document information

| | |
|-----------------------------|--|
| Project Acronym | EURAD |
| Project Title | European Joint Programme on Radioactive Waste Management |
| Project Type | European Joint Programme (EJP) |
| EC grant agreement No. | 847593 |
| Project starting / end date | 1st June 2019 – 30 May 2024 |
| Work Package No. | 2 |
| Work Package Title | Assessment of Chemical Evolution of ILW and HLW Disposal Cells |
| Work Package Acronym | ACED |
| Deliverable No. | 2.9 |
| Deliverable Title | Final technical report on the steel/cement material interactions |
| Lead Beneficiary | IRSN |
| Contractual Delivery Date | 46 |
| Actual Delivery Date | 15/05/2024 |
| Type | Report |
| Dissemination level | PU |
| Authors | Charles Wittebroodt (IRSN), Jules Goethals (Subatech), Laurent De Windt (MINES ParisTech), Margit Fabian (MTA EK), George Dan Miron (PSI), Bojan Zajec (ZAG), Valery Detilleux (Bel-V). |

To be cited as:

Wittebroodt C., Goethals J., De Windt L., Fabian M., Miron G.D., Zajec B., Detilleux V. (2023): Final technical report on the steel/cement material interactions. Final version of deliverable D2.9 of the HORIZON 2020 project EURAD. EC Grant agreement no: 847593.

Disclaimer

All information in this document is provided "as is" and no guarantee or warranty is given that the information is fit for any particular purpose. The user, therefore, uses the information at its sole risk and liability. For the avoidance of all doubts, the European Commission or the individual Colleges of EURAD (and their participating members) has no liability in respect of this document, which is merely representing the authors' view.

Acknowledgement

This document is a deliverable of the European Joint Programme on Radioactive Waste Management (EURAD). EURAD has received funding from the European Union's Horizon 2020 research and innovation programme under grant agreement No 847593.

| Status of deliverable | | |
|-------------------------------|----------------------------|------------|
| | By | Date |
| Delivered (Lead Beneficiary) | Charles Wittebroodt (IRSN) | 2023-10-01 |
| Verified (WP Leader) | Diederik Jacques (SCK CEN) | 2023-11-30 |
| Reviewed (Reviewers) | Paul Wersin | 2023-12-21 |
| Revised (Lead Beneficiary) | Charles Wittebroodt (IRSN) | 2024-02-22 |
| Verified (WP Leader) | Diederik Jacques (SCK CEN) | 2024-03-08 |
| Approved (PMO) | Tara Beattie | 2024-04-18 |
| Submitted to EC (Coordinator) | Andra (Coordinator) | 2024-05-15 |

Executive Summary

Subtask 2.2 of the ACED work package of EURAD relied upon a combined modelling-experimental approach prone to provide key information on carbon steel/cementitious material interactions occurring at 80°C. The results obtained will provide basic data for the up scaling to waste package (Task 3) and disposal cell (Task 4) modelling. The pH effect on anoxic corrosion processes has been investigated by performing in situ and laboratory mock-up experiments involving classic CEM I and CEM II cements ($\text{pH} > 12$) as well as a low-pH cement grout ($10 < \text{pH} < 11$) called BCG. The geochemical evolution of such carbon steel/cementitious material systems has also been characterized for both perfect and imperfect (presence of spatial heterogeneity between steel and cement) interfaces. Corrosion processes, cementitious materials' evolution and porewater monitoring were assessed over a period ranging from one to 2 years of interaction. SEM, XRD and μ -Raman spectroscopy analyses supported by geochemical modelling allowed a full characterization of the corrosion mechanism. The corrosion rates were estimated by continuous monitoring thanks to electrochemical measurements and electrical corrosion sensors as well as by post mortem analyses (weight loss and optical measurements).

Thermodynamic work was done to better understand the conditions favouring Fe-containing hydrates phases formation and stability. A new structurally consistent solid solution model (CASH+ solid solution) was also developed to be able to accurately model the C-S-H phase in equilibrium solid- and pore-water composition of hydrated (blended) cement materials.

For highly alkaline cementitious materials (CEM I/CEM II), generalized corrosion was observed and very low corrosion rates were obtained. In the presence of CEM II/based concrete, a rapid passivation of C-steel surface is observed thanks to magnetite precipitation. Modelling revealed that chemical changes induced by temperature increase did not significantly affect the passivation corrosion process. The corrosion rate of low carbon-steel in the presence of CEM I followed an exponential decay law and corrosion rates values dropped to less than 0.1 $\mu\text{m}/\text{year}$ within 100 days of interaction. Magnetite and Si-hydrogarnet were the only corrosion products observed in the highly alkaline experiments. Such Si-hydrogarnet can form at the expense of magnetite provided that a source of silicon and calcium is available and can reach the surface of the steel prior to reacting to form other phases such as C-S-H. In a tightly closed system, favouring corrosion processes in reducing environment and limited ingress of elements from the cementitious material, magnetite will be predominant.

For all the steel/low-pH cement grout interaction tests (mock-up and in situ) performed in the presence of BCG material (direct or indirect interface), localized corrosion is observed. BCG material favored the formation of corrosion cells that induce localized corrosion primarily due to the presence of sulphides in both CEM III-A and bentonite components and also due to the important amount of residual oxygen able to easily migrate through such highly porous grout material. The corrosion sequence showed that iron sulphides and/or hydroxides are first formed locally in the anodic zone of the corrosion cell. Depending on the remaining amount of oxygen in the system, the depletion of sulphides led to the formation of either a dense magnetite layer or of a porous layer of iron hydroxides. For mock-up tests, we observed that magnetite transformation into iron sulphides/silicates was a slow process because of the stability of the very dense magnetite layer acting as a diffusive barrier. For in situ experiments, the transformation of the more porous hydroxide species was faster and generated large amounts of iron silicates in the corrosion product sequence. The corrosion rate measured for mock-up experiments exhibited initial values of around 10 $\mu\text{m}/\text{year}$ that seems either to stabilize or decrease over time. Several pits with depths ranging from 10 to 100 μm were detected and optical measurements clearly indicated an increase of the number of corroded zones with time, rather than an increase of the pit depth. This observation suggests that the coalescence of these pits would eventually lead to a generalized corrosion process. SEM observations performed on steel samples from in situ tests revealed a uniform CPs layer of around 230 μm that formed over a period of about two years. The high corrosion rate (115 $\mu\text{m}/\text{year}$) associated to such observation is confirmed by ER sensors in situ monitoring and would therefore be more than ten times higher than the corrosion rates obtained after one year of interaction in the corresponding mock-up tests. Such difference could be explained either by the higher amount of residual oxygen trapped in the BCG porosity or by the in situ heating conditions (from internal to external part of

the system) that enhanced the renewal of BCG porewater at the interface and thus favoured sulphide and oxygen ingress at the carbon steel surface or finally by the formation of a galvanic coupling between steel/argillite and steel/BCG contact zones.

Only little information on the nature and density of the microbial population was obtained, limiting the interpretation of the results associated to experiments studying the microbial activity impact on anoxic carbon steel corrosion processes when exposed to BCG material at ambient temperatures. However, some particular corrosion features were obtained (formation of homogeneous iron sulphides layers in the mock-up tests) and attributed to bacterial activity.

Alongside to these experimental activities, modelling of the mock-up experiments has been performed to support the discussion on the nature and sequence of corrosion products of steel. A reassessed thermodynamic database relative to iron containing cement hydrates was used within the reactive transport code HYTEC to model the initial chemistry and mineral assembly of all the materials at ambient temperature and their evolution when exposed to 80°C. Globally, the modelling correctly takes into account the specificities of the mock-up experiments with respect to the effect of temperature, of water chemistry and pH (from low pH cement to highly alkaline pH cement) and of the configuration (steel in contact with aqueous solutions vs. close contact between solid materials).

Table of content

| | |
|--|----|
| Executive Summary..... | 4 |
| Table of content..... | 6 |
| List of figures | 8 |
| List of Tables | 13 |
| Glossary..... | 15 |
| 1. Introduction | 17 |
| 2. Thermodynamic data of iron cement interaction | 19 |
| 2.1 Assessment of the thermodynamic data Fe bearing hydrates | 19 |
| 2.2 Iron uptake in C-S-H..... | 23 |
| 2.3 CASH+ solid solution model discretization..... | 25 |
| 3. Reactive transport modelling approach..... | 28 |
| 3.1 The reactive transport code HYTEC..... | 28 |
| 3.2 Thermodynamic databases | 28 |
| 3.3 Modelling grid of the BACUCE mock-up experiments..... | 30 |
| 3.4 Modelling grid of the MTA EK cell experiments..... | 31 |
| 4. BACUCE in-situ and mock-up experiments | 32 |
| 4.1 BACUCE experiments: general description and objectives | 32 |
| 4.2 BACUCE experiments | 33 |
| 4.2.1 Mock-up experiments | 33 |
| 4.2.2 In situ experiments..... | 35 |
| 4.3 Material and method..... | 39 |
| 4.3.1 Materials | 39 |
| 4.3.2 Methods | 50 |
| 4.4 Results..... | 54 |
| 4.4.1 Evolution of the cementitious materials mineralogy and pore water solution composition | 54 |
| 4.4.2 Impact of bacterial activity on corrosion | 64 |
| 4.4.3 Impact of temperature on corrosion..... | 72 |
| 4.4.4 Corrosion of steel in the presence of CEM I - Effect of cement composition and pH ... | 81 |
| 4.5 General discussion | 86 |
| 4.5.1 Corrosion mechanism and rates in mock-up and <i>in situ</i> tests..... | 86 |
| 4.5.2 Impact of temperature on the chemical evolution of the system | 92 |
| 4.5.3 Impact of microbial activity | 96 |
| 4.5.4 Impact of heterogeneity | 96 |

| | | |
|-------|---|-----|
| 4.6 | Conclusions | 97 |
| 5. | MTA EK experiments (High concentration WG) | 97 |
| 5.1 | Introduction | 97 |
| 5.2 | Experimental details | 98 |
| 5.2.1 | Concrete and steel compositions | 98 |
| 5.2.2 | Design of the cell experiments | 98 |
| 5.3 | Experimental results | 99 |
| 5.3.1 | Corrosion potential..... | 99 |
| 5.3.2 | SEM/EDX measurements and results | 100 |
| 5.3.3 | μRaman spectroscopy results | 104 |
| 5.3.4 | Chemical analysis of aqueous solutions..... | 105 |
| 5.4 | Modelling results..... | 106 |
| 5.4.1 | Foreword..... | 106 |
| 5.4.2 | Initial hydrochemistry and mineralogy of the concrete | 106 |
| 5.4.3 | Evolution of the aqueous chemistry with time | 108 |
| 5.5 | Discussion | 109 |
| 5.5.1 | Corrosion products at 80°C | 109 |
| 5.5.2 | Corrosion mechanism and rate | 111 |
| 5.6 | Conclusions | 111 |
| 6. | Conclusion and perspectives..... | 112 |
| | Appendixes | 115 |
| | References | 123 |

List of figures

| | |
|---|----|
| Figure 1: Comparison of logK solubility constant values as a function of temperature, calculated curves, measured symbols (Dilnesa et al., 2014a). Dashed lines calculated using the reported values for the entropy and heat capacity in Dilnesa et al. (2014a), continuous and dotted line calculated using the values for the entropy and heat capacity estimated using the additivity and VBT methods, respectively. | 21 |
| Figure 2: Comparison of Pourbaix diagrams at 80°C calculated using hydrogarnet properties from Dilnesa et al. (2014a) (a); calculating using the estimated entropy and heat capacity (additivity, Table 2) (b) | 22 |
| Figure 3: Hydration of PC (a, c) and PC blended with silica fume (b, d). Evolution of phase mass (in gram) as a function of time for PC (a) and PC blended with silica fume (b). Distribution of iron between ferrite and hydrogarnet (c) and between stable Fe bearing phases that result from hydration (d). | 24 |
| Figure 4: Effect of temperature on iron distribution between C-S-H and (Al, Fe)Si-hydrogarnet (a) and FeOOH (ferrihydrite) (b). | 25 |
| Figure 5. Code snapshot from the script to discretize the CASH+ model, generate the solubility reactions and export them into CHESS and PHREEQC data files. | 26 |
| Figure 6: Comparison of Pourbaix diagrams at 25 and 80°C of the built (a, b) with the CEMDATA database (D. Miron, PSI, pers. comm.) and (c, d) the Thermochimie database plus updated CAFSH data (chapter 2.1) and Thermodem for ferrihydrite; the diagrams c and d were calculated with CHESS: activity $Fe^{2+} = 10^{-5}$, activity $Ca^{2+} = 10^{-3}$, activity $Al(OH)_4^- = 10^{-4}$, total $H_4SiO_4 = 10^{-4}$ | 29 |
| Figure 7: Generic modelling grid in 2D cylindrical symmetry of the BACUCE mock-up experiments where the cementitious material can be CEM I or the low-pH bentonite grout. | 31 |
| Figure 8: Modelling grid of the experimental cell in cylindrical symmetry. | 31 |
| Figure 9: Schematic representation of the BACUCE in situ experimental set-up in the Tournemire URL at ambient temperature (15°C) or at 80°C (top) and zoom on the heterogeneous configuration of the reactive chamber (bottom). The borehole diameter is 76 mm (BAC-1 and BAC-2) or 101 mm (BAC-3, BAC-4 and BAC-5), and the tube diameter to 55 mm (BAC-1 and BAC-2) or 65 mm (BAC-3, BAC-4 and BAC-5) | 32 |
| Figure 10: Schematic representation of a cell used for laboratory corrosion test (side view)..... | 33 |
| Figure 11: (a) Set -up of the experiment 1 - R with (b) a schematic 3D-view of the cementitious material-steel assembly put in the PTFE reactor; (c) set-up of the experiment 2 -C. | 34 |
| Figure 12: Schematic cross section of the IRSN URL (Tournemire)..... | 35 |
| Figure 13: “Scalped” upper part of TU37B tube | 37 |
| Figure 14:Electrical Resistance (ER) corrosion sensors (developed by ZAG) | 37 |
| Figure 15: Hydrating system composed of (i) PTFE skirt-shape sealing system (white parts) and (ii) three stainless-steel lines. | 38 |
| Figure 16: Modelling of the conversion of ettringite into monosulfoaluminate with C3AH6 but without katoïte in the mineral assemblage..... | 42 |
| Figure 17: (a) Microstructure of the P235GH low carbon steel and (b) chemical composition. The balance is Fe | 43 |
| Figure 18: (a) Microstructure parallel to the rolling direction and composition of the TU37b steel measured by Optical emission spectrometry with a SPECTRO MAXx Ametek©; along with SEM-EDX mapping of the external mill-scale layer of the Tu37b steel. The microstructure of the steel was revealed | |

after polishing the steel surface down to 0.05 μm with silicon colloids following chemical etching with a 2% HNO_3 Nital solution..... 43

Figure 19: Microstructure and composition of the DC03 steel measured by Optical emission spectrometry with a SPECTRO MAXx Ametek. 44

Figure 20: (a) Overcoring operation of BAC 1 in situ experiment, (b) slice of BAC 1 cut from the 1-meter-long core (c) embedding of slice coming from BAC 2 (d) milling of a sub-sampled slice of BAC 1 (e) sub-sampled slice of BAC 1 after milling operation (f) final embedded sample for characterization of the interfaces. 51

Figure 21: XRD patterns of the BCG disks from mock-up tests, after different period of immersion in synthetic porewater solution at 80°C. 55

Figure 22: μ -XCT slices sections of (a) the densified silica fume particles (DSFp) together with grout cement disk sections coming from experiment 2 - C after (b) 0, (c) 28, (d) 93 and (e) 300 days of interaction with BCG-synthetic solution at 80 °C. 55

Figure 23: μ -XCT computed 3D representation of the BCG (left side) and of the macro-porosity of BCG (right side - yellow) obtained on a fragment of grout cement disk coming from experiment 2-C after 28 days of interaction with synthetic solution at 80°C along with the graph showing the evolution of macro porosity (part of total porosity with pore volume superior to 8 μm^3) with time..... 56

Figure 24: *Modelling of the change with time of the chemical composition of the solution in the cell (total aqueous concentration); the experimental data (from exp. 1-R) are given for comparison.* 60

Figure 25: XRD patterns of the cement disks surfaces coming from experiment 2-C. 60

Figure 26: SEM-EDX mapping of a cement cylinder (EXP 1-R) after 354 days of interaction with hyperalkaline synthetic solution at 80°C. 61

Figure 27: Model 2 with C3AH6: zoom on the potassium and sulphate total aqueous concentration, among others relevant for fitting the effective diffusion coefficient of the cement paste. 62

Figure 28: Modelling of the change with time of the chemical composition of the solution in the cell (total aqueous concentration); the experimental data are given for comparison. 63

Figure 29: Macroscopic pictures of the metallic coupons associated to each corrosion tests (different medium: tests performed in “mix 75/25”: sterile test (SC), test without (NIC) or with (IC) microbial inoculation; tests performed in “synthetic Tournemire argillite porewater”: sterile test (SA), test with (IA) microbial inoculation, and contact time). 64

Figure 30: SEM-ES pictures associated to cross-section analyses of metallic coupons of IA-41 (A, B), NIC-24 (C), NIC-48 (D) and IC-42 (E). 65

Figure 31: Selected optical micrographs of samples coming from BAC-1 and BAC-2 experiments 65

Figure 32: Secondary electron (SE) images of metallic coupons surface from SA-41 (A) and SC-41 (C) tests and associated EDX spectra (B et D, respectively). 67

Figure 33: Typical Raman spectra obtained for the metallic coupon surface studied in sterile conditions SA-41 and SC-41 (Magh = maghemite; Magn = magnetite). 67

Figure 34: SEM pictures associated to cross-section analyses of metallic coupons of NIC-9 (A and B), NIC-24 (C and D) and NIC-42 (E and F) tests. Secondary electron (SE) images (A, C, E) and Energy-Dispersive X-ray Spectroscopy (EDX) mapping (B, D, F). Sulphur in yellow color, iron in green color.68

Figure 35: Surface morphology images obtained by SEM-EDX (A, B, C) and associated SEM-EDX elementary analyses of the pointed zone (D, E, F). These results are associated to NIC-9 (A et D), NIC-24 (B, E) and NIC-41 (C, F) tests. 68

| | |
|--|----|
| Figure 36: Typical Raman spectra obtained for the metallic coupon surface studied in non-sterile conditions (IA, NIC and IC tests) (Magh = maghemite; Mn = mackinawite ; G = greigite)..... | 69 |
| Figure 37: SEM-EDX mappings of steel/heterogeneity interface for BAC-1 experiment. | 70 |
| Figure 38: SEM-EDX mappings of steel/BCG interface for BACUCE 1 and BACUCE 2 experiments. 71 | |
| Figure 39: SEM-EDX mappings of steel/BCG/argillite interface for BAC-1 and BAC-2 experiments. ... | 71 |
| Figure 40: Ternary diagrams presenting SEM-EDX analyses obtained for the different interfaces of BAC-1 and BAC-2 experiments. | 72 |
| Figure 41: General corrosion rates that have been measured for the different laboratory corrosion tests in function of time (x axis: duration in weeks)..... | 72 |
| Figure 42: Optical micrographs of the samples coming from the mock-up experiments 2-C (a and b) and 1-R (c and d) with (a) coupon corroded for 93 days, (b) coupon corroded for 300 days after chemical etching, (c) interface between BCG and steel after 28 days and (d) interface between BCG and steel after 354 days. | 73 |
| Figure 43: Optical micrographs of the unpolished samples coming from the BAC-3 in situ experiments. Both steel/BCG and steel/BCG/argillite interfaces are shown. | 74 |
| Figure 44: SEM-EDX mappings of steel/BCG interface after 147 days of interaction for the temperature mock-up experiment 1-R (a) and for the same interface for BAC-3 in situ experiment (b). | 76 |
| Figure 45: Ternary diagram presenting SEM-EDX analyses obtained for the corrosion products analysed at the BCG-steel interface for BAC-3 in situ experiment and mock-up experiment 1-R. | 76 |
| Figure 46: Raman spectra of the corrosion products observed in the mock-up experiment 1 R. The location of the analysed spot is given in Figure 44-a. | 77 |
| Figure 47: Raman spectra of the corrosion products observed in the mock-up experiment 2-C..... | 77 |
| Figure 48: Diffraction patterns of the corrosion products observed at the surface of the coupons from the mock-up experiment 2-C. The (hkl) reflections corresponding to an interreticular spacing of 7.1 and 3.55 Angstroms correspond to phyllosilicates belonging to the kaolinite-serpentine supergroup. | 78 |
| Figure 49: SEM-EDX mappings of steel/BCG/argillite interface for BAC-3 in situ experiment. | 78 |
| Figure 50: Optical measurements of the corroded layer for EXP 1-R with (a) Maximum corroded thickness observed. The values correspond to the maximum reported thickness observed on the external mill scale layer in direct contact with the BCG. The " 0 value" corresponds to the maximum thickness reported for the external mill-scale layer in a pristine steel sample. (b) Statistical histogram of the optical measurements of the corrosion thickness measured on the external mill-scale layer for samples coming from EXP 1-R. More than 250 measurements spaced 50µm apart were performed on each sample. The thickness of the mill-scale layer was not subtracted from the measurement. | 79 |
| Figure 51: Mean corrosion rates of carbon steel obtained from optical measurements of the corroded layer for experiment 1-R (black squares) and from weight loss measurements for experiment 2-C (red circles). | 80 |
| Figure 52: Sensors thickness evolution with time and associated calculated corrosion rates for BAC-3 and BAC-4 in situ experiments. | 80 |
| Figure 53: Pictures of corroded samples coming from mock-up EXP 2-C after 93 days of interaction (a) and from mock-up EXP 1R after 28 days (b) and 254 days of interaction showing both steel/solution interface (c) and steel-cement interface (d). The steel/CEM I (e) and steel/CEM I/argillite (f) interfaces from BAC-5 experiment are also shown. | 81 |
| Figure 54: XRD patterns of the surface of the coupons coming from EXP 2-C after 28 and 300 days of interaction. | 82 |

| | |
|---|-----|
| Figure 55: SEM-BSE picture of the surface of the coupon immersed for 28 days in SYNTHETIC SOLUTION (EXP 2-C) along with EDX spectra of the principal corrosion products and precipitates observed. The chemical composition of HA (hydroandradite) given corresponds to the mean of seven analyses..... | 83 |
| Figure 56: SEM-EDX mapping of the steel/heterogeneity (left side) and steel/CEM I (right side) for the sample immersed for 354 days in the synthetic solution coming from EXP 1-R..... | 83 |
| Figure 57: SEM-EDX mapping of the steel/heterogeneity interface coming from a BAC-5 sample and EDX analyses of localized in the SEM BSE image. | 84 |
| Figure 58: SEM-EDX mapping of the steel/CEM I/argillite interface coming from BAC-5 sample and μ -Raman spectrum associated to the SEM BSE image localization. | 84 |
| Figure 59: Corrosion rates measured by weight loss measurements in experiment 2-C. | 85 |
| Figure 60: Sensors thickness evolution with time for BAC-5 in situ experiment. | 85 |
| Figure 61: Schematic representation of the corrosion process observed for experiment involving BCG at 80°C (PWS = Pore Water Solution; TM = Transformed Media; CaS = oldhamite). | 87 |
| Figure 62: Speciation diagram at 80°C calculated with CHESS: activity $\text{Fe}^{2+} = 10^{-5}$, activity $\text{Ca}^{2+} = 10^{-3}$, activity $\text{Al}(\text{OH})_4^- = 10^{-4}$, pH 10.5 (the stability field of water is not drawn to more clearly represent the $\text{Fe}(0)$ stability domain). | 89 |
| Figure 63: Modelling of the location of CAFSH and magnetite precipitation after 180 days and distribution of the total aqueous Si concentration according to the effective diffusion coefficient D_e at the steel/cement interface. | 92 |
| Figure 64: Simplified geochemical modelling with CHESS at 80°C of the diffusion of an $\text{Fe}(\text{OH})_2$ plume induced by steel corrosion inside the cement/grout material. (A-B) full oxyhydroxide-sulfur-silicate system from the beginning; (C-D) increased chemical complexity: oxyhydroxide system (stage I-a), then oxyhydroxide-sulfur system (stage I-b), and finally the oxyhydroxide-sulfur-silicate system. (stages II and III)..... | 95 |
| Figure 65: Pourbaix diagram at 25°C and 80°C calculated with CHESS: activity $\text{Fe}^{2+} = 10^{-5}$, activity $\text{Ca}^{2+} = 10^{-3}$, activity $\text{Al}(\text{OH})_4^- = 10^{-4}$, total $\text{H}_4\text{SiO}_4 = 10^{-4}\text{M}$?; the yellow circle corresponds to the likely pH – Eh experimental conditions. | 95 |
| Figure 66: Cross-section view of one experimental setup indicating different materials (left) and a photograph showing the parts of the experimental setup in triplicate (right)..... | 99 |
| Figure 67: Evolution with time of the measured corrosion potentials on the standard hydrogen scale for the three cells at 80 °C. | 100 |
| Figure 68: SEM micrograph showing micro-cracks initiated in the steel in contact with concrete after 3 months (SC-3M sample) and the corresponding elemental mapping of Fe, O, Si, Ca and Mn. | 101 |
| Figure 69: SEM micrograph of the steel-concrete interface after 7 (left) and 12 (right) months. | 102 |
| Figure 70: Micro-Raman mapping and characteristic spectra obtained after 3 months (CS-3M). | 104 |
| Figure 71: Micro-Raman mapping and characteristic spectra obtained after 7 months (SC-7M). | 104 |
| Figure 72: Micro-Raman mapping and characteristic spectra obtained after 12 months (SC-12M)... | 105 |
| Figure 73: Effect of the diffusion coefficient on the time evolution of the non-reactive Na^+ concentration; the experimental data of the reservoir are added (blue circles) for the sake of comparison. | 108 |
| Figure 74: Modelling of the time-dependent evolution in concrete pore water at the steel/concrete interface (in red) and the reservoir chemistry (in blue). For the purpose of comparison, experimental data from the reservoir are included as blue dots. | 109 |

Figure 75: Modelling of the evolution with time of the pH of the concrete pore water (in red) and the reservoir (in blue)..... 109

Figure 76: Phase stability diagrams of possible corrosion products of C-steel in slightly to strongly alkaline chemical environments (CHESS/HYTEC code, Thermoddem database); activity $Fe^{2+} = 5 \times 10^{-5}$, activity $Ca^{2+} = 5 \times 10^{-4}$, total $H_4SiO_4 = 1 \times 10^{-5} M$, temperature = $80^\circ C$; the grey zones stand for likely pH – Eh conditions in the present steel/concrete system. 110

List of Tables

| | |
|--|----|
| Table 1: Thermodynamic properties of compounds used to estimate the S_{298}° and C_{p298}° of the hydrogarnet endmembers. | 20 |
| Table 2: Thermodynamic properties of hydrogarnet endmembers estimated using the additivity method (add) and volume-based thermodynamics (VBT), compared with values reported in Dilnesa et al. (2014a) | 21 |
| Table 3: Thermodynamic properties of iron hydrates estimated using the volume-based thermodynamics (VBT), compared with values reported in (Lothenbach et al., 2019)*. | 22 |
| Table 4: Temperature dependence of the solubility constants for iron bearing hydrates, based on the estimated standard molar entropy S_{298}° and heat capacity C_{p298}° using the additivity* and the VBT method. $\log_{10}K^{\circ}(T) = A + B/T + C \cdot \log_{10}(T)$ | 23 |
| Table 5: Selectivity constants of cationic exchange (Gaines-Thomas formalism, Tremosa et al., 2012) and constants of surface complexation reactions (non-electrostatic model, Marques Fernandes et al., 2012) of montmorillonite considered in the modelling of the bentonite fraction of the grout as well as for the clayey phase of the argillite. | 30 |
| Table 6: Borehole and experimental device information and experimental conditions associated to each BACUCE in situ experiments..... | 36 |
| Table 7: Recipe and bulk composition of the bentonite/cement grout. | 39 |
| Table 8: Chemical composition of CEM I from Val d’Azergues and mineralogical analysis provided by the manufacturer. | 40 |
| Table 9: Modelling of the initial mineralogy of the hydrated CEM I paste (Val d’Azergues) at 20°C and after a temperature increase to 80°C. | 42 |
| Table 10: Chemical composition of the synthetic argillite porewater solution. | 44 |
| Table 11: Preliminary modelling of the batch experiment, water chemistry: bentonite/cement grout in contact with demineralized water at 20°C, L/S ratio = 1 (ST1-1-7j). | 45 |
| Table 12: Modelling of initial porewater chemistry of the bentonite/low-pH cement grout at 80°C based on the batch experiments. | 46 |
| Table 13: Conditions applied (culture medium, micro-organisms inoculation, contact time) for all the mock-up anoxic corrosion tests..... | 46 |
| Table 14: Chemical composition of the synthetic solution used for BAC-1 and BAC-2 in situ experiments. Additional salts for bacterial growth are in blue..... | 47 |
| Table 15: Measured and modelled initial chemistry of the synthetic solution used for temperature in situ and mock-up experiments. Values are given in mol/L. | 48 |
| Table 16: Modelled and measured chemical composition and pH of the hyperalkaline solution used in Baccuce mock-up and in situ temperature tests (compared with data from Dauzères (2010). | 48 |
| Table 17: Modelled initial porewater chemistry of the hydrated CEM I paste (Val d’Azergues) at 20°C and after a temperature increase to 80°C. | 49 |
| Table 18: Summary of the relevant operations related to overcoring and sub-sampling operations | 51 |
| Table 19: Modelling of the initial mineralogy of the bentonite/low-pH cement grout at 80°C considering 75% of porosity..... | 57 |
| Table 20: Initial chemical composition of the synthetic solution of the cell considered in the modelling at 80°C (left side: mmol/L; right side: mg/L). | 58 |
| Table 21: Composition of the concrete..... | 98 |

| | |
|---|-----|
| Table 22: SEM-EDX analyses of the corrosion products and the steel for the SC-3M sample the locations of the spectra are given in Figure 68)..... | 102 |
| Table 23: SEM-EDX analyses of the corrosion products and the steel for the SC-7M sample (see Figure 69 left)..... | 103 |
| Table 24: SEM-EDX analyses of the corrosion products and the steel for the SC-12M sample (see Figure 69 right)..... | 103 |
| Table 25: Evolution of the chemistry of the aqueous solution sampled in the external Teflon container (Figure 66). | 105 |
| Table 26: Oxide composition of the clinker and slag considered in the modelling..... | 106 |
| Table 27: Calculated initial amounts of reactive hydrated phases of the concrete. | 107 |
| Table 28: Calculated pore water chemistry of the concrete at 20°C and 80°C..... | 107 |

Glossary

Andra: Agence nationale pour la gestion des déchets radioactifs

BCF: Boda Claystone Formation

BEL-V: Belgian TSO

BCG: Bentonitic Cement Grout

BFp: Blast Furnace particles

Cement notations:

A: Al_2O_3

C: CaO

H: H_2O

S: SiO_2

C₃A: aluminat

C₄AF: aluminoferrite

C₂S: belite

C₃S: alite

AFt: Aluminate Ferrite trisubstituted

AFm: Aluminate Ferrite monosubstituted

CH: Portlandite

C-A-S-H: Calcium Aluminate Silicate Hydrate

C-S-H: Calcium Silicate Hydrate

M-S-H: Magnesium Silicate Hydrate

Cp^{°₂₉₈}: standard heat capacity

CPs: Corrosion Products

C-steel: Carbon steel

DGR: Deep Geological Repository

DPL: Dense Product Layer

DSFp: Densified Silica Fume particles

EBS: Engineered Barrier System

ER sensor: Electrical Resistance sensor

HA: Hydroandradite

HG: Hydrogarnet

HCP: Hydrated Cement Paste

HLW: High-Level radioactive Waste

IC: Ion Chromatography

ICP-OES: Inductively Coupled Plasma – Optical Emission Spectroscopy

IRSN: Institut de Radioprotection et de Sûreté Nucléaire

Kw: Water decomposition product

Mmt: Montmorillonite

MREA: Matériau de Remplissage à l'Extrados de l'Annulaire

MTA EK: Magyar Tudományos Akadémia / Hungarian Academy of Sciences

ONDRAF: Organisme National des Déchets RADIOactifs et des matières Fissiles enrichies

PC: Portland Cement

PM: Porous Media

PTFE: PolyTetraFluoroEthylene

PVC: PolyVinylChloride

REV: Representative Elementary Volume

RTMs: Reactive Transport Models

RWM: Radioactive Waste Management

S°₂₉₈: standard molar entropy

SEM-EDX: Scanning electronic microscopy – Energy dispersive X-rays

SEM-SE: Scanning electronic microscopy – Secondary Electron

SF: Silica Fume

SHE: Standard Hydrogen Electrode

TC: ThermoChimie

TIC/TOC: Total Inorganic/Organic Carbone

TM: Transformed Medium

URL: Underground Research Laboratory

XCT: X-ray Tomography

XRD: X-ray Diffraction

VBT: Volume-Based-Thermodynamic

ZAG: Zavod za gradbeništvo Slovenije / Slovenian National Building and Civil Engineering Institute

1. Introduction

Several concepts for the deep geological disposal of high-level nuclear waste (HLW) have developed barrier systems implying large amount of both metallic and cement-based materials that will get into contact with each other.

According to the French concept, HLW will be embedded in a glass matrix cooled in a stainless-steel container that would be then encapsulated in cylindrical carbon steel overpack and inserted in a carbon steel casing tube within horizontal micro-tunnel drilled in the clay host rock. Ceramic pads would be fixed to the canisters to facilitate insertion in the carbon steel casing and to allow the reversibility of nuclear waste disposal during the operation period (approximately 100 years). A bentonitic cement-based grout (BCG) characterized by relatively low pH values ($10 < \text{pH} < 11$) would be injected between the carbon steel casing and the host rock to (i) neutralize acidity coming from pyrite oxidation while preserving the glass from detrimental highly alkaline media, (ii) limit oxygen diffusion and (iii) passivate the carbon steel casing surface.

Regarding the super-container concept proposed by both Belgium and Dutch national programs, carbon steel overpack (7.5 cm thick) containing the HLW would be encased in prefabricated cylindrical concrete buffer material (OPC/CEM I cement and limestone aggregates) of approximately 2 m in diameter. The use of such cementitious material ensures high pH values (around 12.5) that should effectively passivate the carbon steel overpack surface.

For its part, the Hungarian radioactive waste management company (PURAM) is designing a deep geological repository in the Boda Claystone Formation. The design for HLW relies on low carbon-steel containers containing the waste encased in a prefabricated cylindrical CEM II concrete buffer material.

For all concepts, the heat produced by HLW radioactive decay would induce an increase of the temperature up to 90°C in the disposal cell. Such thermal phase may impact thermodynamically and kinetically the corrosion processes affecting carbon steel elements through the evolution of the geochemical, mineralogical and microstructural composition of the cementitious material induced by temperature increase.

Therefore, to contribute to the long-term safety assessment of deep geological disposals, it appears essential to better understand the geochemical evolution at the interface between steel/cement-based materials that would arise at high temperature for engineered barrier systems. In this context, Subtask 2.2 of the ACED work package of EURAD relies upon a combined modelling-experimental approach prone to provide key information on such steel/cementitious material interfaces interactions occurring at 80°C. The results obtained should provide basic data for the up-scaling to waste package (Task 3) and disposal cell (Task 4) modelling.

The aim of this report is to present both numerical and experimental research works that have been performed within Subtask 2.2 activities and to summarize the main associated outcomes regarding geochemical evolution at steel/cementitious material interfaces (corrosion rates, geochemical/physical alterations). The report is structured as follows:

Chapter 2 presents thermodynamic data of iron in cement phases and proposes modelling approaches developed to better understand the fate of dissolved iron ions, released due to steel corrosion, diffusing into cementitious material and prone to form solid phases;

Chapter 3 details the reactive transport code and the thermodynamic databases that have been used to model initial parameters (chemistry and mineral assembly of cementitious materials at 20°C) and their evolution (80°C) for carbon steel/cement interactions occurring for both BACUCE WG (chap.4) and High Temperature WG (chap.5) mock-up experiments;

Chapter 4 investigates the impact of microbial activity and temperature (80°C) on the anoxic corrosion of carbon steel in contact with cementitious materials (low-pH cement grout or CEM I) in presence of spatial heterogeneity (imperfect interface between steel and cementitious material) thanks to *in situ* and laboratory mock-up experiments supported by geochemical modelling (BACUCE WG);

Chapter 5 presents the work done to characterize carbon steel/CEM II concrete material interactions occurring at high temperature (80°C) in a surrounding clayey geochemical environment representative of one of the Hungarian DGR concept options (High Temperature WG);

Chapter 6 recaps the main information regarding steel/cementitious material interfaces geochemical evolution that have been gathered within Subtask 2.2 and that would be useful for up-scaling modelling. An outlook of the possible improvement and work planned to cover the relevant knowledge gaps and missing processes is also presented.

2. Thermodynamic data of iron cement interaction

A review of Fe-containing cement hydrates can be found in De Windt et al. (De Windt et al., 2020) and Wieland et al. (Wieland et al., 2023). The stability of these phases depends on the composition of the system, including pH, concentrations of Al, Si, Fe, C, and S, as well as temperature. The formation of these phases is influenced by metastability and kinetic constraints. In the absence of silica, (Al, Fe)-monosulfate, (Al, Fe)-ettringite, solid solutions, Fe-monocarbonate, and hemicarbonate phases are stable (Dilnesa, 2012; Dilnesa et al., 2014b, 2012, 2011; Möschner et al., 2009, 2008). In the presence of silica, which is typical in cement systems, (Al, Fe)Si-hydrogarnet is the most thermodynamically stable hydrate, forming at ambient to elevated temperatures (~110 °C) (Dilnesa et al., 2014a, 2014b; Pally et al., 2020; Wieland et al., 2023). This phase is believed to form through corrosion at the interface between cement and steel, utilizing iron released from corrosion, as well as Si and Al from the cement pore solutions. Stabilizing hydrogarnet requires a pH of around 12 or higher, while at lower pH values, magnetite and iron oxy/hydroxides (e.g., ferrihydrite, lepidocrocite, goethite) become more stable (Wieland et al., 2023). Such low pH conditions are common in the early stages of hydration or in low pH cement systems containing silica fume.

Scoping calculations and simple phase stability calculations show that magnetite is predicted to form as a corrosion product under reducing conditions, in solutions relatively rich in iron but poor in Si and Al. With increasing Si (and Al) in the pore solution at high pH, the stability range of hydrogarnet expands, while at lower pH (pH < 12), phyllosilicates become more stable when compared to magnetite. Magnetite becomes more stable with increasing Fe content, conditions favoured closer to the steel surface, although incoming Si may eventually lead to the partial consumption of magnetite. While the formation of (Al, Fe)Si-hydrogarnet is slow at ambient conditions and may not be identifiable in young cement pastes, it readily forms at elevated temperatures and has been identified as a corrosion product of steel in cement solutions under elevated temperature and anoxic conditions (Pally et al., 2020).

The stability of Fe(II) is reduced under high pH conditions, even at low Eh values, as observed in experiments attempting to prevent the oxidation of Fe(II) at high pH (Mancini et al., 2021). Compared to Fe(II), Fe(III) is energetically favoured in hydrolysed form (Fe(OH)₄⁻) or within the structure of solids such as hydrogarnet or mixed with Fe(II) in magnetite. Hallet et al. (2023) observed the formation of (Fe(II), Mg)-Al-layered double hydroxide instead of siliceous hydrogarnet in slag cements when limestone was added. In low pH cements where hydrogarnet is not present, the supply of Ca, Si, and Al from the cement solution can lead to the formation of iron(II)-rich T–O phyllosilicates.

At the interface between steel and cement, (Al, Fe)Si-hydrogarnet, along with magnetite, is a thermodynamically favoured corrosion product. This has been confirmed in experiments. The stability of (Al, Fe)Si-hydrogarnet increases with temperature but decreases with pH. Outside the stability conditions of (Al, Fe)Si-hydrogarnet, depending on the concentrations of Fe, Si, Al, and the redox conditions, magnetite, oxy/hydroxides, and iron-bearing phyllosilicates may also form. These conditions are typical for low pH cement or in late stages of cement degradation.

2.1 Assessment of the thermodynamic data Fe bearing hydrates

Because of the importance of the (Al, Fe)Si-hydrogarnet phase in systems concerning steel-cement interactions the thermodynamic data was reassessed, particularly regarding the dependence of the stability constants with temperature. The currently available thermodynamic data for the iron containing siliceous hydrogarnet comes from the work of Dilnesa et al. (2014a) who synthesized phases of various compositions and measured their solubility at 20 and 50°C. Their experiments demonstrated the formation of a solid solution between C3FS0.84H4.32 and C3FS1.34H3.32. The aluminium endmembers C3AS0.84H4.32 and C3AS1.34H3.32 were also investigated. The presence of iron in the experiments stabilized the garnet phase as a solid solution between hydroandradite and hydrogrossular. This can be modelled as an ideal solid solution between C3AS0.84H4.32 and C3FS0.84H4.32 using the standard thermodynamic properties of the endmembers that were derived from the measured solution composition (Dilnesa et al., 2014a).

Table 1: Thermodynamic properties of compounds used to estimate the S_{298}° and Cp_{298}° of the hydrogarnet endmembers.

| Name | formula | [SiO ₂] | [H ₂ O] | V (cm ³) | S (J/K) | Cp (J/K) | Ref. |
|-----------|--|---------------------|--------------------|----------------------|---------|----------|-----------------------------|
| Andradite | Ca ₃ Fe ₂ (SiO ₄) ₃ | 3 | 0 | 132.0 | 316.4 | 351.9 | (Robie & Hemingway, 1995) |
| Grossular | Ca ₃ Al ₂ (SiO ₄) ₃ | 3 | 0 | 125.3 | 260.1 | 307.7 | (Robie and Hemingway, 1995) |
| Quartz | SiO ₂ | 1 | 0 | 22.7 | 41.4 | 44.6 | (Lothenbach et al., 2019) |
| Water* | H ₂ O | 0 | 1 | 14.75 | 40.9 | 41.3 | (Glasser & Jenkins, 2016) |
| Hydroxyl* | OH- | 0 | 1/2 | 11.08 | 20.7 | 21.2 | (Glasser and Jenkins, 2016) |

* Additive properties in solids (e.g., structural water properties not H₂O(l))

To approximate the temperature dependence of the solubility constants in the range of 0-100°C, known values of the entropy and heat capacity of the reaction can be used. Dilnesa et al. (2014a) derived entropy values for the endmembers from experimental data at the two measured temperatures (20 and 50°C), while heat capacity values were derived from reactions involving structurally similar analog phases (assuming negligible reaction effects). However, when comparing the entropy and heat capacity values of the iron endmembers to similar solid compounds like andradite, grossular, or aluminum-bearing hydrogrossular, the relatively high entropy values for the iron endmembers appear uncertain (Table 1 & Table 2). It is understandable that these values originate from fits to the experimental data of Dilnesa et al. (2014a) and there is no other data available to better constrain them. On the other hand, there are known methods to estimate these values that maintain the consistency with the expected trends as in other similar compounds.

It has been observed that many solids exhibit a relationship between their molar volume, entropy, and heat capacity, allowing for the estimation of the latter two properties based on the known volume (Glasser, 2021; Glasser and Jenkins, 2016; Helgeson et al., 1978). The standard molar entropy S_{298}° and heat capacity Cp_{298}° of the endmembers can be obtained using a volume-based thermodynamics (VBT) approach, utilizing the volume data V_{298}° (Dilnesa et al., 2014a).

$$S_{298}^{\circ} = V_m 1579 + 6 \quad (\text{in J}\cdot\text{mol}^{-1}\cdot\text{K}^{-1}) \quad (2)$$

$$Cp_{298}^{\circ} = V_m 1465 + 11 \quad (\text{in J}\cdot\text{mol}^{-1}\cdot\text{K}^{-1}) \quad (3)$$

where $V_m = 10^{21} \cdot \frac{V_{298}^{\circ}}{N_A}$ in nm³/(formula unit), $N_A = 6.022 \cdot 10^{23}$ is Avogadro's number, and V_{298}° is in cm³·mol⁻¹. A different estimation method is to use exchange reactions between similar solids assuming that the entropy and heat capacity effect of these reactions are zero. Another method to estimate S_{298}° and Cp_{298}° is from additivity reactions using compounds with well known properties as building blocks. The outcome of these estimation methods relies on the selection of structurally similar solids and the inherent uncertainty in their properties. However, the underlying principle of these methods is rooted in the relationship between these properties and the molar volume of solids.

Table 2: Thermodynamic properties of hydrogarnet endmembers estimated using the additivity method (add) and volume-based thermodynamics (VBT), compared with values reported in Dilnesa et al. (2014a)

| Name | Formula | [SiO ₂] | [H ₂ O] | V* (cm ³) | S* (J/K) | Cp* (J/K) | S _{add} (J/K) | Cp _{add} (J/K) | S _{VBT} (J/K) | Cp _{VBT} (J/K) |
|--------------------------------------|--|---------------------|--------------------|-----------------------|----------|-----------|------------------------|-------------------------|------------------------|-------------------------|
| FeSi _{0.84} -Hydroandradite | Ca ₃ Fe ₂ (SiO ₄) _{0.84} (OH) _{8.64} | 0.84 | 4.32 | 148.5 | 840 | 434 | 403 | 443 | 395 | 372 |
| FeSi _{1.34} -Hydroandradite | Ca ₃ Fe ₂ (SiO ₄) _{1.34} (OH) _{6.64} | 1.34 | 3.32 | 144.6 | 820 | 414 | 383 | 424 | 385 | 363 |
| AlFeSi _{0.84} -mixed | Ca ₃ AlFe(SiO ₄) _{0.84} (OH) _{8.64} | 0.84 | 4.32 | 147.3 | 619 | 425 | 374 | 416 | 392 | 369 |
| AlSi _{0.84} -Hydrogrossular | Ca ₃ Al ₂ (SiO ₄) _{0.84} (OH) _{8.64} | 0.84 | 4.32 | 142.5 | 375 | 414 | 347 | 390 | 380 | 358 |
| AlSi _{0.41} -Hydrogrossular | Ca ₃ Al ₂ (SiO ₄) _{0.41} (OH) _{5.18} | 0.41 | 5.18 | 146.1 | 399 | 430 | 365 | 406 | 389 | 366 |

* as reported in (Dilnesa et al., 2014a)

For the additivity method the properties of the compounds in Table 1 are used in the proportion to get the endmember composition for which the properties are estimated. For the VBT method the molar volume from XRD data reported in Dilnesa et al. (2014a) are used. The estimated values for the Al bearing hydrogrossular members are similar to the ones derived from experiments (Dilnesa et al., 2014a). For the iron hydroandradite endmembers, the estimated heat capacities agree with the values reported Dilnesa et al. (2014a) (also estimated), while the estimated entropy values are 400-200 J/K lower than the ones derived from experiments. The new entropy values for the iron endmembers are now similar to the aluminium ones and the difference to the heat capacity is not large, in agreement with the trends present in other similar compounds.

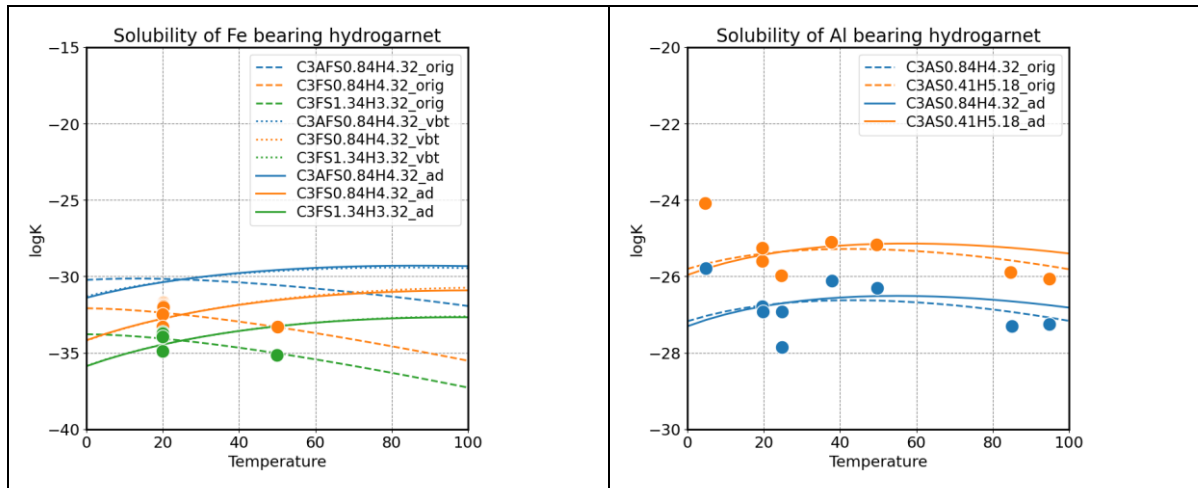


Figure 1: Comparison of logK solubility constant values as a function of temperature, calculated curves, measured symbols (Dilnesa et al., 2014a). Dashed lines calculated using the reported values for the entropy and heat capacity in Dilnesa et al. (2014a), continuous and dotted line calculated using the values for the entropy and heat capacity estimated using the additivity and VBT methods, respectively.

The calculated solubility constants of the Fe endmembers using the estimated values for the entropy and heat capacity, as expected, are not any more in agreement with the two experimental data points (Figure 1). In the case of the Al endmembers the agreement with the values from experiments is still reasonable. Modelling the hydrogarnet phase with the new estimates will have the effect of reducing the stability of the phase when compared to using the values reported in Dilnesa et al. (2014a). This can be seen on the Pourbaix Eh/pH diagram (Figure 2) where the ferrihydrite/hydrogarnet predominance line is shifted from pH 9.2 to 10 at 80 °C using the new estimated data. Iron bearing silicious hydrogarnet is

predicted to be the most stable iron bearing phase at high pH in both oxidized and reduced conditions. The hydrogarnet field is split between the mixed (Al/Fe) endmember and the silica rich iron endmember which is more stable at lower pH.

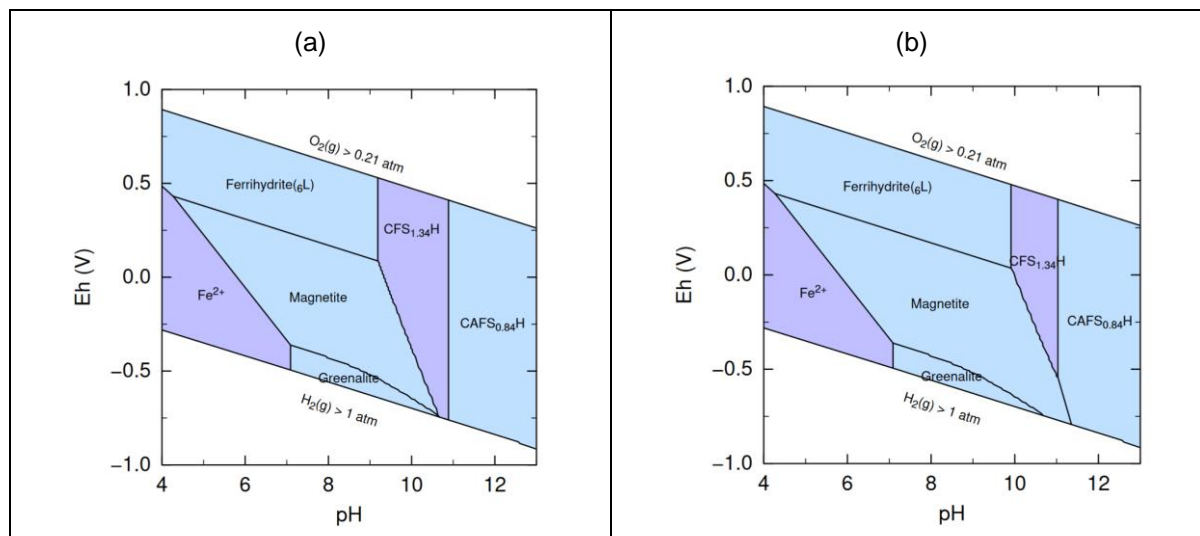


Figure 2: Comparison of Pourbaix diagrams at 80°C calculated using hydrogarnet properties from Dilnesa et al. (2014a) (a); calculating using the estimated entropy and heat capacity (additivity, Table 2) (b)

As demonstrated by Dilnesa et al. (2014a) the stability of iron silicious hydrogarnet surpasses that of other iron bearing cement hydrates such as Fe bearing monocarbonate, hemiacarbonate, monosulfate, and ettringite. In a trial calculation using the estimated entropy and heat capacity values for the hydrogarnet at 80 C in equilibrium with Portland cement pore solution, this phase was predicted to be less stable than the Fe-hemiacarbonate and Fe-monosulfate, contrary to the experiments. Looking at the thermodynamic data for these phases (Fe-hemiacarbonate, Fe-monocarbonate, Fe-monosulfate and Fe Friedel's salt) (Lothenbach et al., 2019), their entropies have larger than expected values, similar to the problem with the Fe hydrogarnet endmembers. This discrepancy was also discussed by Ghazizadeh et al. (2020) Therefore, to be consistent with the new estimates for the hydrogarnet, the same corrections are done for the other iron bearing cement hydrates. In this case the VBT method was used to calculate standard molar entropy S_{298}° and heat capacity $C_{p,298}^{\circ}$ utilizing the volume data V_{298}° (Lothenbach et al., 2019) (Table 3). Parameters for the $\log_{10}K^{\circ}(T)$ consistent with the new estimates for entropy S_{298}° and heat capacity $C_{p,298}^{\circ}$ and the properties of reactants from the PSI/Nagra database (Hummel and Thoenen, 2021) are provided in Table 4. Using the update thermodynamic data, the model predictions are qualitatively in agreement with the experimental observations and with the iron silicious hydrogarnet being the dominant phase at elevated pH both in reduced and oxidized conditions. Additional experimental data are necessary to better constrain the thermodynamic properties.

Table 3: Thermodynamic properties of iron hydrates estimated using the volume-based thermodynamics (VBT), compared with values reported in (Lothenbach et al., 2019)*.

| Name | Formula | V^* (cm ³) | S^* (J/K) | C_p^* (J/K) | S_{VBT} (J/K) | $C_{p,VBT}$ (J/K) |
|-------------------|---|--------------------------|-------------|---------------|-----------------|-------------------|
| Fe-hemiacarbonate | $\text{Ca}_3\text{O}_3\text{Fe}_2\text{O}_3(\text{CaCO}_3)_{0.5}(\text{CaO}_2\text{H}_2)_{0.5}(\text{H}_2\text{O})_{9.5}$ | 273.4 | 1270 | 841 | 723 | 676 |
| Fe-monocarbonate | $\text{Ca}_4\text{O}_4\text{Fe}_2\text{O}_3\text{CO}_2(\text{H}_2\text{O})_{12}$ | 291.7 | 1230 | 950 | 771 | 721 |
| Fe-monosulfate | $\text{Ca}_4\text{Fe}_2\text{SO}_{10}(\text{H}_2\text{O})_{12}$ | 320.6 | 1430 | 968 | 847 | 791 |
| Fe Friedel's salt | $\text{Ca}_4\text{Fe}_2\text{Cl}_2(\text{OH})_{12}(\text{H}_2\text{O})_4$ | 278.0 | 1286 | 855 | 735 | 687 |

Table 4: Temperature dependence of the solubility constants for iron bearing hydrates, based on the estimated standard molar entropy S_{298}° and heat capacity Cp_{298}° using the additivity* and the VBT method. $\log_{10}K^{\circ}(T) = A + B/T + C \cdot \log_{10}(T)$.

| Name | Reaction | A | B | C |
|--------------------------|---|-----------|-------------|-------------|
| *FeSi0.84-Hydroandradite | $(\text{Fe}_2\text{O}_3)\text{Ca}_3\text{O}_3(\text{SiO}_2)_{0.84}(\text{H}_2\text{O})_{4.32} + 4\text{H}^+ = 0.84\text{Si}(\text{OH})_4 + 0.64\text{H}_2\text{O} + 2\text{Fe}(\text{OH})_4^- + 3\text{Ca}^{+2}$ | -78.7073 | 12430.10838 | 23.03442993 |
| *FeSi1.34-Hydroandradite | $\text{Ca}_3\text{Fe}_2\text{O}_6(\text{SiO}_2)_{1.34}(\text{H}_2\text{O})_{3.32} + 1.36\text{H}_2\text{O} + 4\text{H}^+ = 1.34\text{Si}(\text{OH})_4 + 2\text{Fe}(\text{OH})_4^- + 3\text{Ca}^{+2}$ | -75.6106 | 11564.50835 | 21.42254408 |
| *AlFeSi0.84-mixed | $(\text{AlFeO}_3)\text{Ca}_3\text{O}_3(\text{SiO}_2)_{0.84}(\text{H}_2\text{O})_{4.32} + 4\text{H}^+ = 0.84\text{Si}(\text{OH})_4 + 0.64\text{H}_2\text{O} + \text{Fe}(\text{OH})_4^- + 3\text{Ca}^{+2} + \text{Al}(\text{OH})_4^-$ | -24.3842 | 9509.58960 | 5.968827628 |
| Fe-hemicarbonate | $\text{Ca}_3\text{O}_3\text{Fe}_2\text{O}_3(\text{CaCO}_3)_{0.5}(\text{CaO}_2\text{H}_2)_{0.5}(\text{H}_2\text{O})_{9.5} + 5\text{H}^+ = 8.5\text{H}_2\text{O} + 2\text{Fe}(\text{OH})_4^- + 0.5\text{CO}_3^{2-} + 4\text{Ca}^{+2}$ | -134.6042 | 20657.21078 | 42.22779827 |
| Fe-monocarbonate | $\text{Ca}_4\text{O}_4\text{Fe}_2\text{O}_3\text{CO}_2(\text{H}_2\text{O})_{12} + 4\text{H}^+ = 10\text{H}_2\text{O} + 2\text{Fe}(\text{OH})_4^- + \text{CO}_3^{2-} + 4\text{Ca}^{+2}$ | -157.0197 | 15932.77015 | 50.51303769 |
| Fe-monosulfate | $\text{Ca}_4\text{Fe}_2\text{SO}_{10}(\text{H}_2\text{O})_{12} + 4\text{H}^+ = \text{SO}_4^{2-} + 10\text{H}_2\text{O} + 2\text{Fe}(\text{OH})_4^- + 4\text{Ca}^{+2}$ | -132.6885 | 15857.76394 | 42.00215070 |
| Fe Friedel's salt | $\text{Ca}_4\text{Fe}_2\text{Cl}_2(\text{OH})_{12}(\text{H}_2\text{O})_4 + 4\text{H}^+ = 8\text{H}_2\text{O} + 2\text{Fe}(\text{OH})_4^- + 2\text{Cl}^- + 4\text{Ca}^{+2}$ | -112.6288 | 14961.61533 | 36.30677202 |

2.2 Iron uptake in C-S-H

Calcium silicate hydrate (C-S-H) is the main solid phase which contributes to the strength and other durability properties of hydrated Portland cements. The phase is also known to be a main sorbent of cations and anions. A new structurally consistent solid solution model, CASH+, was developed to be able to accurately model the C-S-H phase in equilibrium solid- and pore-water composition of hydrated (blended) cement materials (Kulik et al., 2022; Miron et al., 2022b, 2022a). The CASH+ solid solution is a thermodynamic model of aluminium containing calcium silicate hydrate and is used in calculating the hydration of ordinary Portland cement and low pH silica fume blended cement, for a better description of uptake of alkali metals (e.g., Na and K, major components in the pore solution) in C-S-H (Miron et al., 2022a). The model was extended for the uptake of Fe(III) and Fe(II) (De Windt et al., 2020), using the experimental data of Mancini et al. (2020, 2021). The experimental data showed that Fe(III) uptake in C-S-H is not affected by the Ca/Si with an average K_d of $700'000 \pm 1.5\text{E}05$ (L/kg) which is higher than that of Al. Fe(II) showed ~3 orders of magnitude smaller uptake, K_d Fe(II) 100 ± 20 (L/kg), but similar to other bivalent cations.

Once iron is released from corrosion a complex interplay between metastability, kinetics, local composition, and diffusion will play a role in the retention and mobility of iron in the cement paste (Stefanoni et al., 2020). As discussed before, Fe(II) will tend to be oxidized to Fe(III) species which will interact with the other cement hydrates such as C-S-H or react with the pore solution and precipitate secondary phases such as (Al, Fe)Si-hydrogarnet or oxy/hydroxides (magnetite, ferrihydrite, goethite, depending on the local composition pH and Eh). Upon hydration of the cement clinker C-S-H may form faster than hydrogarnet. In the case of aluminium it has been observed that its uptake in C-S-H decreases over time as it gets more stabilized in the more favourable hydrogarnet (Barzgar et al., 2021; Yan et al., 2023). The same affect may be true for the iron uptake in C-S-H as well. If the formation of iron bearing oxy/hydroxides or hydrogarnet is suppressed due compositional and kinetic effects iron will be sorbed onto C-S-H, otherwise C-S-H will be outcompeted by the other phases. Siramanont et al. (2021) show that when other iron bearing phases such as ferrihydrite hydrogarnet form in the system there is little uptake of Fe in C-S-H and only when these phases are suppressed increased Fe uptake in C-S-H was observed.

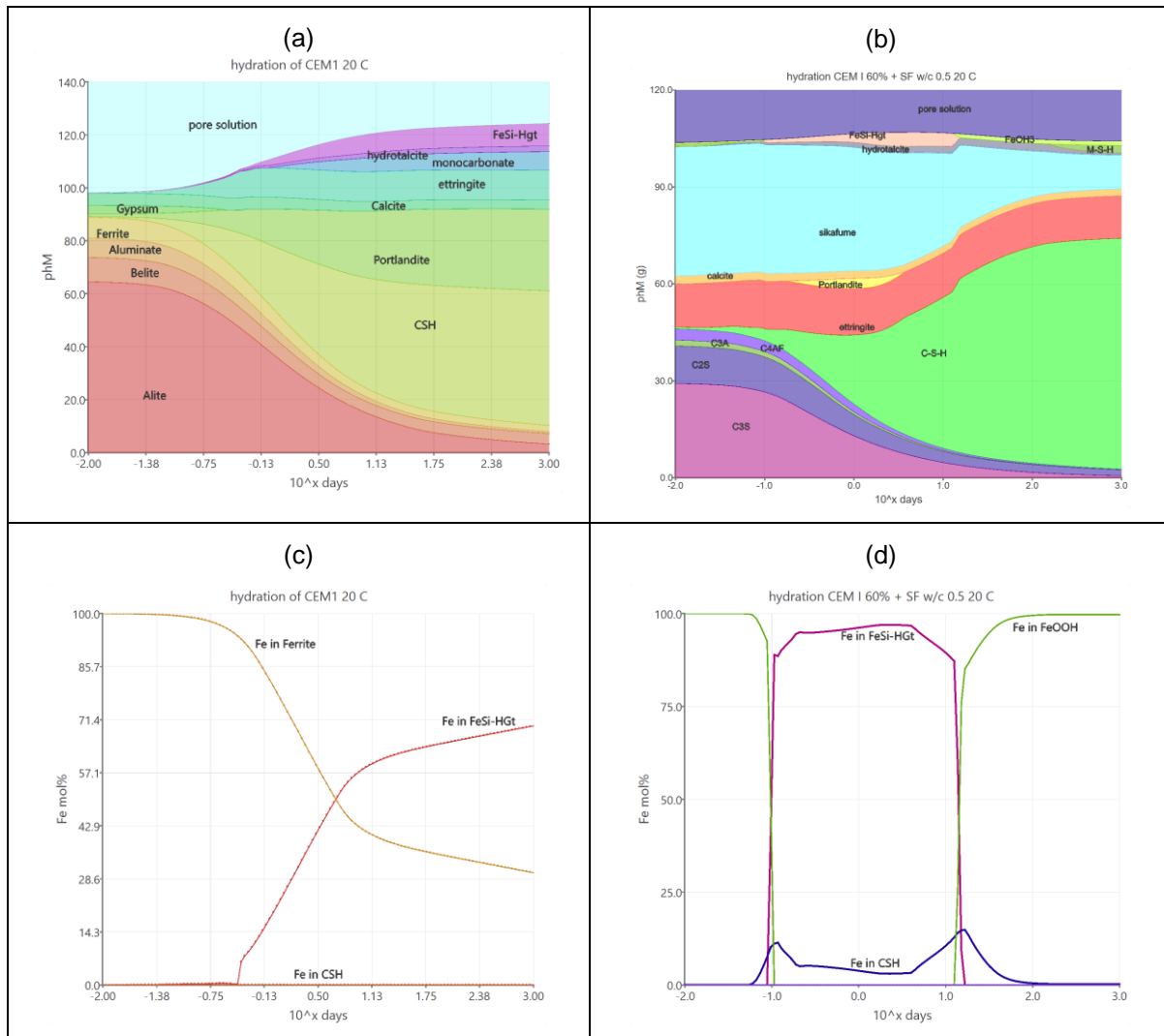


Figure 3: Hydration of PC (a, c) and PC blended with silica fume (b, d). Evolution of phase mass (in gram) as a function of time for PC (a) and PC blended with silica fume (b). Distribution of iron between ferrite and hydrogarnet (c) and between stable Fe bearing phases that result from hydration (d).

Using the extended CASH+ model for the uptake of Fe, scoping calculations were done to assess the competition for Fe between C-S-H, ferrihydrite and (Al, Fe)Si-hydrogarnet. These show that if we exclude metastability and kinetic effects, (Al, Fe)Si-hydrogarnet is the main Fe bearing phase and that in its presence the uptake of Fe in C-S-H is insignificant. In natural systems, over some periods of time, iron may be incorporated into C-S-H initially but with time the amount of Fe in C-S-H will decrease and form (Al, Fe)Si-hydrogarnet, similar to the effect on aluminium (Yan, 2022).

Upon hydration of ordinary Portland cement (PC) clinker (Miron et al., 2022a), Fe is released from the ferrite and assuming equilibrium it is predicted to go into the (Al, Fe)Si-hydrogarnet, with little uptake in C-S-H (Figure 3). In the case of hydration of PC blended with silica fume some uptake of iron in C-S-H is predicted in the intermediate hydration stage while at later stages only FeOOH is stable and takes up all the iron in the system (Figure 3). The uptake of iron in C-S-H is predicted to increase close to the boundaries of other iron containing phases. While the conditions of (Al, Fe)Si-hydrogarnet formation are thermodynamically favourable, at intermediate hydration of PC blended with silica fume, in real systems due to the slow kinetics this might not be observed. An increase in temperature would lead to an even weaker uptake of Fe in C-S-H (Figure 4)

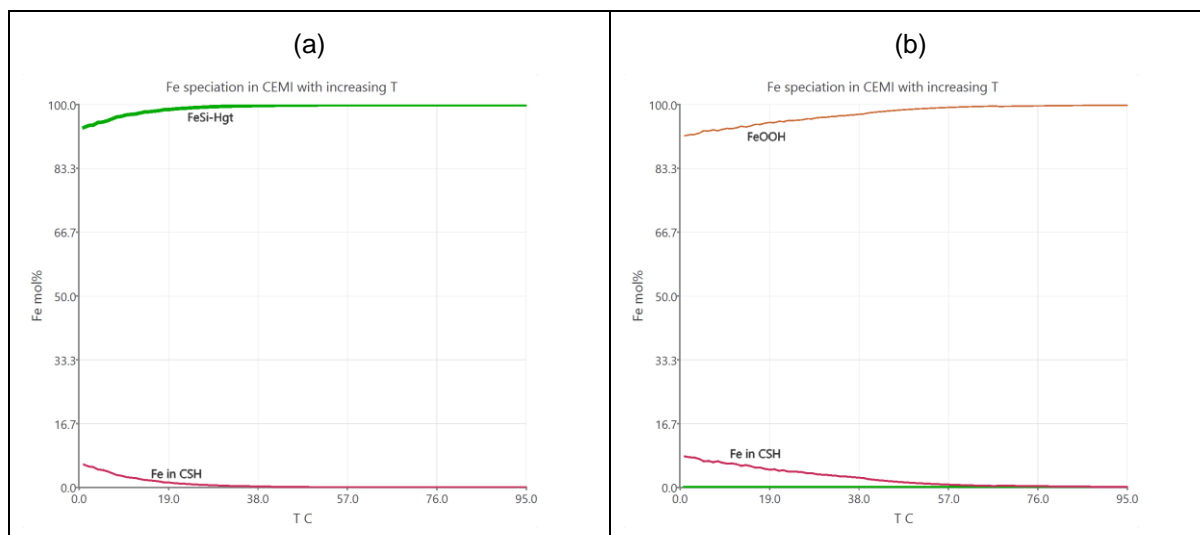


Figure 4: Effect of temperature on iron distribution between C-S-H and (Al, Fe)Si-hydrogarnet (a) and FeOOH (ferrihydrite) (b).

2.3 CASH+ solid solution model discretization

In order to be utilized in codes that do not have the implementation of multisite solid solution formulations, the CASH+ model needs to be discretized into a set of stoichiometric solids within a selected compositional space. These solids will form as distinct pure phases depending on the system composition. The accuracy of the solid solution approximation relies on the number of discrete phases chosen, which should correspond to the extent of property changes with varying composition. Initially, it was suggested (De Windt et al., 2020) that a smart discretization procedure would be necessary to determine the optimal number of discrete phases that adequately approximate the non-ideal solid solution model. However, the task proved difficult, to have both a smooth description of the C-S-H composition and cover the whole compositional space. Employing a small step size and more than two element vectors would significantly increase the number of discrete compositions, making it impractical to provide a pre-discretized model.

```
[1]: # importing necessary functions
from discretizer.cashplus import discretize_cash, add_cash_to_fundb, generate_reactions_one_by_one
...

[2]: # defining discretization; composition interval and steps
discretization = [{'ratio': 'Ca/Si', 'interval': [0.7, 1.7], 'step': 0.1},
                  {'ratio': 'Na/Si', 'interval': [0.0, 0.3], 'step': 0.1 },
                  {'ratio': 'Al/Si', 'interval': [0.0, 0.1], 'step': 0.1 } ]

[3]: # discretizing model calling GEMS to calculate the real solution properties for each composition
dicretized_cash = discretize_cash(discretization)

For Ca/Si 0.7 Na/Si 0.0 Al/Si 0.0 OK after GEM calculation with LPP AIA
(SiO2)1.0(CaO)0.7(H2O)1.0391
For Ca/Si 0.7 Na/Si 0.0 Al/Si 0.1 OK after GEM calculation with LPP AIA
(SiO2)1.0(CaO)0.7(Al2O3)0.025(H2O)1.125
For Ca/Si 0.7 Na/Si 0.1 Al/Si 0.0 OK after GEM calculation with LPP AIA
(SiO2)1.0(CaO)0.7(Na2O)0.05(H2O)1.0963

•[4]: # adding discrete phases to cemdata database
import thermofun as fun
fun_cemdata18 = fun.Database('cemdata18-thermofun.json')

[5]: fun_cemdata18 = add_cash_to_fundb(fun_cemdata18, dicretized_cash)

•[6]: # generating chemical reaqction for new phases, with provided master species
aqueous_master_species = ['H2O@', 'Na+', 'K+', 'Al+3', 'SiO2@', 'Ca+2', 'H+', 'HCO3-']
reactions_dic, reactions_list = generate_reactions_one_by_one(aqueous_master_species,
                                                             [c['formula'] for c in dicretized_cash ] )

0.7Ca+2 + SiO2@ + 1.7391H2O@ = (SiO2)1.0(CaO)0.7(H2O)1.0391 + 1.4H+
0.7Ca+2 + SiO2@ + 0.05Al+3 + 1.9H2O@ = (SiO2)1.0(CaO)0.7(Al2O3)0.025(H2O)1.125 + 1.55H+
0.7Ca+2 + SiO2@ + 0.1Na+ + 1.8463H2O@ = (SiO2)1.0(CaO)0.7(Na2O)0.05(H2O)1.0963 + 1.5H+
0.7Ca+2 + SiO2@ + 0.05Al+3 + 0.1Na+ + 2H2O@ = (SiO2)1.0(CaO)0.7(Na2O)0.05(Al2O3)0.025(H2O)1.175 + 1.65H+

•[7]: # calculating reaction properties for given T list
T_list = [0,25,60,100,150,200,250, 300]
engine = fun.ThermoEngine(fun_cemdata18) # thermofun engine is used to calculate the properties of reactions
# collecting results from the loop
reactions_logKs = [
    [engine.thermoPropertiesReaction(t+273.15001, 0, r).log_equilibrium_constant.val for t in T_list]
    for r in reactions_list ]

[8]: # exporting to CHESSE database format
fun_substances = [fun_cemdata18.getSubstance(c['formula'])for c in dicretized_cash]

from datetime import date
today = date.today()

file_name = today.strftime("%b-%d-%Y")+ '_chess_discrete_data.txt'

from common.export import to_chess
to_chess(file_name, fun_substances, reactions_dic, T_list, reactions_logKs, 'cash+ valid to 100C')

•[9]: # exporting to PHREEQC database format
from common.export import to_phreeqc
to_phreeqc('discrete_cash_phreeqc.txt', engine, fun_substances, reactions_list, reactions_dic,
           'cash+ valid to 100C')
```

Figure 5. Code snapshot from the script to discretize the CASH+ model, generate the solubility reactions and export them into CHESSE and PHREEQC data files.

To solve this issue a script to produce discrete C-S-H phases with associated logK of reaction and its temperature dependence was developed. The script allows to export the phases into PHREEQC (Parkhurst and Appelo, 2013) and CHESSE database format to be further used in calculations. In this way the user can decide based on the compositional space the composition, interval and step size that is relevant to the system that needs to be modelled.

The script is available at the following link to be downloaded and used <https://github.com/thermohub/thermofun-jupyter/tree/master/applications> and it can be directly used in the browser here:

<https://mybinder.org/v2/gh/thermohub/thermofun-jupyter/master?urlpath=lab/tree/applications/>

The user is presented with the option to define the composition interval and steps. Based on this, C-S-H compounds with chemical formula of the discrete composition are created and fed to GEMS chemical solver (Kulik et al., 2013) that calculates the properties of the equilibrated discrete phase form the CASH+ solid solution model (Figure 5).

Using the ChemicalFun and ThermoFun (Miron et al., 2023) libraries, for a given list of master species, the solubility reactions for the discrete phases are generated, their properties calculated and using the export functions the corresponding data files for PHREEQC or CHES code formats are created. The user can then take these data and used them for the modelling. The same functionality was used to export to CHES format the updated data concerning the temperature dependence of the hydrogarnet Fe endmembers and were used in the subsequent calculations of the report.

3. Reactive transport modelling approach

3.1 The reactive transport code HYTEC

Reactive transport models (RTMs) can simulate the transport and chemical reactions of multiple solutes (and gases) and their chemical interaction within the multi-barrier system over various time and spatial scales (Bildstein et al., 2019). Reactive transport models have, therefore, become an invaluable component in assessing the potential performance of a repository, which requires an understanding how the various barriers evolve through space and time (De Windt and Spycher, 2019). The modelling of the lab experiments of Subtask 2.2 were performed with the reactive transport code HYTEC (van der Lee et al., 2003). Deliverable D2.8 (De Windt et al., 2020) gives the main chemical and physical mathematical laws that have been implemented in HYTEC, as well as some key information on the numerical approaches and databases.

This section only provides for the main features of HYTEC relevant for Subtask 2.2. The geochemical module of HYTEC (called CHESS) simulates the chemical equilibrium state of complex aqueous systems, including minerals, organics, colloids and gases. Chemical processes as aqueous speciation, precipitation/dissolution of solid phases, and sorption (surface complexation with electrostatic correction, ion exchange) are accounted for. The aqueous chemistry includes acid/base reactions, oxidation and reduction (redox) processes and aqueous complexation by organic and inorganic ligands. HYTEC uses a mixed kinetic-thermodynamic equilibrium approach. The multicomponent reactive transport was modelled under water saturated conditions considering only diffusion as mass transfer processes. The mass transport was only driven by diffusion when fully hydrated since hydrated cement pastes have low hydraulic conductivities and the cells were not subjected to any pressure gradients. Temperature effect was implemented both on chemical processes (kinetics and thermodynamics) and diffusion.

3.2 Thermodynamic databases

At the beginning of the ACED work package, it was decided that ThermoChimie would be the reference database. For instance, the modelling at the HLW disposal cell scale has been done with this database. ThermoChimie (TC) is the thermodynamic database developed by Andra, ONDRAF and RWM for the performance assessment of the geologic disposal of radioactive waste (Giffaut et al., 2014, <https://www.thermochimie-tdb.com>). TC provides formation constants (at temperatures $\leq 80^\circ\text{C}$) for a wide range of radionuclides and the mineral component of multi-barrier systems, including host-rock solid phases, bentonites, cements, steel, and their evolving secondary phases. The database is formatted for HYTEC and several other reactive transport models. The present modeling of the steel – CEM I system was done with TC.

Thermoddem (TDM) is a database for the thermodynamic properties of interest for hazardous and radioactive wastes, as well as the geochemistry of natural environments (Blanc et al., 2012). The database is developed by the French geological survey (<https://thermoddem.brgm.fr>). The last qualified version of TDM (V1.10, 2017) is formatted for several reactive transport models including HYTEC. TDM has the advantage to be operational over a broader temperature range than TC, i.e. 0 to 100°C . The database includes a large set of zeolites and cementitious phases with a broad composition range with respect to concrete formulae such as CEM I and low-pH cements. The C-A-S-H, C-S-H and M-S-H phases are introduced as discrete elements. A few iron-bearing cement phases are present such Fe-AFm and Fe-Aft, and they are also suitable for modelling iron corrosion products such as iron carbonates, oxyhydroxides, silicates and sulfides. Cronstedtite is an exception since the pure-iron composition, $\text{Fe}_4\text{SiO}_5(\text{OH})_4$, of TC was found to be simpler and more relevant for the present calculations than the mixed aluminium-iron, $\text{Fe}_3\text{SiAlO}_5(\text{OH})_4$, composition of TDM. The present modelling of the steel – bentonite/cement grout was performed with TDM.

Whatsoever, it is worth mentioning that similar results were obtained while considering either the thermodynamic databases Thermodynam, version 10, or ThermoChimie, version 10. The formation constants of the Fe-siliceous hydrogarnets CAFSH and CFSH derived from Dilnesa et al. (2014) were added to TC. Figure 6 indicates that the Pourbaix diagrams of the main corrosion products of steel built with the CEMDATA database and TC database are very similar, both at 25 and 80°C.

The cationic exchangeable properties of montmorillonite were simulated according to the model of Bradbury and Baeyens (2002).

Table 5 gives the constants of cationic exchange and surface complexation reactions used in the present modelling of the bentonite reactivity in the grout. The selectivity constants at 25°C were also considered for the cases at 80°C due to lack of data.

Activity corrections were calculated with the truncated Davies model applicable from low to moderate ionic strength ($I \leq 0.5$ mol/kg). Sensitivity tests made with the B-dot model did not show any significant differences of the modelling results.

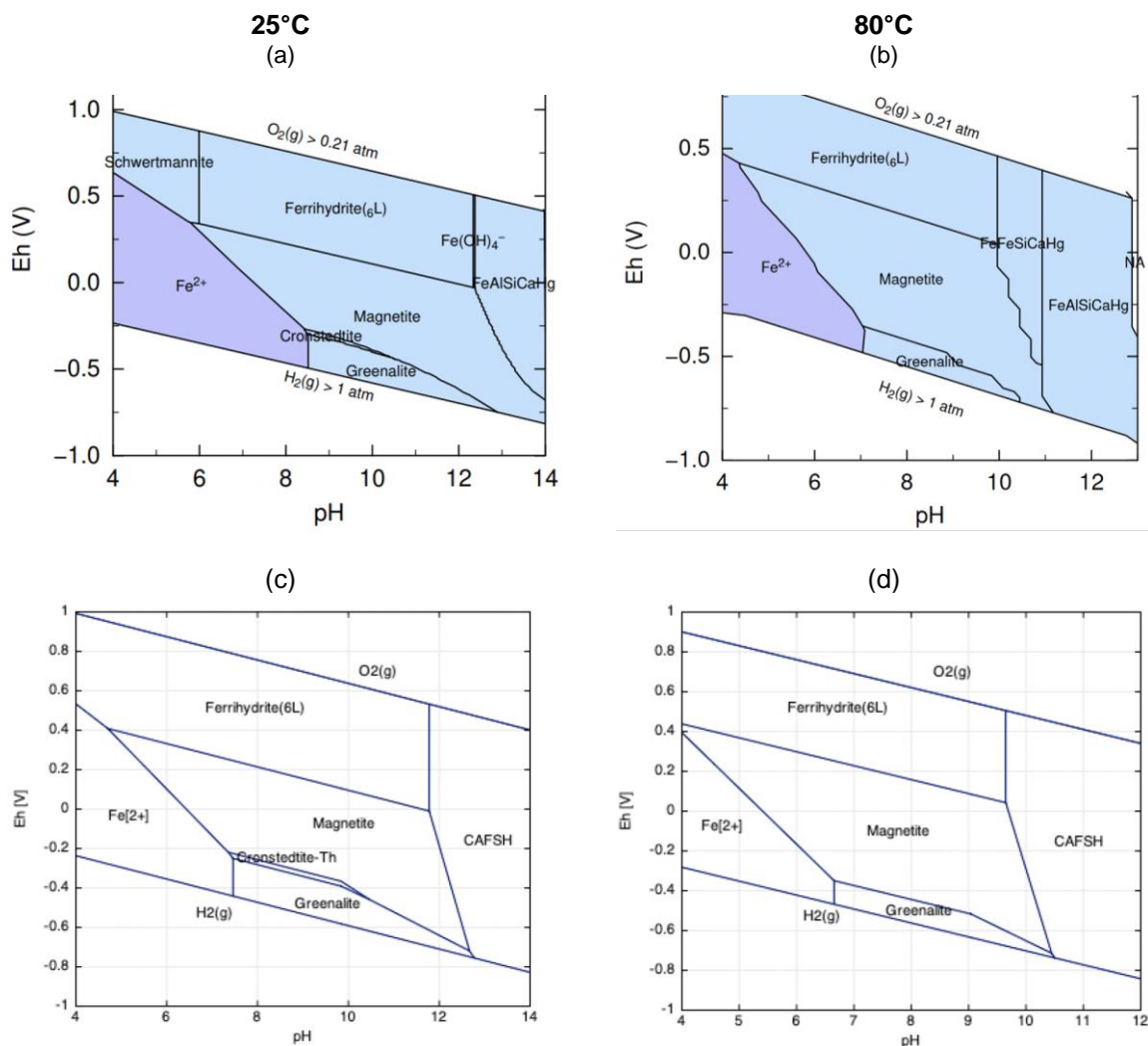


Figure 6: Comparison of Pourbaix diagrams at 25 and 80°C of the built (a, b) with the CEMDATA database (D. Miron, PSI, pers. comm.) and (c, d) the ThermoChimie database plus updated CAFSH data (chapter 2.1) and Thermodynam for ferrihydrate; the diagrams c and d were calculated with CHESS: activity Fe²⁺ = 10⁻⁵, activity Ca²⁺ = 10⁻³, activity Al(OH)₄⁻ = 10⁻⁴, total H₄SiO₄ = 10⁻⁴.

Table 5: Selectivity constants of cationic exchange (Gaines-Thomas formalism, Tremosa et al., 2012) and constants of surface complexation reactions (non-electrostatic model, Marques Fernandes et al., 2012) of montmorillonite considered in the modelling of the bentonite fraction of the grout as well as for the clayey phase of the argillite.

| Reaction | Log K _{ex} (25°C) |
|--|-------------------------------|
| Cation exchange (whole exchanger) | |
| $\overline{\text{Na}} + \text{K}^+ \rightarrow \overline{\text{K}} + \text{Na}^+$ | 0.9 |
| $2 \overline{\text{Na}} + \text{Ca}^{2+} \rightarrow \overline{\text{Ca}} + 2 \text{Na}^+$ | 0.6 |
| $2 \overline{\text{Na}} + \text{Mg}^{2+} \rightarrow \overline{\text{Mg}} + 2 \text{Na}^+$ | 0.6 |
| $2 \overline{\text{Na}} + \text{Fe}^{2+} \rightarrow \overline{\text{Fe}} + 2 \text{Na}^+$ | 0.7 |
| Surface complexation ⁽²⁾ | |
| $\text{S}_1\text{-OH} + \text{H}^+ \rightarrow \text{S}_1\text{-OH}_2^+$ | 4.5 |
| $\text{S}_1\text{-OH} \rightarrow \text{S}_1\text{-O}^- + \text{H}^+$ | -7.9 |
| $\text{S}_2\text{-OH} + \text{H}^+ \rightarrow \text{S}_2\text{-OH}_2^+$ | 4.5 |
| $\text{S}_2\text{-OH} \rightarrow \text{S}_2\text{-O}^- + \text{H}^+$ | -7.9 |
| Site density S ₁ -OH | 1 μmol/m ² |
| S ₂ -OH | 0.05 μmol/m ² |

(1) LogK (Fe) = logK (Ca) + 0.1 (Idiart & Lavina, 2019); (2)

Optional for pH buffering.

3.3 Modelling grid of the BACUCE mock-up experiments

The mock-up experiments investigated the effect of temperature, of water chemistry and pH (from low pH cement to highly alkaline pH cement) and of the configuration (steel in contact with aqueous solutions vs. close contact between solid materials). In a first set of experiments, carbon-steel blocks with parallelepiped form were embedded in CEM I cylinders and placed in PTFE containers in contact with a synthetic young CEM I pore water (Figure 7). In a second similar set, the steel was embedded in bentonite grout (MREA) in contact with a synthetic porewater made of 75 % bentonite grout porewater + 25 % Toarcian argillite porewater. The PTFE containers were placed in an oven at 80°C under anoxic conditions (argon atmosphere). Several containers were retrieved periodically (every 2 weeks for the first two and then every 2 months) to determine the corrosion rate, the evolution of water chemistry and the mineralogical evolution of the buffer materials.

As shown in Figure 7, the HYTEC simulation grid considered a generic modelling grid in 2D cylindrical symmetry based on the real dimensions of the cell compartments, under the representative elementary volume (REV) approach with finite volume calculation.

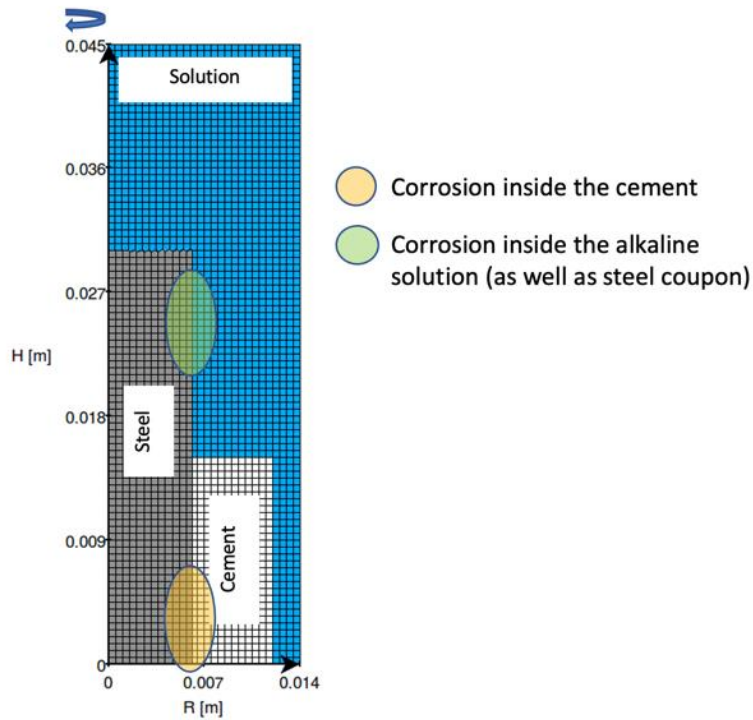


Figure 7: Generic modelling grid in 2D cylindrical symmetry of the BACUCE mock-up experiments where the cementitious material can be CEM I or the low-pH bentonite grout.

3.4 Modelling grid of the MTA EK cell experiments

The modelling grid considered the full experimental cell set-up in 2D-cylindrical geometry (Figure 8). The steel was not explicitly considered in the modelling that focused on the concrete/reservoir system. Steel is a non-porous material that only reacts through its surface and steel corrosion was very low in the present study.

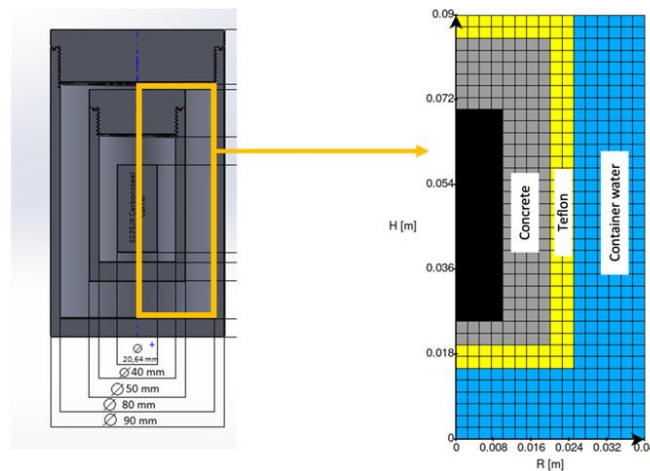


Figure 8: Modelling grid of the experimental cell in cylindrical symmetry.

4. BACUCE in-situ and mock-up experiments

4.1 BACUCE experiments: general description and objectives

The BACUCE experiment aims at studying the steel/cementitious (low-pH and high-pH) interface under the most representative disposal conditions as possible, including *in situ* experiments simulating imperfect contact (voids at the interface) and considering the impact of microbial activity (BAC-1 & BAC-2) or temperature (BAC-3, BAC-4 & BAC-5). It is one of the outstanding experiments of Task 2. A set of complementary tests have also been conducted at the laboratory to bring more specific information and to support the interpretation of the *in situ* results.

The BACUCE *in situ* experiments are taking place in the IRSN underground research laboratory (URL). Figure 9 gives a schematic representation of the BACUCE *in situ* experimental set-up to characterize the interface between carbon steel and two cementitious buffers (a bentonite/cement grout – BCG - and a CEM I cement paste) until 2.5 years of interaction.

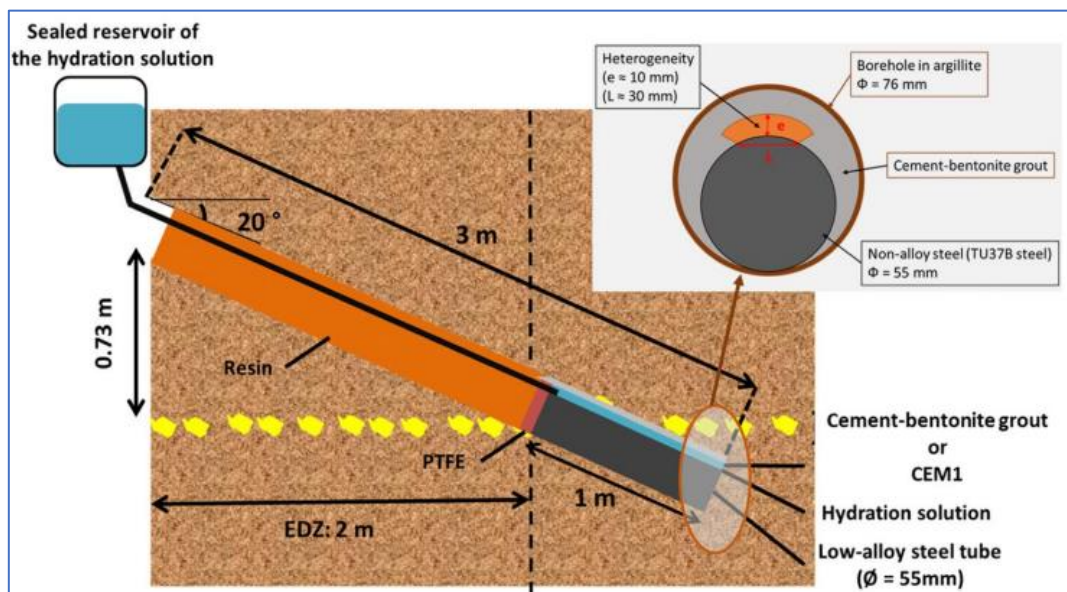


Figure 9: Schematic representation of the BACUCE *in situ* experimental set-up in the Tournemire URL at ambient temperature (15°C) or at 80°C (top) and zoom on the heterogeneous configuration of the reactive chamber (bottom). The borehole diameter is 76 mm (BAC-1 and BAC-2) or 101 mm (BAC-3, BAC-4 and BAC-5), and the tube diameter to 55 mm (BAC-1 and BAC-2) or 65 mm (BAC-3, BAC-4 and BAC-5)

The experiments are conducted either at ambient temperature of 15°C or at 80°C with a heating system. The cementitious buffer is injected in the annular gap between the steel cylindrical tube and the wall of the borehole drilled into the argillite formation. Then, the retrieval of a PTFE rod initially placed in contact with the metallic tube allows the creation of a void space mimicking a heterogeneity of filling by the cementitious material (low-pH bentonite-cement-grout BCG or CEM I).

Then, an external reservoir helps to saturate this heterogeneity with adapted synthetic pore water. The external reservoir should also help to hydrate the grout and cement and afterwards to maintain a water saturation degree of 100 %.

In complement to these field experiments, laboratory mock-up experiments have been carried out to better constrain the processes that would occur *in situ*. Both *in situ* and mock-up experiments have been performed with the same cementitious material under anoxic conditions, at the ambient temperature of 15°C or at 80°C and fully water-saturated conditions.

The aim of these experiments is to consistently assess the impact of microbial activity and/or temperature on both (i) the geochemical, mineralogical and microstructural change of the cementitious

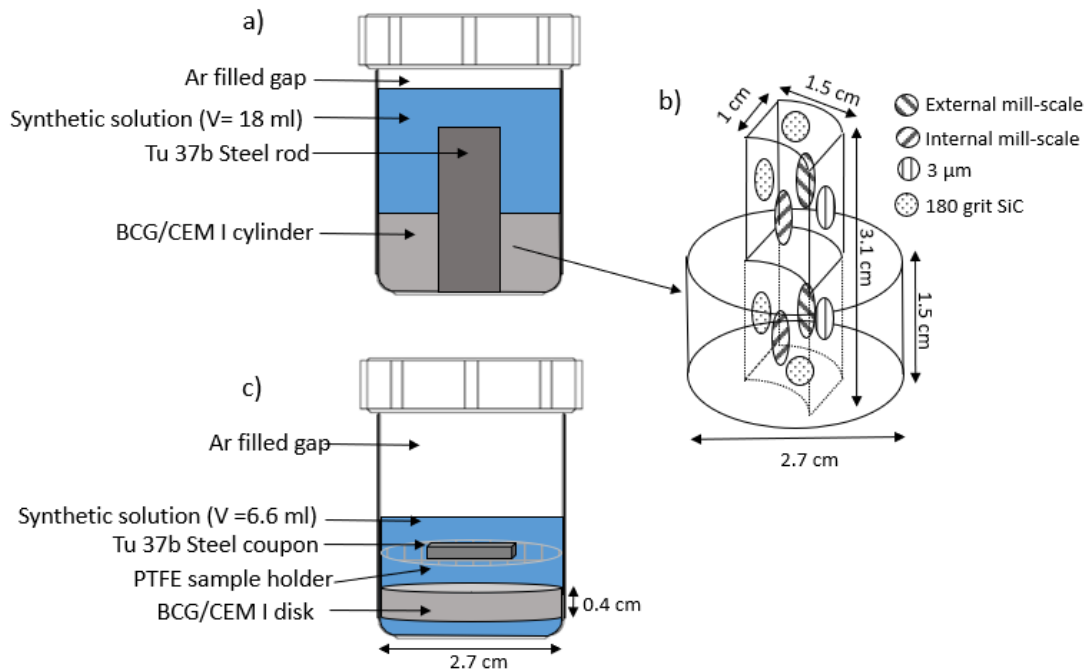


Figure 11: (a) Set-up of the experiment 1 - R with (b) a schematic 3D-view of the cementitious material-steel assembly put in the PTFE reactor; (c) set-up of the experiment 2 -C.

For experiments 1-R metallic samples preparation, TU37b steel rods of $3.0 \times 1.5 \times 1.0 \text{ cm}^3$ were cut from a TU37b tube section. Of the six exposed surfaces of the rod, three were ground with 180 SiC grit paper (top, bottom and left sides), one was polished with diamond paste down to $3 \mu\text{m}$ and on the two other sides, the pristine mill scale layers were preserved (Figure 11-b)

Cementitious materials (either BCG or CEM I) were prepared in an anoxic glove box by mixing the components (see sections 4.3.1) with a spoon and were directly poured in the PTFE reactors so that half of the rod height was embedded in cementitious material (Figure 11-a). After this, cementitious material was let to harden during 30 days in the closed PTFE reactors prior to their partial filling with the saturation solution (see sections 4.3.1).

Even though the samples were prepared in an anoxic glove box, one can note that for experiments 1-R involving both BCG and CEM I, oxidic corrosion processes impacted to some extent the unembedded steel surfaces during the initial phase of cementitious material paste hardening. As it was possible to retrieve the steel rods from the cementitious material, grinding and polishing operations were repeated to remove the corrosion products and the sample were replaced in the material prior to launch the experiment.

Each of the twelve prepared samples (6 for BCG and 6 for CEM I) were put in different PTFE reactors, filled with 18 mL of either BCG-synthetic solution or CEM I-synthetic solution (section 4.3.1) and transferred in an oven under argon atmosphere at 80°C .

For experiments 2-C metallic samples preparation, TU37b steel coupons of $1.0 \times 1.5 \times 0.2 \text{ cm}^3$ were cut perpendicularly to the rolling direction of a TU37b tube section. Cementitious material (BCG or CEM I) disks of $(\phi) 27 \text{ mm} \times (\text{h}) 4 \text{ mm}$ were cut from cementitious material cylinders prepared in a similar manner as the ones produced for experiment 1-R (Figure 11-c). A specific in-house tool was used to machine the disk of the desired dimensions after 32 days of cure. The disks were put at the bottom of PTFE reactors, and the steel coupons were inserted in a PTFE basket located above the disks, to avoid any contact of steel with the disks or the PTFE reactor.

Each of the twelve prepared reactors (6 for BCG and 6 for CEMI), containing one coupon and one cement-grout disk, were filled with 6.6 mL of the *ad hoc* porewater solution (BCG-synthetic solution or CEMI-synthetic solution) and put in an oven under argon atmosphere at 80°C.

For both experiment, samples were periodically retrieved and characterized following the different methods presented in the next sections.

4.2.2 In situ experiments

Several *in situ* experiments have been conducted at the Tournemire URL (Aveyron, France) to study the influence of both bacterial activity and temperature increase on the anoxic corrosion of carbon steel in an alkaline environment.

4.2.2.1 Tournemire URL

The BACUCE experiments are taking place in the Tournemire IRSN underground research laboratory (URL). This experimental platform is located in a century-old tunnel, excavated through 250 m-thick argillaceous and highly-compacted formations of Toarcian and Domerian ages, respectively (Figure 12). The Domerian formation is composed of about 40 m of marl and argillite, whereas the Lower, Middle and Upper Toarcian formation consists of 25 m of organic-rich marl, 20 m of marl, and 160 m of argillite, respectively (Wittebroodt et al., 2012). This argillaceous sequence is surrounded by two limestone aquifers.

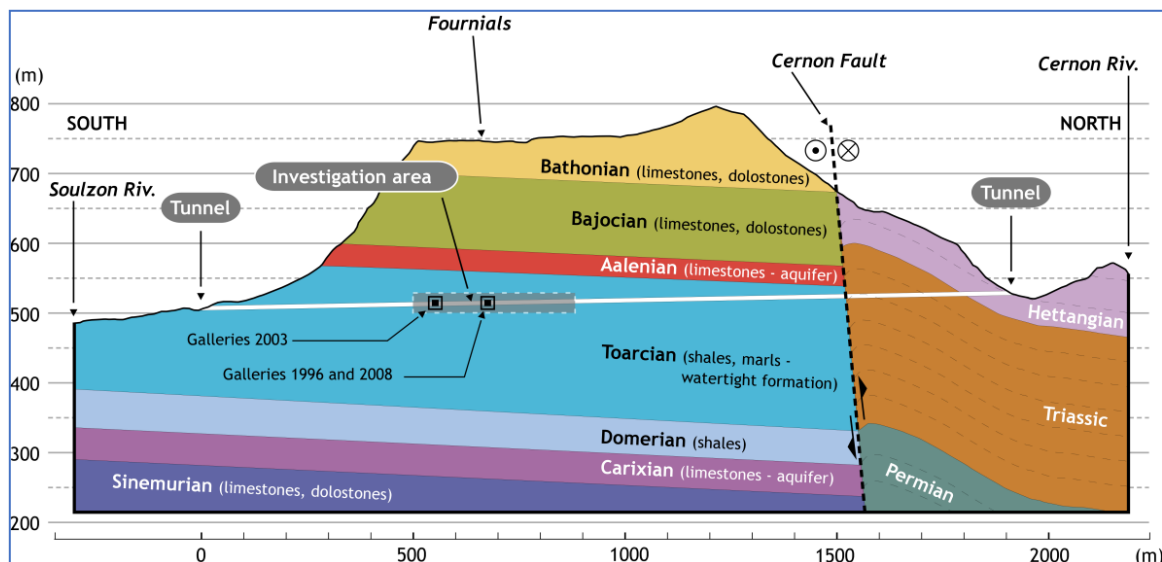


Figure 12: Schematic cross section of the IRSN URL (Tournemire).

4.2.2.2 Impact of microbial activity (BAC-1 and BAC-2) and temperature (BAC-3, BAC-4 and BAC-5)

Despite some minor dimensional differences, the five BACUCE *in situ* experiments have the same design which is presented in Figure 9.

Table 6 presents both borehole information and experimental conditions associated to each *in situ* experiment.

Table 6: Borehole and experimental device information and experimental conditions associated to each BACUCE in situ experiments

| | Borehole | | TU37B | | Cementitious material | | | Solution | | Bacterial inoculate | | T (°C) | |
|-------|----------|-------|-----------|-----------|-----------------------|-----|------|------------------------|-------------------------|---------------------|----|--------|------|
| | D (mm) | L (m) | Dext (mm) | Dint (mm) | scalped | BCG | CEMI | BCG SYNTHETIC SOLUTION | CEMI SYNTHETIC SOLUTION | YES | NO | 13°C | 80°C |
| BAC-1 | 76 | 3 | 55 | 45 | NO | X | | X | | | X | X | |
| BAC-2 | 76 | 3 | 55 | 45 | NO | X | | X | | X | | X | |
| BAC-3 | 101 | 3 | 65 | 45 | YES | X | | X | | | X | | X |
| BAC-4 | 101 | 3 | 65 | 45 | YES | X | | X | | | X | | X |
| BAC-5 | 101 | 3 | 65 | 45 | YES | | X | | X | | X | | X |

➤ in situ experiments implementation

For each experiment, the first step of the implementation was to perform a sub-horizontal (20°) borehole by nitrogen-core drilling technique in order to limit the rock oxidation. The boreholes diameter (D) and length (L) dimensions were (i) 76 mm and 3 m for BAC-1 and BAC-2 and (ii) 101 mm and 3 m for BAC-3, BAC-4 and BAC-5.

Then, the first part of the experimental device was introduced into the borehole and the gap between the rock and the test system was injected either with bentonite-cement grout (BCG) or ordinary Portland-cement (CEMI).

One can note that both BCG injection in BAC-1 and BAC-2 and CEMI injection in BAC-5 were done without any problem. However, BCG injection in BAC-3 and BAC-4 was more difficult and BCG had to be injected under pressure thanks to special syringes (i.e., gravity was not sufficient to ensure a good BCG injection).

The main body of the experimental device is composed of a 1 m-long carbon steel tube (TU37b). Its external and internal diameter are (i) 55 mm and 45 mm for BAC-1 and BAC-2 and (ii) 65 mm and 45 mm for BAC-3, BAC-4 and BAC-5.

For BAC-1 and BAC-2, the center part of the tube was filled with a polypropylene rod in order to (i) minimize the amount of trapped oxygen within the system and (ii) facilitate the future cutting/sampling operation. Once the polypropylene rod installed, the two extremities of the tube were hermetically closed thanks to cover plates screwed to the tube.

For BAC-3, BAC-4 and BAC-5, the center part of the tube hosts the heating system (constituted of mineral insulated resistor coiled around a central aluminium tube equipped with thermocouples – Arquimea®) allowing to reach a constant temperature of 80°C at the inner surface of the carbon-steel tube¹. The two extremities of the tube were hermetically closed thanks to cover plates screwed to the tube. One can also note on Figure 13 that for BAC-3, BAC-4 and BAC-5, the upper part of the tube has been “scalped” over the total length of the tube (i.e., the tube has been cut in its upper part) to obtain a

¹ One can note that if the initial targeted temperature value of 80°C at the inner surface of the metallic tube was reached, the temperature of the solution in contact with the outer surface of the tube reached a value around 30°C only.

horizontal metallic surface dedicated to the emplacement of Electrical Resistance (ER) corrosion sensors developed in the context of BACUCE project by ZAG.



Figure 13: "Scalped" upper part of TU37B tube

These *in situ* ER corrosion sensors (Figure 14), which measure the thickness reduction of the conductive metal (due to corrosion) via its increase in electrical resistivity, allow to continuously monitor the corrosion rates associated with BAC-3, BAC-4 and BAC-5 experiments.



Figure 14: Electrical Resistance (ER) corrosion sensors (developed by ZAG)

For all these experimental devices (BAC-1, BAC-2, BAC-3, BAC-4 and BAC-5), the upper part of the of the metallic tube is topped by a polytetrafluoroethylene (PTFE) system (PTFE rod), forming a void space between the tube top surface and the injected cementitious material. Then, once cementitious material (BCG or CEMI) started to set (6-7 days and 2-3 days after injection for BCG and CEMI, respectively), the PTFE system was manually removed to create the "artificial heterogeneity of filling" geometry (i.e., void space between the metallic tube and the cementitious material) (Figure 9).

Immediately after, the hydrating system was installed on the upper part of the experimental system. Such hydrating system is firstly composed of a PTFE skirt-shape sealing system whose radial dimension matching the internal diameter of the borehole allows to create a physical barrier for the further resin injections and thus protect the main body of the experimental system (Figure 15) against resin ingress.



Figure 15: Hydrating system composed of (i) PTFE skirt-shape sealing system (white parts) and (ii) three stainless-steel lines.

Then, two different resin injections were in the non-isolated upper part of the borehole. The first thick resin (SiKadur 53, SIKA®) injection aimed to create a first barrier prior to the second fluid resin injection (SiKadur 52, SIKA®) whose intent was to fill the cracks of the upper part of the borehole and thus to isolate the experimental system interval from the gallery oxidic atmosphere.

This hydrating system is also equipped with two stainless-steel lines, connected to a stainless-steel reservoir, allowing to (i) inject the artificial solution in the “artificial heterogeneity” area (i.e., the gap between steel and cement) during the entire test duration and (ii) sample the final solution and inject resin at the end of the experiment.

The stainless-steel reservoir is filled with the *ad hoc* artificial solution (Table 6). All the steps associated to the preparation of the solutions/reservoir filling operation were performed in an anoxic glovebox. No special care regarding potential bacterial contamination (i.e., no sterilisation step) was undertaken for BAC-1, BAC-3, BAC-4 and BAC-5 experiments. To study the impact of microbial activity on corrosion processes, the solution injected in BAC-2 was inoculated with the bacterial grown in both argillite and bentonite laboratory culture tests (see section 4.3.1).

One can note that BAC-3, BAC-4 and BAC-5 hydrating systems are equipped with a third stainless-steel line hosting ER corrosion sensor connection cables.

Finally, 28 days after the cementitious material injection, the reservoirs were connected to the stainless-steel upstream lines and the artificial heterogeneities were filled with the *ad hoc* solutions. Taking into account the fact that some solution will be absorbed by the desaturated argillite rock surrounding the borehole, the constant saturation of the artificial heterogeneity was assured by gravity. Monitoring of the reservoir weight allowed to plan solution refilling operation to avoid desaturation of the artificial heterogeneity.

BAC-1 and BAC-2 *in situ* anoxic corrosion experiments were performed at ambient temperature (13°C). For BAC-3, BAC-4 and BAC-5 *in situ* anoxic corrosion experiments, the temperature at the inner surface of the TU37B tube was set at 80°C thanks to the heating system launched few hours after the hydration of the spatial heterogeneities.

4.3 Material and method

4.3.1 Materials

4.3.1.1 Solids

Toarcian clay

The mineralogy of Upper Toarcian argillite is dominated by the clay fraction (50–60 wt.%) which is mainly comprised of illite (30–45 wt.%), kaolinite (20–25 wt.%), illite–smectite mixed layers (20–40 wt.%) and chlorite (5–10 wt.%). This claystone also contains 10–20 wt.% of quartz, 10–20 wt.% of carbonate (mainly composed of calcite with traces of dolomite and siderite), 1 wt.% of pyrite and about 1 wt.% of organic matter (Tinseau et al., 2006, Matray et al., 2007). The Upper Toarcian argillite bulk dry density (ρ_{dry}) is 2450 kg m³ (Tinseau et al., 2006).

BCG

The composition of the BCG used for both laboratory and *in situ* experiments is given in Table 7. The cement that has been used is a blended CEM III/A Rombas cement composed of clinker/anhydrite (34 wt.%) and blast furnace slag (66 wt.%). This cement contains a blast furnace slag fraction (which has a slow hydration kinetic) and, consequently, sulphide ions ($S^{2-} \approx 0.55\%$) prone to induce detrimental effect on steel corrosion processes (Robineau et al., 2017; Robineau et al., 2020; Robineau et al., 2021). Bentonite and hydrotalcite have mainly a rheological role (i.e., they facilitate the injection of the grout). Silica fume reacts with the CEM III/A hydrated phases to prevent any portlandite formation and high pH conditions by the input of silica to form C-S-H phases with a low Ca/Si ratio. The water on cement ratio ($W/C = 1.7$) is high enough to ensure fluidity during the injection and a good level of hydration.

Table 7: Recipe and bulk composition of the bentonite/cement grout.

| Global bulk chemistry for hydration of CEM III + silica fume (kg) | | Composition (kg) | |
|---|--------|--|---------------|
| CaO | 0.30 | | |
| SiO ₂ | 0.75 | CEM III Rombas (35% clinker/gypsum + 65% blast-furnace slag) | 0.600 |
| Al ₂ O ₃ | 0.055 | | |
| MgO | 0.03 | | |
| K ₂ O | 0.0042 | Silica fume | 0.600 |
| Na ₂ O | 0.0024 | Bentonite (Montmor ⁽¹⁾) | 0.160 (0.145) |
| | | Hydrotalcite | 0.04 |
| CaSO ₄ | 0.025 | Water | 2.400 |
| CaCl ₂ ·2H ₂ O | 0.0037 | | |

(1) Na-montmorillonite, exchangeable fraction = 100 % Na⁺.

To prepare the BCG, the different components were ground in an agate mortar and sieved with a 200 µm mesh grid. Then they were weighted in appropriate amounts and thoroughly mixed. The final step was the addition of an appropriate volume of tap-water and mixing/stirring. For temperature mock-up experiment, BCG was prepared inside an Ar filled glovebox to limit the presence of oxygen in the set-up. XRD analyses associated to each of the components are given in Appendix A.

CEM I Val d’Azergues

An ordinary Portland cement (CEM I, 52.5) from Val d’Azergues (Lafarges, France) was employed for mock-up and *in situ* tests dedicated to the study of the impact of temperature on corrosion and its composition is given in Table 8.

Table 8: Chemical composition of CEM I from Val d’Azergues and mineralogical analysis provided by the manufacturer.

| Global bulk chemistry (wt.%) | | Mineralogical composition (g/100g) | |
|--------------------------------|------|------------------------------------|------|
| CaO | 64.6 | Clinker | 93.2 |
| SiO ₂ | 20.7 | including Alite (C3S) | 65.3 |
| Al ₂ O ₃ | 3.2 | Belite (C2S) | 13.5 |
| Fe ₂ O ₃ | 4.5 | Aluminate (C3A) | 0.9 |
| CaO (free) | 1.8 | Ferrite (C4AF) | 13.5 |
| MgO | 0.6 | Gypsum | 3.9 |
| K ₂ O | 0.6 | Filler | 2.9 |
| Na ₂ O | 0.1 | | |
| CO ₂ | 1.1 | | |
| SO ₃ | 2.8 | | |

The hydrated cement paste (HCP) was produced using a water/cement ratio (W/C) of 0.42. After 28 days of hydration at ambient temperature, the mineralogical composition of the HCP was examined. The XRD pattern collected on a disked sample revealed the presence of portlandite, C-S-H, ettringite, hemicarboaluminate, monocarboaluminate, calcite and Si-katoite as the main hydration products. The presence of this latter hydrate is uncommon and related to the Val d’Azergues CEM I. Its occurrence may be explained by the relatively high amount of C₄AF compared to C₃A. The cured cement paste also still contains a large amount of alite, belite, brownmillerite as the main unreacted cement (UC) phases. The amount of portlandite (17 vol%) and calcite (2 vol%) was determined by TG-DSC analyses and the combined amounts of C₂S/C₃S (8 ± 1 vol%) and C₄AF (3 ± 0.5 vol%) were determined by SEM gray level analyses. The porosity (35.7 ± 0.3 %) was obtained from water content measurements on 3 samples.

The modelling of the mineralogy of the hydrated cement paste was made assuming thermodynamic equilibrium based on the bulk composition of the composite material at 20 and 80°C. Full hydration of

the cement anhydrite was assumed, excepted for C_4AF . The Thermoddem thermodynamic database (Blanc et al., 2012) was used. Sorption of Na^+ and SO_4^{2-} on C-S-H was not considered.

After hydration, the calculated mineralogy is as expected for a CEM I hydrated paste with portlandite, C-S-H of high C/S ratio and ettringite (Table 9).

Katoite stabilizes ettringite that should be partly or totally dissolved at 80°C. According to the literature, when ettringite dissolves, the sulphate content is distributed among the pore water solution, sorption onto the C-S-H phases, and as a new mineral, monosulfoaluminate. Figure 16 indicates that the usual conversion of ettringite into monosulfoaluminate will take place after 60°C if one considers C_3AH_6 instead of katoite in the mineral assemblage. Accordingly, two model subsets were assumed in the modeling, with katoite (model 1) or without katoite but with C_3AH_6 (model 2). The key difference in model 2 is that ettringite (AFt) is fully transformed to two AFm phases at 80°C, i.e. monocarboaluminate and monosulfoaluminate.

Table 9: Modelling of the initial mineralogy of the hydrated CEM I paste (Val d’Azergues) at 20°C and after a temperature increase to 80°C.

| Mineral (mol/L of cement paste) | 20°C model 1 with katoïte | 80°C model 1 with katoïte | 80°C model 2 with C3AH6 |
|------------------------------------|---------------------------------|---------------------------------|-------------------------------|
| Portlandite | 6.30 | 6.35 | 5.9 |
| C-S-H 1.6 | 4.40 | 4.39 | 4.1 |
| Ettringite ⁽¹⁾ | 0.13 | 0.12 | - |
| Monosulfoaluminate | - | - | 0.1 |
| Monocarboaluminate | - | 0.1 | 0.1 |
| Katoïte | 0.68 ⁽²⁾ | 0.69 ⁽²⁾ | - |
| C3AH6 | - | - | 0.59 |
| Calcite | 0.39 | 0.39 | - |
| Hydrotalcite | 0.1 | 0.08 | 0.08 |

(1) Ettringite is stable when katoite is present in the modelling; sorption of SO₄ on C-S-H is not considered; (2) assuming thermodynamic equilibrium, probably overestimated.

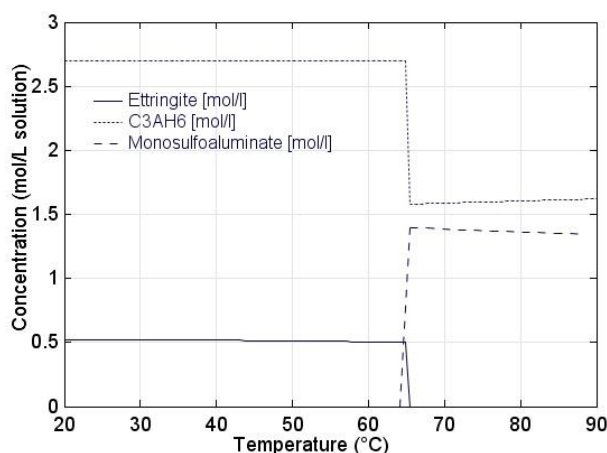


Figure 16: Modelling of the conversion of ettringite into monosulfoaluminate with C3AH6 but without katoïte in the mineral assemblage.

Low carbon steel

Three different types of low carbon steel were employed in this study that are namely P235GH, TU37b and DC03. P235GH was employed for mock-up experiment dedicated to the impact of microbial activity, DC03 was employed in the ER corrosion sensors used for BACUCE in situ test dedicated to the impact of temperature and TU37b was employed for all other experiments.

P235GH is commonly used in such experiments due to its chemical similarity with the alloy selected by ANDRA for the steel casing (i.e., API 5L X65 steel) (El Mendili et al., 2013; Bouakkaz et al., 2019). An optical micrograph of the microstructure of this steel is presented in Figure 17.

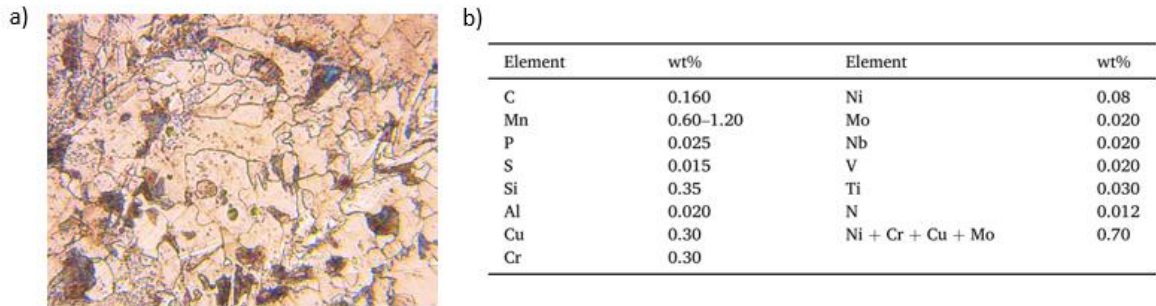


Figure 17: (a) Microstructure of the P235GH low carbon steel and (b) chemical composition. The balance is Fe

TU37b (A37) steel composition is given in Figure 18-a. This steel is equivalent to the P235GH grade of steel (chemical composition) and is formed by hot rolling process. It exhibits a ferrite-pearlite layered structure (Figure 18-a) and its external mill scale layer has a heterogeneous microstructure and presents “indentations” of several tens of micrometres (Figure 18-b). This mill scale layer is primarily composed of magnetite (μ -Raman spectroscopy analysis, not shown). The mill scale layer is covered by a thin layer enriched in Na, P, O, Zn and Fe (Figure 18-b), the Si come mostly from SiC grains. The origin of this layer is unknown as the manufacturer ensures that any corrosive treatment (like phosphating) was not applied to this steel.

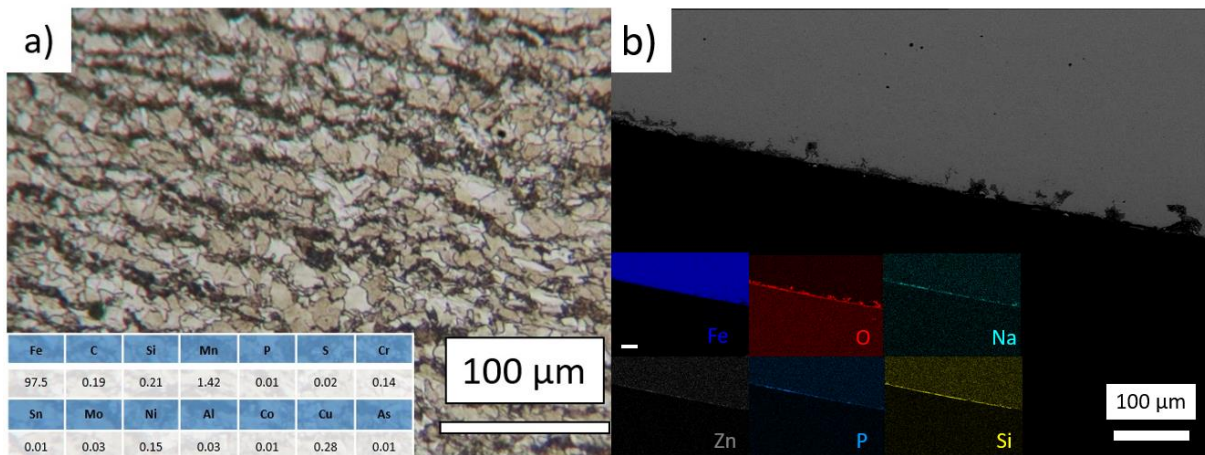


Figure 18: (a) Microstructure parallel to the rolling direction and composition of the TU37b steel measured by Optical emission spectrometry with a SPECTRO MAXx Ametek©; along with SEM-EDX mapping of the external mill-scale layer of the Tu37b steel. The microstructure of the steel was revealed after polishing the steel surface down to 0.05 μm with silicon colloids following chemical etching with a 2% HNO_3 Nital solution.

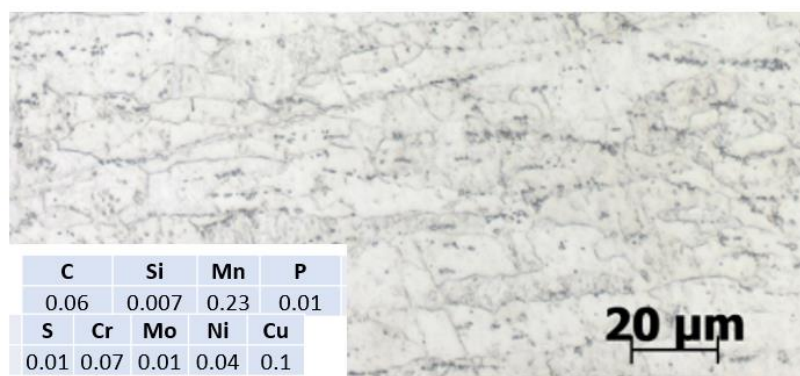


Figure 19: Microstructure and composition of the DC03 steel measured by Optical emission spectrometry with a SPECTRO MAXx Ametek.

The DC03 steel which has a chemical composition similar to the TU37b steel and that also present a ferrite-pearlite microstructure was chosen for the ER sensors, because it could be purchased in the form of thin (0.5 mm) sheets (Figure 19).

4.3.1.2 Porewater solution

Tournemire Porewater solution

The theoretical composition of the Tournemire argillite porewater solution used for this study is based on the synthesis done by Chautard (2013) drafted on different experimental data gained in previous work (Table 10).

Table 10: Chemical composition of the synthetic argillite porewater solution.

| Synthetic argillite porewater solution (theoretical composition) | |
|---|-----------------------|
| Na ⁺ (mol/L) | 2,2.10 ⁻² |
| K ⁺ (mol/L) | 0,3.10 ⁻³ |
| Mg ²⁺ (mol/L) | 1,0.10 ⁻³ |
| Ca ²⁺ (mol/L) | 1,5 .10 ⁻³ |
| Cl ⁻ (mol/L) | 4,5.10 ⁻³ |
| SO ₄ ²⁻ (mol/L) | 9,5.10 ⁻³ |
| TIC (mol/L) | 4,0.10 ⁻³ |
| Si (mol/L) | - |

BCG pore water solution determination

The composition of porewater solution at equilibrium with BCG at ambient temperature (20°C) was determined from preliminary lixiviation tests. For that purpose, cement-bentonite suspensions were obtained by mixing ultrapure water with crushed cement-bentonite paste samples previously cured for one month in a sealed bag at room temperature. Different ultrapure water/BCG (liquid/solid) ratios (1, 4, 9 ml/g) and contact time (24h, 3d, 7d) have been tested and the associated results are presented in Appendix B.

Whatever the studied test, the pH of the solution is alkaline (≈ 11.4), the salinity is pretty low (< 1.3 g/L) and the presence of organic carbon is rather limited (< 18 mg/L). For this microbial study, we selected the chemical composition associated with the leaching test “ST1-1-7j” (liquid/solid = 1 ml/g; 7j stirring) as representative for the BCG porewater (see Table 11).

Previous modelling works have been performed from these experimental data (De Windt et al., 2020) to test the sensibility of both model 1 (take into account C-S-H formation) and model 2 (take into account C-A-S-H formation). Table 11 indicates a reasonably good agreement between the modelled and the experimental data despite some discrepancies (mainly pH value and K, SO₄, Al contents).

Table 11: Preliminary modelling of the batch experiment, water chemistry: bentonite/cement grout in contact with demineralized water at 20°C, L/S ratio = 1 (ST1-1-7j).

| Total concentration | Experimental data | Model 1 with C-S-H | Model 2 with C-A-S-H |
|---------------------------------|-------------------|--------------------|----------------------|
| (mmol.L ⁻¹) | 20°C | 20°C | 20°C |
| pH | 11.3 | 10.7 | 10.4 |
| K ⁺ | 3 | 15 | 15 |
| Na ⁺ | 12 | 15 | 15 |
| Mg ²⁺ | 0.0 | 0.0 | 0.0 |
| Ca ²⁺ | 3 | 5 | 10 |
| Al ³⁺ | 0.01 | 0.1 | 0.08 |
| H ₄ SiO ₄ | 1.5 | 1.6 | 0.8 |
| Cl ⁻ | 7 | 8.5 | 8.5 |
| SO ₄ ²⁻ | 3 | 15 | 21 |

Additional modelling work have been done with both model 1 and model 2 to assess the BCG initial porewater composition at 80°C (Table 12) assuming a porosity of the BCG of 75%. The main effect when moving from L/S = 1 to the porewater is the increase in the concentration of those elements that are mostly dissolved in the porewater and not controlled by the solubility of the solid phases: Na – K – Cl. This leads to a slight increase (factor 2) in the OH⁻ content. The raise in the SO₄ concentration is linked to the destabilization of ettringite at 80°C.

Table 12: Modelling of initial porewater chemistry of the bentonite/low-pH cement grout at 80°C based on the batch experiments.

| Total concentration | Model 1 with C-S-H | Model 2 with C-A-S-H |
|-------------------------------|-----------------------|-------------------------|
| | 80°C | 80°C |
| pH | 9.7 | 9.2 |
| K ^(*) | 45 mmol/L | 45 mmol/L |
| Na ^(*) | 63 mmol/L | 62 mmol/L |
| Mg ²⁺ | 0.0 mmol/L | 0.005 mmol/L |
| Ca ²⁺ | 4 mmol/L | 4 mmol/L |
| Al ³⁺ | 0.3 mmol/L | 0.07 mmol/L |
| Si | 4 mmol/L | 1.6 mmol/L |
| Cl ⁻ | 25 mmol/L | 25 mmol/L |
| SO ₄ ²⁻ | 43 mmol/L | 45 mmol/L |

(*) The concentration is overestimated by a factor about 2 according to the mock-up test (see below).

Synthetic porewater for microbial test (BCG)

➤ Mock-up test

To study bacterial anoxic corrosion in low-pH cement grout environment, carbon steel coupons were immersed at 20°C in different representative solutions, with or without bacteria inoculum (Table 13).

Table 13: Conditions applied (culture medium, micro-organisms inoculation, contact time) for all the mock-up anoxic corrosion tests

| Test | Mix 75/25 | | | | | | | Tournemire synthetic porewater | | |
|---------------------|-----------|-----|----|-----|----|-----|----|--------------------------------|----|----|
| Contact time (week) | 9 | | 24 | | 41 | | | 9 | 41 | |
| Inoculation or not | IC | NIC | IC | NIC | IC | NIC | SC | IA | IA | SA |
| | | | | | | | | | | |

The first solution denoted “Mix 75/25” corresponds to mixture of 75% of BCG pore water (see experimental data in Table 11) and 25% of synthetic Tournemire argillite pore water (Table 13). The second solution corresponds to synthetic Tournemire argillite pore water only (Table 13). One can note that all these liquid mediums were enriched in salts and nutrients to enhance bacterial activity.

Three different configurations are studied in these tests: sterile test (SC and SA), test without (NIC) or with (IC and IA) microbial inoculation. The microbial inoculation is done from the bacteria grown that were able to survive and to develop for both argillite and bentonite culture tests (not shown).

➤ In situ experiments

For the *in situ* tests (BAC-1 and BAC-2), the reservoirs are filled with an artificial solution whose chemical composition mimics the interaction of natural Upper Toarcian argillite pore water with BCG material one. This solution has also been enriched with different salts and organic carbon sources solutions (Table 14) to enhance microbial activity.

Table 14: Chemical composition of the synthetic solution used for BAC-1 and BAC-2 in situ experiments. Additional salts for bacterial growth are in blue.

| Ultra-pure water | 5L |
|---|-----------------------------|
| SiO ₂ | 311.3 mg |
| CaCl ₂ , 2H ₂ O | 574.9 mg |
| CaCO ₃ | 206.3 mg |
| NaNO ₃ | 7.5 mg |
| Na ₂ SO ₄ | 1778,8 mg |
| MgSO ₄ , 7H ₂ O | 307.1 mg |
| NaHCO ₃ | 420 mg |
| NaCl | 87.5 mg |
| KCl | 27.5 mg |
| Na-acetate | 449.3 mg |
| Na-formate | 372.6 mg |
| Na-pyruvate | 602.7 mg |
| Na-Lactate 60% | 986.3 mg |
| (NH ₄) ₂ SO ₄ | 2169,9 mg |
| KH ₂ PO ₄ | 224.7 mg |
| KOH | 3.788 ml - 1 mol/L |
| NaOH | pH adjusting to reach pH 11 |

Synthetic porewater for temperature test (BCG)

For the temperature tests, the recipe used for the microbial activity test was slightly modified. The precursors used to synthesize the pore water solution are similar to the one presented in Table 15 except that (i) additional salt used for bacterial growth were not added and that (ii) SiO₂ was not added to avoid its reaction with Ca and Mg and the formation of C-S-H, M-S-H, and other silicates such as zeolite that can form in subalkaline conditions, and that can easily grow at elevated temperature. The solution was prepared at 20°C in an anoxic glovebox with degassed milliQ® water. The chemical composition and the pH of the solution were controlled after stirring the solution at 20°C by means of ionic chromatography and pH electrode, respectively. These measurements were also performed after heating the solution to 80°C in an anoxic oven and no significant change in the chemical composition were observed. The measured and modelled composition and pH of this solution is presented in Table 15.

Table 15: Measured and modelled initial chemistry of the synthetic solution used for temperature *in situ* and mock-up experiments. Values are given in mol/L.

| | Measured (20°C) | Measured (80°C) | Modelled (80°C) |
|-------------------------------|-----------------------|-----------------------|-----------------------|
| pH | 11.1 | 9.6 | 9.7 |
| Na ⁺ | 6.55×10 ⁻³ | 7.00×10 ⁻³ | 7.00×10 ⁻³ |
| K ⁺ | 7.2×10 ⁻⁴ | 7.7×10 ⁻⁴ | 7×10 ⁻⁴ |
| Mg ²⁺ | 9×10 ⁻⁵ | 6×10 ⁻⁵ | / |
| Ca ²⁺ | 1.7×10 ⁻⁴ | 1.5×10 ⁻³ | 1×10 ⁻⁴ |
| Cl ⁻ | 1.75×10 ⁻³ | 1.87×10 ⁻³ | 2×10 ⁻³ |
| SO ₄ ²⁻ | 2.33×10 ⁻³ | 2.45×10 ⁻³ | 2.5×10 ⁻³ |
| NO ₃ ⁻ | <8×10 ⁻⁶ | <8×10 ⁻⁶ | / |

CEM I synthetic pore water solution (20 and 80°C)

The initial hyperalkaline solution used for mock-up and *in situ* temperature related tests was prepared considering previous measurements and calculations at 25°C (Dauzères, 2010) and its pH and chemical composition was measured at 20 and 80°C (Table 16). For that purpose, NaOH (2 g/L), KOH (15.13 g/L) and Ca(OH)₂ (82 mg/L) were mixed in MilliQ water (18.2 MΩ.cm at 25 °C). It should be mentioned that the preparation of this synthetic porewater was simplified (e.g., sulphate and silicon were not added) because it could further react with the cementitious material to equilibrate at 80°C.

Table 16: Modelled and measured chemical composition and pH of the hyperalkaline solution used in Bacuce mock-up and *in situ* temperature tests (compared with data from Dauzères (2010)).

| | 25°C | | 80°C | |
|-------------------------------|-----------------|-----------------|-------------|-------------|
| | Measured | Modeled | Measured | Measured |
| | Dauzères (2010) | Dauzères (2010) | This study | This study |
| Total concentration | | | | |
| pH | 13.6 | 13.5 | 13.6 | 12.1 |
| K ⁺ | 475 mmol/L | 475 mmol/L | 227 mmol/L | 241 mmol/L |
| Na ⁺ | 50 mmol/L | 50 mmol/L | 51 mmol/L | 52 mmol/L |
| Ca ²⁺ | 1.6 mmol/L | 0.6 mmol/L | 0.75 mmol/L | 1.5 mmol/L |
| SO ₄ ²⁻ | 6.7 mmol/L | 3.8 mmol/L | 0.02 mmol/L | 0.02 mmol/L |

Table 17 gives the modelling of the porewater chemistry at 20°C and 80°C for the two models (i.e., considering either katoite that stabilize ettringite or C₃AH₆). At 20°C, the porewater corresponds to a classical fresh (young) cement pore water enriched in NaOH and KOH with a pH greater than 13.

The calculated pH of 13.6 is slightly overestimated because a fraction of the Na-K-OH loading could be decreased by sorption onto the C-S-H phases.

Heating to 80°C does not change significantly the chemistry, excepted the important increase in sulfate anions from 1 to 144 mmol/L (model 1) and 80 mmol/L (model 2). This increase was validated by indirect analysis that showed that the dissolved sulfate content was at least higher than 65 mmol/L at 70°C (Lalan, 2016). Half of the sulphates were probably adsorbed on the C-S-H (Barbarulo, et al., 2007).

At 80°C, the pH scale changes compare to the usual standard temperature due to the increase of the water decomposition product K_w with temperature. The activity (or total content) of the OH^- species is a better parameter of the “alkaline loading”. The OH^- content decreases at 80°C, it is reduced by a factor 2 approximately. This hydroxyl (OH^-) content represents the aggressiveness of these alkaline solutions. But globally, the basicity remains very high.

Table 17: Modelled initial porewater chemistry of the hydrated CEM I paste (Val d’Azergues) at 20°C and after a temperature increase to 80°C.

| Total concentration | 20°C | 80°C | 80°C |
|-------------------------------|--------------------------|---|--------------------------|
| | model 1 with katoïte | model 1 with katoïte | model 2 with C3AH6 |
| pH | 13.6 ⁽¹⁾ | 11.5 ⁽¹⁾ | 11.7 ⁽¹⁾ |
| K ⁺ | 350 ⁽¹⁾ | 350 ⁽¹⁾ mmol/L 13600 mg/L | 350 mmol/L 13600 mg/L |
| Na ⁺ | 65 ⁽¹⁾ mmol/L | 100 ⁽¹⁾ mmol/L 2300 mg/L | 100 mmol/L 2300 mg/L |
| Ca ²⁺ | 0.9 mmol/L | 4.0 mmol/L 160 mg/L | 1.6 mmol/L (64 mg/L) |
| Mg ²⁺ | 0 mmol/L 0 mg/L | 0 mmol/L 0 mg/L | 0 mmol/L 0 mg/L |
| Al ³⁺ | 0.2 mmol/L | 0.13 mmol/L 4 mg/L | 1.5 mmol/L 42 mg/L |
| Si | 0.05 mmol/L | 0.19 mmol/L 5 mg/L | 0.08 mmol/L 2.5 mg/L |
| HCO ₃ ⁻ | 0.2 mmol/L | 0.1 mmol/L 6 mg/L | 1.8 mmol/L 110 mg/L |
| Cl ⁻ | 15 ⁽²⁾ mmol/L | 50 ⁽²⁾ mmol/L 1770 mg/L | 50 mmol/L 1770 mg/L |
| SO ₄ ²⁻ | 1.1 mmol/L | 144 mmol/L 13860 mg/L | 80 mmol/L 7700 mg/L |

(1) Slightly overestimated due to the lack of sorption of alkali onto C-S-H, can be reduced by 40%; (2) Estimated and entered as NaCl in the model.

4.3.2 Methods

4.3.2.1 Solid characterization

Sample preparation

Samples coming from mock-up experiments and *in situ* test were prepared for further characterization by a set of different technics that are described in the next sections. For both *in situ* and laboratory tests, it should be noticed that most of the preparation operations were performed in aerated conditions. However, some characterizations were directly performed in anoxic conditions on metallic coupons that were retrieved from reactors (without any further preparation step), likely in the mock-up experiment related to bacterial activity and EXP 2-C related to temperature impact on corrosion. For the other experiments, care was taken to limit propagation of oxygen in the samples and analyses were performed readily after the last preparation steps. For the mock-up test, the steel-cementitious material assembly from experiment 1-R was first transferred to an anoxic glove box and immersed in deaerated ethanol (99%) for 4h to stop corrosion. Then, the samples were dried for at least 12h inside the glove box using silica gel prior to be embedded in Struers® Epoxy resin. After this, slices of the cylindrical sample were cut perpendicularly to the rod axis with a diamond wire saw. The samples were then polished with SiC grit paper and diamond paste, down to 1µm.

For *in situ* tests, the sampling and sub sampling procedure was much more challenging and the procedure evolved within the project for the dismantling of the different sets of experiments.

For all *in situ* tests, the following operations were performed:

(1) Disconnection of the reservoir

remark: after either 2 years (BAC-3, BAC-4, BAC-5) or 2.5 years (BAC-1, BAC-2) of interaction

(2) Collection of synthetic solution and drying of the heterogeneity and surrounding material with N₂ flushing

remark: impossible for BAC-2 (presence of a crack overlapping the upper part of BAC-2 artificial heterogeneity) and BAC-3 and BAC-4 (BCG penetration in the heterogeneity). Temperature measured for BAC-5 solution just after sampling is equal to 30°C.

(3) Injection of resin in the heterogeneities (strengthen the system and isolate it from oxygen contamination)

(4) Overcoring of the entire system

(5) Embedding of all system in PVC tube and resin.

(6) Cutting of the 1-meter-long cores into slices of 5 to 10 cm thick.

remark: BAC-4 core has not been sub-sampled in slice (replicate of BAC-3)

(7) Packaging of these slices in aluminium sealed bag or embedding of the slice in resin

remark: BAC-1 slices in aluminium sealed bag, BAC-2, BAC-3 and BAC-5 slices in resin.

(8) sub-sampling of the slices (saw and lathe milling machine) until production of small samples adapted to characterization tools (optical microscopy, SEM and µ-Raman). Some samples were broken to collect powder at the different interface for XRD analyses.

The most relevant operations are summarized in Table 18 and presented in Figure 20.

Table 18: Summary of the relevant operations related to overcoring and sub-sampling operations

| | BAC-1 | BAC-2 | BAC-3 | BAC-4 | BAC-5 |
|----------------------------------|-------|-------|-------|-------|-------|
| Reservoir disconnection (Yes/No) | Y | Y | Y | Y | Y |
| Solution sampling (Yes/No) | Y | N | N | N | Y |
| Resin injection (Yes/No) | Y | Y | Y | Y | Y |
| Overcoring (Yes/No) | Y | Y | Y | Y | Y |
| Core embedding (Yes/No) | Y | Y | Y | Y | Y |
| Slice sample cutting (Yes/No) | Y | Y | Y | N | Y |
| Slice packaging (Bag/Resin) | B | R | R | / | R |
| Sub-sampling (Yes/No) | Y | Y | Y | / | Y |

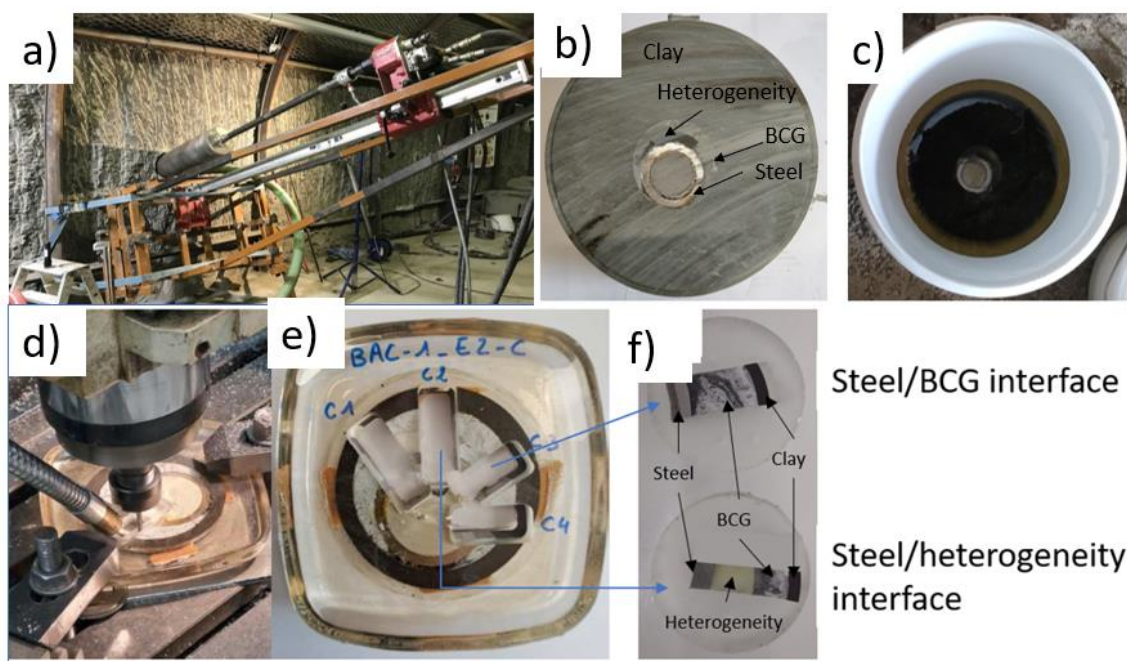


Figure 20: (a) Overcoring operation of BAC 1 in situ experiment, (b) slice of BAC 1 cut from the 1-meter-long core (c) embedding of slice coming from BAC 2 (d) milling of a sub-sampled slice of BAC 1 (e) sub-sampled slice of BAC 1 after milling operation (f) final embedded sample for characterization of the interfaces.

Analyses of solid

SEM-EDX

Scanning Electron Microscopy (SEM) coupled with Energy Dispersive X-ray spectroscopy (EDX) was used to conduct analyses on the embedded polished samples as well as on steel coupons. SEM-EDX analyses were performed with a JEOL 5800 LV microscope operating at 15 kV and 0.5 nA or with a S3500N (Hitachi®). The samples were either carbon coated or embedded in glutaraldehyde for bacterial analyses. For quantitative EDX analyses, the oxygen content was not recalculated stoichiometrically but measured and quantified independently from the other elements due to the potential presence of non-oxide minerals in the corrosion product layer. The following standards were used for calibration: Al₂O₃ for O, halite (NaCl) for Na, sylvite (KCl) for Cl and K, periclase (MgO) for Mg, wollastonite (CaSiO₃) for Ca and Si, pyrite (FeS₂) for Fe and S.

XRD

XRD analyses were conducted on cementitious disks and on steel coupons (coming from EXP 2C). Moreover, cement powder and corrosion products were collected from in situ samples to conduct XRD analyses. For all analyses, the samples were scanned in Bragg Brentano geometry using a D5000 Bruker AXS diffractometer or a Panalytical equipped with a Cu anticathode ($\lambda = 1.5406 \text{ \AA}$) operating at 40 kV and 25 mA and 40 kV and 35 mA, respectively. XRD scans were collected using an anti-air scatter screen in the range $2\theta = 5^\circ$ to 70° with a step size adapted to each sample and diffractometer to obtain a reasonable noise to signal ratio. These scans were treated with the DIFFRACPLUS EVA software (Bruker) and Highscore (Panalytical) and the crystallographic open database (COD) was then used to attribute diffractions peaks to the corresponding mineralogical phases.

μ -Raman

Corrosion products from resin embedded samples and coupons were characterized by confocal μ -Raman spectroscopy. For the latter analyses, the steel coupons were transferred from the glove box to an in-house anoxic cell allowing to avoid further oxidation of the sample during analyses. Raman analyses were conducted with a X'Plora or a Labram® HR800 Evolution (Horiba Jobin Yvon®) spectrometer both equipped with a 1200 lines/mm grating. The Raman excitation was applied using a solid-state 532 nm wavelength and filtered to obtain output energies comprise between 0.4 mW and 1.5 mW maximum, to avoid degradation of corrosion products while obtaining a reasonable signal to noise ratio. The laser beam was focused using 100x and 50x Olympus objectives. The spectra were collected in the range 100 to 1400 cm⁻¹ and the acquisition time on a given sample was comprise between 60 s and 600 s per point. Calibration was performed on a silicon standard using the 520.5 cm⁻¹ band prior to measurements. The spectra were acquired using the Labspec 6® software package and, when possible, the RRUFF database (Lafuente et al., 2015) was used for phase identifications. As corrosion product layers were often heterogeneous, a minimum of 20 Raman spectra were collected on each sample to ensure a good representativeness of the corrosion product layers.

μ -XCT

MicroCT scans were obtained with an Easy Tom XL scanner (RX Solutions, France) equipped with a tungsten x-ray source and a 1516x1920 pixels CCD camera. Parallelepiped samples of cementitious material coming from experiment 2-C were scanned with 100 kV and 100 μ A source settings and without filter. The scanned samples were enclosed in a 5x4x3 mm³ volume and a total of 1440 images were acquired per sample. Reconstruction was handled by the RX Solutions Xact software, producing 3D images with a 3.8 μ m voxel size. The voxel values can then be compared between samples because the geometric, source, detector and reconstruction parameters remained unchanged. Post-processing of the micro-CT scans was performed using Dragonfly 2020.2, Object Research System (ORS) Inc, Montreal, Canada, 2020 (www.theobjectscm.com/dragonfly). For each sample, a cylindrical or polygonal region of $12 \pm 3 \text{ mm}^3$ was selected. Thresholds were manually defined to segment the different component of the cementitious material and to allow the computation of volume rates.

Corrosion rates determination

In order to assess the evolution of the corrosion rates with time, weight loss measurements were performed on steel coupons periodically retrieved from mock-up tests related to bacterial and temperature impact on corrosion, following the ASTM recommendation (ASTM, 2011).

Briefly, steel coupons were taken-off from the reactors in an anoxic glove-box and immersed in 99% pure de-aerated (under vacuum) ethanol for few seconds to stop corrosion. Then the coupons were dried, transferred outside the glove box, and immersed in the following successive baths: 15% HCL – 5% Hexamine solution, 5% Na₂CO₃ and Isopropanol (99%) with intermediate rinsing in deionized water between each bath. After this process, the coupons were weighted with an accuracy of 0.1 mg. This operation was repeated until the weight stabilization of the coupons. The corrosion rates were calculated from the following Equation 1:

$$\text{Equation 1: Corrosion rate } (\mu\text{m} \cdot \text{y}^{-1}) = \frac{3650 \times \text{weight loss (mg)}}{\text{Density } \left(\frac{\text{g}}{\text{cm}^3}\right) \times \text{Area (cm}^2\text{)} \times \text{Time (days)}}$$

with a density of 7.85 (g/cm³) for steel.

Corrosion damage was also assessed by optical measurements on cross-sectioned samples coming from mock-up test related to temperature using a metallographic microscope (Kern, Germany). For these analyses, micrographs were collected along the whole length of the steel rods for each type of exposed surface (3μm mirror polished, 180 grid, external mill scale and internal mill scale). Measurements of the corrosion thickness were realized every 50 μm using ImageJ software, leading to more than 200 measurements per surface type. For the mill-scale exposed surface, the initial mean mill-scale thickness was previously determined by measuring it in a pristine sample with a similar protocol. This thickness was considered as the zero value and subtracted to the measured value of the corroded samples.

The *in situ* BACUCE experiments related to temperature impact (BAC-3, BAC-4 and BAC-5) were also equipped with *in situ* corrosion sensors. Such sensor was located in the heterogeneity that was (supposed to be) filled only with groundwater. Corrosion sensors were electrical resistance (ER) corrosion sensors. This is a device where the thickness reduction of the flat conductive metal (due to the corrosion) is measured *via* its increase in electrical resistivity. In our case the exposed conductor was made of 0.5 mm thick cold-rolled carbon steel sheet with chemical composition close to the one of the tube (Figure 19). The electrical resistance (temperature compensated) and therefore the remaining thickness were read out every 3 hours. It should be stressed that the operating principle of ER corrosion sensor is independent of the environment and does not assume any electrochemical processes.

Analyses of solution

Pore water solutions coming from mock-up tests were analysed to monitor their chemical evolution with time. Periodically, reactors were retrieved from the oven, put in an in-house isothermal container to keep the solutions at 80°C and transferred in an anoxic glove box. pH measurements were made with a pH electrode (Mettler-Toledo) freshly calibrated with IUPAC pH buffer. The other fraction of the solutions was filtered with 0.2 μm PTFE Millipores® membrane filter prior to their analyses. Major anions (Cl, F, SO₄, NO₃) were analysed by means of ionic chromatography with a Metrohm 850 Professional IC and a Metrohm 861 Advanced Compact IC. Major cations (Na, K, Ca, Mg, Sr,) were analysed using either a Metrohm 850 Professional IC or an ICP-OES (Inductively Coupled Plasma – Optical Emission Spectroscopy) ICAP 7000 (Thermo Scientific®). Total inorganic/organic carbon (TIC/TOC) was measured by means of a carbon analyser Analytikjena 2100S and a VARIOTOC (Elementar®). For Fe, Al and Si analyses, both a Q (quadrupole)-ICP-153 MS (Thermo Scientific X Series 2) and the ICP-OES ICAP 7000 (Thermo Scientific®) were used.

For samples heated at 80°C, care was taken to stabilize the temperature during the sampling and pH measurements using thermostatic box and bath. These operations were performed in an Ar filled glove box to prevent carbonation of the samples.

4.4 Results

4.4.1 Evolution of the cementitious materials mineralogy and pore water solution composition

4.4.1.1 Bentonite-cement grout (BCG) experiments – Mock up

BCG mineralogical evolution (T = 80°C)

The bentonite-cement grout is a new type of engineering material of which chemistry and hydration products are not well defined yet both at ambient and high temperatures. A very recent study presenting the chemical and mineralogical study of this material is however available (Bonnet et al., 2022).

Thus, mineralogical and microstructural analyses as well as geochemical modelling were performed to assess the evolution of the mineralogy of this material, particularly at 80°C.

After 32 days of curing time, initial XRD analyses of BCG disks indicated the presence of AFt (aluminum ferrite trisulfate/ettringite), AFm (aluminum ferrite monosulfate), gypsum and calcite that mostly came from hydration of the cementitious phases. Hydrotalcite, cristobalite, calcite, montmorillonite and quartz were also identified and were related to the BCG constituents (Table 7). The presence of amorphous SiO₂ from the silica fume and C-(A)-S-H was also pointed out. The lack of portlandite (CH) was a characteristic of such low-pH cements where silica fume enhanced the formation of C-S-H instead of CH. After being put into contact with solution at 80°C, the main change in time of the bulk mineralogy is the full depletion of ettringite and gypsum (or anhydrite) precipitation and potential degradation of smectite into illite (Figure 21). Note that gypsum formation is unlikely at 80°C and that Bonnet et al. (2022) rather observed disappearance of this phase when heating their BCG at 90°C. The presence of this phase might rather be linked to the high L/S ratio employed in this experiment and to the potential decrease of temperature during dismantling operation leading to precipitation of gypsum. The presence of portlandite at the surface of some BCG disks (not shown) can be explained by the same reason.

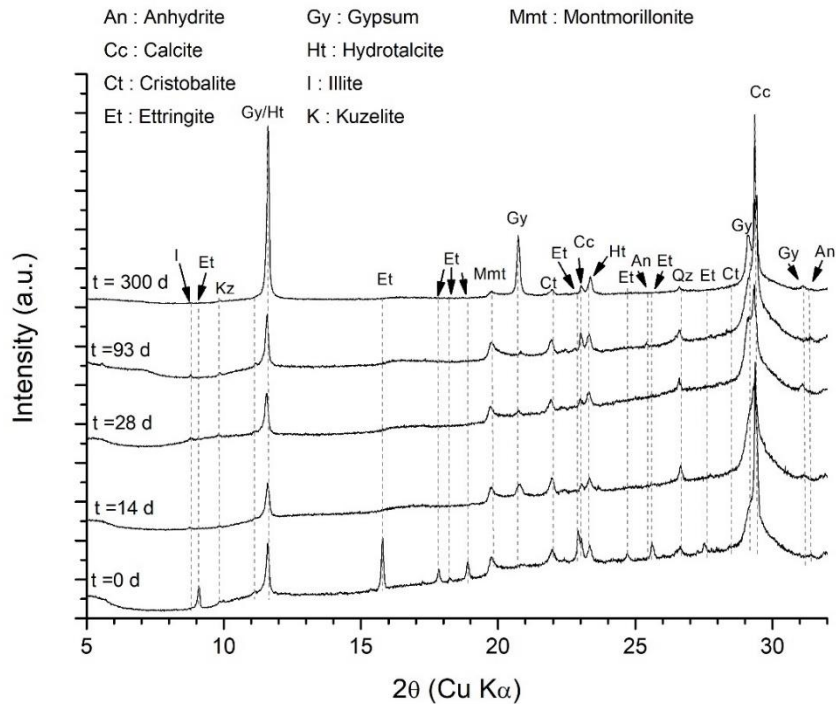


Figure 21: XRD patterns of the BCG disks from mock-up tests, after different period of immersion in synthetic porewater solution at 80°C.

Mineralogical and microstructural evolution of the BCG in contact with synthetic solution at 80°C was also assessed by μ -Xct. This technique allows to differentiate cement phases in function of their relative density, no matter their structural state (i.e., crystalline or amorphous), while preserving the microstructural integrity of the sample. Figure 22 shows μ -XCT slice sections of densified silica fume particles (DSFp) together with BCG disk sections immersed for different periods of time in BCG-synthetic solution at 80°C. Four different components can be differentiated in the pristine sample (i.e., cured for 32 days). They are denoted as Porosity, Blast Furnace particles (BFp), Densified Silica Fume particles (DSFp) and Matrix.

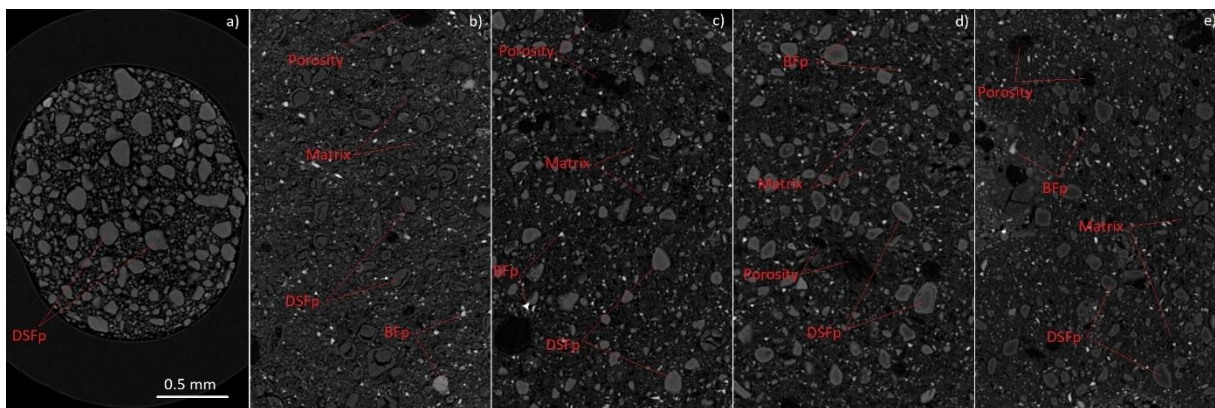


Figure 22: μ -XCT slices sections of (a) the densified silica fume particles (DSFp) together with grout cement disk sections coming from experiment 2 - C after (b) 0, (c) 28, (d) 93 and (e) 300 days of interaction with BCG-synthetic solution at 80 °C.

The BFp component is constituted of bright dense particles measuring several tens of micrometers that mostly come from the blast slag furnace component added in the CEM III-A. Some of these bright particles might also come from the bentonite (i.e., pyroxenes, feldspar, zeolite, quartz, cristobalite, pyrite) or from the crystalline fraction of the silica fume component (i.e., cristobalite, quartz and

moissanite). The volume fraction of the BFp component was determined to be approximately 2 % in the pristine material, and it dropped to 1% for all the other samples immersed in synthetic solution at 80°C. A rapid calculation indicated that more than 50% of this component reacted during the curing at room temperature during 32 days and that it further reacted to 80% after 15 days of immersion at 80°C prior to stabilize.

The DSFp consist of large aggregates of spherical nanoparticles of SiO₂ (Ni et al., 2021). These particles are cracked and totally dissolved in some areas in the pristine sample (t = 0 day) which reflect their porous character and the availability of silicon in solution to form C-(A)-S-H from SF (Silica Fume). Also, these particles are darker than the unhydrated DSFp analysed in similar conditions and thus present a lower density. This latter observation suggests that hydration or partial dissolution of these particles occurred at 20°C. After 28 days of immersion in the synthetic solution at 80°C, the mean grey level of these particles increased, corresponding to an increase of their mean density. Moreover, a density zonation occurred in most of these particles, indicating a porosity and/or a chemical variation in the different layers of these particles. These observations can be attributed to the enrichment in the calcium content of the DSFp which is due to the calcium release from ettringite degradation. This suggested formation of C-(A)-S-H inside these particles with a zonation coming from the dissolution of some layers prior to the immersion of the cementitious disks in the synthetic solution at 80°C. Then, the grey level of the DSFp started to decrease with time, especially in the core of the particles, indicating a decrease in the core density of the DSFp. This result suggested a destabilization of C-(A)-S-H in the DSFp.

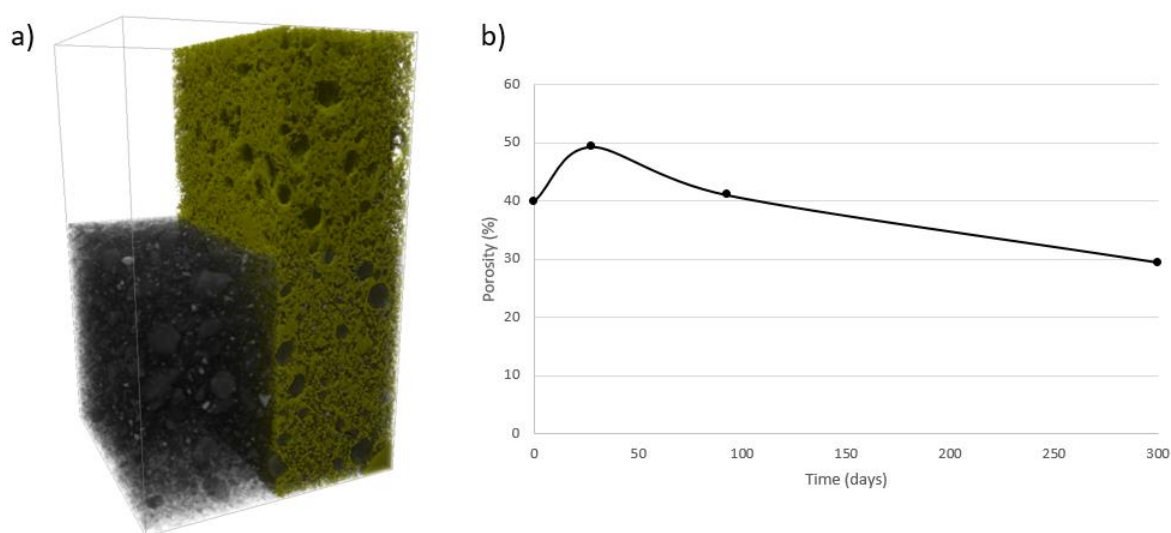


Figure 23: μ -XCT computed 3D representation of the BCG (left side) and of the macro-porosity of BCG (right side - yellow) obtained on a fragment of grout cement disk coming from experiment 2-C after 28 days of interaction with synthetic solution at 80°C along with the graph showing the evolution of macro porosity (part of total porosity with pore volume superior to 8 μm^3) with time.

Figure 23 shows the evolution of the macro porosity (part of total porosity with pore volume superior to 8 μm^3 , which represents the μ CT voxel volume) with time. The initial total porosity of the BCG measured by water porosity measurements is 75% (± 1), and approximately 40% of this porosity corresponds to macro porosity. This macro porosity first increases with increasing temperature due to the degradation of ettringite and further decrease with hydration of the BCG and precipitation of calcium sulphate inside large pores.

Thermodynamic modelling was performed considering the experimental observations. The bulk composition used in the modelling includes the cement phase (and its gypsum additive) and the silica fume, which will be hydrated partly once in contact with water. The bentonite does not account for the bulk composition, it is introduced directly as a mineral in the model with cationic exchangeable properties of montmorillonite. Montmorillonite was not allowed to dissolve in the modelling in a first approximation,

but the fast cation exchange could progress during the hydration of the cement part of the grout. However, it would be interesting in a second step to consider in HYTEC both montmorillonite dissolution and cation exchange. The initial hydrotalcite content is not considered due to its low percentage and because hydrotalcite is readily generated during the hydration process in the modelling.

Two sets of thermodynamic data were tested by using the Thermoddem database (Blanc et al., 2012; version 1.7 for model 1 and version 1.10 for model 2): (i) model 1 with pure C-S-H and straetlingite as a proxy of C-A-S-H; (ii) model 2 with C-A-S-H phases. Note that as straetlingite was not observed by XRD, the latter model seems more representative. In both cases, a total hydration of blast furnace (100%) and silica fume (100%) was assumed for the initial state.

Table 19 gives the modelled initial mineralogy of the hydrated bentonite/cement grout. The C-S-H phase has a lower Ca/Si ratio (C/S = 0.8) than in CEM I (C/S = 1.6) in direct relation with the bulk grout composition that has a smaller relative amount of CaO compared to CEM I (or similarly the silica component is higher in the grout due to the significant SiO₂ input of the silica fume). The CEM III also brings more aluminium in the system than CEM I, which leads to the formation of crystalline C-A-S-H (model 1) or amorphous C-A-S-H (model 2) phases.

Table 19: Modelling of the initial mineralogy of the bentonite/low-pH cement grout at 80°C considering 75% of porosity.

| Mineral | Model 1 with C-S-H | Model 2 with C-A-S-H |
|--|---|-------------------------|
| (wt.%) | 80°C | 80°C |
| C _{0.8} -S-H | 50.5 | - |
| straetlingite (cryst. C-A-S-H) | 9 | - |
| C _{0.8} S-H | - | 5.0 |
| C _{0.7} -A _{0.05} -S-H | - | 59 |
| Ettringite | 0 | 0 |
| Anhydrite | 2.0 | 2.0 |
| Hydrotalcite | 5.5 | 5.5 |
| quartz | 24 | 19.5 |
| Montmorillonite | 9 ⁽¹⁾ | 9 ⁽¹⁾ |
| exchangeable equiv. fraction | Ca ²⁺ 45 % Na ⁺ 55 % | 45 % 55 % |

(1) As a first approximation since montmorillonite dissolution by pozzolanic reactivity is likely at 80°C on the long term and as transformation of Mmt to illite was experimentally observed.

The hydration and evolution of such BCG material are quite complex and involve plenty of interconnected processes. The geochemical model can capture some of them explaining the consistency between experimental and model results. However, some of the processes were not taken into account for the sake of simplicity, leading to observed differences.

First, the hydration of silica fume is complex because it is present as DSFp in the BCG and thus, the availability of this silica source evolved during hydration due to (i) either the formation of diffuse barrier around the DSFp grains, as suggested by the presence of Ca rich rim around DSFp in BACUCE *in situ* low temperature experiment (BAC-1 and BAC-2, not shown) (ii) or a decrease of the Ca content, inducing a destabilization of C-A-S-H. In both cases, the formation and/or stability of C-A-S-H is limited as also observed by Bonnet et al. (2022).

Secondly, the presence of carbonate is not predicted by the model, but experimental results show that their amount is quite important. This is due to the fast carbonation of slag rich cement in air compared to classical Portland cement (Boukni et al., 2009; Litvan et al., 1986; Osborne, 1986; Sisomphon et al., 2007). As the porosity of this material is very high and as this material will dry in oxic condition during the exploitation, a large amount of carbonate might form. As portlandite is absent in BCG, carbonation of C-(A)-S-H occurred mobilizing calcium from this phase. This would lead to a decrease in the Ca/Si ratio of C-(A)-S-H phase, that might be even smaller than the one predicted by the model as observed by Bonnet et al. (2022). Interestingly, the study of Bonnet et al. (2022) showed that at temperature of 90°C, the calcite was transformed into vaterite and aragonite and this phase transition was not observed in our study.

Finally, it is worth mentioning that the hydration of the CaO oxide strongly modifies the cationic exchange composition of montmorillonite in the model, since one evolves from a pure Na-clay phase to a mix between Ca-clay and Na-clay phase (Table 19). In the present study, this mechanism was not deeply investigated but the study of Bonnet et al. (2022) reports that the montmorillonite fraction of the bentonite turns from Na-Mmt to Ca/Mg-Mmt at 90°C in a relatively short period of time.

Synthetic pore water in contact with BCG evolution (T = 80°C)

The composition and pH of the synthetic pore water in the reservoir of mock-up EXP 1-R were followed with time and modelled. Table 20 gives the composition of the cell reservoir considered in the modelling grid. Again, it is worth noting that the cell is “an open system” since the pore water inside the reservoir is not necessarily identical to the chemistry of the pore water.

Table 20: Initial chemical composition of the synthetic solution of the cell considered in the modelling at 80°C (left side: mmol/L; right side: mg/L).

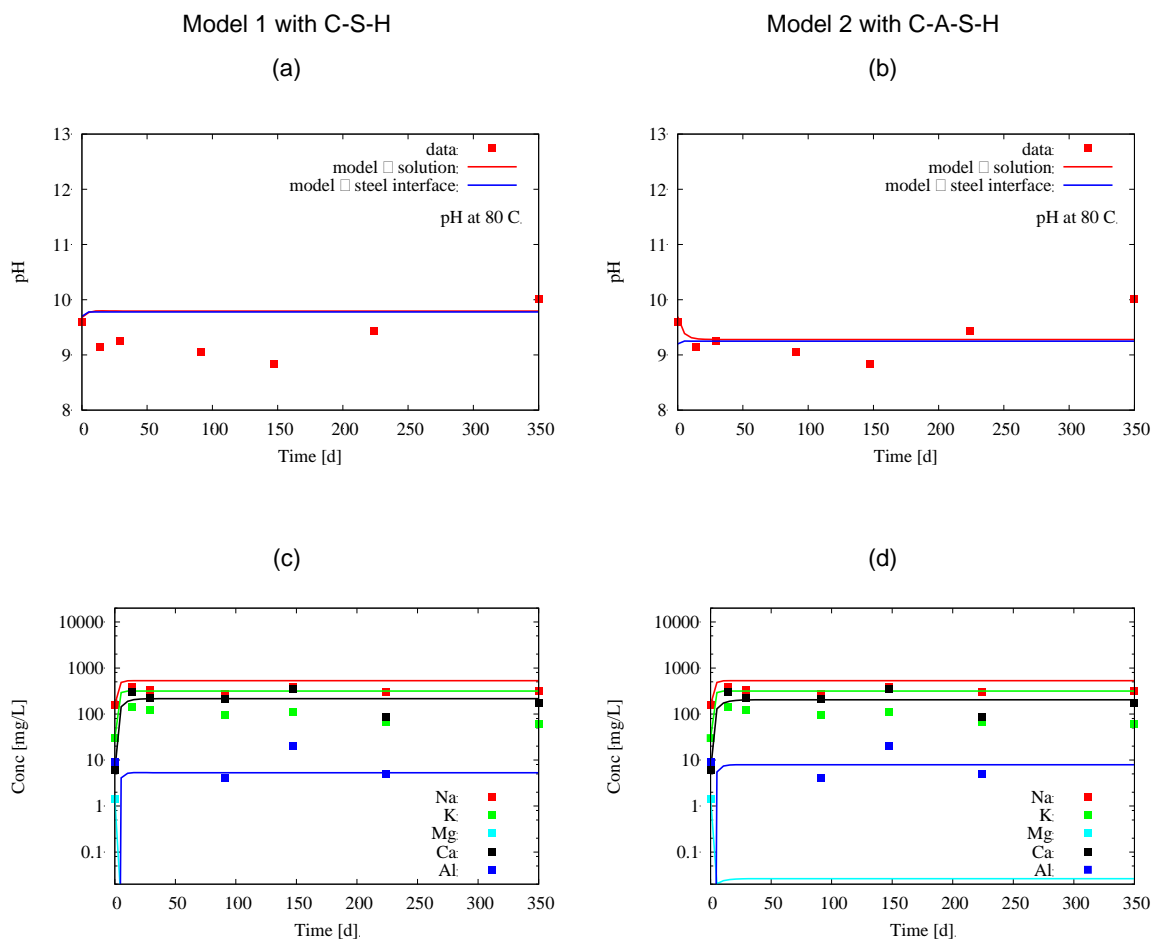
| Total concentration | 80°C | 80°C |
|-------------------------------|------------|----------|
| pH | 9.7 | 9.7 |
| K ⁺ | 0.7 mmol/L | 30 mg/L |
| Na ⁺ | 7 mmol/L | 160 mg/L |
| Ca ²⁺ | 0.1 mmol/L | 6 mg/L |
| Cl ⁻ | 2 mmol/L | 66 mg/L |
| SO ₄ ²⁻ | 2.5 mmol/L | 235 mg/L |

Figure 24 shows the modelling of the evolution with time of the chemistry of the cell reservoir obtained for both model 1 (with C-S-H) and model 2 (with C-A-S-H) compared the data that were measured during the experiment (mock-up EXP 1-R). Overall, there is a good agreement between modelled and measured data, despite that the model of the initial state has been blind built on previous batch experiments. The releases of the cations K^+ , Ca^{2+} and the anions Cl^- , SO_4^{2-} into the cell reservoir are similar for the two models. They demonstrate the relevance of the effective diffusion coefficient fixed in the modelling (the porosity was fixed to 75 % and the effective diffusion to $1.5 \times 10^{-10} \text{ m}^2/\text{s}$ at 80°C). However, the modelled concentration in Na^+ , K^+ and SO_4^{2-} are overestimated by roughly a factor 2

(Appendix C), probably because the sorption of K^+ (and Na^+) on C-S-H phases was not included in the model.

The pH only changes over a month too and then does not vary significantly over time in the modelling, whereas the pH slightly increases at the end of the experiment. The global agreement between the modelled and measured pH is better with model 2 than model 1.

Mg concentrations are very low (outside the limits of the graphs) for both measured and modelled data. Both models predict a low Al concentration compared to the other elements which is confirmed by experimental observations. The carbonate concentrations are also well simulated by both models. Only the dissolved silica concentration is not well captured by the modelling. Model 2 underestimates the Si concentration, although model 1 is closer to the experimental data. This underestimation might be linked to the presence of mixed C-(A)-S-H phase and SiO_2 hydrated gel that have different solubility products.



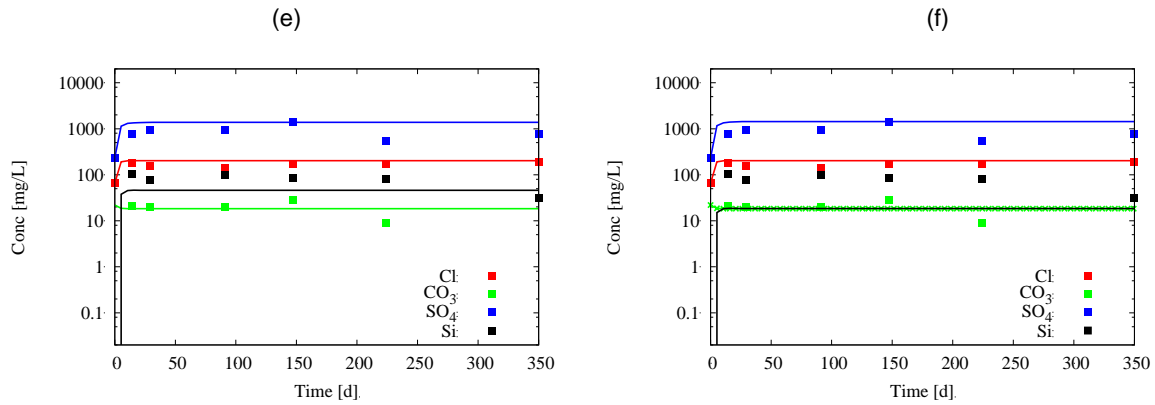


Figure 24: Modelling of the change with time of the chemical composition of the solution in the cell (total aqueous concentration); the experimental data (from exp. 1-R) are given for comparison.

4.4.1.2 CEM I Val d’Azergues – Mock up experiments

CEM I mineralogical evolution (T = 80°C)

The evolution of the cement mineralogy at 80°C with time (mock-up EXP 2-C) was qualitatively followed by XRD (Figure 25). After one month of hydration at 80°C, ettringite was completely depleted at the surface of the cement disk as revealed by the disappearing of the reflections corresponding to this phase. The increase in the relative intensity over time of the sharp peak located near 29° 2θ indicated the formation of well crystallized C-S-H. Moreover, the relative intensity of the reflections corresponding to Si-Katoite (Ca₃Al₂(SiO₄)_y(OH)_{4(3-y)}) indicated the growth of this phase over time. The increase in the relative intensity of reflections corresponding to hydrated cement phases is to link with the decrease in the relative intensity of unreacted cement (Alite (C₃S), Belite (C₂S), Brownmillerite (C₄AF)). The precipitation of arcanite (K₂SO₄) at the surface of the disk immersed for 300 days might have been triggered by evaporation of residual synthetic solution during sampling and portlandite (Ca(OH)₂) crystals were frequently observed at the surface of the cement disks due to the low solubility of this phase in such conditions.

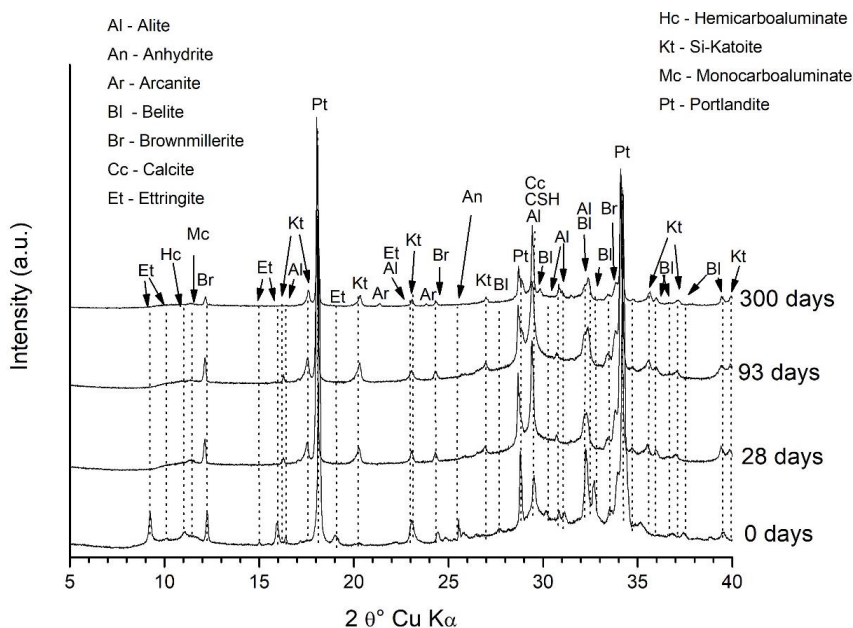


Figure 25: XRD patterns of the cement disks surfaces coming from experiment 2-C.

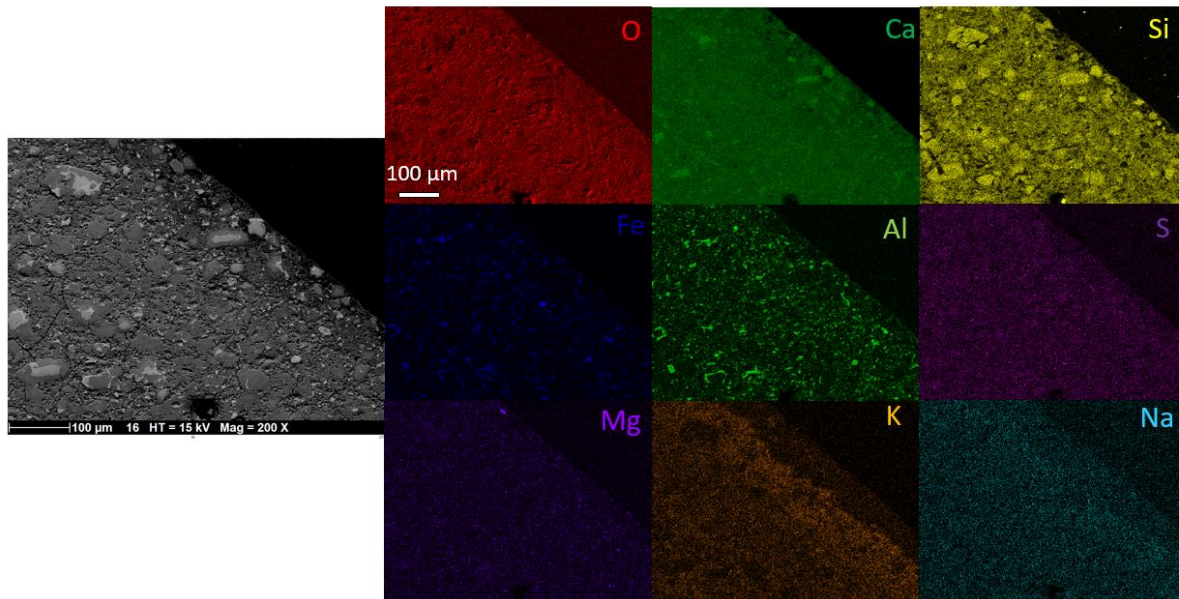


Figure 26: SEM-EDX mapping of a cement cylinder (EXP 1-R) after 354 days of interaction with hyperalkaline synthetic solution at 80°C.

The SEM-EDX mapping of the HCP hydrated for 354 days at 80°C (mock-up EXP 1-R) (Figure 26) confirmed the depletion of ettringite in the whole HCP and the S-mapping revealed the complete release of sulphate in the solution. This result also indicated that generally amorphous monosulfate, if initially present in the HCP, were also completely depleted at 80°C. The BSE mode imaging also showed the large hydration of C₂S and C₃S after 354 days, whereas only slight hydration of C₄AF occurred. At the direct contact with synthetic solution the porosity strongly increased indicating the dissolution of hydrates and accumulation of K was probably associated to its sorption in C-S-H as this element was not associated to any K-bearing phase in the XRD patterns (except arcanite).

In order to assess the extent of CEM I evolution in the BAC-5 *in situ* test, SEM-EDX mapping was acquired at the interface between CEM I and the heterogeneity (Appendix D). The mapping reveals that the S-bearing phase (AFt and/or AFm) are still present in the CEM I even at direct interface with the heterogeneity and the degradation front is very limited compared to the one observed in the mock-up tests. This is certainly linked to a large temperature difference in the two types of experiments. Indeed, the temperature reached by the synthetic solutions in the mock-up tests (80°C) was much larger than the temperature of the solution in the heterogeneity for *in situ* test ($\approx 30^\circ\text{C}$)

In addition to these experimental results, the evolution of the system using grid cells was modelled using the two different models.

The results of these 2 models (model 1 with katoite and model 2 with C₃AH₆) are presented in Appendix E. The general trends can be described as follow:

- Total depletion of SO₄-containing phase after 40 days is simulated by model 2 in agreement with experimental results. It is worth noting that this dissolution is driven by the “open state” of the cell system with diffusion of dissolved SO₄ into the cell reservoir. Monosulfoaluminate would have probably stayed stable without any external reservoir. The dissolution pattern progresses from the most external zones in direct contact with the reservoir towards the core of the hydrated cement paste.
- The Al liberated in solution readily reprecipitate as C₃AH₆ in model 2.
- Model 1 leads to a similar mineralogical transformation but this time ettringite dissolves and katoite precipitates. The disappearance of ettringite during the experiment has been noticed by XRD analysis. As already mentioned in the previous section, the dissolution of ettringite and the consequent release of SO₄ in the reservoir look too fast compared to the experimental data. The precipitation of katoite occurs over the whole cement paste but is a little bit more important at the periphery of the cell reservoir.

- Model 1 and model 2 indicates that the monocarboaluminate remains mostly undissolved during the experiment.
- Neoformation of portlandite is modelled at the boundary with the reservoir, probably due to the release of Ca^{2+} by ettringite and the high pH (thus high OH^- dissolved content) brought by the reservoir solution. Experimental conditions (pH, temperature, E/C and portlandite solubility) also favor the precipitation of portlandite at the surface of the cement paste sample.

Synthetic CEM I solution evolution (T = 80°C)

The composition and pH of the synthetic pore water in the reservoir of mock-up EXP 1-R containing CEM I was followed with time and modelled.

Figure 27 and Figure 28 show the evolution with time of the chemistry of the cell reservoir that was measured during the experiment. It is worth noting that the cell is a kind of “open system” in the sense that the concentrations measured in the reservoir results from the diffusion, and thus possible dilution, of the pore water inside the reservoir and is not necessarily equal to the chemistry of the pore water contained in the porosity of CEM I material.

Figure 27 corresponds to a zoom on the release of potassium which is almost an unreactive tracer indicative of the diffusion properties of the CEM I hardened paste, as well as the release of sulphate which depends both on diffusion and the dissolution of primary cement phases like ettringite (model 1) or monosulfoaluminate (model 2, Figure 28). The K release profile is eventually not indicative because the estimated initial composition of the synthetic pore water masks the signal coming from the cement porewater. That is to say, the initial estimate of the synthetic pore water was not far from the content of the real pore water. The release of sulphate is more informative. The effective diffusion seems reasonably near to reality to fit the experimental SO_4 concentrations measured over the first hundred days in the reservoir.

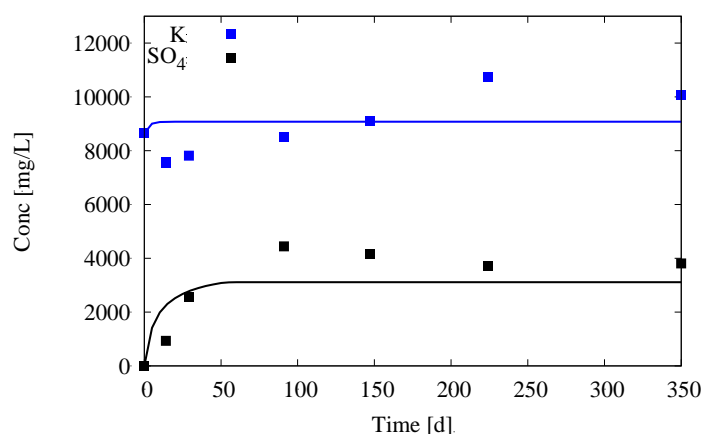


Figure 27: Model 2 with C3AH6: zoom on the potassium and sulphate total aqueous concentration, among others relevant for fitting the effective diffusion coefficient of the cement paste.

Figure 28 brings the full picture of the chemical changes over time for both model assumptions. Overall, there is a good to fair agreement with the solution chemistry. The same conclusions as for K can be drawn for the (almost) conservative elements Na and Cl. The release of SO_4 is better simulated by model 2 than model 1. The behaviour of Ca is also almost constant despite that its concentration is controlled by the pH due to portlandite equilibrium, i.e. $(\text{Ca}^{2+}) = K_s/(\text{OH}^-)^2$. But the pH itself does not vary significantly over time. As a matter of fact, the pH in the cell reservoir was initially fixed to a high value that globally maintained the whole pH high over the time. It is not yet clear why the measured pH is higher from 0.3 unit than the modelled one, but it is probable that the use of a IUPAC standard with a maximum pH of 12.46 at 80°C was not adapted for such measurements.

The silica dissolved concentration is very well captured both by models 1 and 2 although the modelling did not introduce any silica in the initial cell reservoir. The carbonate concentration better fits with the measured one in the model 2. The carbonate concentration better fits with the measured one in the model 2, partly because Al total concentration is higher (but further away from the experimental data) leading to a lower CO_3 total concentration through the solubility product of monocarboaluminate at thermodynamic equilibrium. Furthermore, calcite precipitation was forbidden in model 1 due to numerical instability. Both models predict a low Al concentration compared to the other elements, but still higher than experimental data. Model 1 is closer to reality for Al. Eventually, Mg concentrations are very low (outside the limits of the graphs) both in the experiment as in the modelling.

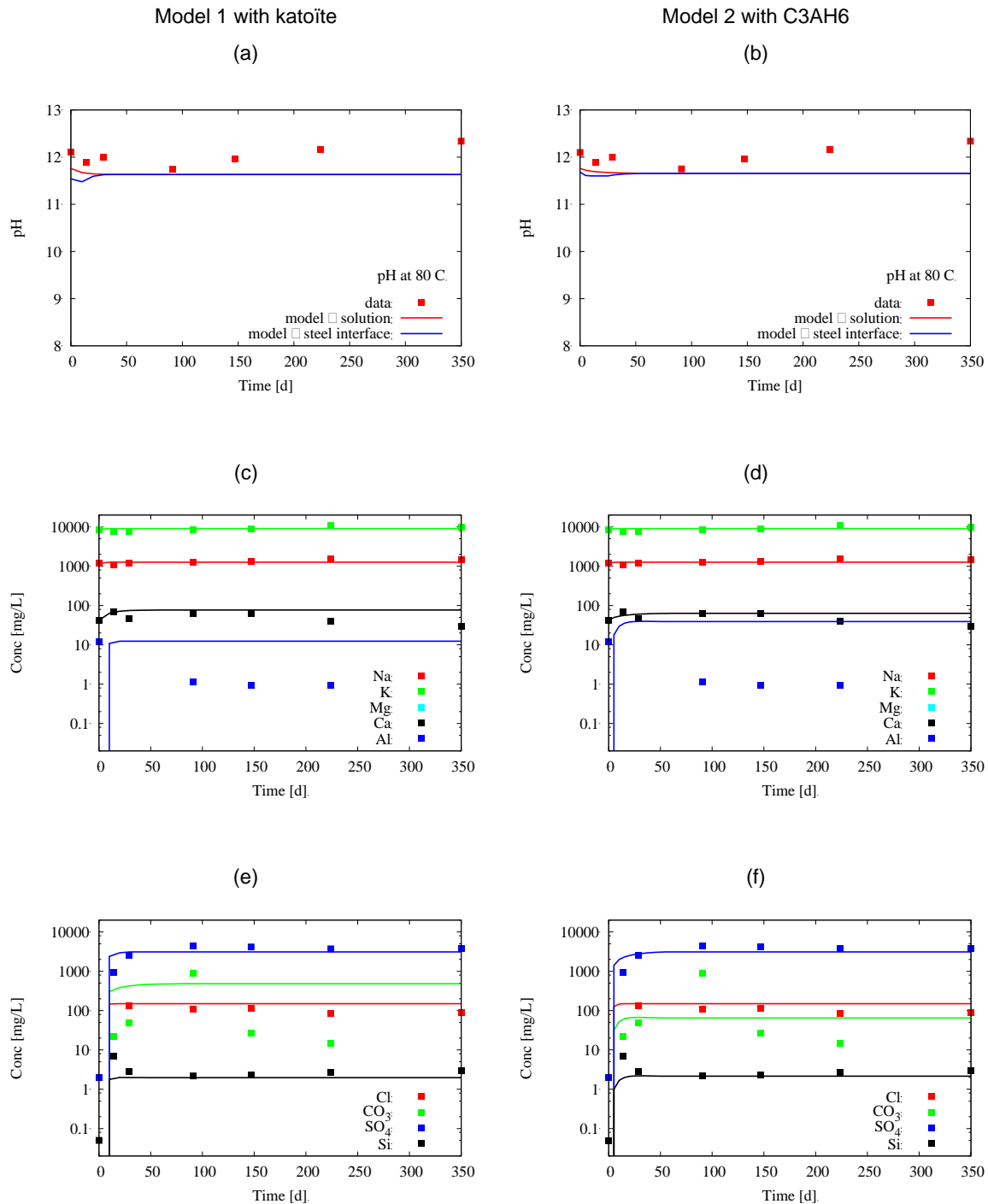


Figure 28: Modelling of the change with time of the chemical composition of the solution in the cell (total aqueous concentration); the experimental data are given for comparison.

4.4.2 Impact of bacterial activity on corrosion

4.4.2.1 General aspects

Mock-up tests

Figure 29 shows macroscopic pictures of the metallic coupons associated to each corrosion test of the mock-up tests before soaking (i.e., different medium and contact time).

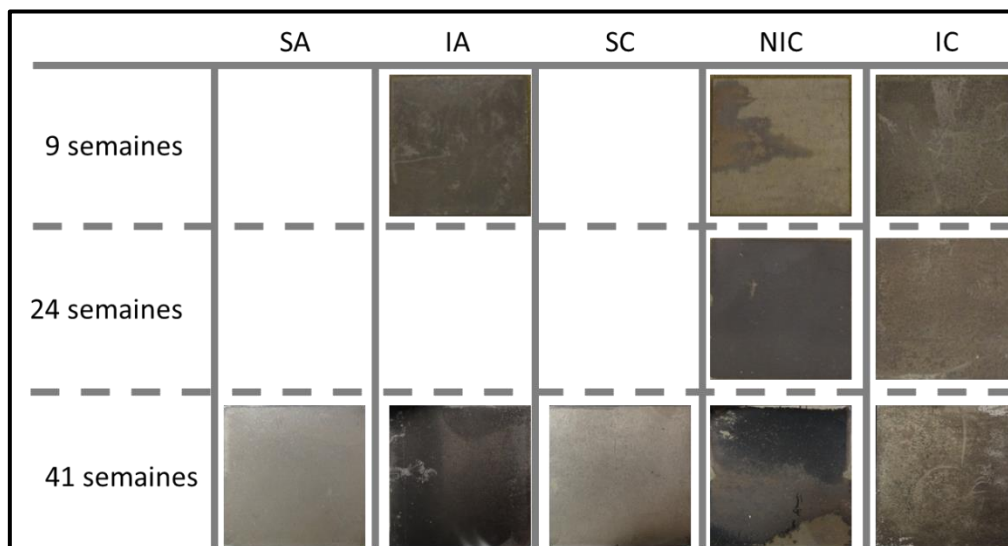


Figure 29: Macroscopic pictures of the metallic coupons associated to each corrosion tests (different medium: tests performed in “mix 75/25”: sterile test (SC), test without (NIC) or with (IC) microbial inoculation; tests performed in “synthetic Tournemire argillite porewater”: sterile test (SA), test with (IA) microbial inoculation, and contact time).

First of all, the coupons associated to sterile test (SA-41 and SC-41) show no macroscopically visible corrosion products even after 41 weeks of interaction with synthetic solutions. For all other tests, the coupons are progressively covered with corrosion products with time, without traces of localized corrosion phenomena. For samples in argillaceous pore water with inoculation (IA), the corrosion product layer is dark and uniform. For tests with BCG-argillite mixed pore water (NIC and IC), the corrosion products are also dark and brownish.

In order to analyse the possibility of localized corrosion processes, cross sections of the coupons were prepared and analysed by SEM (Figure 30). This figure shows that corrosion is globally uniform, with the presence of irregularities that might be explained by the presence of defects on the steel surface.

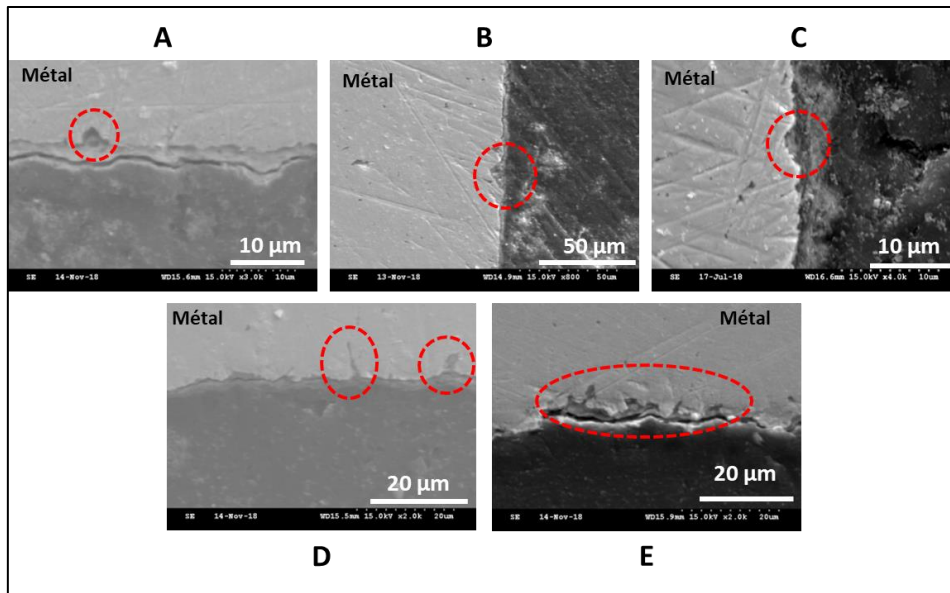


Figure 30: SEM-ES pictures associated to cross-section analyses of metallic coupons of IA-41 (A, B), NIC-24 (C), NIC-48 (D) and IC-42 (E).

In situ experiments

Figure 31 shows typical corrosion features of the samples coming from BAC-1 and BAC-2 *in situ* experiments for 3 different interfaces (i.e., steel/heterogeneity; steel/BCG; steel/BCG/argillite interfaces).

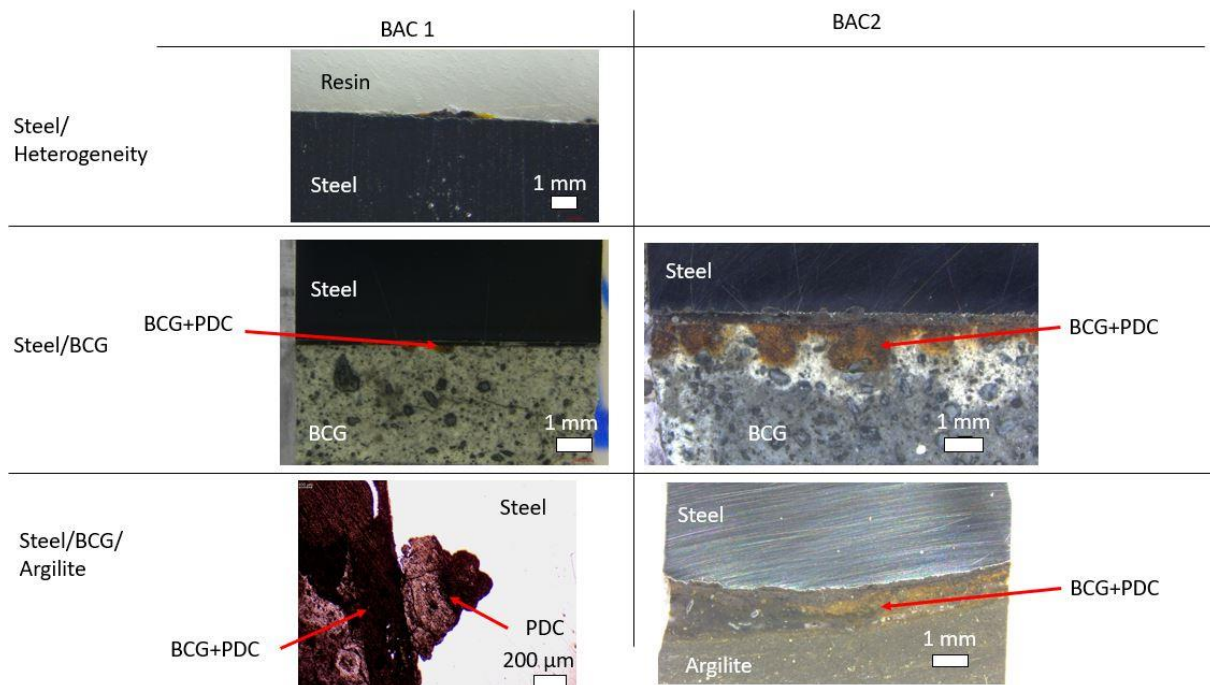


Figure 31: Selected optical micrographs of samples coming from BAC-1 and BAC-2 experiments

The optical measurements performed on several samples for each interface and experiments lead to the following conclusions:

- (i) At the steel/heterogeneity interface, corrosion is very limited. In some samples from BAC-1 and BAC-2, dark/brownish corrosion products are observed locally.
- (ii) At the steel/BCG interface, the corrosion phenomenon is heterogeneous. Most of the samples coming from both experiments were only slightly corroded from a macroscopical point of view. Localized corrosion spots appeared clearly with the presence of brownish/orange corrosion products inside the BCG at the vicinity of the steel. For some BAC-2 samples, corrosion of steel was much more advanced. The presence of hemispheric holes of hundreds of micrometers width and with a maximum depth of $\approx 100 \mu\text{m}$ were observed all along the surfaces of some samples.
- (iii) At the interface between steel/BCG/argillite, all examined sample were highly corroded. In some samples, the entire surface was entirely corroded more or less homogeneously and some large pits/tubercles ($>500\mu\text{m}$ in depth) were observed in some other samples. Even if the viscosity of the BCG is high, the filling of the small space between steel and argillite was not optimal and the presence of voids after dismantling was revealed by μ -XCT (Appendix F).

The main difference between the mock-up test and *in situ* experiment is the observation of localized corrosion phenomena in the latter ones.

4.4.2.2 Characterization of the corrosion products

Analyses of the sample coming from the mock-up and *in situ* tests were conducted by means of SEM-EDX, μ -Raman and XRD.

Mock-up tests

The SEM-EDX analyses on the coupons coming from the mock-up sterile tests revealed the presence of iron oxides and iron silicates (Figure 32). In order to gain more information on the nature of these corrosion products, μ -Raman analyses were performed at the surface of the coupons. They revealed that the nature of the iron oxide is either maghemite ($\gamma\text{-Fe}_2\text{O}_3$) or magnetite (Fe_3O_4). Indeed, even if these two phases display a similar spinel structure, μ -Raman is an adapted tool to discriminate these phases, especially in the presence of a magnon mode near 1400 cm^{-1} (El Mendili et al., 2016). However, the Raman spectra is dependent on the crystallinity of these phases and the poor quality of the Raman spectra presented in Figure 33 might be linked to the low crystallinity of these corrosion products. Nevertheless, the formation of maghemite can be attributed to the dry aerobic corrosion process that the coupons underwent during the period (few weeks) before the experiments started. The absence of Raman signal arising from iron silicates is not surprising as the characterization of these phases by this tool often fail (e.g., de Combarieu et al., 2011; Schlegel et al., 2014).

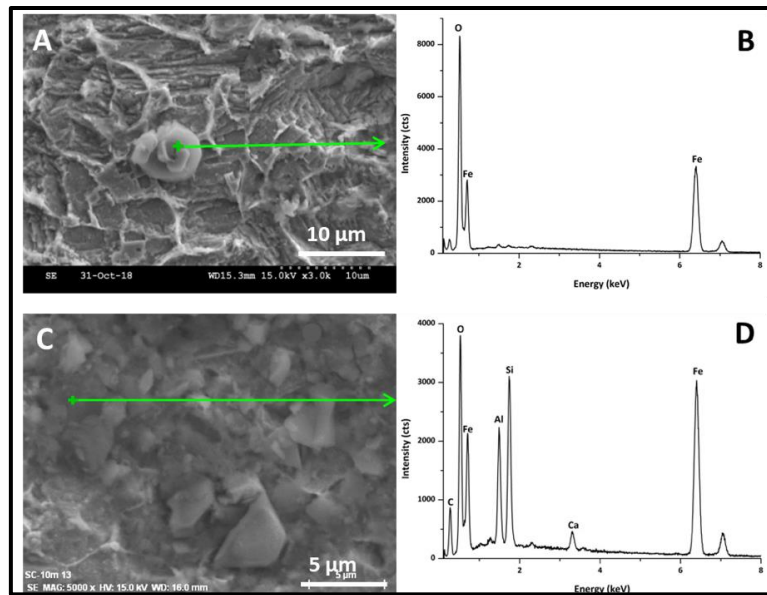


Figure 32: Secondary electron (SE) images of metallic coupons surface from SA-41 (A) and SC-41 (C) tests and associated EDX spectra (B et D, respectively).

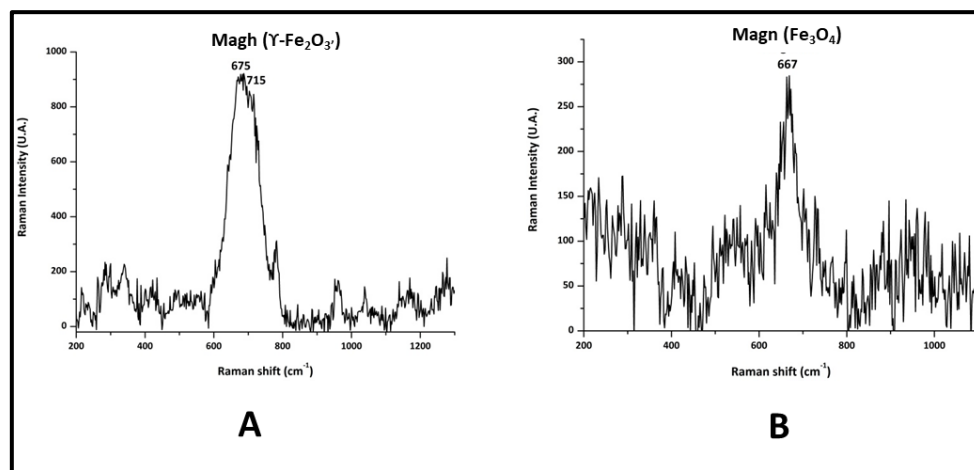


Figure 33: Typical Raman spectra obtained for the metallic coupon surface studied in sterile conditions SA-41 and SC-41 (Magh = maghemite; Magn = magnetite).

For all the other tests (i.e., with or without inoculation for both “75% of BCG pore water and 25% of synthetic argillite pore water solution” and “synthetic argillite pore water solution only” media), SEM-EDX analyses showed that the corrosion product layer is composed of iron (Fe), sulphur (S) and oxygen (O). Figure 34 shows the SEM pictures obtained for the cross-section analyses performed on the metallic coupons studied without inoculation in the “75% of BCG porewater and 25% of synthetic argillite porewater solution” media (NIC tests). One can note that the same kind of patterns have been also observed for both (IA) and (IC) tests.

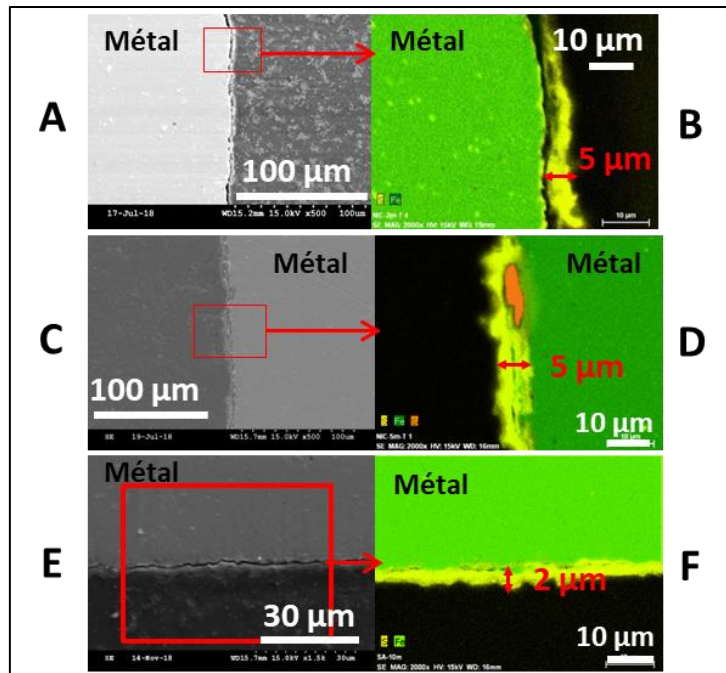


Figure 34: SEM pictures associated to cross-section analyses of metallic coupons of NIC-9 (A and B), NIC-24 (C and D) and NIC-42 (E and F) tests. Secondary electron (SE) images (A, C, E) and Energy-Dispersive X-ray Spectroscopy (EDX) mapping (B, D, F). Sulphur in yellow color, iron in green color.

Moreover, one can note that the SEM-EDX analyses performed at the surface of these metallic coupons (i.e., all the coupons associated to IA, NIC and IC tests) showed the formation of structure exhibiting a “intertwined filament cluster” morphology (Figure 35).

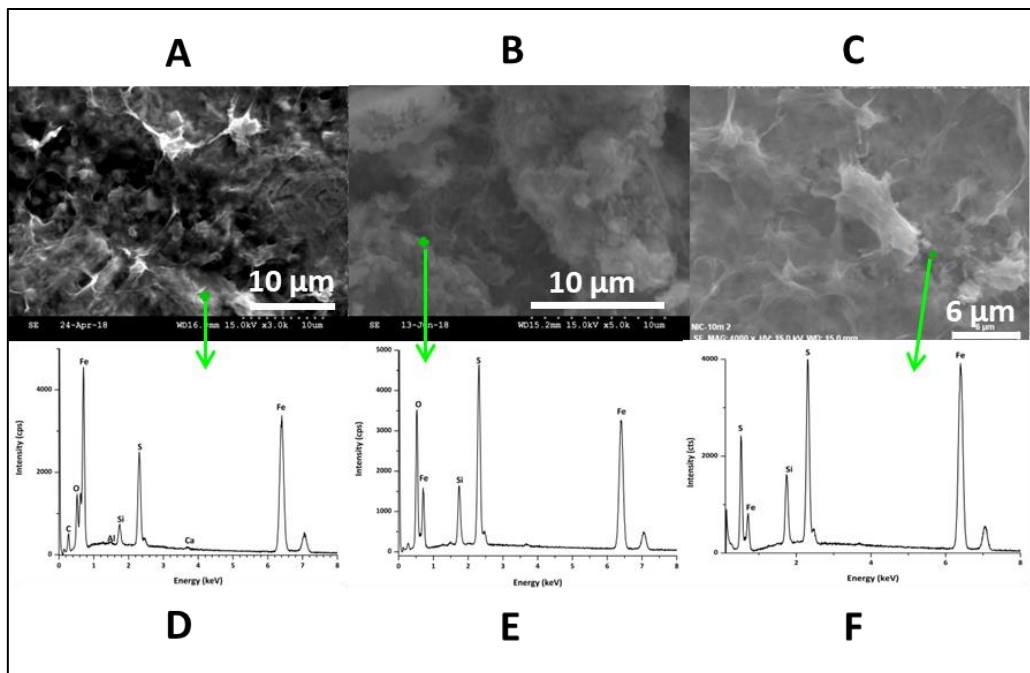


Figure 35: Surface morphology images obtained by SEM-EDX (A, B, C) and associated SEM-EDX elementary analyses of the pointed zone (D, E, F). These results are associated to NIC-9 (A et D), NIC-24 (B, E) and NIC-41 (C, F) tests.

The μ -Raman analyses performed on the metallic coupons associated to these non-sterile tests (i.e., with or without inoculation for both “75% of BCG pore water and 25% of synthetic argillite pore water solution” and “synthetic argillite porewater solution only” media) indicated that the corrosion product layer is mainly composed of two iron-sulphur species: mackinawite (FeS) and greigite (Fe₃S₄) (Figure 36).

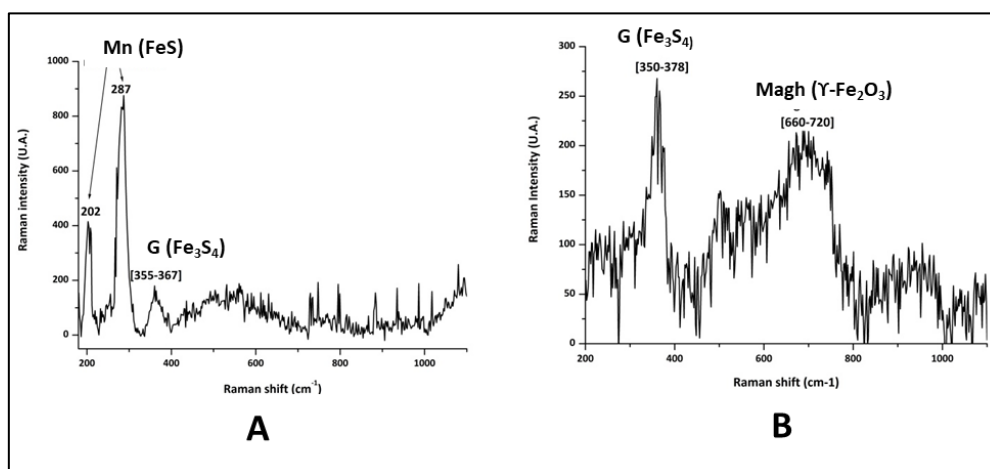


Figure 36: Typical Raman spectra obtained for the metallic coupon surface studied in non-sterile conditions (IA, NIC and IC tests) (Magh = maghemite; Mn = mackinawite ; G = greigite).

In situ experiments

For the *in situ* tests, several samples of the three different types of interfaces were studied and representative analyses are given in this report.

One important point to notice is that the protective layer is probably made of phosphate and Na silicate constituting the mill scale layer is still present in all the examined samples. However, this layer could have at least partly reacted at some interfaces. The relic of this layer is marked with the Na layer observed in the different SEM mappings (Figure 37, Figure 38 and Figure 39) and allows to determine the trace of original steel surface.

Figure 37 shows a SEM-EDX map of steel/heterogeneity interface (i.e., steel not in direct contact with BCG) for BAC-1 experiment. The selected area corresponds to the dark brownish phase cluster presented in Figure 31. The examination of this area revealed that the supposed corrosion products (CPs) might rather be a fragment of BCG or a precipitate (from synthetic solution) that have reacted with steel. Indeed, the cluster observed between the steel and the heterogeneity filled by resin is laterally heterogeneous in composition, has a low density and is not incrustated into the steel as generally observed for CPs². The composition of this cluster suggests that it might be a C-A-S-H more or less enriched in each of its constituting elements that could have trapped an important quantity of iron (see ternary diagram Figure 40) by either sorption and/or nanoparticles' precipitation mechanisms. Precipitation of C-A-S-H from the solution would have been triggered by the reaction between the BCG and the surrounding solution and the super-saturation of this phase with respect to the composition of the synthetic solution. Nucleation of this phase would have been favoured by the presence of the steel surface and corrosion of steel leading to incorporation of iron in this cluster would have been triggered by the local environment changes (presence or absence of solid at contact with steel).

² Sometimes corrosion products are not adhering the steel surface due to the sample preparation mechanical stress that can desolidarize steel and CPs. In such case the trace of the nesting between steel and CP is still visible.

Nevertheless, as observed by optical measurements, the corrosion of such interface is very limited for all observed samples coming from BAC-1 and BAC-2.

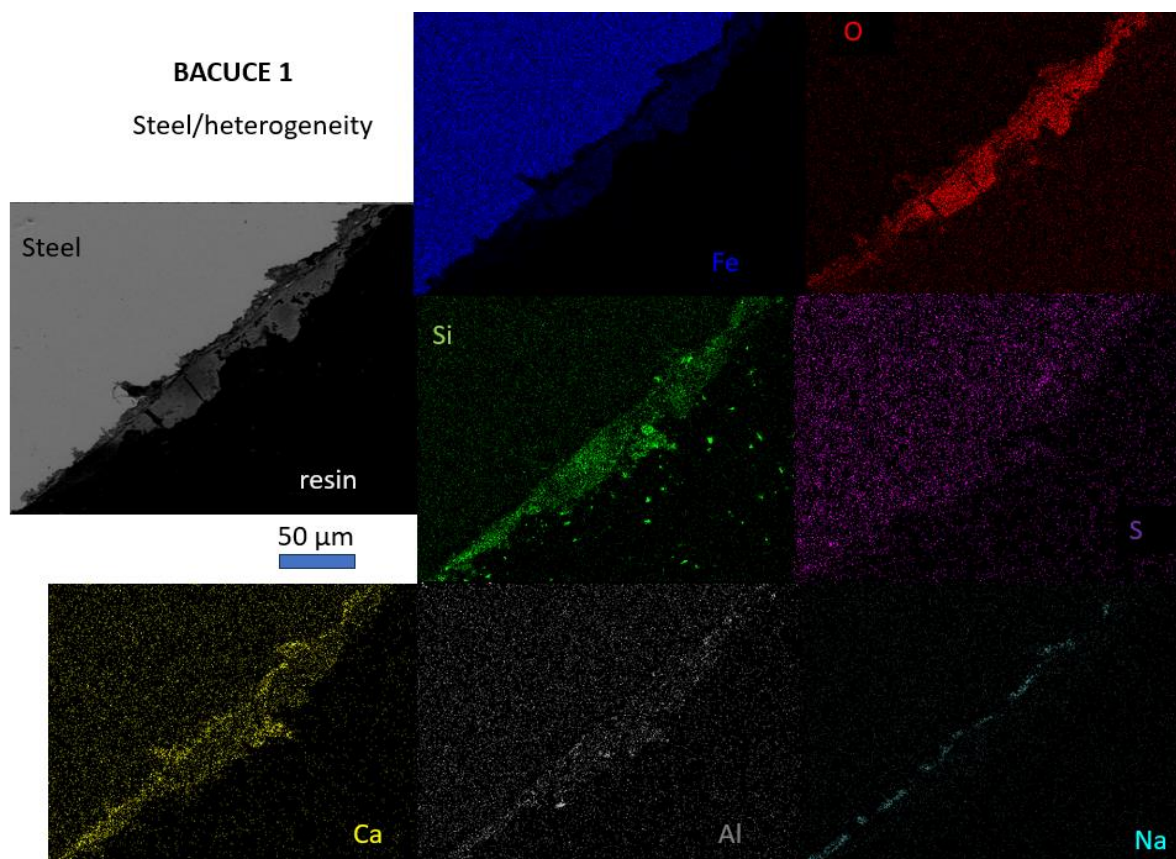


Figure 37: SEM-EDX mappings of steel/heterogeneity interface for BAC-1 experiment.

Figure 38 shows typical SEM-EDX mapping of the interface between BCG and steel for BAC-1 and BAC-2 experiments and the EDX analyses performed in the different CPs layers are presented in a ternary diagram (Figure 40). For this interface the following conclusions can be drawn:

- (i) The extent of corrosion depends on the analysed sample reflecting the heterogeneity of the tube corrosion and the localized corrosion phenomenon for both experiments.
- (ii) Most of the corrosion products are enriched in Fe and O, and the μ -Raman analyses conducted on this CPs revealed that they correspond to magnetite and goethite (not shown). However, the silicon content of these CPs is not negligible.
- (iii) The presence of sulphur in the outermost region of the CPs layer is locally observed in both experiments. The nature of the sulphur enriched phase could not be determined by any technique (probably due to their low crystallinity) but the presence of iron sulphides in these areas is highly suspected due to the prevailing reducing conditions.
- (iv) Iron oxy(hydr)oxides were also observed in the transformed medium (TM) (i.e., medium previously composed of BCG that is transformed with the income of iron) indicating that some of the iron migrated through the BCG and precipitated in the gap between the BCG and steel and also in the porous network of BCG. Part of this iron also reacted with the components of BCG but the exact nature of the transformed products was not determined. However, XRD analyses conducted on TM samples from BAC-1 and BAC-2 revealed the presence of magnetite and goethite (not shown).

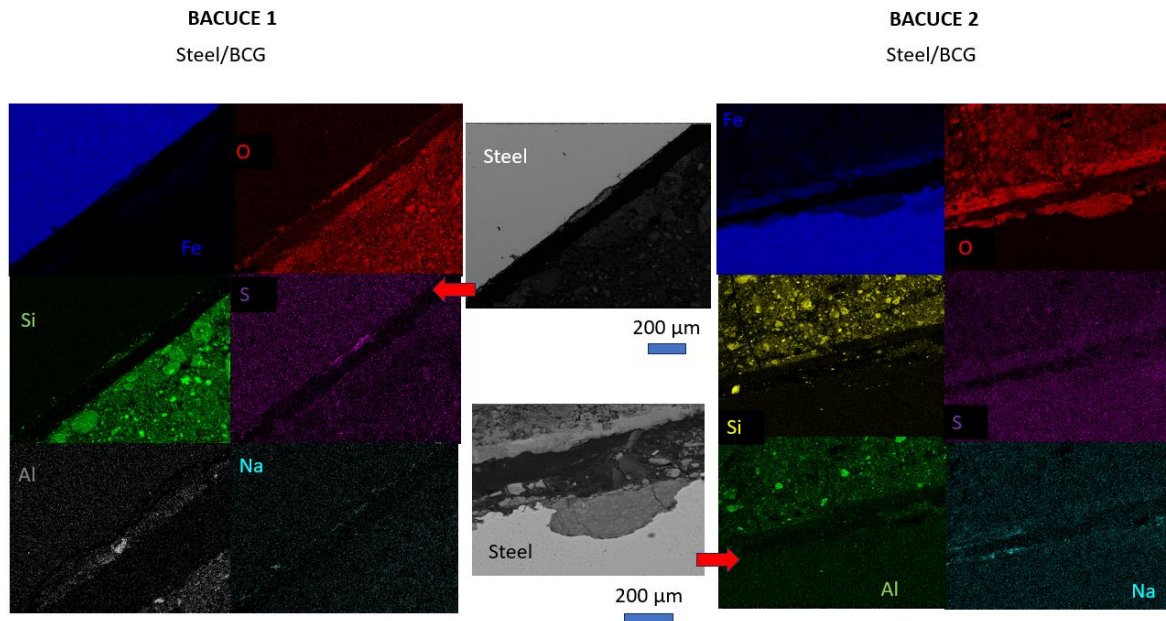


Figure 38: SEM-EDX mappings of steel/BCG interface for BACUCE 1 and BACUCE 2 experiments.

Figure 39 shows SEM-EDX mapping obtained at the steel/BCG/argillite interface for BAC-1 (pits observed in Figure 31) and BAC-2 experiments. Again, the associated EDX analyses are presented in the ternary diagram of Figure 40. Apart from the corrosion pattern (i.e., presence of a large pit/tubercle in one case and uniform corrosion in the other) there is at least one noticeable difference. In BAC-1, the pit/tubercle is mostly composed of iron oxy(hydr)oxide as also confirmed by μ -Raman analyses in the innermost region of this pit (not shown). Only the outermost region of the pit is enriched in silicon and the original surface of the tube (i.e., the mill scale layer) is highly enriched in sulphur. For BAC-2 samples, the original surface of the tube is also highly enriched in sulphur, again suggesting the formation of iron sulphides (not confirmed by other techniques) but the main difference is that the S profile reaches much deeper into the corrosion product layer. The outermost corrosion layer is also enriched in silicon as in the BAC-1 outermost layer, thus Si and S mixed iron CPs are formed in the same area. The innermost region of the CPs layer is also mainly composed of iron and oxygen.

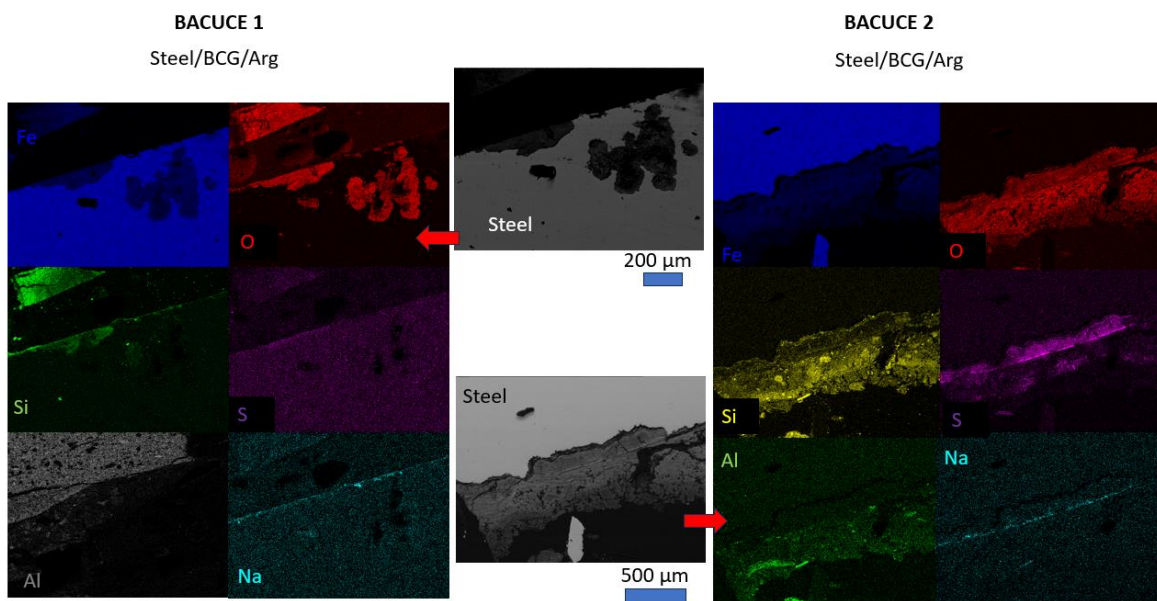


Figure 39: SEM-EDX mappings of steel/BCG/argillite interface for BAC-1 and BAC-2 experiments.

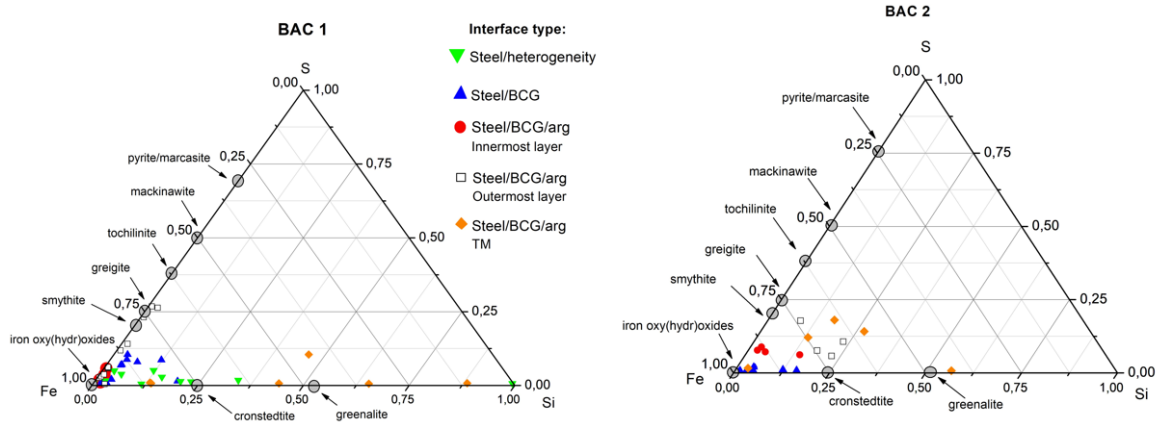


Figure 40: Ternary diagrams presenting SEM-EDX analyses obtained for the different interfaces of BAC-1 and BAC-2 experiments.

4.4.2.3 Corrosion rates

Due to the localized corrosion process and to the heterogeneity in the corrosion thickness observed for in situ experiment, it was impossible to provide an accurate mean corrosion rate.

Figure 41 presents the general corrosion rates that have been measured by loss of mass method for the different laboratory corrosion tests.

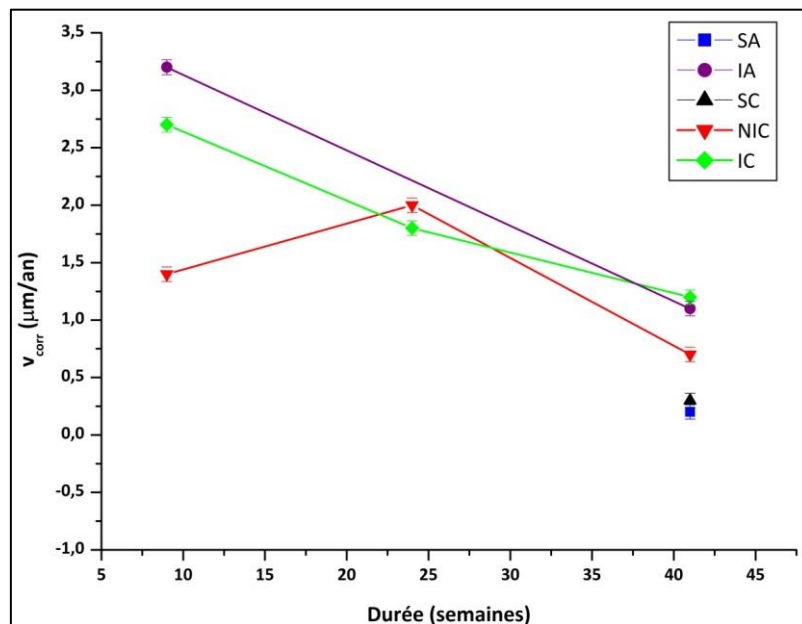


Figure 41: General corrosion rates that have been measured for the different laboratory corrosion tests in function of time (x axis: duration in weeks).

The corrosion rates obtained from mock-up test are relatively low and tends to decrease with exposure time. These results are in agreement with a uniform corrosion process in which passivation finally occur.

4.4.3 Impact of temperature on corrosion

This section presents the results obtained from BAC-3 *in situ* test and from mock-up tests conducted at 80°C (EXP 1-R and EXP 2-C). For the latter, more detailed results are available in Goethals et al. (2023).

It should be noticed that the mock-up and *in situ* tests dedicated to the impact of temperature on corrosion are complementary, but also much more similar in design than the same tests dedicated to the impact of bacterial activity on corrosion. Thus, a direct comparison between mock-up and *in situ* test is made in this section.

4.4.3.1 General aspects

Figure 42 presents optical micrographs of samples coming from mock-up tests (EXP 1-R and 2-C). These micrographs clearly revealed traces of localized corrosion, with formation of tubercles (Figure 42 a and b) and sometimes of worm shaped corrosion products (Figure 42 a). For the samples where steel was placed in direct contact with BCG, localized corrosion is observed through the formation of CPs halos made of brownish and dark corrosion products (Figure 42 c). With increasing interaction time, the coalescence of halos is observed leading eventually to the formation of a large halo covering almost the entire surface of steel (Figure 42 d). After 1 year of interaction, traces of iron diffusion at more than 5 mm from the interface are optically visible.

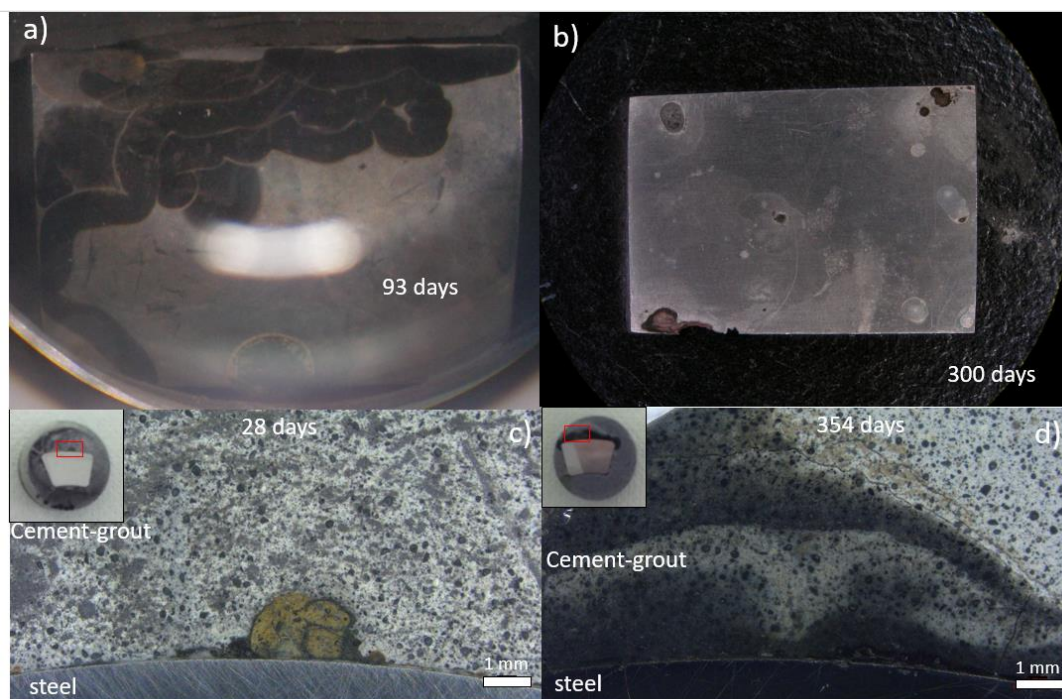


Figure 42: Optical micrographs of the samples coming from the mock-up experiments 2-C (a and b) and 1-R (c and d) with (a) coupon corroded for 93 days, (b) coupon corroded for 300 days after chemical etching, (c) interface between BCG and steel after 28 days and (d) interface between BCG and steel after 354 days.

Figure 43 presents optical micrographs of the steel/BCG and steel/BCG/argillite interface for the samples coming from BAC-3 *in situ* experiment. For both interfaces, steel seems to be homogeneously corroded and the iron diffusion front through the BCG reaches a distance of 2.5-3 mm forming a homogeneous layer of transformed BCG. For both interfaces, the corrosion products observed in the BCG are orange/brownish, suggesting the presence of Fe³⁺-bearing CPs. The surface of the tube is highly damaged and corrosion is visible at this scale.

BACUCE 3

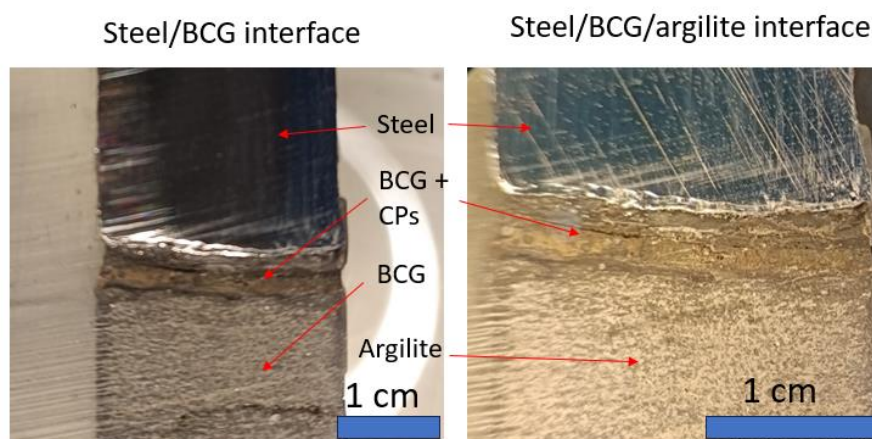


Figure 43: Optical micrographs of the unpolished samples coming from the BAC-3 *in situ* experiments. Both steel/BCG and steel/BCG/argillite interfaces are shown.

4.4.3.2 Corrosion product layers

Figure 44 shows SEM-EDX mappings of steel/BCG interfaces from samples coming from high temperature (80°C) mock-up tests and from BAC-3 *in situ* experiments. For both samples, the corrosion product layers can be described as a series of sublayers in the following way:

Innermost layer: In principle, this layer should be made of the most recent corrosion product due to its location in the sample. However, corrosion product can further react with the surrounding environment leading to their transformation from the outer part of the corrosion layer to the inner part. In both samples, this layer is principally composed of iron oxy(hydr)oxide and also contains a small amount of sulphur with some halos highly enriched in this latter element (see ternary diagram Figure 45). The μ -Raman analyses of this layer for the mock-up test revealed the presence of goethite (Figure 46 b) and most of the time, the phase present in this layer was unstable under the beam. The μ -Raman spectra collected at very low energy resulted in the spectra presented in Figure 46 a. The collection of such spectra will be explained in the next sub-section. Despite the presence of sulfur, iron sulphides were not detected in this sublayer. This might be due to the sensitivity of iron sulphides under the beam, when analyses are conducted in the presence of oxygen or without a water protective layer (Genchev and Erbe, 2016). However, the μ -Raman analyses collected in an oxygen-free cell, on the 28 and 93 days aged coupons coming from EXP 2-C (Figure 47 a and b) revealed the presence of oxidized mackinawite (FeS), suggesting that this CP can be also present in the present innermost layer. Unfortunately, it was not possible to obtain qualitative μ -Raman spectra for the *in situ* sample to confirm this hypothesis.

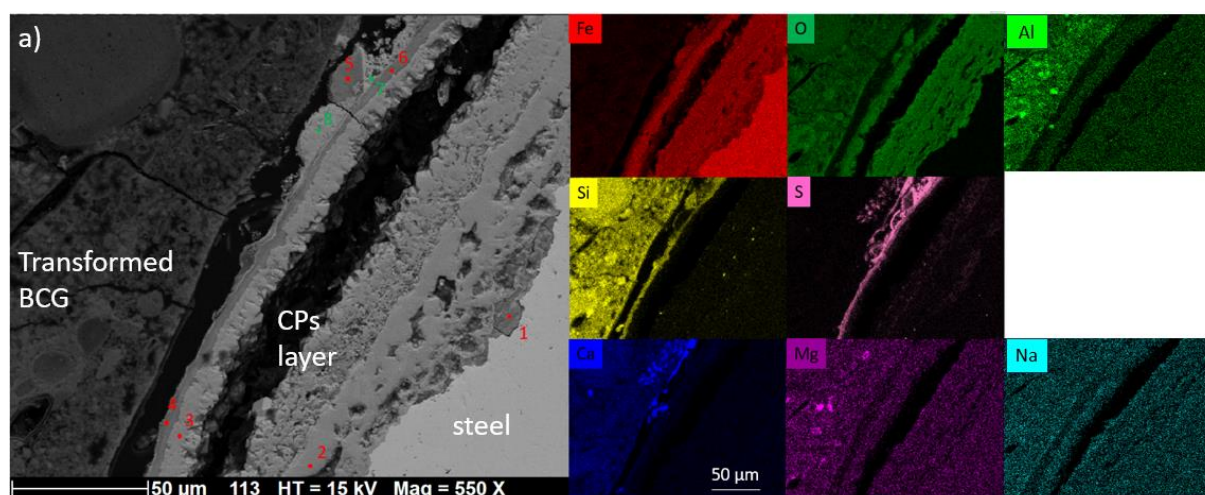
Medium layer: This layer is completely different when comparing the sample coming from mock-up test and the one from *in situ* test. In the mock-up test, this layer is very dense and made of a CP principally composed of iron and oxygen (Figure 44 a, Figure 45) and the μ -Raman analyse of this layer revealed that it is made of magnetite (Figure 46 c). This SEM observation suggests that the CPs of the innermost layer are progressively transformed to magnetite. This observation can explain the μ -Raman spectra of Figure 46 a, that would correspond to goethite progressively transformed into magnetite. For the *in situ* test (Figure 44 b), this layer is much less dense and highly enriched in silicon. The different analyses (μ -Raman, XRD) conducted to characterize this phase were unsuccessful and the EDX analyses of this layer revealed that it was chemically heterogeneous in terms of Si content and it also contains a slight amount of S (Figure 45). Thus it might be primarily composed of iron silicate, probably poorly crystallized.

Outermost layer: Again, some differences are observed between the mock-up test and *in situ* samples for this layer. In the mock-up samples, a fringe enriched in Fe, Si, S and O is observed in the outermost region of the CPs layer and this fringe is clearly replacing the magnetite from the medium layer.

Furthermore, some sulphur rich and silicon free phase are precipitating next this fringe. The μ -Raman analyses of the fringe and of the sulphur rich precipitates are presented in Figure 46 e and f, respectively. For both, the Si rich fringe, it was not possible to identify the nature of the constituting phase(s) but XRD analyses conducted on the coupons samples coming from EXP 2-C revealed the presence of an iron silicate presenting (hkl) reflections corresponding to a phyllosilicate from the Serpentine subgroup and probably greenalite or cronstedtite due to its chemical composition (Figure 48). For the S-rich precipitates, it was also not possible to identify the species, but similar iron sulphides were observed by Robineau et al. (2021) and Sherar et al. (2013) in sample corroded in subalkaline conditions. For the samples coming from the *in situ* tests, the outermost layer is enriched in sulphur. The SEM-EDX mappings revealed that the mill scale layer enriched in Na, P and Zn reacted with sulphur, probably to form a sulphide species. Contrary to the outermost layer of the mock-up test, it is probable that these iron sulphides formed in the first step of the corrosion because of their location in the CPs layer and because there are no indications of the presence of another corrosion product at this location prior to the formation of these sulphides. However, the S profile reaches quite deep into the Si enriched layer suggesting that an ingress of S after the formation of the iron silicate layer is possible.

Transformed medium: For the *in situ* test, Fe diffusion through BCG reached several centimeters making the microscopic examination of such large area quite difficult. In the mock-up test some samples presented halos (not shown). These halos are denser and less porous than the rest of the BCG. They are constituted of three layers. The innermost layer of the 147-day sample is mainly enriched in Fe and O, the second one in S, Fe, Si and O, and the outermost one in Fe, Si and O. This sequence is similar to the one observed in the DPL in the vicinity of the steel, except that Fe-sulphides are also observed in the first layer of the DPL. Such a sequence would demonstrate that some Fe did not precipitate at the surface of the steel but migrated in the highly porous BCG. The subsequent precipitation of Fe-oxides occurred inside the TM, probably as magnetite and/or FeO(OH) due to local variations in pH. Eventually, the diffusion of HS⁻ and of Si coming from the BCG promoted the transformation of the Fe-oxides to Fe-sulphides and Fe-silicates.

In the heterogeneity area where steel was not supposed to be placed in contact with BCG, the corrosion layer presented a similar subsequence but it was much thinner (not shown). The amount of BCG that covered the steel surface was limited.



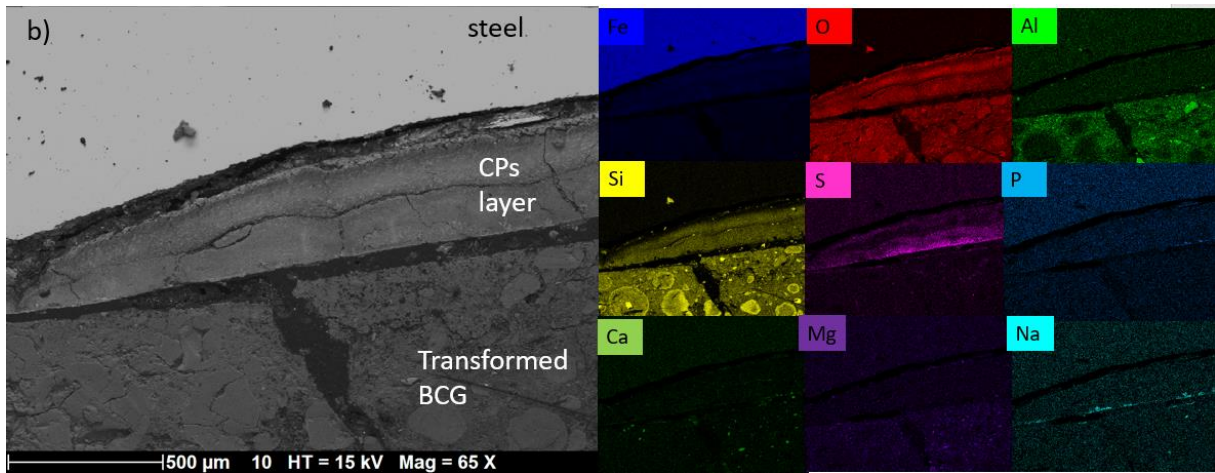


Figure 44: SEM-EDX mappings of steel/BCG interface after 147 days of interaction for the temperature mock-up experiment 1-R (a) and for the same interface for BAC-3 in situ experiment (b).

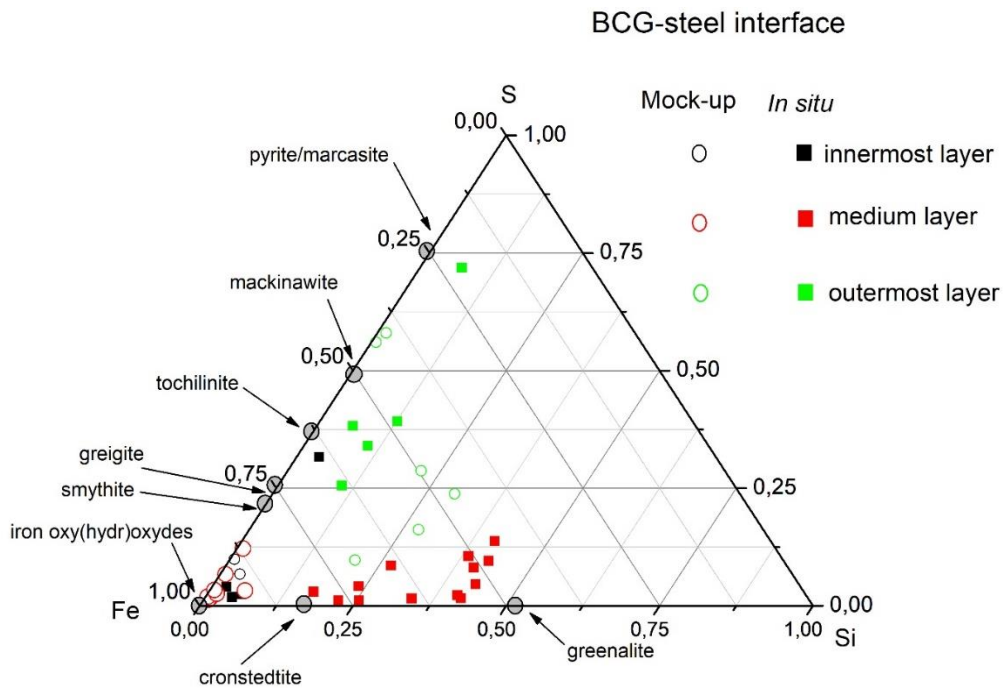


Figure 45: Ternary diagram presenting SEM-EDX analyses obtained for the corrosion products analysed at the BCG-steel interface for BAC-3 in situ experiment and mock-up experiment 1-R.

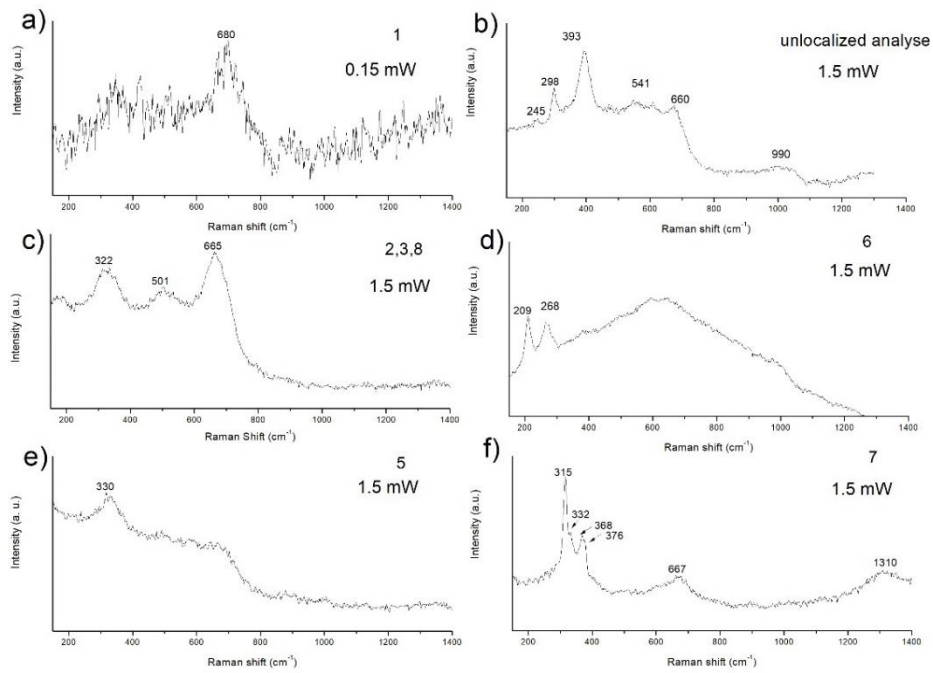


Figure 46: Raman spectra of the corrosion products observed in the mock-up experiment 1 R. The location of the analysed spot is given in Figure 44-a.

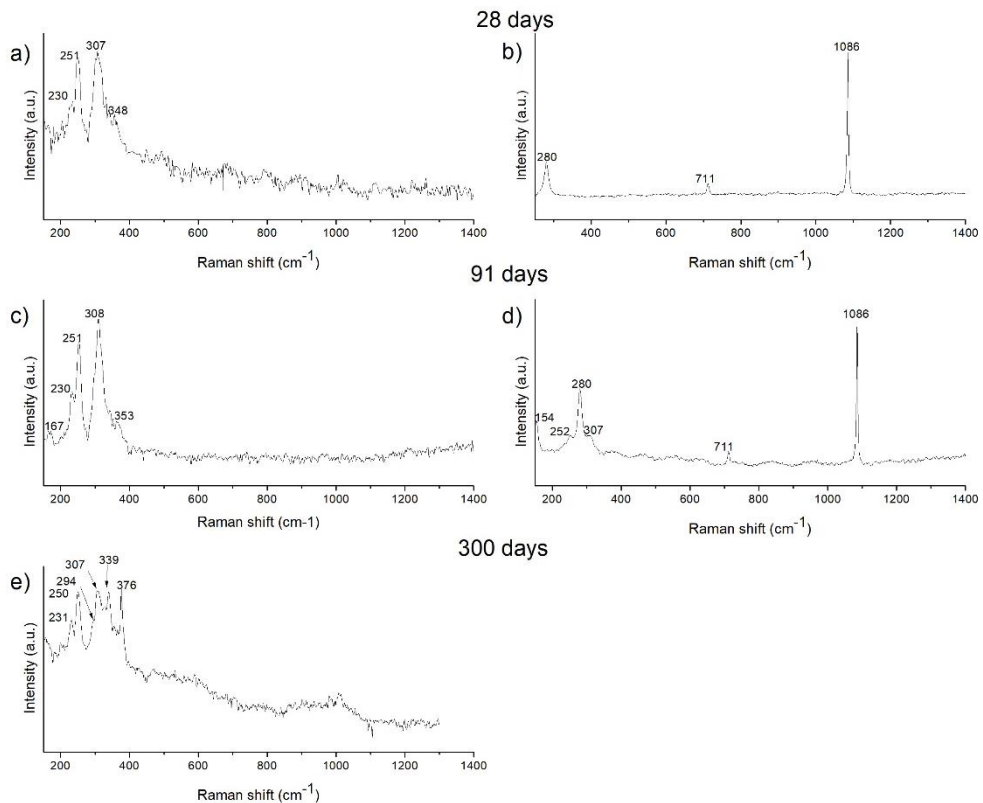


Figure 47: Raman spectra of the corrosion products observed in the mock-up experiment 2-C.

4.4.3.3 Corrosion rates

Results showed that localized corrosion was clearly evidenced for sample coming from both mock-up tests and in situ experiments. To assess the extension of the localized corrosion phenomenon, the variation on the optical corrosion thickness measurement of the samples coming from EXP 1-R is reported in Figure 50 b. The histogram shows that most of the measurements (>60 %) are in the range [0-10] μm for all samples, which principally corresponds to areas unaffected by corrosion, confirming the localized corrosion phenomenon. However, microscope observations visible in Figure 50a clearly indicated an increase of the number of damaged zones with time, rather than an increase of the pit depth. Indeed, a large increase of the number of pits with depth limited to 40 μm is clearly depicted after 350 days of interaction, whereas the number of percentage of pits >40 μm is not increasing anymore (Figure 50 b). This observation suggests that the coalescence of these pits would eventually lead to a generalized corrosion process. This observation seems to be confirmed by the results from the *in situ* experiment that lasted for 2.5 years.

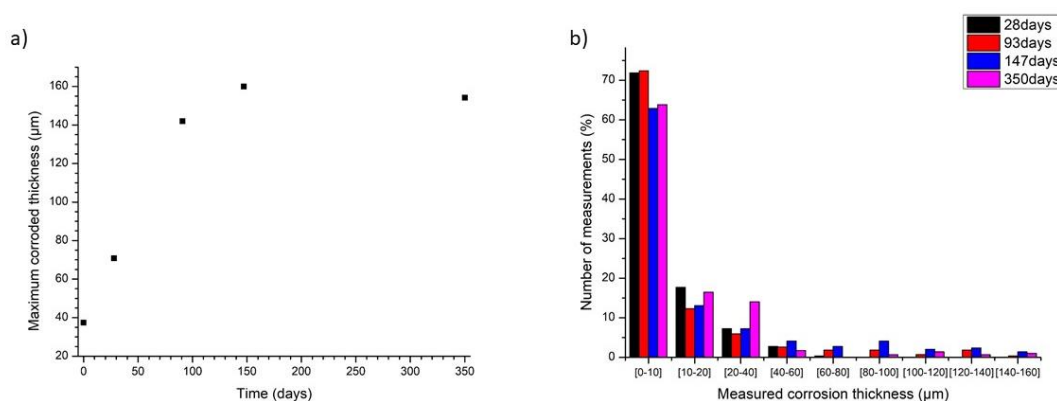


Figure 50: Optical measurements of the corroded layer for EXP 1-R with (a) Maximum corroded thickness observed. The values correspond to the maximum reported thickness observed on the external mill scale layer in direct contact with the BCG. The "0 value" corresponds to the maximum thickness reported for the external mill-scale layer in a pristine steel sample. (b) Statistical histogram of the optical measurements of the corrosion thickness measured on the external mill-scale layer for samples coming from EXP 1-R. More than 250 measurements spaced 50 μm apart were performed on each sample. The thickness of the mill-scale layer was not subtracted from the measurement.

For the sake of comparison, the mean corrosion rates obtained by optical measurements for EXP 1-R and by weight loss measurements for EXP 2-C are presented in Figure 51. A first increase in the corrosion rate is depicted in the first 224 days for EXP 1-R and in the first 93 days for EXP 2-C up to values reaching 10.8 $\mu\text{m}/\text{y}$ and 8 $\mu\text{m}/\text{y}$, respectively. Then, the mean corrosion rates seem to stabilize for 2-C experiment, or even to decrease for 1-R experiment.

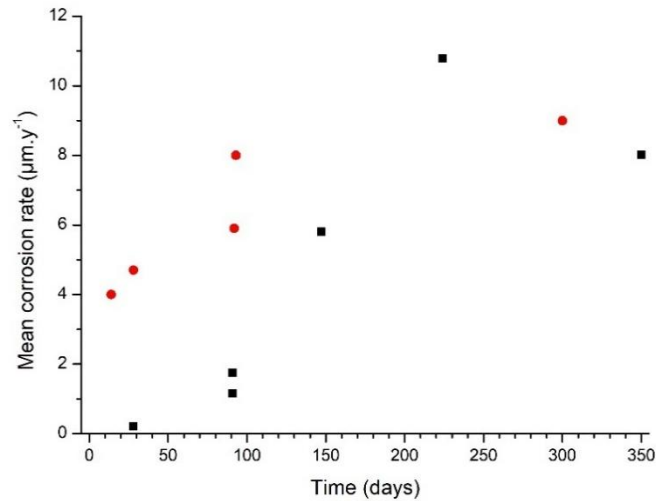


Figure 51: Mean corrosion rates of carbon steel obtained from optical measurements of the corroded layer for experiment 1-R (black squares) and from weight loss measurements for experiment 2-C (red circles).

For the corresponding steel/BCG interface in the BAC-3 *in situ* experiment, the SEM observations revealed a uniform CPs layer of 230 (± 10) μm . In this sample, the remnant mill scale layer would indicate the original surface of steel, which is at the outermost region of the CPs layer. This is surprising because CPs are less dense than iron and expand to the outer surface of steel. However, a large fraction of iron migrated through the BCG explaining such volume deficit and similar patterns were observed for the mock-up tests (i.e., no corrosion products observed just next to the original steel surface). Consequently, the corrosion rate (115 $\mu\text{m}/\text{year}$) would be more than ten times superior to the corrosion rates obtained after one year of interaction in the corresponding mock-up tests.

The three *in situ* experiments aiming to study the impact of temperature on corrosion processes (BAC-3, BAC-4 and BAC-5) have been equipped with Electrical Resistance (ER) corrosion sensors to continuously monitor the corrosion rate associated to these tests. For BAC-3 and BAC-4 experiments, the sensors might have been partially or completely covered by BCG, and thus also presented a steel/BCG interface. The results presented in Figure 52 show that the corrosion rates (about 150 $\mu\text{m}/\text{year}$ if considering generalized corrosion) are in the same order as the one calculated from SEM measurement of the CPs layer. This rate is even more important for the BACUCE 4 replicate experiment. However, *post mortem* examination of the sensors is necessary to correctly interpret such high rates. This was not possible in the allotted time for the project.

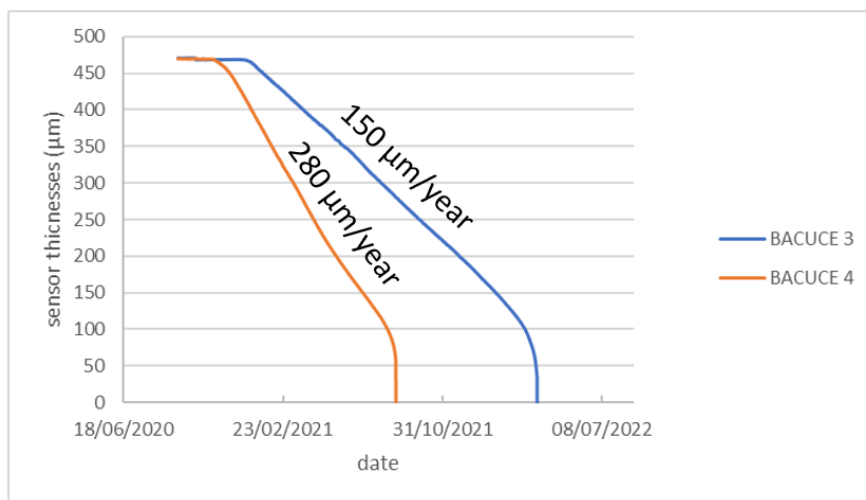


Figure 52: Sensors thickness evolution with time and associated calculated corrosion rates for BAC-3 and BAC-4 *in situ* experiments.

4.4.4 Corrosion of steel in the presence of CEM I - Effect of cement composition and pH

4.4.4.1 General aspects

Figure 53 shows macroscopic features of the corrosion for some selected samples coming from both mock-up and in situ tests. In EXP 2-C, all the retrieved coupons presented a uniform layer of adhering white crystals covering the whole surface of the coupons, as can be seen in Figure 53a. In EXP 1-R, the whitish layer was also generally observed, but the layers were less uniform and sometimes showing a precipitation front in the vicinity of the cement cylinder as can be seen in Figure 53b. Generally, dried samples coming from EXP 1-R also presented iridescent reflects. As corrosion products are generally opaque, this observation indicated the precipitation of a very thin layer of corrosion products at the surface of the rods. Moreover, some fractured samples coming from EXP 1-R evidenced white/translucent non adhering crystals at the surface of steel that was in contact with HCP. These crystals were generally platy and were also present at the bottom of the reactors. The samples coming from BAC-5 in situ experiment show no macroscopically visible corrosion for both steel/CEM I and steel/CEM I/argillite interfaces (Figure 53e and f).

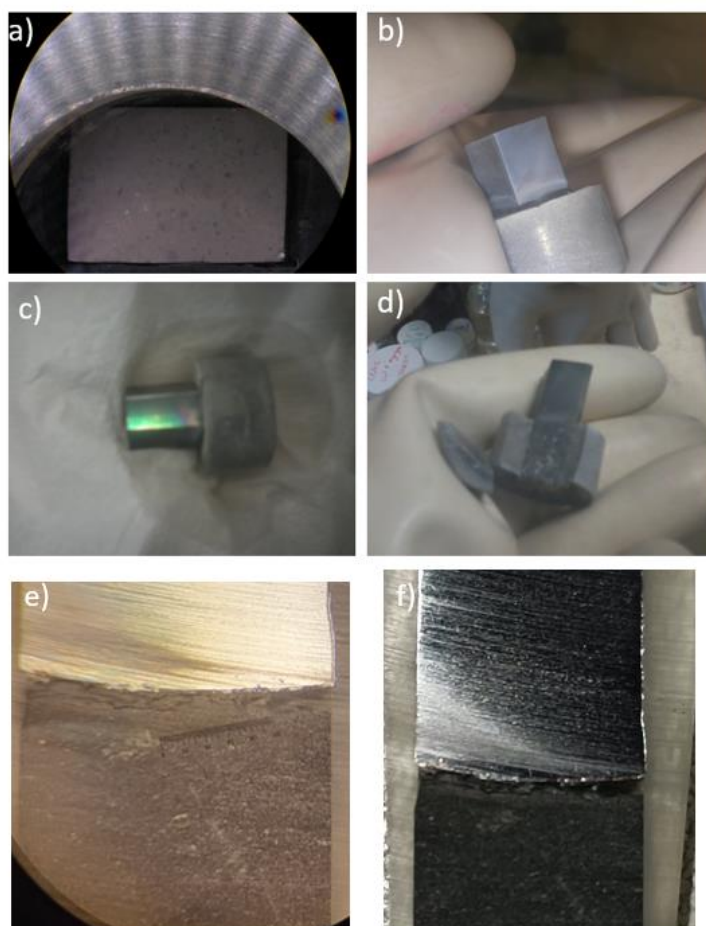


Figure 53: Pictures of corroded samples coming from mock-up EXP 2-C after 93 days of interaction (a) and from mock-up EXP 1R after 28 days (b) and 254 days of interaction showing both steel/solution interface (c) and steel-cement interface (d). The steel/CEM I (e) and steel/CEM I/argillite (f) interfaces from BAC-5 experiment are also shown.

4.4.4.2 Corrosion product layers

Figure 54 shows XRD patterns collected at the surface of two steel coupons coming from EXP 2-C. After 28 days of interaction, the XRD pattern revealed the formation of a phase belonging to the hydrogarnet group at the surface of the coupon. It should be noticed that this phase presents a variety of compositions in the range $\text{Ca}_3(\text{Al}_{(1-x)}\text{Fe}_x)_2(\text{SiO}_4)_y(\text{OH})_{4(3-y)}$, with for instance, katoite as the pure Al and Si free end-member and hydroandradite (HA), being the Al free end-member. The peaks were correctly indexed using the COD [1524032](#) corresponding to the $\text{Ca}_3\text{Al}_{1.096}\text{Fe}_{0.904}\text{Si}_{2.823}\text{O}_{12}\text{H}_{0.708}$ formula. After 300 days of interaction, the relative intensity of the peaks corresponding to HA compared to (110) reflection of iron increased, signifying the growth of this phase with time. Reflections corresponding to portlandite were also identified at the surface of the coupon.

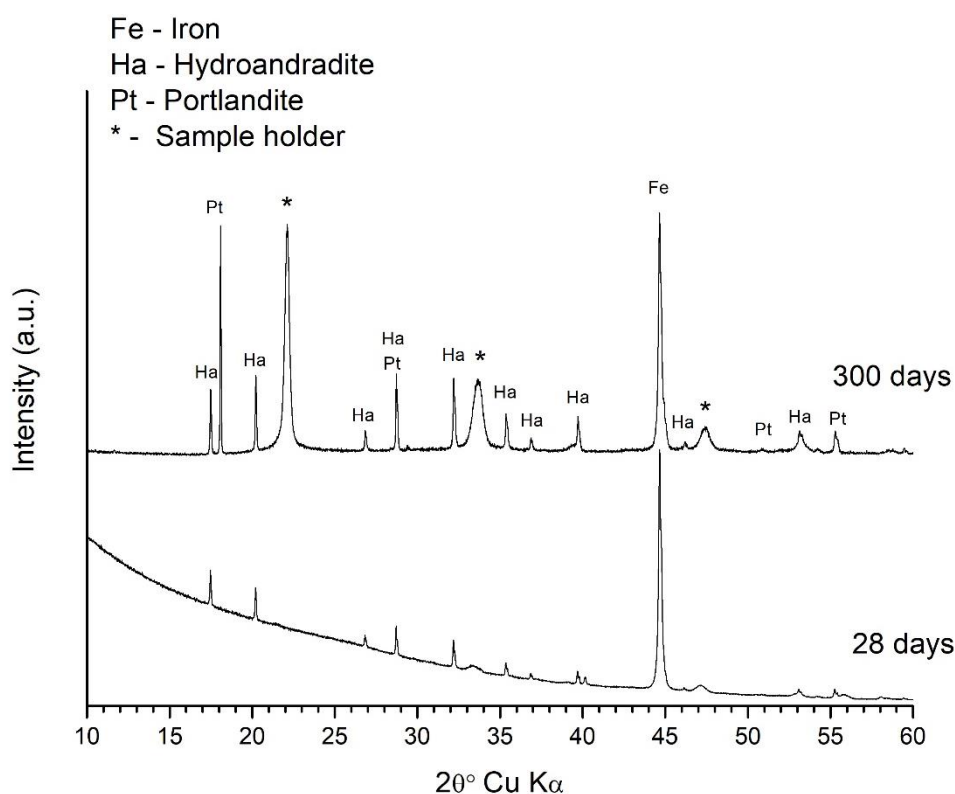


Figure 54: XRD patterns of the surface of the coupons coming from EXP 2-C after 28 and 300 days of interaction.

To gain information on the microstructure and composition of this phase, SEM-EDX analyses were conducted on a coupon corroded for 28 days (Figure 55). The SEM-SE pictures revealed the presence of rounded shaped crystal covering almost entirely the surface of the coupon. The composition of this phase is reported in Figure 55 b and the corresponding formula, considering only major elements, would be $\text{Ca}_{3.2}\text{Fe}_{1.25}\text{Al}_{0.8}\text{SiO}_{4.6}(\text{OH})_{7.43}$ normalizing the atomic proportion to 12 oxygens which correspond to garnet formulas. Such formula is very close to hydroandradite formed in old mortars (Dilnesa et al., 2014). Moreover, a low amount of S ($\approx 1\%$) was detected in this phase, as already observed by (Kyritsis et al., 2009). The presence of KCl grains was also depicted at the surface of the coupon in a relatively low amount.

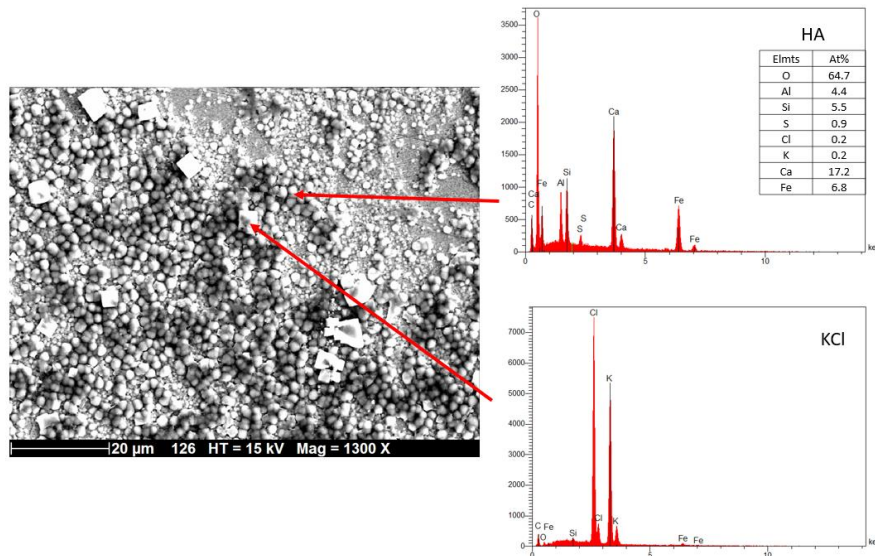


Figure 55: SEM-BSE picture of the surface of the coupon immersed for 28 days in SYNTHETIC SOLUTION (EXP 2-C) along with EDX spectra of the principal corrosion products and precipitates observed. The chemical composition of HA (hydroxapatite) given corresponds to the mean of seven analyses.

In EXP 1-R, SEM-EDX observations also revealed the formation of Ca, Si, Fe, Al, O containing phase at both interfaces (i.e., steel/CEM I and steel/heterogeneity) as presented in Figure 56. The latter result suggested that HA also formed in this experiment. The Si/Ca ratio of this phase are globally comprised between 0.3 and 0.4 and the Al/Fe ratio comprised between 0.3 and 0.5. This is consistent with the formation of HA.

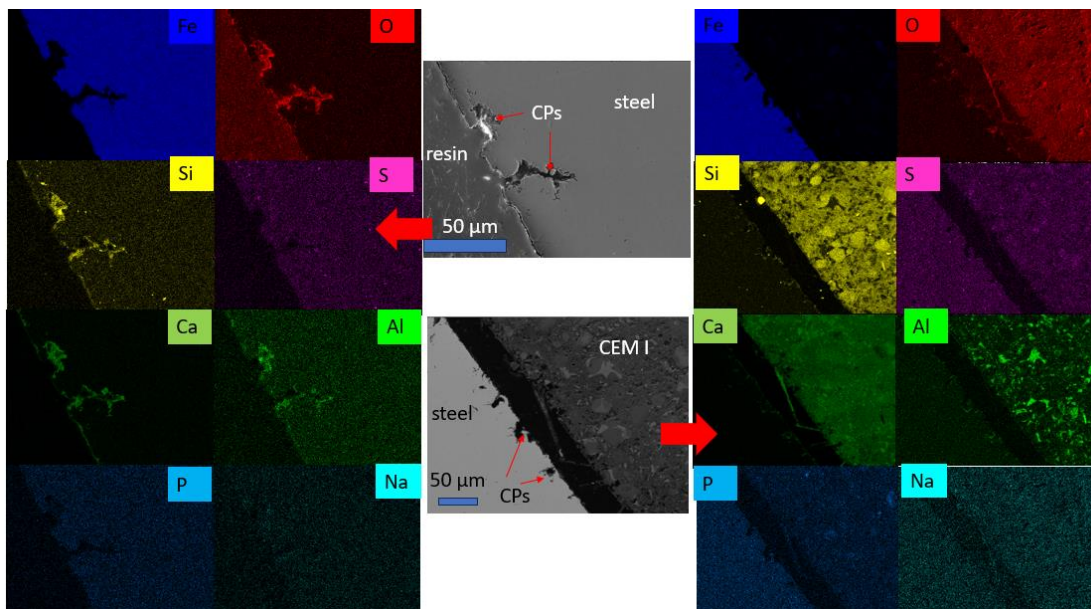


Figure 56: SEM-EDX mapping of the steel/heterogeneity (left side) and steel/CEM I (right side) for the sample immersed for 354 days in the synthetic solution coming from EXP 1-R.

For BAC-5 *in situ* test, the presence of a Ca, Si, Al, O and Fe containing phase at the edge of the steel surface in the heterogeneity was also revealed (Figure 57). However, this phase rather seems to have precipitated at the surface of the steel and its composition is heterogeneous (Figure 57) and far from the composition of the hydrogarnet (HG) formed in the mock-up tests.

It is also possible that it corresponds to cement dust that was trapped at the surface of the steel after the dismantling and cutting operations. Apart from these phases, no corrosion products were clearly evidenced at the steel surface for both CEM I/steel and heterogeneity/steel interface.

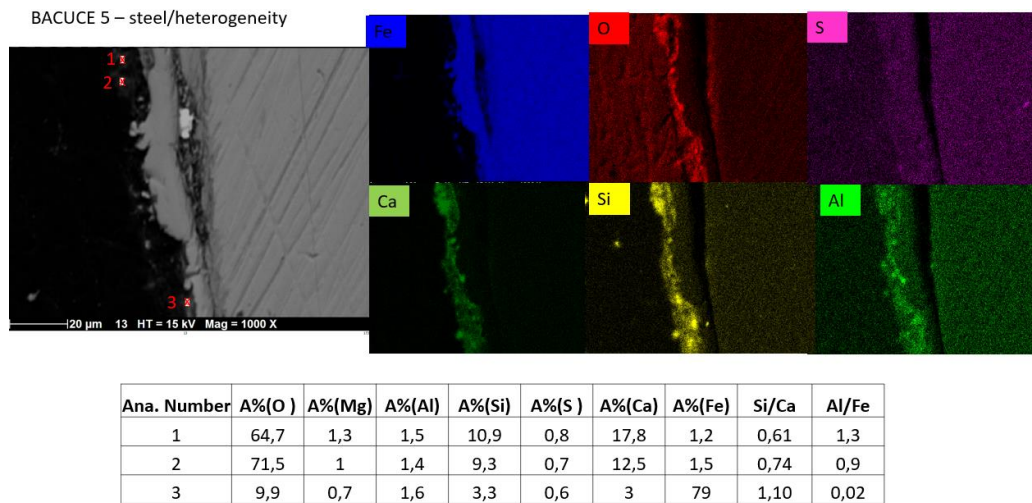


Figure 57: SEM-EDX mapping of the steel/heterogeneity interface coming from a BAC-5 sample and EDX analyses of localized in the SEM BSE image.

For the last interface (steel/CEM I/argillite), Figure 58 shows localized corrosion with the presence of a corrosion sphere. However, this phenomenon was very limited. In the corroded areas, the innermost CPs layer is composed of Fe, O and S principally whereas the outermost layer is principally made of needles composed of Fe and O. The μ -Raman analyses of these needles revealed that it was made of magnetite (Figure 58) but it was not possible to determine the nature of the S enriched phase by μ -Raman. Again, the S enriched phase might be a poorly crystallized iron sulphide phase.

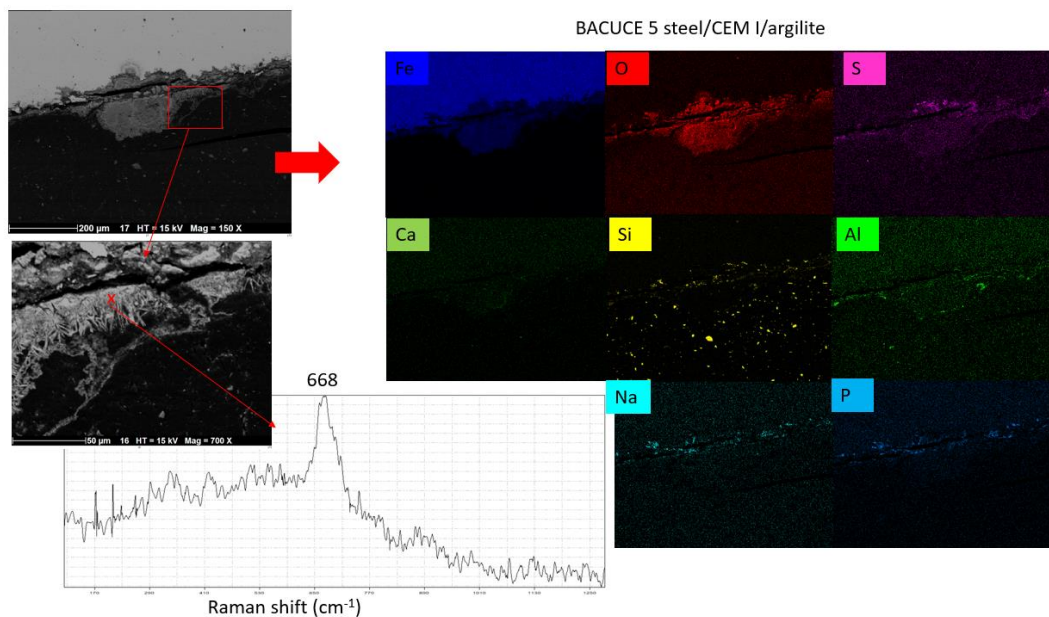


Figure 58: SEM-EDX mapping of the steel/CEM I/argillite interface coming from BAC-5 sample and μ -Raman spectrum associated to the SEM BSE image localization.

4.4.4.3 Corrosion rates

Figure 59 shows the evolution of the corrosion rate with time, obtained by weight loss measurement for EXP 2-C. As expected, the corrosion rate dropped with time (from 1.7 to 0.4 $\mu\text{m}/\text{y}$) and the decrease can be approximately described with an exponential decay law, as generally observed in experiment conducted in similar conditions (e.g., Smart et al., 2017). However, the residual corrosion rates are quite high and 2 orders of magnitude higher than those observed in the latter experiments where corrosion rate were derived from hydrogen pressure measurements. It should be noticed that high variations are measured at 54 days on three different coupons ($\approx 10\%$ relative error) and that longer time experiment would have been necessary to predict the long-term corrosion rates.

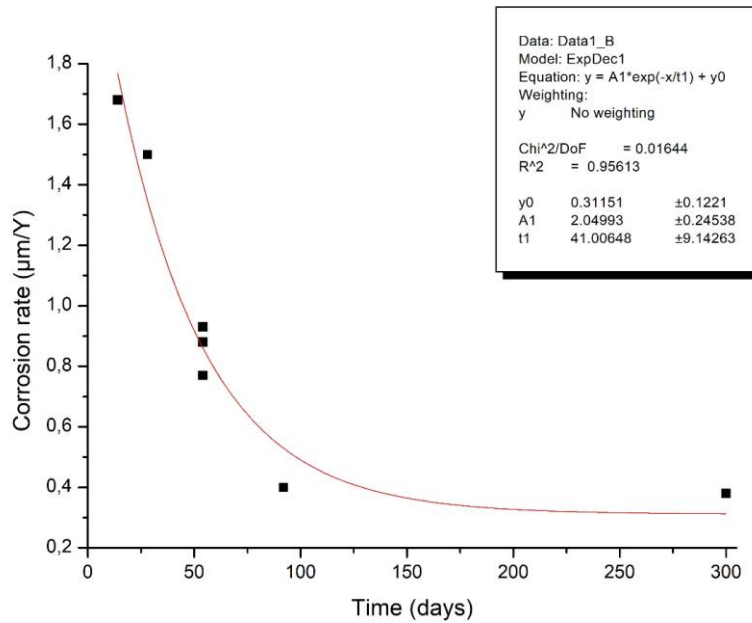


Figure 59: Corrosion rates measured by weight loss measurements in experiment 2-C.

For BAC-5 *in situ* test, the corrosion sensors revealed a slight increase of the electrode thickness. This slight increase can be related either to (i) solid deposit from solution onto the steel electrode acting as an additional path for electrical current (i.e., resistance decrease) or (ii) solution ingress in the sensor body containing the reference electrode causing a shift in the compensated resistance calculation. However, this result clearly indicates that the corrosion phenomenon was extremely limited for this experiment (Figure 60).

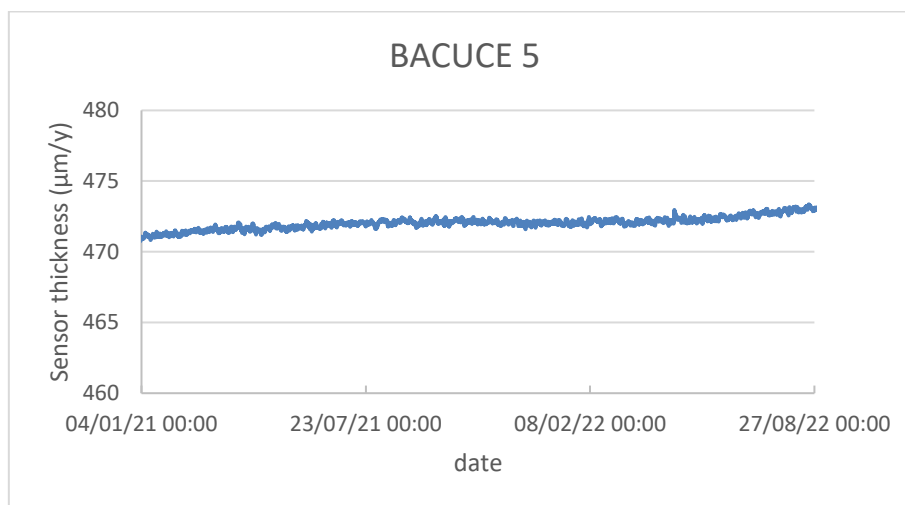


Figure 60: Sensors thickness evolution with time for BAC-5 *in situ* experiment.

4.5 General discussion

4.5.1 Corrosion mechanism and rates in mock-up and *in situ* tests

4.5.1.1 Localized corrosion phenomenon

In all the experiments involving the presence of BCG or argillite solid material (Temperature impact tests), localized corrosion was generally observed whereas mock-up experiments with only pore water at equilibrium with BCG and/or argillite (Microbial activity impact), as well as experiments with CEM I, revealed uniform corrosion patterns. This first important result indicates that the solid material has a leading role in the corrosion of steel. Indeed, both BCG and argillite contain sulphides prone to have detrimental effect on corrosion. The origin of these sulphides is discussed in the next section of the report.

Figure 61 shows the schematic representation of the corrosion processes that would have impacted metallic samples for BCG mock-up experiments. The sequence can be divided into 4 successive steps:

Step 1: formation of corrosion cells: (i) magnetite act as cathodic layer and HS^- ions from BCG react with iron to form iron sulphides in the anodic area and/or (ii) presence of residual O_2 favour the formation of iron oxy(hydr)oxide.

Step 2 – step 3: large amount of magnetite is formed either due to direct magnetite precipitation (occurring after the consumption of the first source of hydrogen sulphides – HS^-) or due to the progressive transformation of iron oxy(hydr)oxide into magnetite. When magnetite formed in anodic zone, OH^- ions are produced in the cathodic ones and they enhance the dissolution of hydrated silica fume in the vicinity of the corroded area. The presence of a highly soluble silica source promoted the transformation of magnetite into iron silicates as observed in the third step.

The presence of a second source of sulphides in the BCG is responsible for the formation of a second iron sulphide containing layer.

Experimental observations suggested that magnetite is partly replaced by both iron silicates and iron sulphides.

Step 4: a third source of sulphide (originated from pyrite dissolution) induced the precipitation of iron sulphides in the outermost layer.

We also observe that the dense magnetite layer is not totally destabilized by the iron silicate formation and acts as a diffusion barrier for aggressive species. This is confirmed by the drop of corrosion rate values with time that have been obtained.

Thus, localized corrosion can be explained by the following processes:

Formation of corrosion cells: The formation of corrosion cells is induced by the presence of an electron conductive layer (here magnetite), acting as the cathodic area, and the ingress of HS^- from the BCG that reacts with iron to form FeS in the anodic area (step 1, Figure 61). This process has been observed in various environments (oxic, anoxic) (Robineau et al., 2017; Robineau et al., 2020) and well described in the study of Robineau et al. (2020). The electron conductive layer is either (i) already present at the surface of the steel (mill-scale layer) or (ii) can form by the Schikorr reaction or (iii) by a solid-state reaction implying Fe diffusion from the steel and O diffusion toward the steel bulk, through O vacancies diffusion toward the surface (Pally et al., 2020). The presence of structural defects in this layer is either already present (defective mill scale layer) or local chemical depassivation of this layer can occur due to (i) HS^- reaction with magnetite at moderate alkaline pH (i.e., $9 < \text{pH} < 10$) provided that the concentration of dissolved sulphides is high enough or (ii) at a high $[\text{Cl}^-]/[\text{OH}^-]$ ratio that is superior to a certain threshold value (Angst et al., 2009; Robineau et al., 2020).

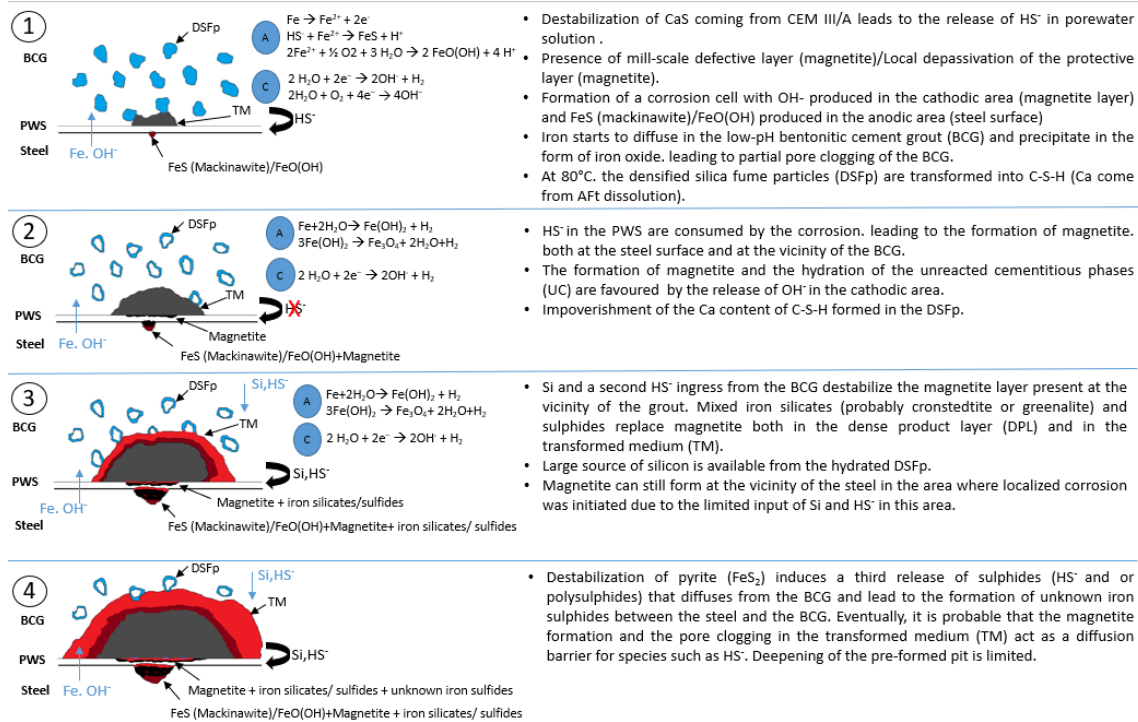


Figure 61: Schematic representation of the corrosion process observed for experiment involving BCG at 80°C (PWS = Pore Water Solution; TM = Transformed Media; CaS = oldhamite).

Surprisingly, localized corrosion was observed for the BCG/steel interface in BAC-1 and BAC-2 *in situ* experiments where the presence of sulphides was scarce or even not visible. In the recent study from Bonnet et al. (2022), the authors measured the concentration of sulphides in water at equilibrium with BCG at 20°C and the amount of sulphide was very low (< 10⁻⁶ mol/L), which is not high enough to promote iron sulphides formation. Thus, other reasons are necessary to explain the localized corrosion phenomenon observed.

Residual O₂: The presence of residual O₂ in the BCG might also be responsible for the initiation of localized corrosion. Indeed, in some areas, the first layer of corrosion products was mainly composed of iron hydroxides. At the beginning of the experiment, residual O₂ coming from the cement could have diffused through this material and been progressively consumed by the corrosion process to form Fe-hydroxides. The ingress of O₂ to the surface of the steel was transport-limited. Sherar et al. (2011) showed that localized corrosion can occur at trace levels of O₂, with the formation of locally corroded areas induced by the formation of a corrosion cell with magnetite layer acting as cathodic zone.

Other decoupling of anodic and cathodic area: Eventually, it was shown that localized corrosion could be triggered by the presence of porous and heterogeneous mill scale layer composed of both magnetite (Fe₃O₄) and hematite/maghemite (Fe₂O₃). For instance, Qin et al. (2004) demonstrated that a decoupling of anodic and cathodic reactions could occur with iron oxidation and Fe₂O₃ reductive dissolution in anodic and cathodic areas, respectively. In the present experiments, it is possible that Fe₂O₃ was present in some areas (not detected by μ-Raman), especially because the tube was stored for a long time in contact with oxygen prior to be used which led to the initiation of localized corrosion.

4.5.1.2 Generalized corrosion

In the experiment implying CEM I, the corrosion process is much simpler and prediction of the evolution of the system on the long term is facilitated. In the mock-up tests, formation of the iron rich hydrogarnet called hydroandradite (HA) covering the whole surface of exposed steel was observed in the first days of the experiment and the corrosion rate dropped to values lower than 1 μm/year within less than 100 days of interaction. In the experiment conducted by Pally et al. (2020), magnetite was observed in the

innermost layer of the corrosion layer. The authors explained that it can form either by a solid state reaction or by the Schikorr reaction prior to the ingress of elements favouring the formation of HA (Ca,Si,Al). Formation of nanometric dense layers is known to create a passivation film that drastically inhibit the corrosion of steel. Such passivating magnetite layer was not observed in our study but the methods employed to characterize nanometric layers of oxide were not adapted, explaining why it was not visible here. The use of Transmission Electron Microscopy (TEM) would be relevant to determine the presence or absence of such nanometric layer. Moreover, macroscopic observation suggests the formation of such layer in the upper parts of the steel rods where HA was not observed. If such film was formed, it could have been destabilized by the presence of other elements coming from the cement to form HA. It was shown in this study that the formation of such phase also tends to passivate steel even in defective surfaces (mill scale presenting layer). Indeed, the HA layers densify with time and limit the diffusion of elements coming from the cement to the surface of steel.

4.5.1.3 Impact of the experimental device dimensions and geometrical/design aspects

For the experiment with BCG studying the temperature impact, the difference between the corrosion rates obtained for mock-up and *in situ* tests is of one order of magnitude. For the mock-up tests, corrosion is initiated locally within the first days of the experiment and the decrease of the mean corrosion rate is associated to the densification of the CPs layer together with the coalescence of the pits leading to a uniform corrosion mechanism. For the *in situ* tests, it is also probable that a similar mechanism occurred and that the uniform layer observed after 2 years of interaction is the result of the coalescence of all pits. However, several parameters might have played a major role on the large difference in the obtained mean corrosion rates. First, the amount of residual oxygen was more important in the *in situ* test, because the volume of BCG employed was larger and because it was not possible to remove oxygen from the BCG as easily as for the mock-up tests.

As indicated in the previous subsection, residual oxygen is prone to induce localized corrosion and to favour the formation of porous goethite instead of dense magnetite that acts as a diffusive barrier. Secondly, the heating conditions were completely different for mock-up and *in situ* tests. The systems were heated from the outer to the inner part and from the inner part to the outer part, respectively. In the *in situ* tests, the cold pore water coming from BCG to the surface of the steel was heated by conduction. The renewal of solution at the surface of the steel was favoured in such system. Such renewal might have favoured the ingress of HS⁻ and oxygen at the surface of the steel. As the corrosion product layer remained poorly dense even after transformation of goethite to iron silicates, corrosion rates remained high. Finally, the presence of argillite/steel and BCG/steel interfaces for the *in situ* test might have led to the formation of large corrosion cells. It was recently shown that galvanic coupling can occur in such system and that temperature plays a role in this galvanic process (Robineau, 2023). At low temperature, area covered by argillite correspond to anodic zones and area covered by BCG are cathodic zone whereas at 80°C, the anodic and cathodic zones are inverted.

For CEM I experiments, the up-scaling rather limits the corrosion of steel that was already very slow in the mock-up tests. Indeed, no corrosion product were observed (at least by SEM) for BAC-5 *in situ* test and the corrosion rates obtained by the corrosion sensors were extremely low. First, the temperature reached by the synthetic solution in the heterogeneity was lower than the one reached in mock-up tests and thus, the degradation of cement phases at contact with the heterogeneity was limited. Thus, the amount of Ca, Si and Al in the synthetic solution coming from the cement was also limited, which favoured formation of magnetite instead of HA. Secondly, the gap between steel and cement was limited in the *in situ* test due to (i) the use of a tube instead of rods that created cracks at their edges and (ii) the position of the tube that rested on the cement. Moreover, the diffusion of oxygen through the surface of steel was also limited in the *in situ* test compared to the mock-up one. In the *in situ* test a very small surface of cement was exposed to the synthetic solution compared to the mock-up tests in which synthetic solution could circulate very easily. Such difference in the experimental design influences the nature of the formed corrosion products and thus also the corrosion rates via the following parameters:

Dissolved silica activity: Fe-siliceous hydrogarnet needs the input of silica. The higher the silica activity, the more stable Fe-siliceous hydrogarnet (CAFSH in Figure 62). The input of silica can be driven by the silica diffusion flux brought by the dissolution of cement hydrates.

Dissolved Al content: Fe-siliceous hydrogarnet could be stabilized by the integration of Al in their structures. Al is independent on the redox potential contrarily to Fe. It is worth noting that the activity of Al in Fig. 62 was fixed by the main Al species $Al(OH)_4^-$ in the basic range and close to the Al total concentration calculated with the set of mineral assembly (see Table 17) at 80°C.

Redox state. Fe-siliceous hydrogarnet is constituted by Fe(III) species only. The higher the pH, the stronger the occurrence of Fe(III) vs. Fe(II). But under very reducing conditions, magnetite will be the more stable phase even at very alkaline pH. Closed system conditions as typically favoured in the *in situ* test can lead to very low Eh potential.

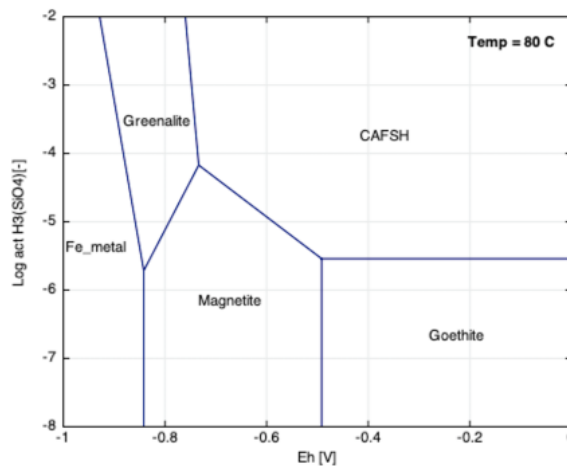


Figure 62: Speciation diagram at 80°C calculated with CHESS: activity $Fe^{2+} = 10^{-5}$, activity $Ca^{2+} = 10^{-3}$, activity $Al(OH)_4^- = 10^{-4}$, pH 10.5 (the stability field of water is not drawn to more clearly represent the $Fe(0)$ stability domain).

| | |
|--|--|
| CAFSH | Magnetite |
| base case – intermediate D_e at the steel/cement interface | base case – intermediate D_e at the steel/cement interface |

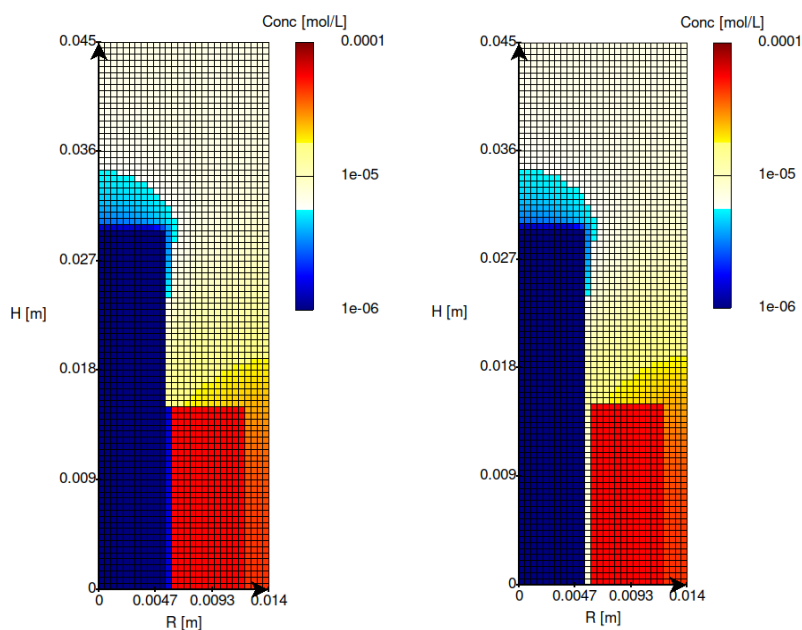
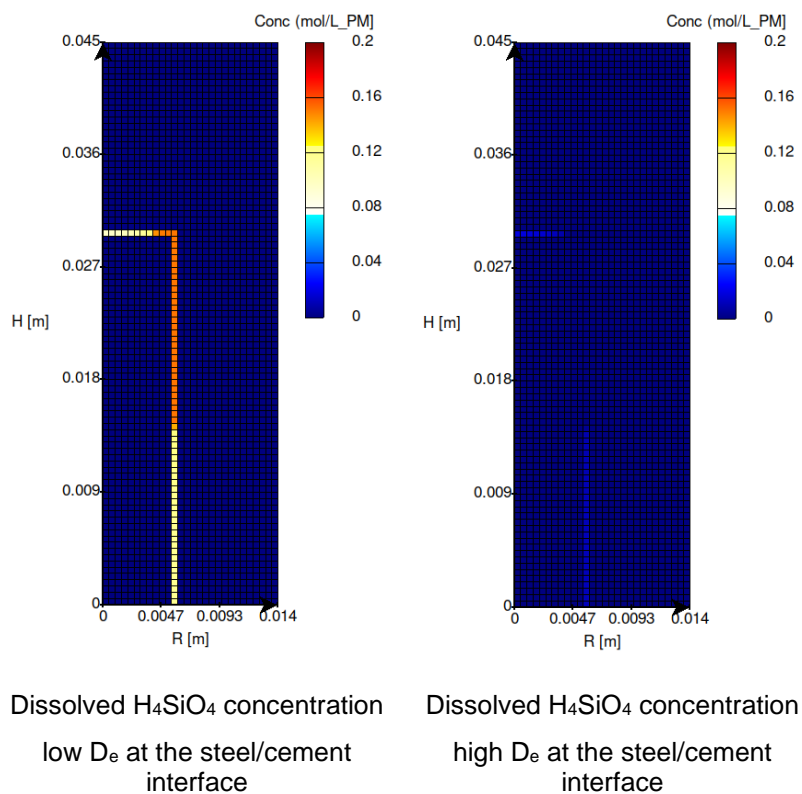
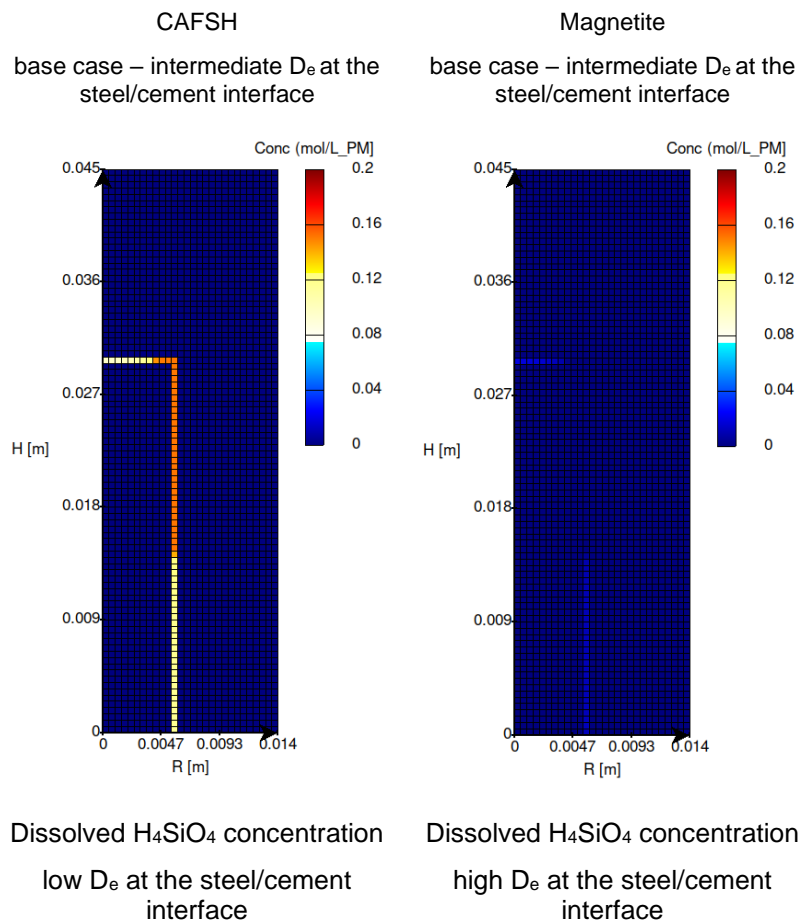


Figure 63 illustrates the possible effect of dissolved silica on the competition between magnetite and FeSi-hydrogarnet (CAFSH) formation. This was yet a preliminary modeling exercise that will be further developed after the ACED project. The goal was to simulate the diffusive transfer of dissolved Fe-Al-Si in the experimental set-up, especially those parts of the steel in direct contact with the synthetic solution and those parts embedded in the cement paste but possibly in contact with the solution due to an imperfect contact between the steel and the paste. A constant generalized corrosion rate of $1 \mu\text{m}/\text{year}$ (close to the experimental rate during the first 6 months) was applied to metallic iron $Fe(0)$ considered

as a representative proxy of C-steel. Under those chemical conditions, CAFSH is the main corrosion products over the whole surface of the steel rod with a predominance at the steel/solution interface. Magnetite also precipitates but at a much lower concentration than CAFSH. But if one decreases the D_e at the steel/cement interface, magnetite becomes predominant at the expense of CAFSH (not shown). Figure 63 also shows that a higher diffusion coefficient at the steel/cement interface increases the diffusive flux of Ca and Si from the solution cell, but also from the cement itself. Inversely, a lower diffusion coefficient at the steel/interface (slightly) decreases the flux of Si and enhances the proportion of magnetite in the cement paste.



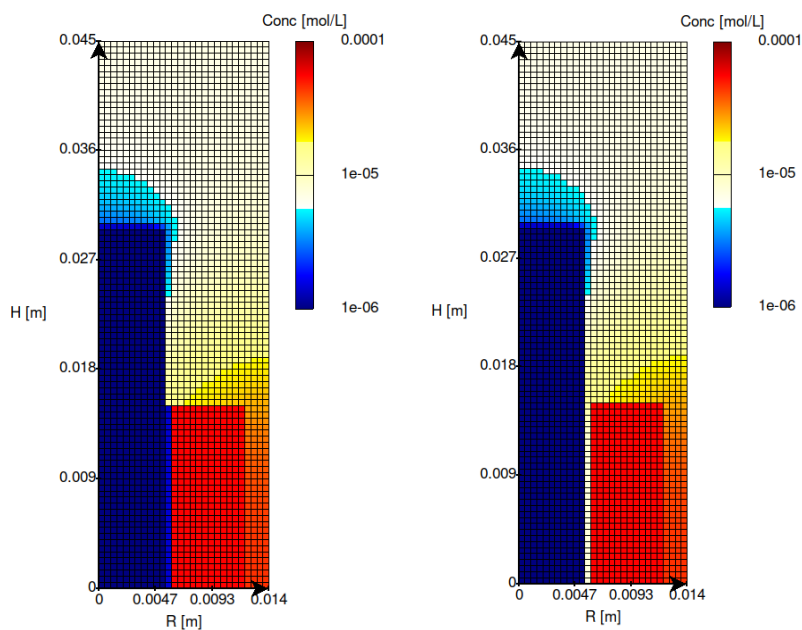


Figure 63: Modelling of the location of CAFSH and magnetite precipitation after 180 days and distribution of the total aqueous Si concentration according to the effective diffusion coefficient D_e at the steel/cement interface.

4.5.2 Impact of temperature on the chemical evolution of the system

Globally, temperature will have direct and indirect impacts on the corrosion processes. The principal direct impact is the effect on the kinetics. Indeed, the formation or the transformation of some CPs is kinetically hindered at low temperature. Moreover, temperature will decrease the resistivity of the electrolyte which can have an impact on the corrosion rates. Most of the corrosion processes observed in these experiments are due to indirect impact of temperature. The first one is linked to the pH stability domain of CPs that is dependent of temperature (principally due to the temperature dependency of the dissociation product of water (K_w)). For instance, Figure 65 shows the Pourbaix diagrams for the CEM I system at 20 and 80°C. This figure clearly illustrates this phenomenon, showing that the stability domain of hydrogarnet is more important at 80°C than at 20°C. Phase precipitation can be favoured at higher temperature and in a similar manner, phase dissolution can be enhanced. The dissolution of these phases can provide elements for the formation of some corrosion products resulting in a second indirect impact of temperature in the corrosion process. The third impact would be even more indirect and linked to the hydration of cementitious assemblages. Indeed, temperature will impact the nature of the phases in the cementitious assemblage as well as its microstructure and thus affect the diffusional properties of the material. As some elements diffuse from the material toward the interface to interact with steel, such phenomenon must be considered especially for long term corrosion process. Eventually, the temperature will affect the bacterial activity at moderate alkaline pH that will also impact the corrosion processes. In the case of the BCG experiment, phase formation and phase transformation arising from temperature increase are the most relevant processes.

4.5.2.1 Steel/BCG experiments:

Transformation of iron ox(hydr)oxide into iron silicates and iron sulphides

For the samples coming from both *in situ* and mock up experiments dedicated to the study of corrosion at 80°C, large amount of iron sulphides and iron silicates were observed. In the mock-up experiments, iron silicates and a fraction of the iron sulphides formed from the dense magnetite layer. The formation

of this magnetite layer occurred after the initial consumption of both oxygen and HS⁻ ions coming from a first source of sulphides (easily accessible for reaction). This magnetite formation arises from both transformation of goethite into magnetite and direct formation of magnetite processes.

In the *in situ* experiment, iron silicates (mostly) and some iron sulphides rather formed from a porous iron oxi(hydr)oxide layer (probably goethite). This might explain the large difference in the iron silicate/sulphides layer thicknesses for mock-up and *in situ* test samples, because diffusion of sulphur and silicon was more efficient in the porous layer. In both cases, such transformation arises from the production of a silica and/or sulphide source from the material.

Silica source and iron silicate formation

When iron oxi(hydr)oxide (i.e., magnetite or probably goethite) formed in the anodic zone, OH⁻ ions are produced in the cathodic ones, enhancing the dissolution of the hydrated silica fume from the BCG in the vicinity of the corroded area, promoting the formation of iron silicates. Regarding the nature of these Fe-silicates, XRD and SEM-EDX analyses performed on steel coupons from experiment 2-C indicated that they belong to the kaolinite-serpentine group. Based on their chemical formulas, as well as their structural and morphological features (Goethals et al., 2023) they could correspond to greenalite and/or cronstedtite. Such Fe-silicates are often found associated to magnetite, iron sulphides and iron carbonates in primitive chondrites (Pignatelli et al., 2018) or at the iron/clay (Schlegel et al., 2014; Lanson et al., 2012) or iron/glass (Dillmann et al., 2016) interfaces. Prerequisites for the formation of cronstedtite are the presence of metallic iron, neutral or alkaline pH and a temperature between 50 and 120 °C (Lanson et al., 2012). It has recently been shown that the nature of serpentine-like Fe-silicates strongly relied upon the precursors involved in their formation (Pignatelli et al., 2020), with berthierine ((Fe²⁺,Fe³⁺,Al)₃(Si,Al)₂O₅(OH)₄) most likely formed from iron and kaolinite reaction, and cronstedtite formed from iron and quartz reaction. Hydrated silica fume (which does not contain aluminium) was the major source of silicon in the present study, which explains the low Al content of the Fe-phyllsilicates observed in our work in comparison to Fe-phyllsilicates formed from iron and kaolinite reaction.

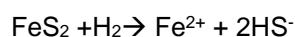
It should be noticed that outermost corrosion layers in BAC-1 and BAC-2 *in situ* experiments (13°C) were sometimes also enriched in silicon. These layers are less enriched in silicon than the one formed at higher temperature and the nature of the Si-bearing phases that formed is unknown, but still, iron oxi(hydr)oxide CPs can react with silicon at low temperature.

Sulphide source and iron sulphide formation

The formation of iron sulphides was observed at different step of the corrosion process. Thus, the presence of two different sulphide layers separated by S-free layers arise either from (i) the presence of a second source of sulphides in the BCG or (ii) to a change in the mechanism of sulphide release. Indeed, it is probable that the sulphides came from CEM III/A and bentonite that contained oldhamite (CaS) and pyrite (FeS₂), respectively. In blast furnace slag, CaS is present either in the form of free dendritic crystals or in inclusion in mellilite (Scott et al., 1986; Roy, 2009). Thus, free crystals of CaS were readily available as a first source of sulphides in our experiment and then a second source would be available after the partial dissolution of mellilite crystals during the hydration of the BCG.

Iron sulphides were also observed in the outermost region of the CPs layer in the mock-up tests, these unidentified sulphides would have formed after a longer time of reaction. They might come from the dissolution of pyrite that is more stable than CaS.

For instance, it is possible that H₂ release from corrosion triggered pyrite reduction via the following reaction:



Such pyrite reduction was observed by Schlegel et al, who studied the corrosion of steel in contact with CO_x at 90°C and in anoxic conditions (Schlegel et al., 2019).

Thermodynamic equilibrium calculations were performed in order to simulate the observed transformation of magnetite into iron silicates and iron sulphides in the CPs layer for mock-up experiments (Figure 64). The starting point assumed a full hydration of the bentonite/cement-grout components and a porosity of 0.75 (i.e., 75 % of water and 25% of solid phases in volume). Such a large porosity is due to the very high Water/Cement ratio and is in agreement with water porosity measurements performed on this material (not shown).

Furthermore, the aluminous, sulphated and carbonated phases were not considered. That is to say that the full hydrated grout was initially composed of C-S-H with a Ca/Si of 0.8 (0.35 kg/L of porous media (PM)) and some remaining silica fume (0.15 kg/L of PM) modelled as cristobalite. The initial sulphide content was fixed to 1 wt.% (brought by CEM III/A and bentonite) and modelled as pyrite (0.026 kg/L of PM). Temperature was set to 80°C and the initial pH to 9.5. The effect of steel corrosion under anoxic conditions was tackled through the diffusion of an alkaline/hydroxide Fe(II) plume modelled as the progressive addition (i.e., a titration-like model) of Fe(OH)₂ that were free to react with the hydrated grout assumed to be located very close to the steel interface.

Figure 64a shows that, in Stage I, pyrite is progressively transformed into mackinawite in parallel (“simultaneously”) to the neoformation of cronstedtite (greenalite was not included in the model). However, the initial amount of iron silicate (cristobalite) is much higher than the initial amount of iron sulphide (pyrite) and cronstedtite keeps precipitating in Stage II.

Magnetite starts to precipitate (Stage III) only once the silica source (cristobalite) is fully exhausted in the thermodynamic calculation. It is worth mentioning that the pH remains in a narrow range close to the values measured experimentally all along the mineralogical sequence (Figure 64b). The redox potential Eh shifts towards very reducing conditions at the boundary between elemental iron and mackinawite/cronstedtite equilibrium (Fig. 64d, Fig. 64b). The second set of graphs (Fig. 64c, d) splits the global reaction into a subset of increased chemical complexity. Stage I-a considered only the oxyhydroxide system, then stage I-b broadened it to the oxyhydroxide-sulphur system, and stages II and III included the full oxyhydroxide-sulphur-silicate system. The calculation mainly indicates that cronstedtite can form at the expense of magnetite in the presence of cristobalite, provided a Fe(OH)₂ source is supplied by steel corrosion. This phase would form until complete consumption of the Si source, which would be most probably hydrated silica fume in these experiments (modelled as cristobalite in the calculations). These results are in agreement with the observed corrosion product sequence in the CPs layer and suggest that the magnetite layer would not be totally destabilized by Fe-silicates from the drop in the corrosion rate (step 4 in Figure 61).

Note that, the second ingress of sulphides is not considered in this titration like model for the sake of simplicity. However, this model showed that Fe-sulphides and Fe-silicates can form simultaneously as observed experimentally.

4.5.3 Impact of microbial activity

In addition to the complex corrosion processes involved at BCG-steel interface in anoxic or sub-anoxic conditions, microbial activity can influence steel corrosion even at alkaline pH as high as 12 (Rizoulis et al., 2012; Charles et al., 2017; Pitty et al., 2011; Takai et al., 2001). In two recent study from ANDRA (Diler et al., 2021; Diler et al., 2023) it was shown that the corrosion rate of steel in contact with similar BCG was not enhanced by the presence of bacteria. Particularly, the use of more alkaline BCG limited the microbial biomass and diversity, thus limiting the risk associated to microbial induced corrosion. Surprisingly, the authors generally observed no localized corrosion and low corrosion rates in their inoculum-free tests, even if they used BCG containing sulphides and with a high porosity (high oxygen content available). The two main differences between our and their tests are the very low oxygen content in their experiments due to the constant N₂ flushing of the experimental cells and the renewal of the pore water solution in their case. Thus, the presence of residual oxygen certainly played a major role in the corrosion of steel in our setups and the renewal of the solution in their case also favoured the elimination of sulphides from the BCG.

In our study, only little information on the nature and density of the microbial population was obtained, limiting the interpretations of the results. However, some particular corrosion features were obtained and attributed to bacterial activity.

- The formation of homogeneous iron sulphide layers in the mock-up tests, regardless of the synthetic solution composition, inoculated or not, indicates bacterial activity (sulphate and/or thiosulfate reduction). Indeed, sulphides were not added to the synthetic solutions and reduction of sulphate or thiosulfate into sulphides without bacterial activity is unlikely in such conditions. As consumption of sulphate was limited for all experiments (Appendix G), it might indicate that the production of sulphide rather arised from thiosulfates.
- For the *in situ* tests, the iron sulphides observed at the different interfaces can have different origins. Indeed, as already detailed, BCG contains different source of sulphides and argillite contains an important amount of pyrite. However, the dissolution of such sulphides is limited at low temperature (Bonnet et al., 2023) and the low diffusion coefficient of argillite limits the ingress of sulphides from it. Thus, the important amount of iron sulphides observed at the interface between steel/BCG/argillite in BAC-2 experiment might be explained by an important bacterial activity.

Due to the lack of data, it is difficult to evidence any bacterial activity not linked with the presence of iron sulphides.

4.5.4 Impact of heterogeneity

In experiments with BCG, the surfaces exposed to synthetic solution only were less corroded than the surfaces directly exposed to BCG. This result is consistent with a diffusion-controlled process. Indeed HS⁻ ions released from the BCG were able to rapidly react at the surface of the steel prior to diffusing in the solution (electrolyte). Moreover, the presence of a restricted volume of water between the steel and the BCG locally affects the pH and the chemistry of synthetic solution. This local change might have contributed to the extension of corrosion. However, it seems that the distance between the steel and the BCG has no effect on the observed corrosion mechanism. Indeed, similar corrosion products were observed in experiment 2-C mock up in which steel was separated from the BCG by a large volume of solution.

In experiments with CEM I, the presence of an heterogeneity favoured the ingress of elements coming from the cementitious material to the steel surface, as already discussed in the previous sections. Such heterogeneity will thus clearly favour Fe-siliceous hydrogarnet instead of magnetite formation as a corrosion product of steel. It should be noticed that a crack in the cement paste would have approximately the same effect as an heterogeneity of filling, except that a crack can be rapidly filled by precipitation processes (depending on the size of the crack) limiting the ingress of elements through it.

4.6 Conclusions

- This study provides insight on the effect of temperature on the corrosion of steel in different types of cementitious environment (low-pH cement-BCG and ordinary Portland cement CEM I)
- To a lesser extent, it provides information on bacterial activity on steel corrosion in BCG.
- Thermodynamic calculations obtained on the evolution of the steel/cementitious materials assemblages are in fair agreement with experimental data.
- In the case of low pH cement-BCG, localized corrosion occurred due to the presence of sulphides and residual oxygen in the material. Such processes cannot be implemented in the models at larger scale. However, the transformation of iron oxy(hydr)oxides into iron silicates was evidenced in this study and can be considered relevant for long term predictions.
- In the case of ordinary Portland cement, uniform corrosion was observed at a low rate, in agreement with the literature data. However, the formation of hydrogarnet, instead of magnetite was sometimes observed. The formation of such phase is predicted by thermodynamic calculations and was also recently observed by Pally et al. (2020). Some questions remain on the formation of this phase but it seems that it is not detrimental for corrosion.
- In both cases, the study of the cement and pore water evolution with time and/or temperature allowed a better comprehension of the corrosion mechanisms.

5. MTA EK experiments (High concentration WG)

5.1 Introduction

The aim of the experiments was to gain information on corrosion processes that can impact carbon-steel/concrete interfaces for different applied conditions (temperature, saturated conditions).

We performed comprehensive characterization of the systems, with special focus on the proper understanding of the processes occurring on the surface of the steel/concrete interface.

The Hungarian radioactive waste management company (PURAM) is designing a DGR in the Boda Claystone Formation (BCF) in West-Mecsek (SW-Hungary). The interface between carbon steel and CEM II-based concrete is a key issue in the design of a disposal cell for vitrified HLW in argillaceous rock formations for the Hungarian national waste disposal program (Nos, 2020; IAEA-NS-ARTEMIS, 2023; Honti, 2019). The design relies on low carbon-steel (C-steel) containers (containing the HLW) encased in a prefabricated cylindrical concrete buffer material. The concrete is originated from the Public Limited Company for Radioactive Waste Management (PURAM) and it is considered as the buffer material in the final disposal program in Hungary (Feil et al., 2014). The present investigations is intended to help to optimize the Hungarian repository concept with the aim of ensuring its long-term safety.

This study focuses on C-steel corrosion in contact with CEM II-based concrete at 80°C to gain further information on the chemical-physical alteration of the steel/concrete interface for conditions representative of geologic disposal. Lab scale experiments were performed during 12 months at a temperature of 80°C, under water-saturated and anaerobic conditions. A set of complementary characterization methods were applied to the liquid and solid phases with the support of geochemical modelling (Fabian et al., 2023).

5.2 Experimental details

5.2.1 Concrete and steel compositions

The concrete originated from the National Radioactive Waste Repository in Bataapati (Hungary). This underground repository ensures the final disposal of short-lived low- and intermediate-level solid or solidified radioactive waste of nuclear power plant origin (Honti, 2019). The concrete was made of CEM II/B (18 wt.%), siliceous sand/gravel (54 wt.%), limestone flour (15 wt.%) and tap water (11 wt.%), as detailed in Table 21.

The steel container was made of untreated S235JR carbon steel. The chemical purity of the C-steel corresponded to ≤ 0.17 C, ≤ 0.3 Si, ≤ 1.4 Mn, 0.035 P, 0.035 S, ≤ 0.55 Cu, ≤ 0.012 N in wt.%.

Table 21: Composition of the concrete.

| Materials | Density [kg/dm ³] | Mass [kg/m ³] | Volume [L/m ³] | |
|------------------------------|-------------------------------|---------------------------|----------------------------|-----|
| Main components | | | | |
| Aggregates | Sand | 2.7 | 920 | 347 |
| | Gravel | 2.7 | 230 | 87 |
| Cement | CEM II/B-S 42.5 N | 3.1 | 385 | 126 |
| Limestone flour | limestone flour | 2.7 | 315 | 117 |
| Water | tap water | 1.0 | 231 | 231 |
| Minor components | | | | |
| Fiberglass | | 2.6 | 1 | 0.5 |
| Admixtures [SikaFume (2023)] | Sika ViscoCrete | 1.1 | 5 | 5 |
| | Sika Control-40 | 1.0 | 10 | 10 |
| | Sika LPS A-94 | 1.0 | 1 | 1 |
| | SikaFume HR/TU | 2.2 | 26 | 11 |
| Total | | 2 124 | 935 | |

5.2.2 Design of the cell experiments

The experimental set-up was prepared in triplicate as shown in Figure 66. For each cell two Teflon containers were built to ensure water saturation during the experiments. The concrete was poured into the Teflon mould, placing the C-steel container in the centre. The core of the cell was composed of a steel container with a height of 45 mm and diameter of 20.64 mm (see also Figure 8). The external Teflon container had a height of 160 mm, a diameter of 90 mm. The internal Teflon container had a height of 100 mm and a diameter of 50 mm. The internal Teflon container surface area was about 140 cm² and 5 holes with 0.7 mm diameter were randomly drilled through it. The soaking water was made by mixing 77 g of crushed concrete with 700 ml of MQ-water for three days. To exclude leakage and ensure saturation, the mass of each experimental setup was inspected monthly. All three cells were closed in anoxic glove-box to keep anaerobic conditions.

A constant temperature of 80 ± 2 °C was imposed during the whole experiment. The corrosion potential was monitored using a platinum wire that has been embedded within the concrete and C-steel wire (also S235JR) spot welded on the container. Measurements were taken at 20-second intervals. Initially, the potential between the platinum wire and a calomel electrode was checked using a Metrohm Autolab PGStat204 potentiostat. The measurements were conducted in the soaking water under specific conditions, namely at pH 11.9 and for a temperature of 22.8 °C.

To ensure accurate interpretation and comparison of the results, the obtained corrosion potential was then adjusted using an offset correction. This correction was applied to align the results with the standard hydrogen electrode (SHE) scale. By making this adjustment, the corrosion potential values can be properly referenced and analysed in relation to other electrochemical systems or experiments conducted using the SHE scale. Experimental setups were opened for post-mortem characterization after 3, 7 and 12 months (hereafter referred as SC-3M, SC-7M, SC-12M, respectively). After disassembling the experimental setup, the C-steel containers were covered with adhering concrete layer making direct characterization of steel surface difficult. The corrosion interfaces were thus investigated on cross-sections.

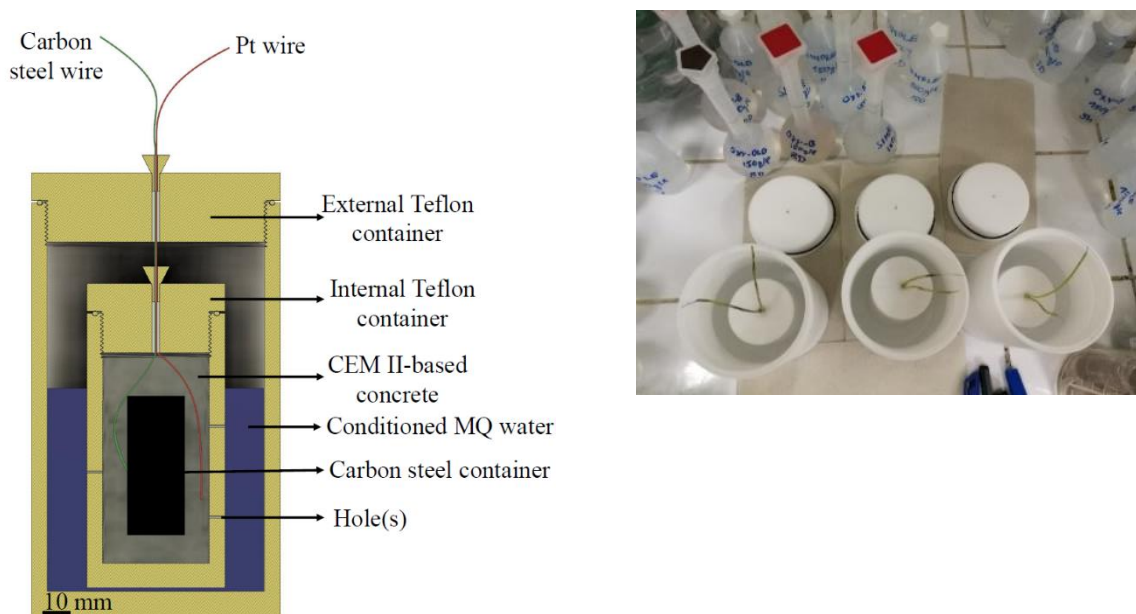


Figure 66: Cross-section view of one experimental setup indicating different materials (left) and a photograph showing the parts of the experimental setup in triplicate (right).

5.3 Experimental results

The corrosion products formed on the C-steel/concrete interfaces (anoxic environment and 80°C) were characterized using different techniques such as SEM/EDX analysis and micro-Raman (μ Raman). Changes of cation/anion concentrations in the surrounding soaking water (soaking water was made by mixing 77 g of crushed concrete with 700 ml of MQ-water for three days) were measured by ICP-OES and IC.

5.3.1 Corrosion potential

Figure 67 gives the relationship of corrosion potential with months of exposure. The evolutions of the corrosion potential measured on the three steel/concrete setups (3M, 7M, 12M) follow the same

characteristics at all stages of experiments. The strongly negative values in the first two months are linked to the corrosion of the C-steel. Afterwards, the potentials increase to reach small constant positive values that are assumed to be driven by the formation of a passivation layer. Such film passivation in less than 50 days is remarkable for all three setups.

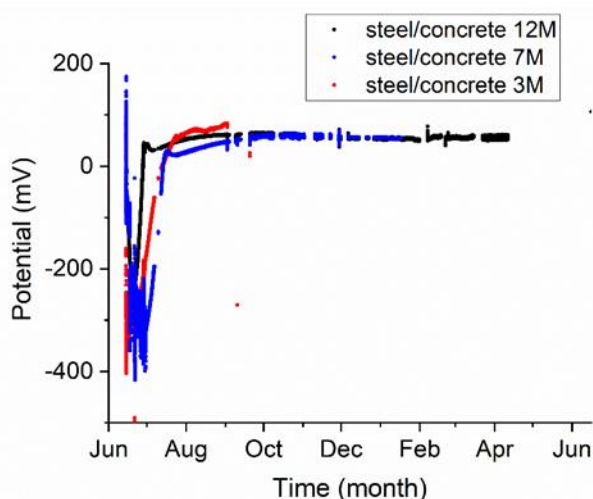


Figure 67: Evolution with time of the measured corrosion potentials on the standard hydrogen scale for the three cells at 80 °C.

A decreasing corrosion potential with the time on the CSC-12M sample can be observed after the corrosion is initiated. After that equilibrium was reached, the potential assumed a constant value with a small rise indicating film repassivation, which is remarkable for the CSC-12M sample. Negative potential has been detected throughout the experiments, which is generally considered to be consistent with a higher probability of C-steel corrosion.

5.3.2 SEM/EDX measurements and results

The composition and nature of alteration products formed on the steel and within the concrete were investigated by scanning electron microscopy/energy dispersive X-ray spectroscopy (SEM/EDX). The measurements were performed at 20 kV, 1.6 nA, using a Thermo Scientific Scios2 dual beam microscope, Oxford X-maxn 20 SDD EDX.

Figure 68 presents SEM-EDX images of the steel/concrete interfaces after 3, 7, 12 months experimental time. There is no indication of void or free space in between the concrete and the steel. The pouring of the concrete had let to tight interfaces since the beginning of the experiments. On each of the three samples the formation of 20-60 μm long Fe-oxide ingrowths were detected. These SEM results show that micro-cracks appeared even in a short term (3 months) and could have initiated changes of the carbon steel surface (Figure 68). However, these ingrowths remained relatively short and did not exceed 100 μm in length after 7 and 12 months (Figure 69).

Table 22 gives SEM-EDX analyses for minerals at the corrosion interfaces after 3 months (SC-3M) based on the points marked in Figure 68. Corrosion products consisting of Fe – O (spectra 1-3) can be distinguished from the C-steel (spectra 4 and 5), which is primarily composed of Fe.

Table 23 gives the EDX analyses after 7 months with again a Fe – O signature typical of iron oxide corrosion products (spectra 2). But there is also a mixed signal composed of Ca – Al – Si – S and Fe oxide. Table 24 provides results like those of Table 22.

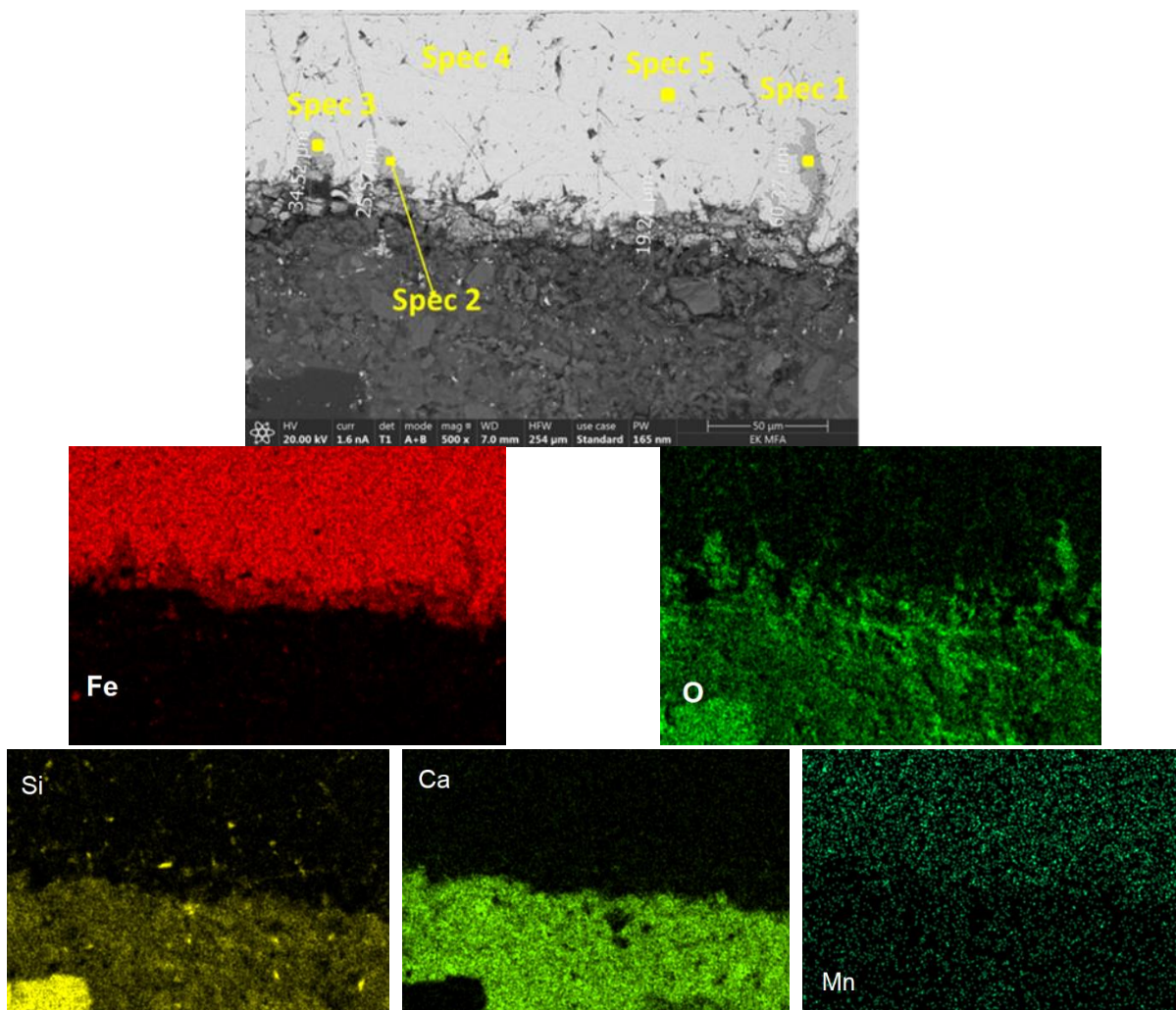


Figure 68: SEM micrograph showing micro-cracks initiated in the steel in contact with concrete after 3 months (SC-3M sample) and the corresponding elemental mapping of Fe, O, Si, Ca and Mn.

Table 22: SEM-EDX analyses of the corrosion products and the steel for the SC-3M sample the locations of the spectra are given in Figure 68).

| [at. %] | Spec 1 corr. prod. | Spec 2 corr. prod. | Spec 3 corr. prod. | Spec 4 C-steel | Spec 5 C-steel |
|---------|-----------------------|-----------------------|-----------------------|-------------------|-------------------|
| O | 47.09 | 44.01 | 47.64 | - | - |
| Si | 1.67 | 0.18 | 0.47 | 0.65 | 0.97 |
| Ca | 0.16 | 0.15 | 0.11 | - | - |
| Mn | 0.36 | 0.28 | 0.21 | 0.59 | 0.61 |
| Fe | 50.72 | 55.38 | 51.57 | 98.76 | 98.42 |
| Total | 100.00 | 100.00 | 100.00 | 100.00 | 100.00 |

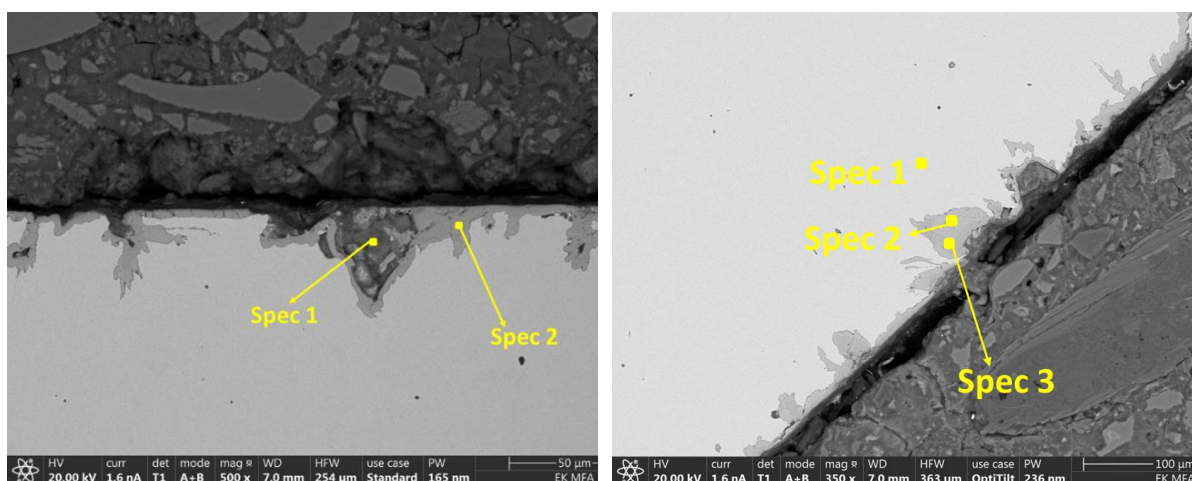


Figure 69: SEM micrograph of the steel-concrete interface after 7 (left) and 12 (right) months.

Table 23: SEM-EDX analyses of the corrosion products and the steel for the SC-7M sample (see Figure 69 left).

| [at. %] | Spec 1 concrete/corr. prod. | Spec 2 corr. prod. |
|---------|--------------------------------|-----------------------|
| O | 56.45 | 46.84 |
| Mg | 3.43 | - |
| Al | 2.41 | - |
| Si | 12.10 | 0.34 |
| P | 0.06 | - |
| S | 0.51 | - |
| Cl | 0.05 | - |
| K | 0.08 | - |
| Ca | 3.59 | 0.14 |
| Ti | 0.06 | - |
| Mn | 0.15 | 0.37 |
| Fe | 21.13 | 52.31 |
| Total | 100.00 | 100.00 |

Table 24: SEM-EDX analyses of the corrosion products and the steel for the SC-12M sample (see Figure 69 right).

| [at. %] | Spec 1 C-steel | Spec 2 corr. prod. | Spec 3 corr. prod. |
|---------|-------------------|-----------------------|-----------------------|
| O | - | 51.46 | 58.26 |
| Si | 0.46 | - | - |
| Ca | - | 0.08 | 0.12 |
| Fe | 99.54 | 48.46 | 41.62 |
| Total | 100.00 | 100.00 | 100.00 |

5.3.3 μ Raman spectroscopy results

According to the results of the SEM/EDX, the corrosion processes had an impact on the steel-concrete interfaces. Therefore, micro-Raman investigations were performed to better identify the corrosion products. The analyses were carried out using a HORIBA JobinYvon LabRAM HR 800 Raman microspectrometer. A frequency doubled Nd-YAG green laser with a 532 nm excitation wavelength was used to illuminate the samples, displaying ~ 0.2 mW on the sample surface. An OLYMPUS 50 \times (N.A. = 0.6) and 100 \times (N.A. = 0.9) objective was used to focus the laser. For Raman mapping, 100 μ m confocal hole, 600 grooves/mm optical grating, 4-10 s cumulated exposition time were used. The spectral resolution of measurements was 3.0 cm^{-1} . The step size of the Raman maps varied between 1 and 0.5 μ m for magnifications 50 \times and 100 \times , respectively.

Mainly magnetite (Fe_3O_4) and hematite ($\alpha\text{-Fe}_2\text{O}_3$) can be identified as corrosion products after 3 months (SC-3M sample, Figure 70) and 7 months (SC-7M sample, Figure 71). The corrosion protrusion is formed by magnetite, no other corrosion products could be identified by micro-Raman. After 12 months of experiments, no substantial change in the Raman spectra was observed (Figure 72). Mainly magnetite (Fe_3O_4) and hematite ($\alpha\text{-Fe}_2\text{O}_3$) were still detected. During the whole exposure time, magnetite was identified as the main corrosion product. No iron-carbonates or iron-sulphides were identified.

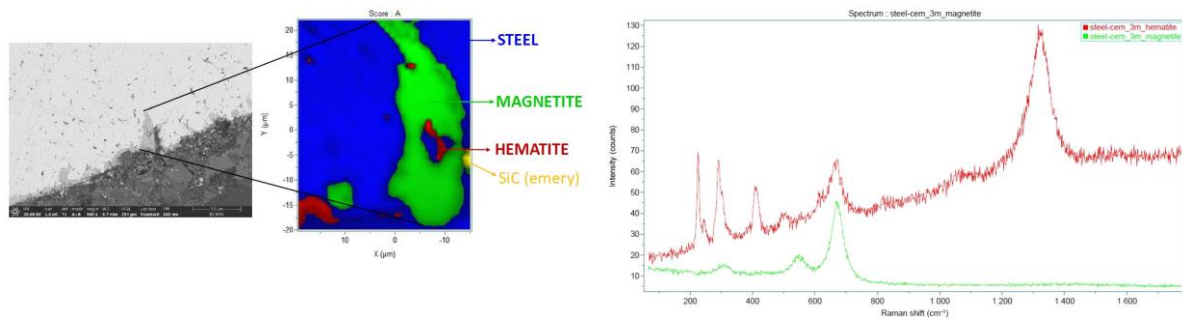


Figure 70: Micro-Raman mapping and characteristic spectra obtained after 3 months (CS-3M).

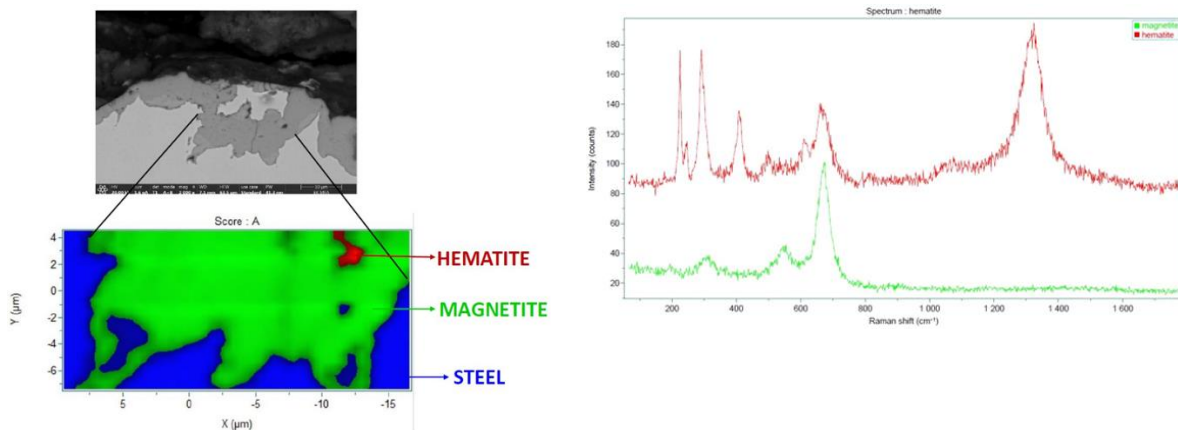


Figure 71: Micro-Raman mapping and characteristic spectra obtained after 7 months (SC-7M).

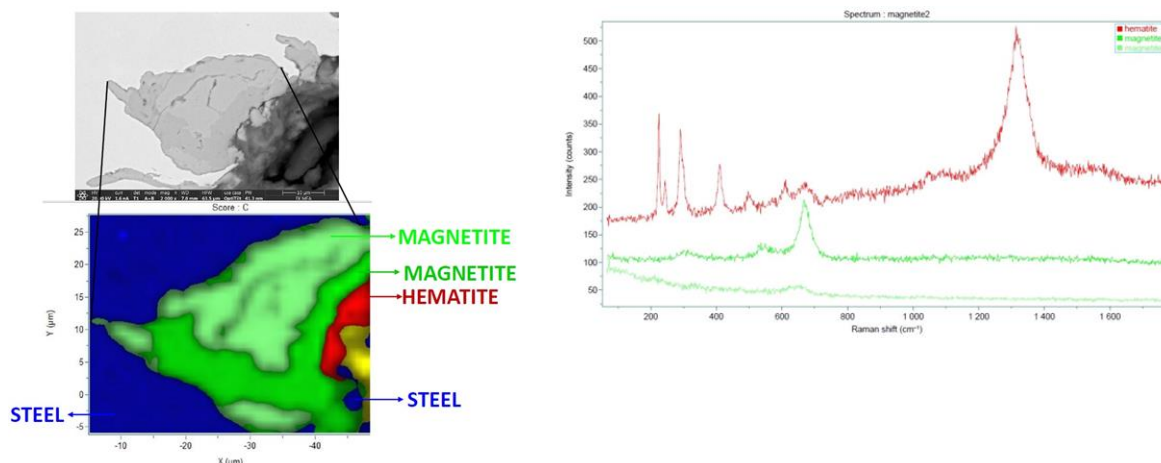


Figure 72: Micro-Raman mapping and characteristic spectra obtained after 12 months (SC-12M).

5.3.4 Chemical analysis of aqueous solutions

The liquid phase (aqueous solution) was sampled from the external Teflon container after 3, 7 and 12 months. Ca, K, Mg, Na and Si concentrations were determined using inductively coupled plasma - optical emission spectrometry (ICP-OES), while ion chromatography (IC) was used for Cl⁻ and SO₄²⁻. ICP-OES measurements were carried out on a Perkin Elmer Avio 200 sequential instrument. All elements were tested in radial view using Y as internal standard. The leachates were filtered through a cellulose acetate membrane (dp > 220 nm) and then were acidified with 2 m/m% HNO₃. All elements were tested in radial view using 1 ppm of Y as internal standard and a calibration of 4 points was applied for all measured elements (0.01, 0.1, 1 and 10 ppm). The power of the generator was set to 1200 W during the measurements and the use of plasma argon was 12 l/min. IC analyses were performed on Thermo Scientific Dionex Aquion equipment with 4.5 mM Na₂CO₃/0.8 mM NaHCO₃ eluent composition and at a flowrate of 0.25 mL/min. The separation of the components was carried out by a Dionex IonPac AS23 2 mm x250 mm analytical column coupled with a Dionex AERS 500 Carbonate electrochemical suppressor.

Table 25 shows that the Na and Ca concentrations progressively, but moderately, increased with time. The concentration of K and Si did not change significantly. A higher Mg concentration was measured after 12 months. The evolution of chloride and sulphate concentrations were less smooth, but the increase after 12 months was near 25% for chloride and 50% for sulphate.

Table 25: Evolution of the chemistry of the aqueous solution sampled in the external Teflon container (Figure 66).

| Concentration [mg/L] | Ca | K | Mg | Na | Si | Fe | Al | Cl ⁻ | SO ₄ ²⁻ |
|----------------------|-----|----|----|-----|----|------|-----|-----------------|-------------------------------|
| Soaking water | 97 | 24 | 2 | 219 | 43 | 0.4 | 0.8 | 505 | 100 |
| 3 months | - | - | - | - | - | - | - | 449 | 157 |
| 7 months | 117 | 19 | 1 | 238 | 44 | <DL* | <DL | 505 | 115 |
| 12 months | 135 | 26 | 18 | 299 | 47 | <DL | <DL | 618 | 145 |

* DL stands for detection limit.

5.4 Modelling results

5.4.1 Foreword

As discussed in Chapter 2, the reactive transport code HYTEC was used to model the initial geochemistry of the concrete as well as its evolution with temperature and time. The goal was to provide a robust estimation of the chemical conditions that had taken place in the cell and at the steel/concrete interface. To the best of our knowledge, this is the first modelling of the CEM-II based concrete of relevance for the Hungarian radioactive waste management. The thermodynamic database Thermoddem (Blanc et al., 2012) was selected. The formation constants of the Fe-siliceous hydrogarnet (C3FS0.84H4.32) (Dilnesa et al., 2014) was added to the database.

5.4.2 Initial hydrochemistry and mineralogy of the concrete

The modelling was based on the recipe of the PURAM concrete detailed in Table 21. The oxide composition of the CEM II-B-S 42.5 N was taken from Lubloy et al. (2016). The proportions of the CEM II-B components were fixed to 73.5 wt.% CEM I clinker, 24.5 wt.% blast furnace slag and 2 wt.% anhydrite (CaSO₄). The oxide compositions of the clinker and slag are detailed in Table 26. The hydration of the CEM I clinker was assumed to be complete, whereas only one half of the slag was assumed to have reacted. The limestone was considered as 100% CaCO₃, the silica fume as 100% SiO₂. The siliceous sand and gravel aggregates were assumed to be non-reactive during the time frame of the experiment and were not included in the modelling.

Table 26: Oxide composition of the clinker and slag considered in the modelling.

| Composition [wt. %] | Clinker | Slag |
|--------------------------------|---------|------|
| SiO ₂ | 21.3 | 37.4 |
| Al ₂ O ₃ | 5.0 | 7.3 |
| Fe ₂ O ₃ | 3.4 | 1.2 |
| CaO | 64.8 | 43.9 |
| MgO | 2.1 | 5.7 |
| K ₂ O | 1.0 | 0.56 |
| Na ₂ O | 0.11 | 0.55 |
| Cl | 0.03 | 0.03 |
| CaSO ₄ | 2.50 | - |

Table 27 gives an estimation of the initial reactive mineralogy of the concrete calculated at room temperature and 80°C.

The mineralogy is in line with the literature on clinker/slag cements (Lothenbach et al., 2008; 2012). The rather high amount of Al in the slag leads to C-A-S-H phases instead of pure C-S-H ones. Al also promotes the formation of monocarboaluminate (AFm phases) and ettringite (AFt phase). Mg is mostly found in hydrotalcite. In relation to the objective of this study, a sensitivity analysis was conducted to assess the impact of the ratio and degree of hydration on the mineralogy. The results indicated that, apart from the presence or absence of a small quantity of portlandite, no significant differences were observed.

A higher degree of slag hydration (i.e., upper the 50% assumed) may favour C-A-S-H at the expense of portlandite. The increase of temperature from 20°C to 80°C mainly results in the full dissolution of ettringite (and partial dissolution of monocarboaluminate) to form monosulfoaluminate (and calcite) in agreement with study of Lothenbach et al. (2008).

Table 27: Calculated initial amounts of reactive hydrated phases of the concrete.

| Solid phases * [kg/dm ³ of concrete] | T = 20°C | T = 80°C |
|--|----------|----------|
| C1.5-A-S-H | 0.357 | 0.357 |
| Portlandite** | 0.044 | 0.044 |
| Ettringite | 0.031 | 0.000 |
| Monocarboaluminate | 0.054 | 0.028 |
| Monosulfoaluminate | 0.000 | 0.044 |
| Hydrotalcite | 0.025 | 0.025 |
| Calcite | 0.350 | 0.355 |

* The non-reactive sand and gravel aggregates were not assumed to be reactive phases.

** Portlandite occurrence depends upon the degree of slag reactivity.

Table 28 provides for an estimation of the initial pore water chemistry of the concrete calculated at 80°C in thermodynamic equilibrium with the reactive minerals of Table 27.

The pH of the young cement water is about 11.9 at 80°C. This high pH value is driven by the dissolution of Na₂O and K₂O in water to form NaOH and KOH. The initial contents in Na₂O and K₂O were not accurately known. The modelling assumed that 50% of these alkali hydroxides were sorbed onto the C-A-S-H phases. The increase of temperature decreases the pH and significantly increases sulphate concentration in the pore water. In the current modelling approach, the sorption of sulphate onto C-S-H was not taken into account. However, it is important to note that if this sorption process were considered, the dissolved sulphate concentration would be reduced by approximately 50 %.

On the other hand, the presence of chlorides, which can exacerbate steel corrosion, was assumed to be fully dissolved in the pore water without being influenced by sorption or a mineral phase. At both temperatures, the initial chloride concentration was approximately 1200 mg/L.

Table 28: Calculated pore water chemistry of the concrete at 20°C and 80°C.

| Total concentration [mg/L] | T = 20°C initial | T = 80°C Initial | T = 80°C Steel interface, 12 months |
|---------------------------------|------------------|------------------|-------------------------------------|
| pH | 13.6 | 11.9 | 11.25 |
| Na ⁺ | 4350 | 4350 | 540 |
| K ⁺ | 7450 (750 *) | 7450 (750 *) | 605 (60) |
| Ca ²⁺ | 35 | 29 | 148 |
| Mg ²⁺ | 0 | 0 | 0 |
| Al ³⁺ | 1 | 145 | 28 |
| Cl ⁻ | 1200 | 1200 | 563 |
| HCO ₃ ⁻ | 14 | 27 | 1 |
| SO ₄ ²⁻ | 256 | 3300 | 66 |
| H ₄ SiO ₄ | 5 | 9 | 1 |

* K⁺ concentration required to fit the data of the Teflon container.

5.4.3 Evolution of the aqueous chemistry with time

A reactive transport modelling had been performed in a second step based on the calculated initial chemistry and mineralogy of the concrete. The modelling grid has been given in Chapter 3 (section 3.4).

The porosity and effective diffusion coefficient of the concrete was set to 10 % and $6 \times 10^{-12} \text{ m}^2/\text{s}$ at 80°C , respectively. These parameters had not been measured directly but estimated as a reasonable set according to the literature and provided a good fit to the concentrations of the (almost) no-reactive elements Na^+ and Cl^- measured in the external Teflon container. The effective diffusion coefficient of the Teflon container, $3 \times 10^{-13} \text{ m}^2/\text{s}$, could only be estimated/fitted on the same data set. It is clear that the 5 drilled holes were sufficient to keep water saturation but induced a very low diffusive transfer. A sensitivity analysis on the effective diffusion coefficient of the container is given in Figure 73.

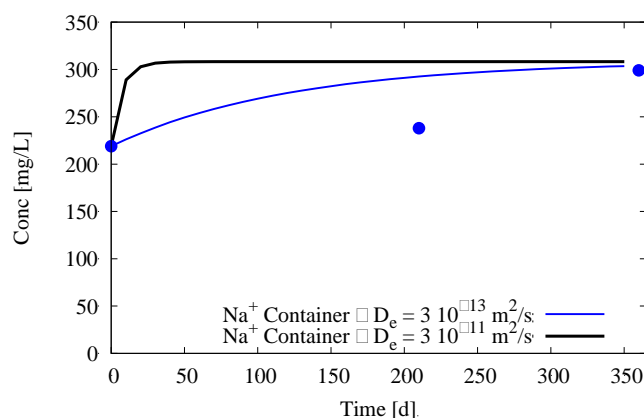


Figure 73: Effect of the diffusion coefficient on the time evolution of the non-reactive Na^+ concentration; the experimental data of the reservoir are added (blue circles) for the sake of comparison.

Figure 74 a-b show the evolution over 1 year of the concentration of the weakly reactive elements Na^+ and Cl^- that are only present as dissolved species in the model. Both concentrations are higher inside the concrete than in the soaking water. The gradient of concentration induces diffusion from concrete towards the external reservoir, which progressively leads to uniformized concentrations in the whole system. The good fit of the calculated concentrations after 1 year with the experimental data brings some confidence in the modelling.

The decrease of the pH from 11.9 to about 11.2 inside the concrete (Figure 75) is mainly due to the diffusion of the Na-K-OH plume towards the reservoir. Despite diffusion the pH remains quite high in the concrete and hence also at the interface with steel. The time evolution of the concentrations of Ca and sulphate (Figure 74c-d, reactive species) are dependent upon diffusion but also the equilibrium with the minerals of the cement, equilibrium dependent itself upon the pH. Table 28 gives the change in concentration of all the elements at the steel/concrete interface after 12 months. Such a relatively complex coupling between the chemical reactions and diffusion can only be handled with modelling. Again, the reasonably good agreement between the calculated and the experimental data gives credit to the model.

The main effect on the mineralogy of the concrete is due to the temperature increase up to 80°C . Afterwards, the globally weak diffusive transfer does not induce any significant change in the mineral contents. The only driven modification is the continuation of the transformation of monocarboaluminate to monosulfoaluminate and calcite at the boundary of the concrete with the reservoir but not around the steel/concrete interface.

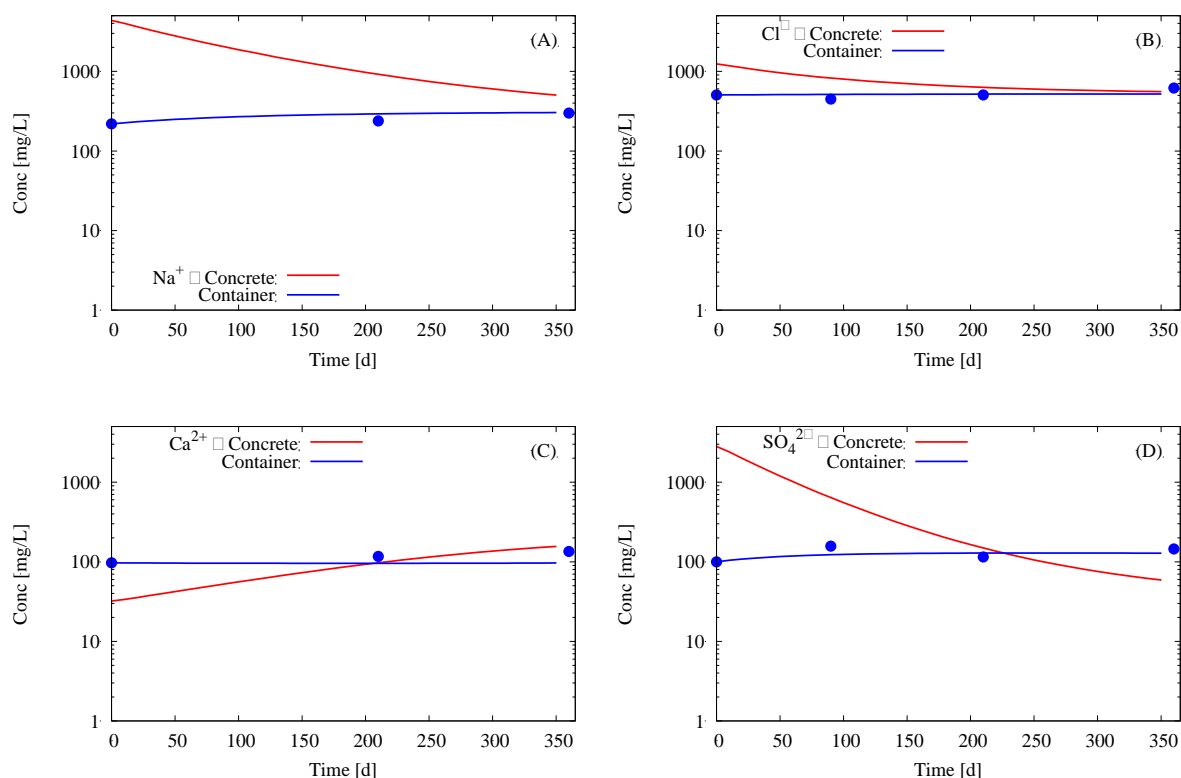


Figure 74: Modelling of the time-dependent evolution in concrete pore water at the steel/concrete interface (in red) and the reservoir chemistry (in blue). For the purpose of comparison, experimental data from the reservoir are included as blue dots.

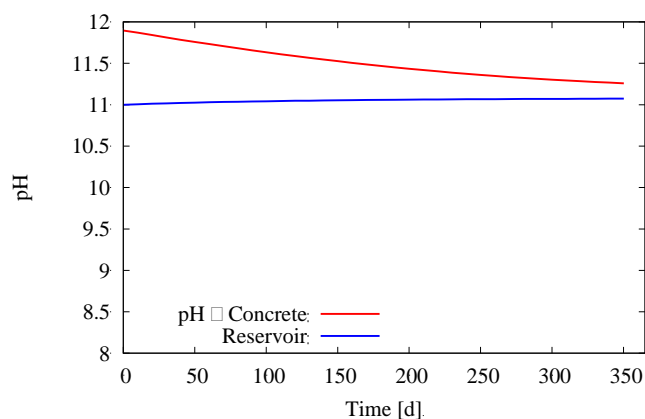


Figure 75: Modelling of the evolution with time of the pH of the concrete pore water (in red) and the reservoir (in blue).

5.5 Discussion

5.5.1 Corrosion products at 80°C

The geochemical and reactive transport modelling provides a reasonably accurate estimation of the mineralogy and chemical conditions at the steel interface with respect to temperature rise and diffusion within the system. These geochemical parameters (evolution of the mineralogy, diffusion coefficient of the concrete and reservoir, pH at the steel/concrete interface...), which are difficult to measure directly, were effectively considered. Although the mineralogy remains relatively stable throughout the process,

the chemistry of the pore water undergoes some changes, yet remains predominantly highly alkaline overall. Regarding the redox conditions induced by the concrete itself, it is currently uncertain. However, considering the anaerobic nature of the setup and the presence of slag, it is expected that reducing conditions would be prevalent. Introducing metallic iron at trace level in the modelling of the initial geochemistry gives a calculated redox potential (Eh, SHE) ranging from -600 mV (with HS/SO₄ couple) to -750 mV (without HS/SO₄) at a pH of 11.9 and a temperature of 80 °C.

Figure 76 shows some possible corrosion products that may form at the steel/concrete interface for the calculated chemical conditions. The Fe – O system points out the competition between goethite (Fe(III) oxyhydroxide) and magnetite (Fe(III)-Fe(II) oxide) according to the redox potential. It is worth mentioning that hematite will replace goethite in the same diagram if included in the system. If the system is further complexified by introducing Ca and Si, silica-hydrogarnet can prevail on magnetite at high alkaline pH but mildly reducing redox potential. Oxidizing conditions could not occur in the present experimental closed system but may take place during the operational phase of the repository when air would be present. Under such hypothetical oxidizing conditions, goethite or ferrihydrite would be less stable than CAFSH inside or close to the concrete. Fe(II)-silicates corrosion products such as greenalite can only precipitate at pH values lower than 10.5 at 80°C and reducing conditions.

Magnetite was clearly identified as the main corrosion product by micro-Raman. The SEM-EDX analyses in Fe and O of corrosion products are also consistent with magnetite. Magnetite is usually the main product under anoxic corrosion of the carbon steel (Shannon et al., 2016; Diomidis, 2014; Smart, 2009; Wieland et al., 2023). No other corrosion products than Fe-silicate or Fe-sulphide were identified by this technique. Magnetite remained stable over the 12 months and did not convert to iron silicates and/or iron sulphides as it has been observed in cementitious/bentonite grout at lower pH (Goethals et al., 2023). Hematite has been identified in most crossed-sections, usually close to the steel surface and always in relatively low quantity compared to magnetite. It is possible that hematite was present since the beginning as mill scale (Angst et al., 2017), or else due to the transformation of early oxidic corrosion products during the preparation of the experimental set-ups and then heating to 80°C.

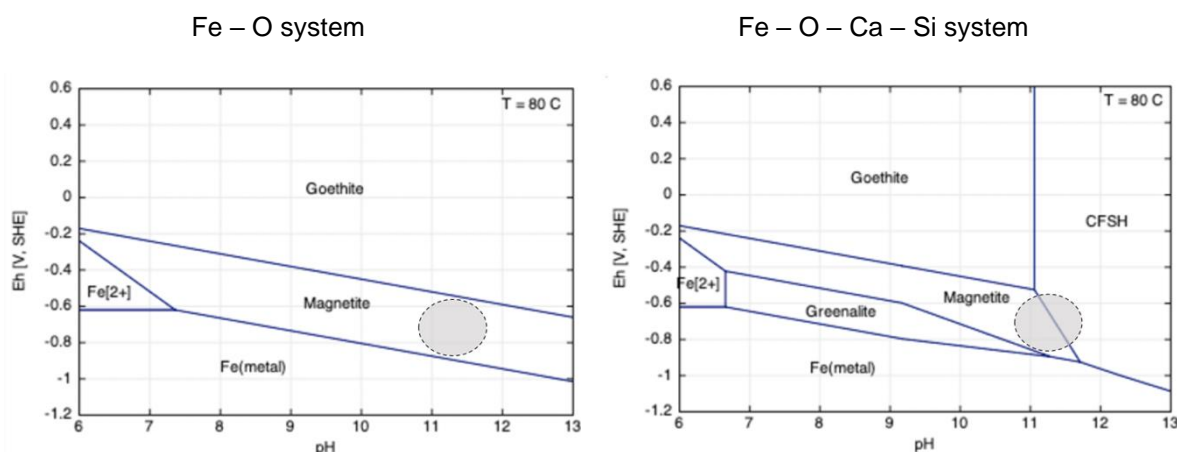


Figure 76: Phase stability diagrams of possible corrosion products of C-steel in slightly to strongly alkaline chemical environments (CHESS/HYTEC code, Thermoddem database); activity Fe²⁺ = 5×10⁻⁵, activity Ca²⁺ = 5×10⁻⁴, total H₄SiO₄ = 1×10⁻⁵M?, temperature = 80°C; the grey zones stand for likely pH – Eh conditions in the present steel/concrete system.

5.5.2 Corrosion mechanism and rate

Microstructural characterization shows strong similarities in the corrosion patterns in 3, 7 and 12-months samples. Magnetite was found all along the steel surface although the formation of 20-60 μm long Fe-oxide ingrowths were also identified. The literature (Goethals et al., 2023; Chomat et al., 2017) states that the carbon steel surface is likely to be passivated due to the formation of a stable magnetite film. This is in line with the short transient stage of negative corrosion potential measured in the three cells for 50 days at maximum. The occurrence of a uniform passive corrosion mechanism is, therefore, likely. A mean corrosion rate was derived from observed thicknesses during SEM analysis and from the obtained corrosion potential curve (estimating that the altered layer was formed only in the first 50 days). In this study the estimated corrosion rate is in order of magnitude of 10 $\mu\text{m}/\text{year}$. Similar values of early corrosion rates have been found for CEM I and the corrosion rates usually decrease exponentially with time to reach rate smaller than 0.01 $\mu\text{m}/\text{year}$ within a year (Smart et al., 2017). The long-term corrosion rate could not be determined in the present experiments but was clearly much lower than 10 $\mu\text{m}/\text{year}$. Temperature increase seems to be inoperative for the long-term corrosion rates (Smart et al., 2017). There was no trace of any localized corrosion mechanisms. The moderated aqueous concentrations in chloride (500 – 1000 mg/L) had no effect, in agreement with that did not find any consequences of high concentrations of chloride on the corrosion of steel under highly alkaline anoxic conditions (Smart et al., 2017).

5.6 Conclusions

The current experimental setup examined the combined chemical evolution of two major components, namely the metallic waste canister and the concrete buffer, used in deep geologic disposals at a temperature of 80 °C. The materials chosen for analysis, S235JR carbon steel and CEM II/B based concrete, are commonly used as reference materials in Hungarian disposal concepts. However, the findings are applicable to other disposal systems and engineering barriers as well.

During the experiments, it was observed that a uniform corrosion process occurred, resulting in the rapid passivation of the C-steel cylinders. Throughout the entire 12-month duration of the experiment, magnetite was identified as the primary corrosion product, even after only 3 months of exposure.

Modelling revealed that the increase in temperature and lateral diffusion of the concrete pore water led to a slight decrease in pH and chloride concentrations, as well as an increase in sulphate concentration due to the dissolution of ettringite. However, these chemical changes did not significantly affect the passivation corrosion process. Although the formation of Fe-siliceous hydrogarnets was thermodynamically possible at 80 °C, it did not hinder the formation of magnetite.

Overall, these results indicate that the containers would have a long lifespan under the studied disposal conditions.

6. Conclusion and perspectives

The combined modelling-experimental approach developed within Subtask 2.2 of the ACED work package of EURAD allowed to study the carbon steel/cementitious material interactions occurring at 80°C. The pH effect on anoxic corrosion processes has been investigated by performing in situ and laboratory mock-up experiments involving classic CEM I and CEM II cements ($\text{pH} > 12$) as well as a low-pH cement grout ($10 < \text{pH} < 11$) called BCG. The geochemical evolution of such carbon steel/cementitious material systems has also been characterized for both perfect and imperfect (presence of spatial heterogeneity between steel and cement) interfaces.

Corrosion processes, cementitious materials' evolution and pore water monitoring were assessed over a period ranging from one to two years of interaction. SEM, XRD and μ -Raman spectroscopy analyses supported by geochemical modelling allowed a full characterization of the corrosion mechanism. The corrosion rates were estimated by continuous monitoring thanks to electrochemical measurements and electrical corrosion sensors as well as by post mortem analyses (weight loss and optical measurements).

Thermodynamic work was done to better understand the conditions favouring Fe-containing hydrates phases formation and stability. A new structurally consistent solid solution model (CASH+ solid solution) was also developed to be able to accurately model the C-S-H phase in equilibrium solid- and pore-water composition of hydrated (blended) cement materials.

In the presence of a highly alkaline cementitious material (CEM I/CEM II), generalized corrosion was observed and very low corrosion rates were obtained confirming previous literature data. In the presence of CEM II-based concrete, a rapid passivation of C-steel surface is observed thanks to magnetite precipitation. Modelling revealed that chemical changes induced by temperature increase did not significantly affect the passivation corrosion process. The corrosion rate of low carbon-steel in the presence of CEM I followed an exponential decay law and corrosion rates values dropped to less than 0.1 $\mu\text{m}/\text{year}$ within 100 days of interaction. Magnetite and Si-hydrogarnet were the only corrosion products observed in such high alkaline experiments. The study revealed that Si-hydrogarnet can form at the expense of magnetite provided that a source of silicon and calcium is available and that such elements can reach the metallic surface to form Si-hydrogarnet prior to reacting to form other phases such as C-S-H. In a tightly closed system, favouring very reductive corrosion and limiting ingress of elements from the cementitious material, magnetite will be predominant.

The results associated to carbon steel/low-pH cement grout interaction experiments showed that localized corrosion mechanism is observed for all the tests (mock-up and in situ) performed in presence of solid BCG material (direct or indirect interface) highlighting the leading role of such cementitious phase in steel corrosion processes. BCG material favoured the formation of corrosion cells that induce localized corrosion primarily due to the presence of sulphides in both CEM III-A and bentonite components and also to the important amount of residual oxygen able to easily migrate through such highly porous grout material. The corrosion sequence showed that iron sulphides and/or hydroxides are first formed locally in the anodic zone of the corrosion cell. Depending on the remaining amount of oxygen in the system, the depletion of sulphides led to the formation of either a dense magnetite layer or of a porous layer of iron hydroxides. This was observed for mock-up and in situ tests, respectively. Finally, the transformation of magnetite (or iron hydroxide) to iron silicates mixed with iron sulphides was observed in the corrosion sequence. Such transformation is facilitated by the dissolution of hydrated silica fume occurring at the vicinity of the cathodic area where hydroxyl ions are produced in combination with the release of a second source of sulphides, (probably included in blast slag furnace particles that dissolve with time and temperature). For mock-up tests, we observed that magnetite transformation into iron sulphides/silicates was a slow process because of the stability of the very dense magnetite layer acting as a diffusive barrier. For in situ experiments, we observed that the transformation of the more porous hydroxide species was faster and generated large amount of iron silicates in the corrosion product sequence. The corrosion rate measured for mock-up experiments exhibited initial values around

10 µm/year that seems to stabilize or decrease over time. Several pits with depth ranging from 10 to 100 µm were detected and optical measurements clearly indicated an increase of the number of damaged zones with time, rather than an increase of the pit depth. This observation suggests that the coalescence of these pits would eventually lead to a generalized corrosion process. This observation seems to be confirmed by the results from the in situ experiment that lasted for more than 2 years. SEM observations performed on in situ tests steel samples revealed a uniform CPs layer of around 230 µm that formed over a period of about two years. The high corrosion rate (115 µm/year) associated to such observation is confirmed by ER sensors in situ monitoring and would therefore be more than ten times superior to the corrosion rates obtained after one year of interaction in the corresponding mock-up tests. Such difference could be explained either by the higher amount of residual oxygen trapped in the BCG porosity or by the in situ heating conditions (from internal to external part of the system) that enhanced the renewal of BCG pore water at interface and thus favoured sulphide and oxygen ingress at the carbon steel surface or finally by the formation of a galvanic coupling between steel/argillite and steel/BCG contact zones. Eventually, the discrepancies existing between in situ and mock-up laboratory tests highlight the impact that experimental design can have on corrosion processes (corrosion product/rate) and thus emphasize the need to perform experimental investigation at different scale to gain relevant information regarding mass transfer and geochemical interactions.

Regarding the experiments dedicated to study the impact of microbial activity on carbon steel anoxic corrosion processes when exposed to BCG material at ambient temperatures, only limited information on the nature and density of the microbial population was obtained, limiting the interpretations of the results. However, some particular corrosion features were obtained and attributed to bacterial activity, as for example the formation of homogeneous iron sulphides layers in the mock-up tests. Since these mock-up tests didn't involve any solid BCG/argillite sample and since sulphide were not added to the synthetic solution, the formation of such iron sulphides species can only be originated from a biocatalysed sulphate reduction reaction.

Alongside to these experimental activities, modelling of the mock-up experiments involving either CEM I, CEM II or BCG has been performed to support the discussion on the nature and sequence of corrosion products of steel. Reassessed thermodynamic database relative to iron containing cement hydrates (Fe-hydrogarnet, CASH) were used within the reactive transport code HYTEC to model the initial chemistry and mineral assembly of all the materials (C-steel, CEM I, CEM II and BCG) at ambient temperature and their evolution when exposed to 80°C. These results have been used to design the chemistry of the synthetic pore waters used in the experiments. Globally, the modelling correctly tackles the specificities of the mock-up experiments with respect to the effect of temperature, of water chemistry and pH (from low pH cement to highly alkaline pH cement) and of the configuration (steel in contact with aqueous solutions vs. close contact between solid materials).

Perspectives

Having these first conclusions in mind, it appears that additional experimental and modelling studies are still required to ensure a better understanding of the anoxic corrosion processes taking place for such carbon steel/cementitious materials interfaces:

The nature of the first corrosion products formed on the metallic surface and its associated properties could strongly impact the future corrosion processes (and thus the corrosion rates). Performing corrosion experiments in anoxic/reductive conditions (long term DGR post closure condition) on carbon steel samples that have been already corroded in oxic conditions (interim storage of metallic elements) should help to better understand the effects induced by such initial corrosion products on the development of the global corrosion sequence.

Compared to the low corrosion rates measured at high alkaline pH (12.3 – 13), the relative increase of the corrosion rate at moderate alkaline pH (10.5 – 11.5) would require some complementary investigations with other low-pH cementitious systems than the ones studied in ACED.

Hydration of complex cementitious materials characterized by high water/cement ratio is not trivial and still difficult to predict by a numerical model, especially when temperature increases. For instance, the progressive degree of hydration of silica fume and slag should be better simulated.

At the same time, reactive transport models could be developed at the micron scale (representative elementary volume at continuum scale) for a better description of corrosion products layer development.

Relevant contributions of Task 2 to Task 3 and Task 4

Subtask 2.2 of the ACED work package of EURAD allowed to gain relevant information regarding corrosion processes impacting carbon steel/cementitious materials systems at high temperature (80°C) for relatively small scale (metal/cement interface) that could be used to model more complex systems at waste package scale (Task 3) and disposal scale (Task 4). Key parameters required by the models are corrosion rates (kinetics) as a function of pH and temperature, and the nature of the corrosion products (thermodynamics) under those pH – T conditions, as well as the evolution of these parameters over time (typically passivation by corrosion product layers). A subset of data has already been used in the modelling of task 4, especially the nature of the silicate corrosion products.

Data relative to both cementitious materials and pore water evolution when temperature increases should help to better describe the physico-chemical changes that may impact the system at higher scale.

The fact that initial localized corrosion processes can evolve with time (and pits coalescence process) to generalized (or non-localized) corrosion processes should also be taken into account for future modelling.

In the presence of solid argillite phases, the development of steel/BCG/argillite interfaces inducing galvanic coupling processes may lead to the formation of large corrosion cells that have to be taken into account in further modelling.

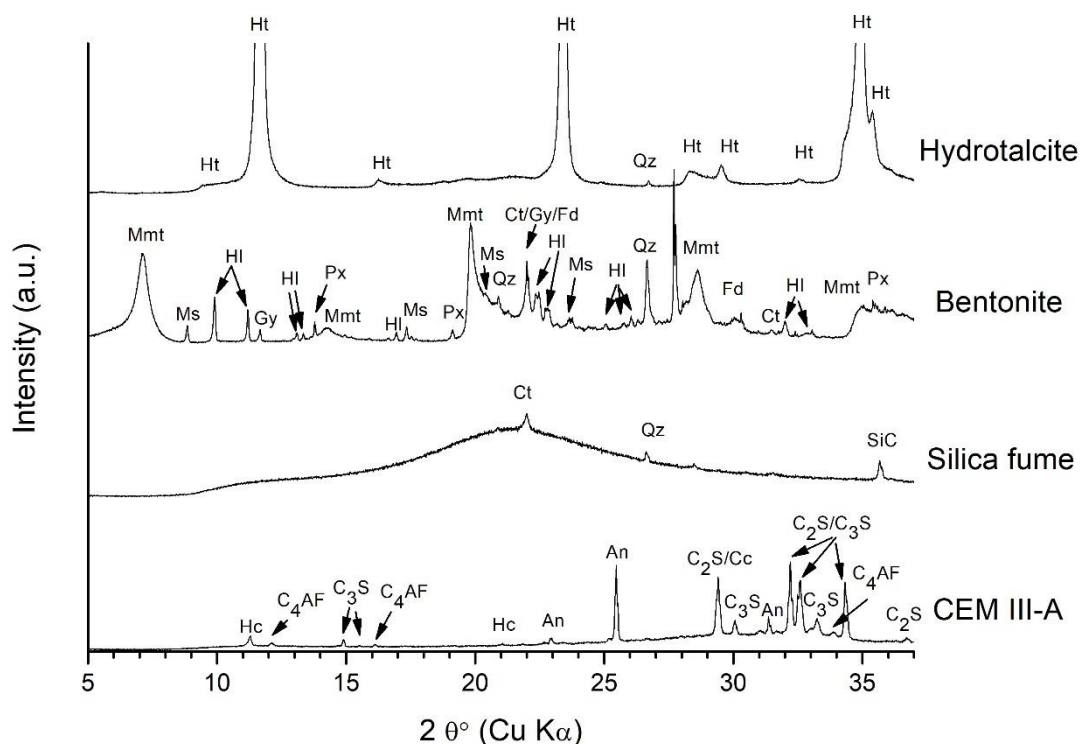
According to the physico-chemical conditions, the progressive transformation of initial iron oxy(hydr)oxides (goethite, magnetite) to iron silicates phases (greenalite, cronstedtite) should be considered for low-pH cement grout materials. The fact that the formation of such iron silicates constitutes a protective film passivating the metallic surface is also an important input for modelling.

The formation of iron rich hydrogarnet (hydroandradite – HA) at the expense of magnetite also represents an important information for modelling steel/CEM I interfaces occurring at high temperature. The passivating properties of hydroandradite phase have been demonstrated and should be taken into account for such interface evolution.

Appendixes

Appendix A.

XRD patterns of the precursors used for the synthesis of BCG



Appendix B.

Summary of the different leaching tests (different L/S ratios and contact times) performed to determine the BCG porewater composition, as well as chemical composition, pH and salinity values associated to each leaching test performed to determine the BCG porewater composition.

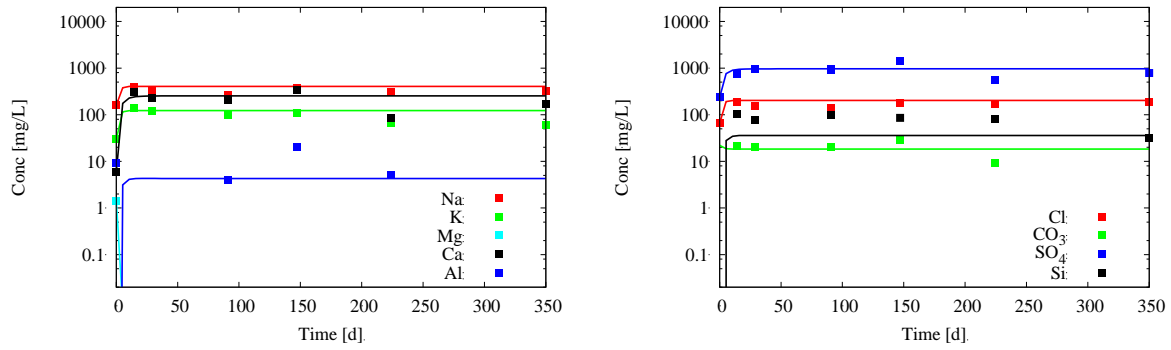
| Identification | ST1-9-24h | ST1-9-3j | ST1-9-7j | ST1-4-24h | ST1-4-3j | ST1-4-7j | ST1-1-24h | ST1-1-3j | ST1-1-7j |
|--|-----------|----------|----------|-----------|----------|----------|-----------|----------|----------|
| <i>liquid volume</i> <i>solide mass</i> | 9 ml/g | 9 ml/g | 9 ml/g | 4 ml/g | 4 ml/g | 4 ml/g | 1 ml/g | 1 ml/g | 1 ml/g |
| Contact time | 24h | 3 days | 7 days | 24h | 3 days | 7 days | 24h | 3 days | 7 days |

EURAD Deliverable D2.9 - Final technical report on the steel/cement material interactions

| Echantillons eau cimentaire | ST1-9-24h | ST1-9-3j | ST1-9-7j | ST1-4-24h | ST1-4-3j | ST1-4-7j | ST1-1-24h | ST1-1-3j | ST1-1-7j |
|-----------------------------|-----------|----------|----------|-----------|----------|----------|-----------|----------|----------|
| Eau/Roche (ml/g) | 9 | 9 | 9 | 4 | 4 | 4 | 1 | 1 | 1 |
| Durée turbula | 24 heures | 3 jours | 7 jours | 24 heures | 3 jours | 7 jours | 24 heures | 3 jours | 7 jours |
| pH | 11,4 | 11,3 | 11,4 | 11,5 | 11,4 | 11,4 | 11,4 | 11,33 | 11,3 |
| Conductivité (µS/cm) | 965 | 983 | 1025 | 1315 | 1375 | 1439 | 2360 | 2410 | 2530 |
| Salinité (g/l) | 0,4 | 0,4 | 0,5 | 0,6 | 0,6 | 0,7 | 1,2 | 1,2 | 1,3 |
| TC (mg/l) | 5,8 | 7,2 | - | 7,7 | 11,0 | - | 15,6 | 19,5 | - |
| TIC (mg/l) | 1,9 | 2,0 | - | 2,0 | 1,4 | - | 1,9 | 1,9 | - |
| TOC (mg/l) | 3,8 | 5,2 | - | 5,7 | 9,6 | - | 13,7 | 17,6 | - |
| TNB (mg/l) | 1,2 | 1,2 | - | 3,5 | 3,4 | - | 9,9 | 10,9 | - |
| Acetate (mmol/l) | 0,04 | 0,05 | 0,04 | 0,06 | 0,08 | 0,07 | 0,16 | 0,16 | 0,18 |
| Acétate (mg/l) | 2,45 | 2,67 | 2,61 | 3,78 | 4,45 | 4,25 | 9,68 | 9,62 | 10,77 |
| Formate (mmol/l) | 0,00 | 0,01 | 0,00 | 0,01 | 0,01 | 0,01 | 0,01 | 0,01 | 0,02 |
| Formate (mg/l) | 0,20 | 0,32 | 0,22 | 0,26 | 0,29 | 0,34 | 0,56 | 0,62 | 0,71 |
| Chlorure (mmol/l) | 1,09 | 1,13 | 1,15 | 2,25 | 2,40 | 2,40 | 6,60 | 6,56 | 6,85 |
| Chlorure (mg/l) | 38,56 | 40,10 | 40,87 | 79,89 | 84,97 | 84,97 | 233,94 | 232,50 | 242,75 |
| Nitrate (mmol/l) | 0,02 | 0,01 | 0,01 | 0,02 | 0,01 | 0,01 | 0,03 | 0,02 | 0,01 |
| Nitrate (mg/l) | 1,08 | 0,73 | 0,70 | 1,25 | 0,92 | 0,80 | 1,63 | 1,18 | 0,90 |
| Nitrite (mmol/l) | | 0,00 | | 0,00 | | 0,00 | 0,00 | 0,00 | 0,00 |
| Nitrite (mg/l) | - | 0,29 | - | 0,30 | - | 0,30 | 0,33 | 0,33 | 0,33 |
| Bromure (mmol/l) | | 0,01 | 0,01 | 0,01 | | 0,01 | 0,01 | | 0,01 |
| Bromure (mg/l) | - | 0,56 | 0,56 | 0,61 | - | 0,63 | 0,85 | - | 0,89 |
| Sulfate (mmol/l) | 0,51 | 0,63 | 1,11 | 0,79 | 1,21 | 1,77 | 2,80 | 3,75 | 3,21 |
| Sulfate (mg/l) | 48,96 | 60,13 | 106,31 | 75,83 | 116,39 | 169,59 | 268,95 | 360,67 | 308,23 |
| Iodure (mmol/l) | 0,99 | 1,23 | 1,30 | 2,38 | 3,02 | 2,95 | 6,76 | | 9,26 |
| Iodure (mg/l) | 125,19 | 156,59 | 164,72 | 302,00 | 383,79 | 374,74 | 858,12 | - | 1174,59 |
| Al (mmol/l) | 0,02 | 0,01 | 0,01 | 0,01 | 0,01 | 0,01 | 0,01 | 0,01 | 0,01 |
| Al (mg/l) | 0,41 | 0,34 | 0,25 | 0,37 | 0,34 | 0,20 | 0,29 | 0,28 | 0,14 |
| B (mmol/l) | 0,02 | 0,02 | 0,02 | 0,02 | 0,02 | 0,02 | 0,03 | 0,02 | 0,02 |
| B (mg/l) | 0,18 | 0,21 | 0,22 | 0,24 | 0,27 | 0,27 | 0,28 | 0,27 | 0,25 |
| Ca (mmol/l) | 1,18 | 1,40 | 1,60 | 1,37 | 1,55 | 1,77 | 2,42 | 2,99 | 3,16 |
| Ca (mg/l) | 47,22 | 56,16 | 64,30 | 54,91 | 62,11 | 71,10 | 97,03 | 119,83 | 126,66 |
| K (mmol/L) | 1,01 | 1,13 | 1,12 | 1,46 | 1,64 | 1,58 | 2,53 | 2,86 | 2,71 |
| K (mg/l) | 39,54 | 44,01 | 43,71 | 57,25 | 64,17 | 61,82 | 98,87 | 111,75 | 105,92 |
| Li (mmol/L) | 0,06 | 0,07 | 0,07 | 0,11 | 0,12 | 0,12 | 0,23 | 0,26 | 0,27 |
| Li (mg/l) | 0,44 | 0,49 | 0,51 | 0,75 | 0,84 | 0,85 | 1,63 | 1,77 | 1,84 |
| Mg (mmol/L) | 0,00 | 0,00 | 0,00 | 0,00 | 0,00 | 0,00 | 0,00 | 0,00 | 0,00 |
| Mg (mg/l) | 0,03 | 0,02 | 0,05 | 0,03 | 0,03 | 0,03 | 0,05 | 0,05 | 0,04 |
| Mo (mmol/L) | 0,00 | 0,00 | 0,00 | 0,00 | 0,00 | 0,00 | 0,00 | 0,00 | 0,00 |
| Mo (mg/l) | 0,02 | 0,02 | 0,02 | 0,04 | 0,05 | 0,04 | 0,11 | 0,09 | 0,13 |
| Na (mmol/L) | 3,00 | 3,28 | 3,31 | 5,18 | 5,66 | 5,45 | 10,83 | 12,00 | 11,76 |
| Na (mg/l) | 68,86 | 75,45 | 76,15 | 119,04 | 130,23 | 125,26 | 249,08 | 275,79 | 270,46 |
| Si (mmol/L) | 1,38 | 1,51 | 1,64 | 1,51 | 1,52 | 1,58 | 1,25 | 1,18 | 1,46 |
| Si (mg/l) | 38,83 | 42,30 | 46,08 | 42,32 | 42,70 | 44,45 | 34,99 | 33,20 | 41,00 |

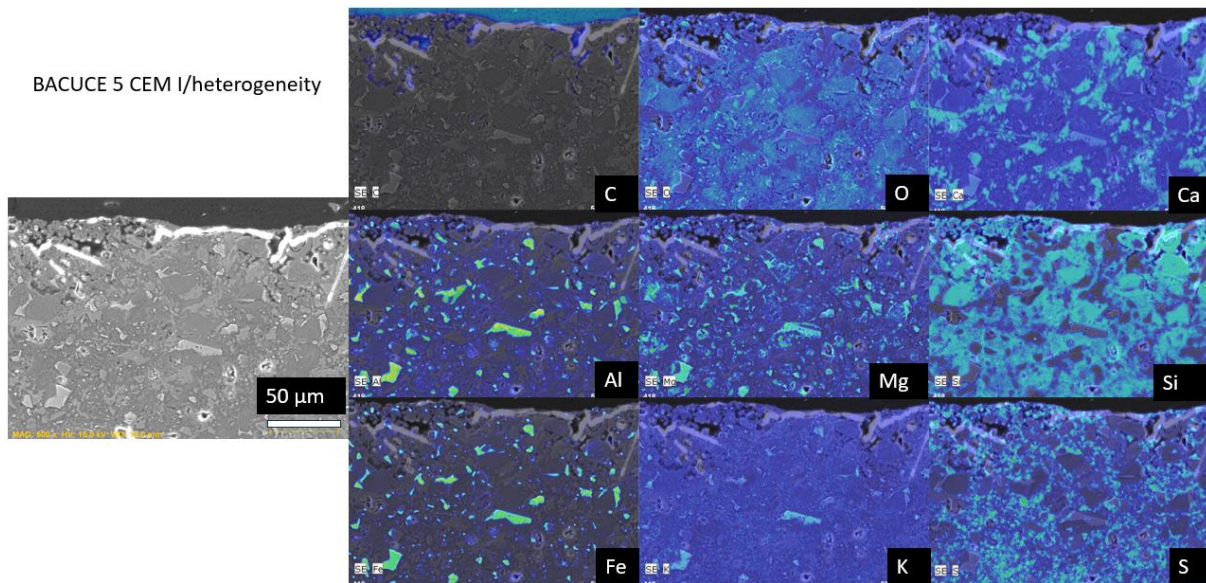
Appendix C.

Complement to the modelling of the BCG. Adjustment of the total concentrations of Na⁺, K⁺ and SO₄²⁻ (divided by a factor 2 approximately) on the experimental data (model 1).



Appendix D.

SEM-EDX mapping of the CEM I/heterogeneity of a sample coming from BACUCE 5 in situ experiment.



Appendix E.

Modelled mineralogical evolution of the CEM I paste

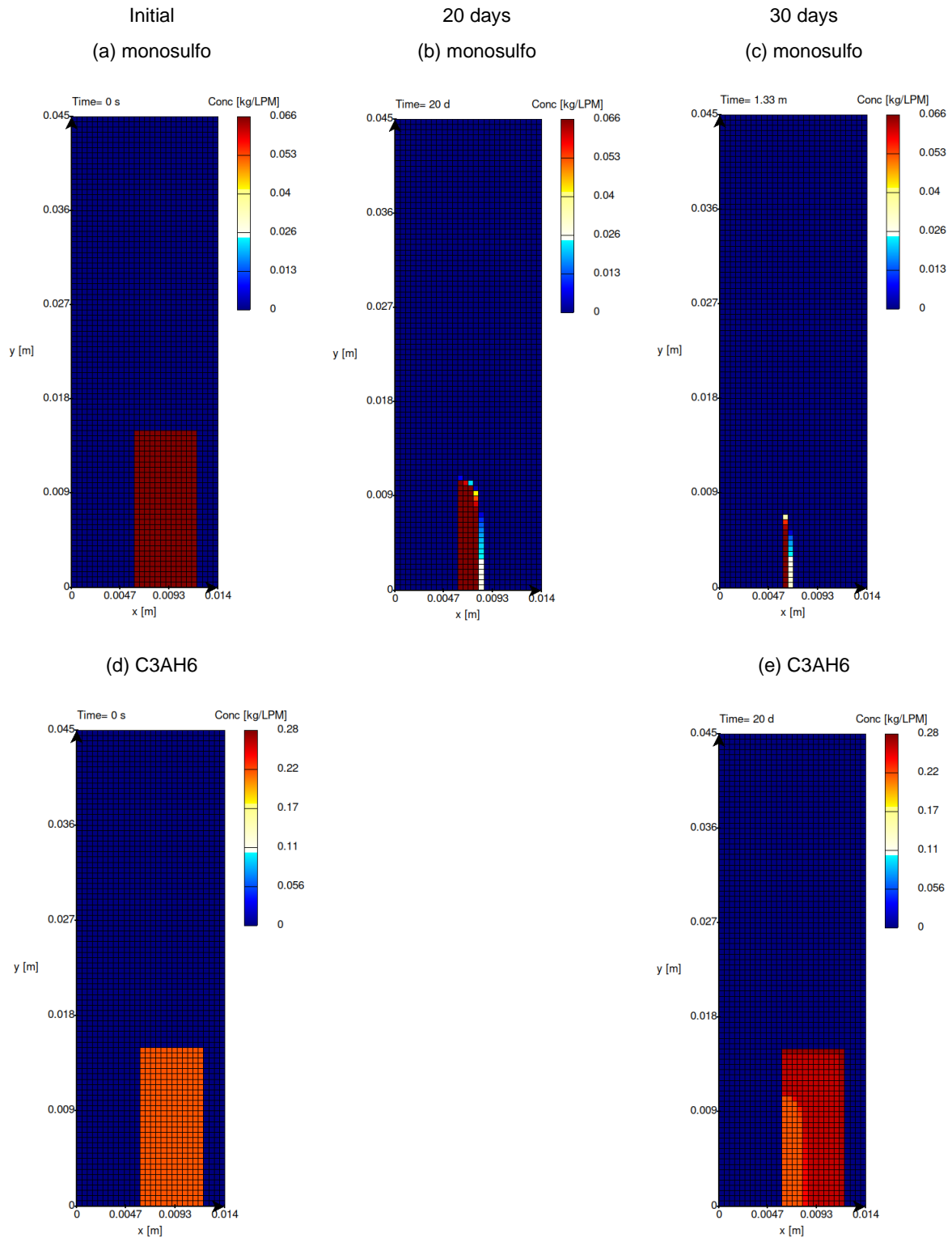


Figure E-1: Model 2 with C3AH6: progressive dissolution of monosulfoaluminate with a partial reprecipitation of Al as C3AH6.

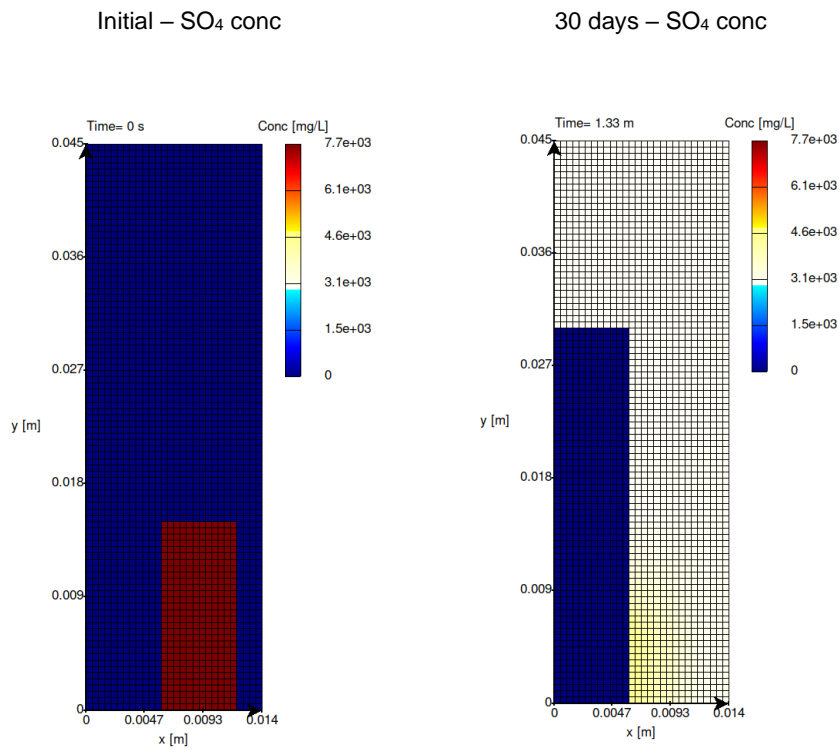


Figure E-2: Model 2 with C3AH6: progressive increase of the total aqueous concentration in sulfates inside the solution cell due to monosulfoaluminate dissolution.

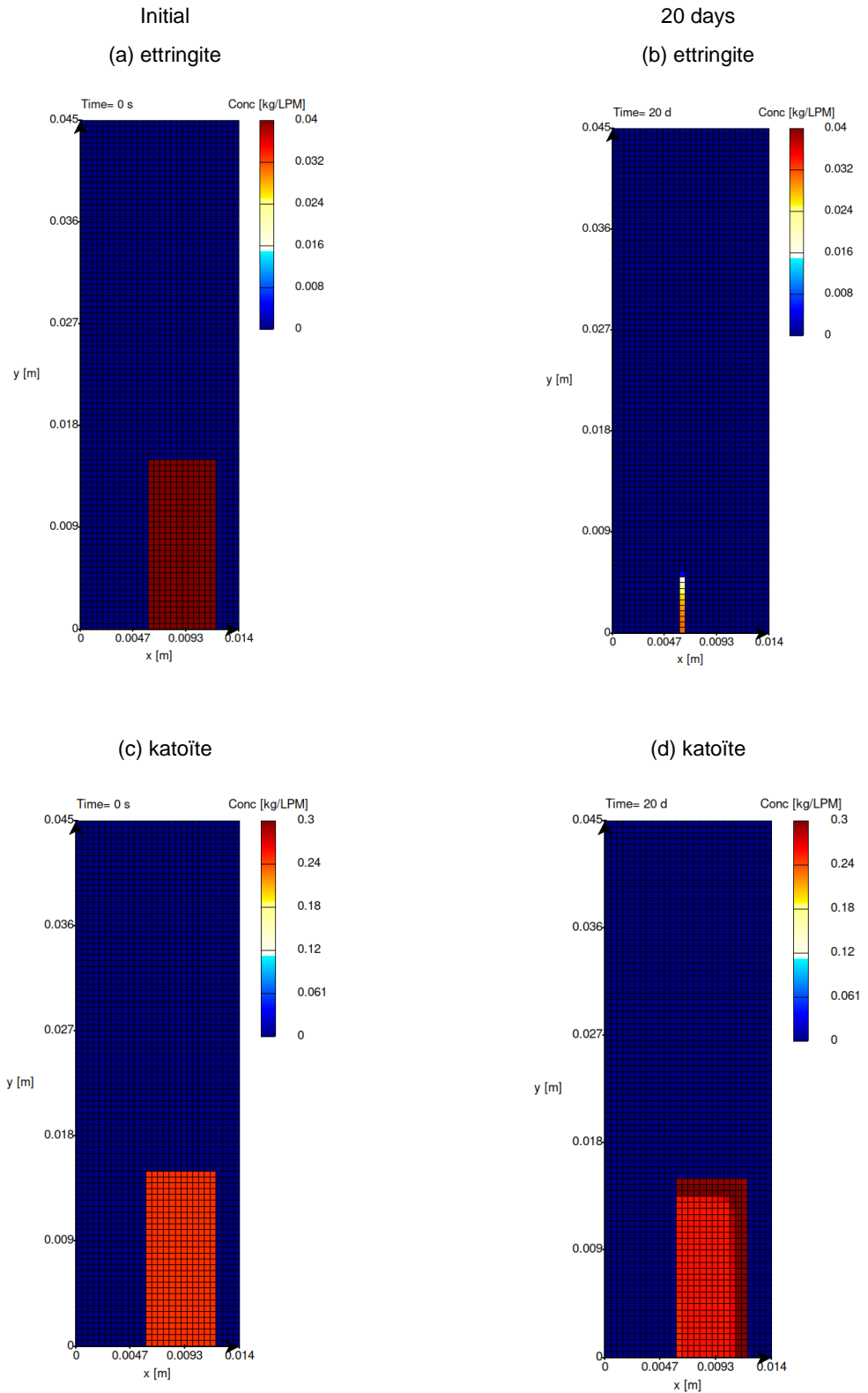


Figure E-3: Model 1 with katoïte: progressive dissolution of ettringite with a partial reprecipitation of Al as katoïte.

Initial

20 days

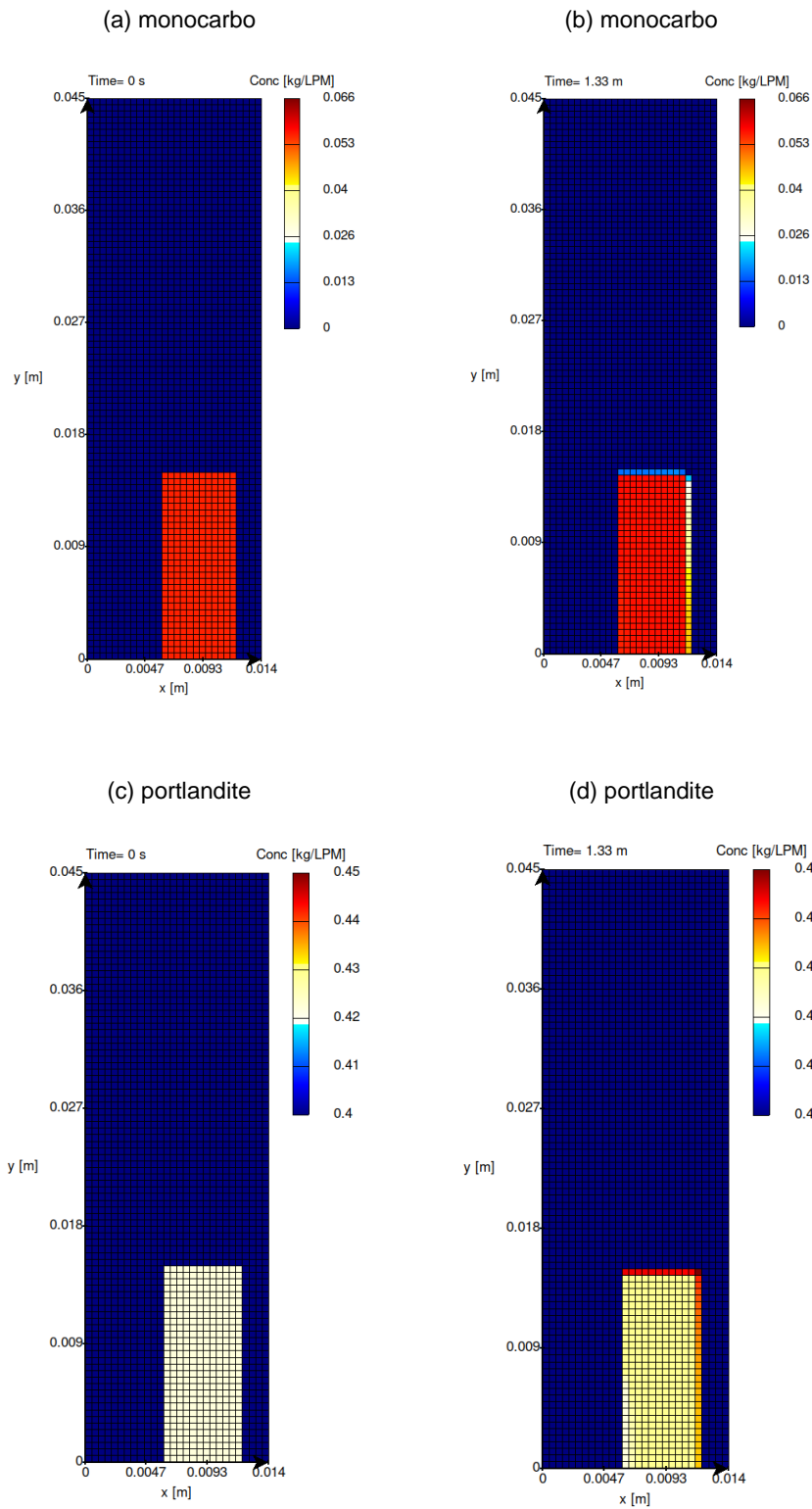
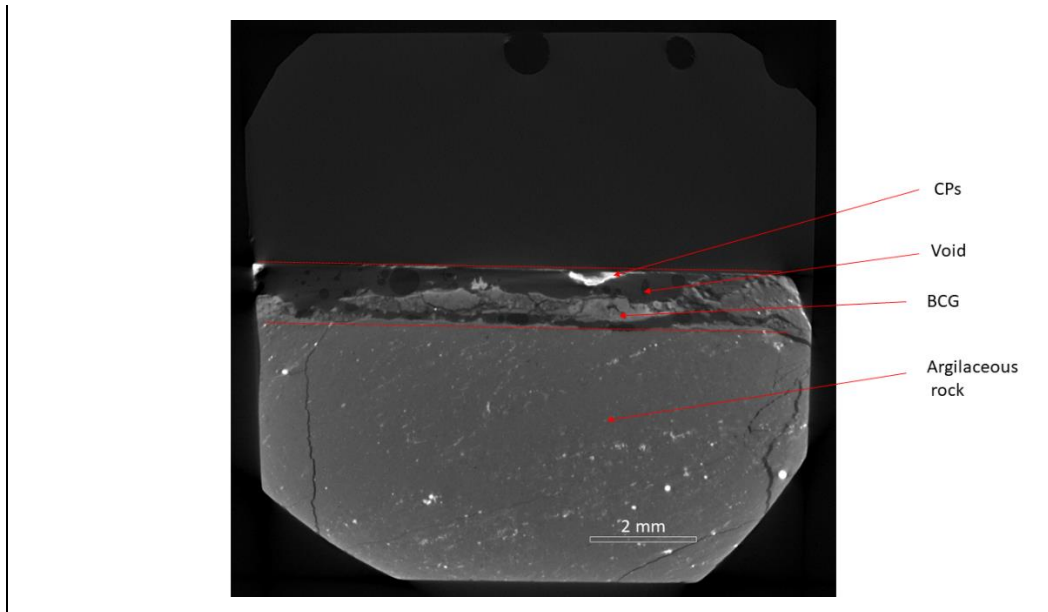


Figure E-4: Model 1 with katoite: coupled evolution of monocarboaluminate dissolution and portlandite precipitation.

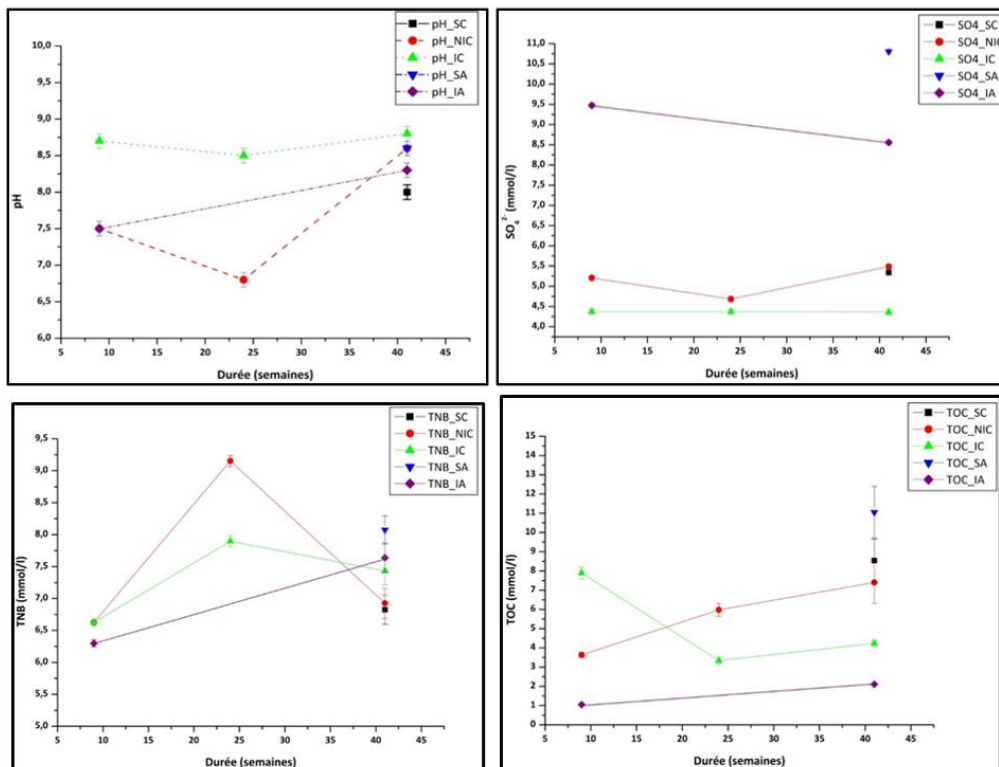
Appendix F.

X-ray μ -tomography scan of the interface between steel/BCG/argillite for a sample from BAC-1 in situ experiment



Appendix G.

Appendix B. pH and chemical evolution of the synthetic solutions used for mock-up test related to the impact of bacterial activity on corrosion



References

- Agullo, J., Bataillon, C., Michau, N., 2017. Preliminary electrochemical corrosion monitoring of iron in mixture cement paste–bentonite, *Corros. Eng. Sci. Technol.* 52, 155–161. doi:10.1080/1478422X.2017.1305675.
- Angst U M et al., The steel–concrete interface, *Materials and Structures* 50, 1-24 (2017).
- Angst, U., Elsener, B., Larsen, C.K., Vennesland, Ø. 2009. Critical chloride content in reinforced concrete - A review. *Cement and Concrete Research* 39, 1122–1138. <https://doi.org/10.1016/j.cemconres.2009.08.006>.
- ASTM. 2011. Standard Practice for Preparing, Cleaning, and Evaluating Corrosion Test Specimens., 19428–2959.
- Barbarulo, R., Peycelon, H., Leclercq, S., 2007. Chemical equilibria between C–S–H and ettringite, at 20 and 85 C. *Cement and Concrete Research*, 37 1176–1181.
- Barzgar, S., Tarik, M., Ludwig, C. & Lothenbach, B. (2021): The effect of equilibration time on Al uptake in C-S-H. *Cement and Concrete Research* 144, 106438.
- Benning, L.G., Wilkin, R.T., Barnes, H.L. 2000. Reaction pathways in the Fe-S system below 100°C. *Chemical Geology* 167, 25–51. [https://doi.org/10.1016/S0009-2541\(99\)00198-9](https://doi.org/10.1016/S0009-2541(99)00198-9).
- Bildstein, O., Claret, F., Frugier, P., 2019. RTM for Waste Repositories. *Reviews in Mineralogy and Geochemistry* 85, 419–457.
- Blanc, P., Lassin, A., Piantone, P., Azaroual, M., Jacquemet, N., Fabbri, A., Gaucher, E.C. 2012. Thermoddem: A geochemical database focused on low temperature water/rock interactions and waste materials. *Applied Geochemistry* 27, 2107–2116. <https://doi.org/10.1016/j.apgeochem.2012.06.002>.
- Bonnet, J., Mosser-Ruck, R., Sterpenich, J., Bourdelle, F., Verron, H., Michau, N., Bourbon, X., Linard, Y. 2022. Chemical and mineralogical characterizations of a low-pH cementitious material designed for the disposal cell of the high-level radioactive waste (HLW). *Cement and Concrete Research* 162, 107013.
- Bouakkaz, R., Abdelouas, A., El Mendili, Y., David, K., Grambow, B. 2019. Alteration of ²⁹Si-doped SON68 borosilicate nuclear waste glass in the presence of near field materials. *Applied Geochemistry* 111, 104436.
- Bouikni, A., Swamy, R.N., Bali, A. 2009. Durability properties of concrete containing 50% and 65% slag. *Construction and Building Materials* 23, 2836–2845. <https://doi.org/10.1016/j.conbuildmat.2009.02.040>.
- Bourdoiseau, J.A., Jeannin, M., Rémazeilles, C., Sabot, R., Refait, P. 2011. The transformation of mackinawite into greigite studied by Raman spectroscopy. *Journal of Raman Spectroscopy* 42, 496–504. <https://doi.org/10.1002/jrs.2729>.
- Bradbury, M.H., Baeyens, B., 2002. Sorption of Eu on Na- and Ca-montmorillonites: Experimental investigations and modelling with cation exchange and surface complexation. *Geochimica et Cosmochimica Acta* 66, 2325–2334.
- Carriere, C., Neff, D., Martin, C., Tocino, F., Delanoë, A., Gin, S., Michau, N., Linard, Y., Dillmann, P. 2020. AVM nuclear glass / steel / claystone system altered by Callovo – Oxfordian poral water with and without cement – bentonite grout at 70°C. *Materials Corrosion* 72, 474–482. <https://doi.org/10.1002/maco.202011766>.
- Charles, C. J., Rout, S. P., Garratt, E. J., Patel, K., Laws, A. P., Humphreys, P. N. 2017. Floc Formation Reduces the pH Stress Experienced by Microorganisms Living in Alkaline Environments. *Applied and Environmental Microbiology* 83:6.

- Chautard, C., 2013. Interactions fer/argile en conditions de stockage géologique profond - Impacts d'activités bactériennes et d'hétérogénéités, Ecole nationale supérieure des mines de Paris.
- Chomat L, Amblard E, Varlet J, Blanc C, Bourbon X, Passive corrosion of steel reinforcement in blended cement-based material in the context of nuclear waste disposal. *Corrosion Engineering, Science and Technology* 52, 148-154 (2017).
- Collier, N.C., Milestone, N.B., Hill, J., Godfrey, I.H. 2009. Immobilisation of Fe floc: Part 2, encapsulation of floc in composite cement. *Journal of Nuclear Materials* 393, 92-101.
- Cudennec, Y., Lecerf, A. 2006. The transformation of ferrihydrite into goethite or hematite, revisited. *Journal of Solid State Chemistry* 179, 716–722. <https://doi.org/10.1016/j.jssc.2005.11.030>.
- Dauzères, A. 2010. Etude expérimentale et modélisation des mécanismes physico-chimiques des interactions béton-argile dans le contexte du stockage géologique des déchets radioactifs. PhD thesis, Université de Poitiers (France).
- de Combarieu, G., Schlegel, M.L., Neff, D., Foy, E., Vantelon, D., Barboux, P., Gin, S. 2011. Glass-iron-clay interactions in a radioactive waste geological disposal: An integrated laboratory-scale experiment, *Applied Geochemistry* 26, 65–79. <https://doi.org/10.1016/j.apgeochem.2010.11.004>.
- De Windt L., Miron G. D., Fabian M., Goethals, J., Wittebroodt C. (2020). First results on the thermodynamic databases and reactive transport models for steel-cement interfaces at high temperature. Deliverable D2.8 of the HORIZON 2020 project EURAD. EC Grant agreement no: 847593.
- De Windt L., Samper J., Cochebin B., Garcia E., Mon A., Montenegro L., Samper A., Rimbault L., Veilly E. (2023). Integrated reactive transport models for assessing the chemical evolution at the disposal cell scale. Deliverable D2.17 of the HORIZON 2020 project EURAD. EC Grant agreement no: 847593.
- De Windt, L., Spycher, N., 2019. Reactive transport models for long-term safety assessment of nuclear waste disposal. *Elements* 15, 99–102.
- Deissmann G., Ait Mouheb N., Martin C., Name N., Jacques, D., Weetjens E., Kursten B., Leivo M., Somervuori, M., Carpen, L., 2020. Experiments and numerical model studies on interfaces. Deliverable D2.5 of the HORIZON 2020 project EURAD. EC Grant agreement no: 847593.
- Diler, E., Leblanc, V., Gueuné, H., Larché, N., Deydier, V., Linard, Y., Crusset, D., Thierry, D. 2021. Potential influence of microorganisms on the corrosion of carbon steel in the French high- and intermediate-level long-lived radioactive waste disposal context. *Materials Corrosion* 72, 218–234. <https://doi.org/https://doi.org/10.1002/maco.202011779>.
- Diler, E., Leblanc, V., Gueuné, H., Maillot, V., Linard, Y., Charrier, G., Crusset, D. 2023. Potential influence of microorganisms on the corrosion of the carbon steel in the French high-level long-lived nuclear waste disposal context at 50°C. *Materials and Corrosion*, 1-18.
- Dillmann, P., Gin, S., Neff, D., Gentaz, L., Rebiscoul, D. 2016. Effect of natural and synthetic iron corrosion products on silicate glass alteration processes. *Geochimica and Cosmochimica Acta* 172, 287–305. <https://doi.org/10.1016/j.gca.2015.09.033>.
- Dilnesa, B.Z. (2012): Fe-containing Hydrates and their Fate during Cement Hydration. <https://doi.org/10.5075/EPFL-THESIS-5262>
- Dilnesa, B.Z., Lothenbach, B., Le Saout, G., Renaudin, G., Mesbah, A., Filinchuk, Y., Wichser, A. & Wieland, E. (2011): Iron in carbonate containing AFm phases. *Cement and Concrete Research* 41, 311–323.
- Dilnesa, B.Z., Lothenbach, B., Renaudin, G., Wichser, A. & Wieland, E. (2012): Stability of monosulfate in the presence of iron. *Journal of the American Ceramic Society* 95, 3305–3316.

- Dilnesa, B.Z., Lothenbach, B., Renaudin, G., Wichser, A., Kulik, D., 2014a. Synthesis and characterization of hydrogarnet $\text{Ca}_3(\text{Al}_x\text{Fe}_{1-x})_2(\text{SiO}_4)_y(\text{OH})_{4(3-y)}$. *Cem. Concr. Res.* 59, 96–111.
- Dilnesa, B.Z., Wieland, E., Lothenbach, B., Dähn, R. & Scrivener, K.L. (2014b): Fe-containing phases in hydrated cements. *Cement and Concrete Research* 58, 45–55.
- Diomidis N, Scientific Basis for the Production of Gas due to Corrosion in a Deep Geological Repository, Nagra Working Report NAB, 14-21 (2014).
- El Mendili, Y., Abdelouas, A., Ait Chaou, A., Bardeau, J.F., Schlegel, M.L. 2014. Carbon steel corrosion in clay-rich environment. *Corrosion Science* 88, 56–65. <https://doi.org/10.1016/j.corsci.2014.07.020>.
- El Mendili, Y., Abdelouas, A., Bardeau, J.-F. 2013. Insight into the mechanism of carbon steel corrosion under aerobic and anaerobic conditions. *Physical Chemistry Chemical Physics* 15, 9197–9204.
- El Mendili, Y., Bardeau, J.F., Randrianantoandro, N., Greneche, J.M., Grasset, F. 2016. Structural behavior of laser-irradiated $\gamma\text{-Fe}_2\text{O}_3$ nanocrystals dispersed in porous silica matrix : $\gamma\text{-Fe}_2\text{O}_3$ to $\alpha\text{-Fe}_2\text{O}_3$ phase transition and formation of $\epsilon\text{-Fe}_2\text{O}_3$. *Science and Technology of Advanced Materials* 17, 597-609.
- Fabian, M., Czompoly, O., Tolnai, I., De Windt, L. (2023). Interactions between C-steel and blended cement in concrete under radwaste repository conditions at 80 °C. *Sci Rep* 13, 15372 . <https://doi.org/10.1038/s41598-023-42645-6>
- Feil F, Elter E, Otterbein J, Nenyey A, Reducing the volume of liquid radioactive waste at the MVM Paks Nuclear Power Plant (in Hungarian), *Nukleon VII.* 167-169 (2014).
- Gam, Z., Daumas, S., Casalot, L., Bartoli-Joseph, M., Necib, S., Linard, Y., Labat, M., 2016. *Thermanaeromonas burensis* sp. nov., a thermophilic anaerobe isolated from a subterranean clay environment, *Int. J. Syst. Evol. Microbiol.* 66, 445–449. doi:10.1099/ijsem.0.000739.
- Genchev, G. and Erbe, A. 2016. Raman Spectroscopy of Mackinawite FeS in Anodic Iron Sulfide Corrosion Products. *Journal of The Electrochemical Society* 163, C333–C338. <https://doi.org/10.1149/2.1151606jes>.
- Ghazizadeh, S., Hanein, T., Provis, J.L. & Matschei, T. (2020): Estimation of standard molar entropy of cement hydrates and clinker minerals. *Cement and Concrete Research* 136, 106188.
- Giffaut, E., Grivé, M., Blanc, P., Vieillard, P., Colàs, E., Gailhanou, H., Gaboreau, S., Marty, N., Madé, B., Duro, L., 2019. Andra thermodynamic database for performance assessment: *ThermoChimie, Appl. Geochem.* 49, 225–236.
- Glasser, L. & Jenkins, H.D.B. (2016): Predictive thermodynamics for ionic solids and liquids. *Physical Chemistry Chemical Physics* 18, 21226–21240.
- Glasser, L. (2021): The effective volumes of waters of crystallization & the thermodynamics of cementitious materials. *Cement* 3, 100004.
- Goethals, J., de Windt, L., Wittebroodt, C., Abdelouas, A., de la Bernardie, X., Morizet, Y., Zajec, B., Detilleux, V. 2023. Interaction between carbon steel and low-pH bentonitic cement grout in anoxic, high temperature (80 °C) and spatially heterogeneous conditions. *Corrosion Science* 211, p. 110852.
- Grousset, S., Urios, L., Mostefaoui, S., Dauzères, A., Crusset, D., Deydier, V., Linard, Y., Dillmann P., Mercier-Bion, F., Neff, D. 2020. Biocorrosion detection by sulphur isotopic fractionation measurements. *Corrosion Science* 165. <https://doi.org/10.1016/j.corsci.2019.108386>.
- Hallet, V., Pedersen, M.T., Lothenbach, B., Winnefeld, F., Eykens, L., De Belie, N. & Pontikes, Y. (2023): The hydration of ternary blended cements with Fe-rich slag from non-ferrous metallurgy and limestone. *Cement and Concrete Research* 169, 107155.

- Hanesch, M. 2009. Raman spectroscopy of iron oxides and (oxy)hydroxides at low laser power and possible applications in environmental magnetic studies. *Geophysical Journal International* 177, 941–948. <https://doi.org/10.1111/j.1365-246X.2009.04122.x>.
- Helgeson, H.C., Delany, J.M., Nesbitt, H.W. & Bird, D.K. (1978): Summary and critique of the thermodynamic properties of rock-forming minerals. *American Journal of Science* 278A, 1–229.
- Honti G, NRWR-National Radioactive Waste Repository, Ed. Gabriella Honti, https://rhk.hu/storage/338/NRHT_nagy-_angol_kicsi.pdf (2019).
- Hummel, W. & Thoenen, T. (2021): The PSI Chemical Thermodynamic Database 2020. Nagra Technical Report, NTB 21-03. Villigen, Switzerland.
- Hunger, S., Benning, L.G. 2007. Greigite: A true intermediate on the polysulfide pathway to pyrite. *Geochemical Transactions* 8, 1–20. <https://doi.org/10.1186/1467-4866-8-1>.
- IAEA-NS-ARTEMIS Integrated review service for radioactive waste and spent fuel management, decommissioning and remediation (ARTEMIS), 2022 Ed. Department of Nuclear Safety and Security (https://www.iaea.org/sites/default/files/documents/review-missions/final_artermis_report_-_hungary.pdf) Accessed 26 June 2023
- Kulik, D.A., Miron, G.D. & Lothenbach, B. (2022): A structurally-consistent CASH+ sublattice solid solution model for fully hydrated C-S-H phases: Thermodynamic basis, methods, and Ca-Si-H₂O core sub-model. *Cement and Concrete Research* 151, 106585.
- Kulik, D.A., Wagner, T., Dmytrieva, S. V., Kosakowski, G., Hingerl, F.F., Chudnenko, K. V. & Berner, U.R. (2013): GEM-Selektor geochemical modeling package: Revised algorithm and GEMS3K numerical kernel for coupled simulation codes. *Computational Geosciences* 17, 1–24.
- Kyritsis, K., Meller, N., Hall, C. 2009. Chemistry and Morphology of Hydrogarnets Formed in Cement-Based CASH Hydroceramics Cured at 200°C to 350°C. *Journal of the American Ceramic Society* 92, 1105-1111.
- Lafuente, B., Downs, R. T., Yang, H., Stone, N. 2015. The power of databases: the RRUFF project., in: *Highlights in Mineralogical Crystallography*. T Armbruster R M Danisi, Eds. Berlin, Ger. W. Gruyter, 2015: pp. 1–30.
- Lalan, P., Dauzères, A., De Windt, L., Bartier, D., Sammaljärvi, J., Barnichon, J.D., Techer, I., Detilleux, V., 2016. Impact of a 70 °C temperature on an ordinary Portland cement paste/claystone interface: An in situ experiment, *Cement and Concrete Research* 83, 164-178.
- Lalan, P., Dauzères, A., De Windt, L., Sammaljärvi, J., Bartier, D., Techer, I., Detilleux, V., Siitari-Kauppi, M., 2019. Mineralogical and microstructural evolution of Portland cement paste/argillite interfaces at 70 °C – Considerations for diffusion and porosity properties. *Cement and Concrete Research* 115, 414–425.
- Lanson, B., Lantenois, S., Van Aken, P.A., Bauer, A., Plançon, A. 2012. Experimental investigation of smectite interaction with metal iron at 80 °c: Structural characterization of newly formed Fe-rich phyllosilicates. *American Mineralogist* 97, 864–871. <https://doi.org/10.2138/am.2012.4062>.
- Litvan, G.G. and Meyer, A. Carbonation of granulated blast furnace slag cement concrete during twenty years of field exposure. 1986. ICA Special Publication, in: 91, Fly, Ash, Silica Fume, Slag, and Natural Pozzolans in Concrete: Proceeding of the 2nd International Conference: 1986, Madrid, Spain, 1986, pp. 1445–1462. Collection: NRC Publications Archive.
- Lothenbach B, Scrivener K, Hooton R D, Supplementary cementitious materials, *Cement and Concrete Research* 41, 1244-1256 (2011).
- Lothenbach L, Le Saout G, Ben Haha M, Figi R, Wieland E, Hydration of a low-alkali CEM III/B–SiO₂ cement (LAC), *Cement and Concrete Research* 42, 410–423 (2012).

- Lothenbach, B., Kulik, D.A., Matschei, T., Balonis, M., Baquerizo, L., Dilnesa, B., Miron, G.D. & Myers, R.J. (2019): Cemdata18: A chemical thermodynamic database for hydrated Portland cements and alkali-activated materials. *Cement and Concrete Research* 115, 472–506.
- Lothenbach, B., Matschei, T., Möschner, G., Glasser, F.P., 2008. Thermodynamic modelling of the effect of temperature on the hydration and porosity of Portland cement. *Cem. Concr. Res.* 38, 1–18.
- Lublóy E, Kopecko K, Balazs G L, Szilagyí I M, Madarasz J, Improved fire resistance by using slag cements, *J Therm Anal Calorim* 125, 271-279 (2016).
- Mancini, A., Wieland, E., Geng, G., Dähn, R., Skibsted, J., Wehrli, B. & Lothenbach, B. (2020): Fe(III) uptake by calcium silicate hydrates. *Applied Geochemistry* 113.
- Mancini, A., Wieland, E., Geng, G., Lothenbach, B., Wehrli, B. & Dähn, R. (2021): Fe(II) interaction with cement phases: Method development, wet chemical studies and X-ray absorption spectroscopy. *Journal of Colloid and Interface Science* 588, 692–704.
- Marques Fernandes, M., Baeyens, B., Dähn, R., Scheinost, A.C., Bradbury, M.H. (2012). U(VI) Sorption on Montmorillonite in the Absence and Presence of Carbonate: A Macroscopic and Microscopic Study. *Geochimica et Cosmochimica Acta* 93, 262–277.
- Matray, J.-M., Savoye, S., Cabrera, J., 2007. Desaturation and structure relationships around drifts excavated in the well-compacted Tournemire's argillite (Aveyron, France). *Engineering Geology* 90, 1–16.
- Miron, G.D., Kulik, D.A. & Lothenbach, B. (2022a): Porewater compositions of Portland cement with and without silica fume calculated using the fine-tuned CASH+NK solid solution model. *Materials and Structures* 2022 55:8 55, 1–13.
- Miron, G.D., Kulik, D.A., Yan, Y., Tits, J. & Lothenbach, B. (2022b): Extensions of CASH+ thermodynamic solid solution model for the uptake of alkali metals and alkaline earth metals in C-S-H. *Cement and Concrete Research* 152, 106667.
- Miron, G.D., Leal, A.M.M., Dmytrieva, S. V. & Kulik, D.A. (2023): ThermoFun: A C++/Python library for computing standard thermodynamic properties of substances and reactions across wide ranges of temperatures and pressures. *Journal of Open Source Software* 8, 4624.
- Möschner, G., Lothenbach, B., Rose, J., Ulrich, A., Figi, R. & Kretzschmar, R. (2008): Solubility of Fe-ettringite ($\text{Ca}_6[\text{Fe}(\text{OH})_6]_2(\text{SO}_4)_3 \cdot 26\text{H}_2\text{O}$). *Geochimica et Cosmochimica Acta* 72, 1–18.
- Möschner, G., Lothenbach, B., Winnefeld, F., Ulrich, A., Figi, R. & Kretzschmar, R. (2009): Solid solution between Al-ettringite and Fe-ettringite ($\text{Ca}_6[\text{Al}_1 - x\text{Fe}_x(\text{OH})_6]_2(\text{SO}_4)_3 \cdot 26\text{H}_2\text{O}$). *Cement and Concrete Research* 39, 482–489.
- Necib, S., Linard, Y., Crusset, D., Michau, N., Dumas, S., Burger, E., Romaine, A., Schlegel, M.L., 2016. Corrosion at the carbon steel–clay borehole water and gas interfaces at 85 °C under anoxic and transient acidic conditions, *Corrosion Science* 111, 242–258. doi:10.1016/j.corsci.2016.04.039.
- Ni, C., Wu, Q., Yu, Z., Shen, X. 2021. Hydration of Portland cement paste mixed with densified silica fume: From the point of view of fineness. *Construction Building Materials* 272. <https://doi.org/10.1016/j.conbuildmat.2020.121906>.
- Nos B, Needs of countries with longer timescale for deep geological repository implementation, *EPJ Nuclear Sci. Technol.* 6, 22 (2020).
- Osborne, G.J. 1986. Carbonation of blast furnace slag cement concretes. *Durability of Building Materials* 4, 81–96.
- Page, C., Short, N., El Tarras, A., 1981. Diffusion of chloride ions in hardened cement pastes. *Cement and Concrete Research* 11, 395–406.

- Pally, D., Le Bescop, P., Schlegel, M.L., Miserque, F., Chomat, L., Neff, D., L'Hostis, V. 2020. Corrosion behavior of iron plates in cementitious solution at 80 °C in anaerobic conditions, *Corrosion Science* 170, 108650. <https://doi.org/10.1016/j.corsci.2020.108650>.
- Parkhurst, D.L. & Appelo, C. a. J. (2013): Description of Input and Examples for PHREEQC Version 3 — A Computer Program for Speciation, Batch-Reaction, One-Dimensional Transport, and Inverse Geochemical Calculations. U.S. Geological Survey Techniques and Methods, book 6, chapter A43, 497 p., Techniques and Methods, book 6, chapter A43. U.S. Geological Survey.
- Pignatelli, I., Bourdelle, F., Bartier, D., Mosser-Ruck, R., Truche, L., Mugnaioli, E., Michau, N. 2014. Iron-clay interactions: Detailed study of the mineralogical transformation of claystone with emphasis on the formation of iron-rich T-O phyllosilicates in a step-by-step cooling experiment from 90 degrees Celsius to 40 degrees Celsius. *Chemical Geology* 387, 1–11. <https://doi.org/10.1016/j.chemgeo.2014.08.010>.
- Pignatelli, I., Mosser-Ruck, R., Mugnaioli, E., Sterpenich, J., Gemmi, M. 2020. The Effect of the Starting Mineralogical Mixture on the Nature of Fe-Serpentines Obtained during Hydrothermal Synthesis AT 90 degrees Celsius. *Clays and Clay Minerals* 68, 394–412.
- Pignatelli, I., Mugnaioli, E., Marrocchi, Y. 2018. Cronstedtite polytypes in the Paris meteorite. *European Journal of Mineralogy* 30, 349–354. <https://doi.org/10.1127/ejm/2018/0030-2713>.
- Pitty, A., Alexander, R. 2011. (Eds.), Maqarin Phase IV Report, NDA RWMD516 2011. <https://nora.nerc.ac.uk/id/eprint/20953/>
- Qin, Z., Demko, B., Noël, J., Shoesmith, D., King, F., Worthingham, R., Keith, K. 2004. Localized dissolution of millscale-covered pipeline steel surfaces. *Corrosion* 60, 906–914. <https://doi.org/10.5006/1.3287824>.
- Rémazeilles, C., Saheb, M., Neff, D., Guilminot, E., Tran, K., Bourdoiseau, J.A., Sabot, R., Jeannin, M., Matthiesen, H., Dillmann, P., Refait, P. 2010. Microbiologically influenced corrosion of archaeological artefacts: Characterisation of iron(II) sulfides by Raman spectroscopy, *Journal of Raman Spectroscopy* 41, 1425–1433. <https://doi.org/10.1002/jrs.2717>.
- Rizoulis, A., Steele, H. M., Morris, K., Lloyd, J. R. 2012. The potential impact of anaerobic microbial metabolism during the geological disposal of intermediate-level waste. *Mineralogical Magazine* 76, 3261.
- Robie, R. & Hemingway, B.S. (1995): Thermodynamic Properties of Minerals and Related Substances at 298.15K and 1 Bar, U.S. Geological Survey Bulletin.
- Robineau, M., Deydier, V., Crusset, D., Bellefleur, A., Neff, D., Vega, E., Sabot, R., Jeannin, M., Refait, P. 2021. Formation of iron sulfides on carbon steel in a specific cement grout designed for radioactive waste repository and associated corrosion mechanisms. *Materials (Basel)*. 14. <https://doi.org/10.3390/ma14133563>.
- Robineau, M., Romaine, A., Sabot, R., Jeannin, M., Deydier, V., Necib, S., Refait, P. 2017. Galvanic corrosion of carbon steel in anoxic conditions at 80 °C associated with a heterogeneous magnetite (Fe₃O₄)/mackinawite (FeS) layer, *Electrochimica Acta* 255, 274–285. <https://doi.org/10.1016/j.electacta.2017.09.183>.
- Robineau, M., Sabot, R., Jeannin, M., Deydier, V., Crusset, D., Refait, P. 2020. Mechanisms of localized corrosion of carbon steel associated with magnetite/mackinawite layers in a cement grout. *Materials Corrosion* 72, 194–210. <https://doi.org/10.1002/maco.202011696>.
- Robineau, M. 2023. Personal communication at EuroCorr2023.
- Roy, A. 2009. Sulfur speciation in granulated blast furnace slag: An X-ray absorption spectroscopic investigation. *Cement and Concrete Research* 39, 659–663. <https://doi.org/10.1016/j.cemconres.2009.05.007>.

- Schlegel, M.L., Bataillon, C., Brucker, F., Blanc, C., Prêt, D., Foy, E., Chorro, M. 2014. Corrosion of metal iron in contact with anoxic clay at 90°C: Characterization of the corrosion products after two years of interaction. *Applied Geochemistry*. 51, 1–14. <https://doi.org/10.1016/j.apgeochem.2014.09.002>.
- Schlegel, M.L., Martin, F., Fenart, M., Blanc, C., Varlet, J., Foy, E., Prêt, D., Trcera, N. 2019. Corrosion at the carbon steel-clay compact interface at 90°C: Insight into short- and long-term corrosion aspects. *Corrosion Science* 152, 31–44. <https://doi.org/10.1016/j.corsci.2019.01.027>.
- Scott, P.W., Critchley, S.R., Wilkinson, F.C.F. 1986. The chemistry and mineralogy of some granulated and pelletized blast furnace slags. *Mineralogical Magazine* 50, 141–147. <https://doi.org/10.1180/minmag.1986.050.355.19>.
- Shannon L W H, Electronic Thesis and Dissertation Rep. The University of Western Ontario, Graduate program in Chemistry (2016).
- Sherar, B.W.A., Keech, P.G., Shoesmith, D.W. 2011. Carbon steel corrosion under anaerobic-aerobic cycling conditions in near-neutral pH saline solutions - Part 1: Long term corrosion behaviour. *Corrosion Science* 53, 3636–3642. <https://doi.org/10.1016/j.corsci.2011.07.015>.
- Sherar, B.W.A., Keech, P.G., Shoesmith, D.W. 2011. Carbon steel corrosion under anaerobic-aerobic cycling conditions in near-neutral pH saline solutions. Part 2: Corrosion mechanism. *Corrosion Science* 53, 3643–3650. <https://doi.org/10.1016/j.corsci.2011.07.008>.
- Sherar, B.W.A., Keech, P.G., Shoesmith, D.W. 2013. The effect of sulfide on the aerobic corrosion of carbon steel in near-neutral pH saline solutions. *Corrosion Science* 66, 256–262. <https://doi.org/10.1016/j.corsci.2012.09.027>.
- Sherar, B.W.A., Power, I.M., Keech, P.G., Mitlin, S., Southam, G., Shoesmith, D.W. 2011. Characterizing the effect of carbon steel exposure in sulfide containing solutions to microbially induced corrosion. *Corrosion Science* 53, 955–960. <https://doi.org/10.1016/j.corsci.2010.11.027>.
- SikaFume HR/TU, Product Data Sheet, 2009 https://hun.sika.com/content/dam/dms/hucon/6/sikafume_hrtu_hu0910ta.pdf Accessed 26 June 2023
- Siramanont, J., Walder, B.J., Emsley, L. & Bowen, P. (2021): Iron incorporation in synthetic precipitated calcium silicate hydrates. *Cement and Concrete Research* 142, 106365.
- Sisomphon, K. and Franke, L. 2007. Carbonation rates of concretes containing high volume of pozzolanic materials. *Cement and Concrete Research* 37, 1647–1653. <https://doi.org/10.1016/j.cemconres.2007.08.014>.
- Smart N R, Corrosion behavior of carbon steel radioactive waste packages: A summary review of Swedish and U.K. Research, *Corrosion* 65(3), 195-212 (2009), <https://doi.org/10.5006/1.3319128>
- Smart, N.R., Rance, A.P., Nixon, D.J., Fennell, P.A.H., Reddy, B., Kursten, B. 2017. Summary of studies on the anaerobic corrosion of carbon steel in alkaline media in support of the Belgian supercontainer concept. *Corrosion Engineering Science and Technology* 52, 217–226. <https://doi.org/10.1080/1478422X.2017.1356981>.
- Stefanoni, M., Angst, U. & Elsener, B. (2020): The mechanism controlling corrosion of steel in carbonated cementitious materials in wetting and drying exposure. *Cement and Concrete Composites* 113, 103717.
- Takai, K., Moser, D. P., Onstott, T. C., Spoelstra, N., Pfiffner, S. M., Dohnalkova, A., Fredrickson, J. K. 2001. *Alkaliphilus transvaalensis* gen. nov., sp. nov., an extremely alkaliphilic bacterium isolated from a deep South African gold mine. *International Journal of Systematic and Evolutionary microbiology* 51:4, 1245.

- Tinseau, E., Bartier, D., Hassouta, L., Devol-Brown, I., Stammose, D., 2006. Mineralogical characterization of the Tournemire argillite after in situ interaction with concrete. *Waste Management* 26, 789-800.
- Van der Lee, J., De Windt, L., Lagneau, Goblet, P., 2003. Module-oriented modeling of reactive transport with HYTEC. *Computers and Geosciences* 29, 265–275.
- Wieland, E., Miron, G.D., Ma, B., Geng, G., Lothenbach, B. 2023. Speciation of iron(II/III) at the iron-cement interface: a review. *Materials and Structure* 56:31.
- Wilkin, R.T., Barnes, H.L. 1996. Pyrite formation by reactions of iron monosulfides with dissolved inorganic and organic sulfur species. *Geochimica and Cosmochimica Acta* 60, 4167–4179. [https://doi.org/10.1016/S0016-7037\(97\)81466-4](https://doi.org/10.1016/S0016-7037(97)81466-4).
- Wittebroodt, C., Savoye, S., Frasca, B., Gouze, P., Michelot, J.-L., 2012. Diffusion of HTO, ³⁶Cl- and ¹²⁵I- in Upper Toarcian argillite samples from Tournemire: Effect of initial iodide concentration and ionic strength. *Applied Geochemistry* 27, issue 7, 1432-1441.
- Yan, Y. (2022): Effect of alkali, aluminium and equilibration time on calcium-silicate-hydrates. <https://doi.org/10.5075/EPFL-THESIS-9572>
- Yan, Y., Bernard, E., Miron, G.D., Rentsch, D., Ma, B., Scrivener, K. & Lothenbach, B. (2023): Kinetics of Al uptake in synthetic calcium silicate hydrate (C-S-H). *Cement and Concrete Research* 172, 107250.